Validation and development of extravascular bubble models for decompression sickness using collagen hydrogels

Claire Walsh

A dissertation submitted in partial fulfillment

of the requirements for the degree of

Doctor of Philosophy

of

University College London.

CoMPLEX

University College London

February 6, 2017

I, Claire Walsh, confirm that the work presented in this thesis is my own. Where information has been derived from other sources, I confirm that this has been indicated in the work.

Abstract

For over 200 years, the formation of bubbles in the body as a result of ambient pressure changes has been linked to decompression sickness (DCS). The mechanisms by which bubbles may lead to DCS are poorly understood, despite this long history of research. Mathematical modelling has played a key role in DCS prevention through the development of dive computer algorithms. Algorithms which incorporate mechanistic bubble models must make assumptions about a selected bubble property being statistically related to the incidence of DCS. This poses a problem for the validation of such algorithms. Given the uncertain relationship between the mechanistic model output and the symptoms of DCS, direct bubble observation is required to validate the mechanistic portion of the model; such measurements, however, are not currently possible *in vivo*. The use of biomimetic *in vitro* models provides a new research avenue to investigate the causal mechanism as well address the validation problem currently faced.

In the work described in this thesis an *in vitro* matrix model (collagen type I gel) was used to validate and further develop a 3D computational model of extravascular bubble dynamics. The collagen gels together with a microscope compatible pressure chamber provided the means to directly measure bubble formation and dynamics within the gels during decompression profiles. The effect of material and dive parameter variations on bubble growth was first investigated and validated. Bubble-bubble interaction and coalescence were then analysed. Both the computational and experimental results of these analyses indicated that a model of bubble nucleation would be essential to model bubble dynamics accurately. The possible nature and distribution of nucleation sites was investigated. Options for incorporation of the nucleation findings are analysed. Finally the influence of live cells bubble dynamics through oxygen consumption and the effect bubble proximity has on cell viability were investigated.

Acknowledgements

I would like to acknowledge some of the many people who have helped and supported me throughout my PhD. Firstly to my supervisors, Dr Umber Cheema, I would like to thank you for your unflinching optimism and encouragement in all aspects of my research. Dr Nick Ovenden, thank you for all the guidance and support you have given me throughout my years of study, I appreciate all the comments and insightful questions. To Professor Eleanor Stride, for so many useful pieces of advice which enabled me to solve problems I struggled to see through.

In addition I would like to thank several people for their specific expertise and advice. Rebecca Porter, you were there for every crisis, always with advice and practical solutions. Thanks to Dr Steve Taylor, for re-teaching me electronics I had forgotten. To Paul Rademayer and James Fisk, for much needed advice and expertise in pressure chamber building. To John Curchwell, for his help in acquiring and then understanding Raman spectra. Thanks also to Anita Sanghani and Liza Osagie,for their help with cell culture.

I would also like to thank all the students at IOMS and CoMPLEX, particularly Katerina, Tarig, Jospehine, Noah, Julia, Judith and Liz thanks for keeping me on track. To Nick Bushell for always being infectiously enthusiastic about my research.

Finally to my family, Maia and Pete you have supported me in absolutely every way, I would not have made it without you. Mum and Dad, without your love and support I would not have the confidence and capability to achieve any of my goals. Thank you.

Contents

1 Introduction **29**

1.1 Decompression sickness (DCS) 29

1.1.1 Symptoms, treatment and prevention 30

1.1.2 Gas kinetics 30

1.1.3 Bubble dynamics 32

1.2 Thesis aims and outline 34

1.2.1 Chapter outlines 35

2 The use of *in vitro* models in DCS **37**

2.1 Decompression sickness 37

2.2 How bubbles cause DCS 38

2.2.1 Immediate mechanical action 38

2.2.2 Proinflammatory 40

2.2.3 The Endothelium 41

2.3 Measuring bubbles 43

2.3.1 Venous gas embolism measurement 43

2.3.2 Correlation of VGE and DCS 44

2.3.3 Measurement techniques for extravascular bubbles 45

2.3.3.1 Published Data 51

2.3.3.2 In vivo decompression with histology or autopsy . . . 52

2.3.3.3 *Ex vivo* 54

2.3.3.4 Transparent animals 55

2.3.3.5 *In vitro* 56

2.4 Computational models 59

2.4.1 How are bubbles modelled 60
2.4.2 Parameterisation and validation 69
2.4.3 Modelling summary 71
2.5 Conclusion 71

3 Experimental system design and build 73
3.1 Collagen gels as *in vitro* models 73
3.1.1 Collagen *in vivo* 73
3.1.2 Collagen production, extraction and the creation of hydrogels . 74
3.1.3 Comparison to native tissue and other models 75
3.2 Approaches to chamber design 77
3.3 Pressure chamber description 79
3.3.1 Chamber body 79
3.3.2 Window design 80
3.3.3 Temperature and pressure, control and monitoring 82
3.3.4 Pressure control 82
3.3.5 Temperature control 84
3.4 Image analysis techniques 85
3.4.1 Matlab analysis 86
3.5 Basic experiment outline 87
3.6 Conclusion 89

4 Computational Model Derivation 91
4.1 Introduction 91
4.2 Gas Transfer 92
4.2.1 Gas laws 92
4.2.2 Diffusive Laws 93
4.3 Tissue mechanics 94
4.3.1 Solid mechanics 97
4.3.1.1 Linear elasticity 99
4.3.1.2 Hyperelasticity 105
4.3.2 Implementation 108
4.4 Derivation of the computational model 111

4.4.1 Assumptions . . . 111
4.5 Summary and Conclusion . . . 113

5 Code implementation and Sensitivity analysis 115
5.1 Introduction . . . 115
5.2 Numerical Implementation . . . 115
5.2.1 Structure of the code . . . 115
5.2.1.1 Numerical forms of the governing equations . . . 118
5.2.2 Stability and Simulation length . . . 119
5.2.3 Bubble boundary . . . 121
5.2.3.1 Bulk diffusion . . . 122
5.2.3.2 Gradient at the bubble tissue interface . . . 124
5.2.4 Mass conservation . . . 125
5.3 Summary of numerical implementation . . . 129
5.4 Material Parameters sensitivity analysis . . . 129
5.5 Parameter literature review . . . 131
5.5.1 Diffusion coefficient . . . 131
5.5.2 Shear modulus . . . 132
5.5.3 Solubility . . . 133
5.5.4 Surface tension γ . . . 135
5.5.5 Model sensitivity results . . . 135
5.6 Conclusions and Summary . . . 139

6 Validation 141
6.1 Introduction . . . 141
6.2 Diffusion coefficient validation . . . 142
6.2.1 Methods . . . 143
6.2.1.1 Experimental . . . 143
6.2.1.2 Computational . . . 144
6.2.2 Diffusion coefficient validation results . . . 145
6.2.2.1 Experimental results . . . 145
6.2.2.2 Computational results . . . 146
6.3 Diffusion coefficient summary . . . 152

6.4 Sensitivity to dive parameters . . . 153
6.4.1 Experimental sensitivity methods . . . 154
6.5 Sensitivity results . . . 156
6.6 Summary of Dive sensitivity . . . 163
6.7 Bubble-Bubble interaction . . . 165
6.8 Conclusion . . . 167

7 Nucleation chapter 171
7.1 Introduction . . . 171
7.1.1 Nucleation mechanisms . . . 171
7.1.2 Models of nucleation . . . 175
7.2 Overview . . . 177
7.3 Types of dopant . . . 179
7.4 Experimental Methods . . . 180
7.4.1 Prep of powder samples . . . 180
7.4.2 Transmission electron microscopy (TEM) . . . 180
7.4.3 Polymeric collagen extraction . . . 181
7.4.4 Cell culture, differentiation and staining . . . 181
7.4.5 Raman spectroscopy . . . 182
7.5 Results . . . 183
7.5.1 Preliminary investigations . . . 183
7.5.2 Non-biological dopants . . . 183
7.5.3 Biological dopants . . . 185
7.5.3.1 Bone and HANPs . . . 185
7.5.3.2 Polymeric collagen . . . 186
7.5.3.3 Cellular surfaces . . . 193
7.5.4 Summary of dopant nucleation . . . 196
7.5.5 Dive parameter sensitivity . . . 197
7.6 Conclusions and Summary . . . 202

8 Cell-bubble interactions 205
8.1 Introduction . . . 205
8.1.1 Cellular metabolism of oxygen and the oxygen window . . . 206

8.1.2 Mechanism of cell damage during diving and decompression . . 208
8.1.2.1 Increased oxygen partial pressure ($pp\mathrm{O}_2$) 208
8.1.2.2 Mechano-sensitive responses of cells 209
8.2 Methods 209
8.3 Results and discussion 211
8.3.1 Effect of cellular metabolism on bubble nucleation and growth . 211
8.3.2 Effect of bubbles on cell viability 216
8.4 Conclusions 221

9 General Conclusions **223**
9.1 Further Work 231
9.1.1 Experimental set up development 231
9.1.2 Tissue mechanics 231
9.1.3 Numerical implementations 232
9.1.4 Validation 232
9.1.5 Nucleation 232
9.1.5.1 Development of a nucleation model 233

Appendices **235**

A Solid mechanics **235**
A.1 Derivation of quartic expression for the solution to the bubble expansion problem using linear elastic constitutive equations 235
A.1.1 Nims term 236
A.1.2 Gent term 236

B Numerical Code **237**

Bibliography **238**

List of Figures

2.1 Diagram representing the subpopulation of bubbles that VGE measures 46

2.2 Chart showing the distributions of techniques used to investigate extravascsular bubbles 48

2.3 Illustration of mechanism by which air bubble contact elicits a calcium transient and mitochondrial depolarisation through two parallel mechanism. 1) the IP3 dependent Ca^{2+} influx and the PKC-α dependent mitochondrial membrane lowering pathway. [1] 57

2.4 Diagram of the apparatus used in [2] 58

2.5 Taken from [3] showing the exponential saturation and desaturations for a mixed linear-exponential approach as used by (Thalmann). 60

2.6 Pressure schedule with specific pressures indicated 62

2.7 Two and three region models as described by [4] 65

3.1 (Left) An exploded view of the pressure chamber components from the final CAD design, (Right) the final chamber with the base plate removed to show the window, o-ring and inner sample holder 79

3.2 The clamped (top) and unclamped (bottom) configurations for pressure window design 80

3.3 Bottom: cross-sectional view of the chamber, dimensions are shown in millimetres. Top left: Enlarged view of the O-ring seal showing the dimension of the O-ring and the groove. Top right: Plan view from the lid the six screws are used in both the top and bottom plate. The inner sample holder is not shown 81

3.4 Diagram of the equipment setup 82

3.5 Showing a comparison of input and output pressure profiles. The bottom left shows the initial lag phase of the chamber filling.The lower right graph shows the oscillation associated with pressure changes. . . 84
3.6 Showing the temperature fluctuation of the air inside the chamber associated with the decompression from 80 psi over 85
3.7 Showing the image analysis technique for the imageJ portion of the semi-automated technique 87
3.8 Showing the input of the raw bubble traces from the image J analysis (left) and the final output after the assignment of each data point to a specific bubble trajectory (right). In the right hand panel each coloured line represents a single bubble's growth from the start of decompression at 0 secs till 1hr 30 after the end of the profile. 88

4.1 Showing how the derivation is set out with the reference configuration and the changes in bubble size depending on the change in external pressure. 99
4.2 Comparison of the correct linear elastic model with the originally proposed model and with a hyperelastic model. A pressure change from 101MPa - 0.1MPa (1000-1atm) was modelled with: $\mu = 3.54kPa$, $\gamma = 0.07N/m$, $K = 2.2x10^3$ MPa [5], $M = 1x10^4$ MPa/μm^3 - Taken from [6] 103
4.3 Typical stress strain curve of a tissue with the configuration of collagen fibres shown above. 105
4.4 The Gent term for variations in the parameter $\frac{\gamma}{\mu r_0}$, ($J_{lim} = \infty$ for all lines) 109
4.5 Comparison of the Gernhardt term model with the Gent hyperelastic term using the Boyle's law model. The parameters used to generate these plots are: $\mu = 3.54kPa$ (see lit search on param) atm, $\gamma = 0.7$ atm μm, $M = 1e4$ MPa/μm^3 - Taken from [6] 110
4.6 Comparison of the Gernhard and Gent terms for variations in M. 111

5.1 Diagram representing the execution of the code 117
5.2 The time step size requirements for various spatial resolutions h to meet the stability criteria. 119

5.3 representation of the upwind and downwind sweeps in a 2-dimensional ADE scheme, the red points show points calculated in the previous spacial step 121

5.4 diagram of sharp (left) and diffuse (right) interfaces 122

5.5 Diagram showing the masks, Left boundary mask, Right phase mask . 123

5.6 Diagram showing the case where a boundary point is reached in the FTSC bulk diffusion calculation (only a 2D representation is shown). Boundary points are shown as open circles, points inside the bubble are shown in red and bulk points as filled black. Consider the point marked 'boundary point': for the standard FTSC stencil one of the points lies within the bubble (red point). This is replaced by a point on the bubble surface and Δh shows the reduced distance between the boundary point and bubble edge. The reduced distance necessitates the use of inverse distance weighted interpolation, rather than the a space centred approximation 123

5.7 2D Diagram showing the spherical points (squares) surrounding the bubble used to calculate the concentration gradient. The concentration of the radial points are given by interpolation from the surrounding cartesian mesh points as indicated by the arrows in the right hand panel. 124

5.8 Showing the jumps in the total tissue gas mass as the number of nodes in the tissue changes 126

5.9 Showing the bubble imposed on the finite difference grid in 2D, the inset shows the radial distance to the bubble surface, note that the angle between the bubble surface and the line from the centre of the bubble to the node point will always be 90° 127

5.10 Showing a single cell with the bubble surface estimated by a plane. The line l is the total length of the line from the bubble surface to the node which lies within the cell. The line p is the distance from the node to the plane, intersecting the plane at 90°. The angles θ and ϕ are shown. In this instance it can be seen that the line l passes through the front of the cube xy plane and as such the z length of the triangle will be 0.5, from knowledge of one side and angle θ and ϕ the length l can be calculated by $lcos(\theta) = 0.5$. Similarly this could be done if $x = 0.5$ or $y = 0.5$ using both θ and ϕ 127

5.11 Showing the mass conservation for an oscillatory pressure profile with no flux boundary conditions at the grid edge. All masses have been non-dimensionalised to the initial total mass of the system, as can be seen there are only very small fluctuations in the total mass. 128

5.12 Sensitivity of the material parameters of the model for a single bubble of initial size 0.04mm. In all cases the fixed parameter values are the modal values of the range ($\gamma = 0.056$N/m, $L_{N_2} = 0.0436$, $L_{O_2} = 0.02$, $\mu = 2 \times 10^6$Pa, $D = 1.4 \times 10^{-9} m^2/s$). Left is the bubble radius profile with time, Right is the response of the two features, (bubble maximum radius and time to maximum) to changes in the parameter value. Note the y-axis scales are not even across all panels 137

5.13 comparison of all parameters on the range of max bubble sizes (Left) and time to max bubble size (Right) 138

6.1 Showing the oscillatory pressure profile, ... 143

6.2 The time course of successive minima and maxima for the dense and hydrogels (n = 5) gels. Mean and standard error are shown. 146

6.3 Left-hand panel- Showing the normalised radius for the dense and hydrogels where the minima and maxima have been split over two graphs for clarity (top and bottom respectively). Mean and standard error in mean are shown, the measurements, change in maxima and change in minima are indicated and the astrix denotes the oscillation at which the minimum radius was measured. Right-hand panel- showing final minima, final maxima and change in the minima and maxima, statistically significant difference between the hydrogel and dense gel can be seen for the final maximum, change in maxima and change in minima. The initial distributions (not shown) were tested for equivalence using a TOST test and found to be equivalent at $\varepsilon = 0.55$ standard deviations. 147

6.4 Showing the successive maxima for a computational simulation of a bubble of 0.2mm initial radius for a range of diffusion coefficients D and constant μ of 40 Pa values. Mean experimental maxima are shown in dotted lines for both hydrogel and dense gel 148

6.5 Showing the successive maxima the computational simulation of a bubble of 0.2mm initial radius for a variations in the bubble diffusion coefficent. Left: the functional relation to the radius of the bubble is varied. Right: The initial value of the bubble surface diffusion coefficient is varied in all cases the bulk diffusion coefficient was $D = 2.5 \times 10^{-9}$. . . 148

6.6 Bubbles within a compressed collagen hydrogel. Arrows indicate the outline of the bubble prior to compression these could show areas of compressed collagen and be a cause of the decreased diffusion coefficient. 149

6.7 Showing the optimisation of the diffusion coefficient on a least squares comparison to the mean experimental profile. Left: The hydrogel was optimised for both the function and fold change from the bulk diffusion coefficient based radius profile. The R^2 value with a 30 fold decrease in initial bubble surface diffusion coefficient is seen to be the optimal parameter values Right: The bulk diffusion coefficient for the dense gel was optimised using the same fold change ($D_0^{surf} = D_{bulk}/30$) and function $D_{surf} \propto R^2$. The optimal value was found to be $1.7x10^{-9}$, however the dense gel is less well optimised than the hydrogel 150

6.8 Showing the computationally optimised oscillatory simulation with the function, fold change and bulk diffusion coefficient found from the least squares analysis above. The dotted line show the mean experimental dense and hydrogel results. It can be seen that the hydrogel is better optimised than the dense gel 151

6.9 Comparison of the optimised simulated and experimental results, left- the hydrogel, right- the dense gel. The simulations used an initial radial distribution which was matched to the experimental values. For the hydrogel no significant differences were found between the simulated and experimental measures using paired T-tests in each case. For the dense gels significant differences for the change in minima and maxima was found as well as the final maximum 152

6.10 Comparison of the simulated dense gels and hydrogels. Significant differences found for all measures using paired t-tests 152

6.11 Showing an example of the non-linear regression analysis with the half-life and plateau values marked 155

6.12 Radial trajectories over long time scales post decompression, each line is a bubble radius trajectory from a separate experiment conducted under the same conditions. 156

6.13 Showing the plateau values and half lives of the bubbles for each experimental condition, also the number of bubbles nucleated within in each gel, where error bars are shown the mean an 95% confidence interval is plotted. Linear regression was performed for all samples other than the number of bubbles with variation in compression rate for which non-linear regression was used. The regression R^2 values are reported for each condition and for each dive profile N=3 gels. 157

6.14 Showing a plot of the half live against the plateau radius bubbles under the various conditions. In each case the dotted line indicates the linear regression for the individual bubbles whilst the solid black line indicates the regression line for all data. A statistically significant slope is found for the decompression rate plot as compared to the total data line. 158

6.15 Showing the relationship between the initial rate of bubble growth and the rate of decompression - no significant correlation found p=0.0974. . 159

6.16 Showing the radial trajectories where tau is linearly dependent on plateau with the relation found from the linear regression of the experimental data 159

6.17 Showing the variation in radial profile caused by the position of the bubble within the gel. Left shows the birds eye view and cross section of the simulated bubbles in the left-hand panel. The size of the bubbles in the left-had panel is the final plateau radius. 161

6.18 Showing a comparison of the simulated sensitivity analysis and the experimental. Mean and standard deviation shown 162

6.19 Showing the effect that initial radius has on the bubble growth. It can be seen that bubbles of larger initial radii, grow to larger plateau sizes. This effect appears non-linear with initial radius. 164

6.20 Showing the proportion of bubble-bubble contacts which result in coalescence 168

7.1 A study into the variation amongst batches of 500nm carbon and activated charcoal. As can be seen the charcoal does not show particular variation however the carbon shows one batch (batch 16) with very high nucleating power by comparison to other batches. Kruskal-wallis test finds that there are no significant differences between batches (p-value = 0.058 for activated charcoal, p-value = 0.052 for 500nm carbon). Even though there was not a significant difference, batch number was maintained going forward. 184

7.2 Showing the relation between compression rate and nucleation in 500nm carbon with two different batches of carbon batch 16 is one suspected of contamination 185

7.3 representative TEM images for the comparison of (A) bone fragments and (B) hydroxyapatite particles, the radar plot shows the distribution of crevice angles from all images. 186

7.4 Changes in nucleation as a result of variation in the concentration of polymeric collagen. Linear regression reformed r^2 value reported with p-value. 187

7.5 Treatment of polymeric collagen in order to sterilise it and use in cellular gels was done via three methods. Vigorously stirred with chloroform, fumigated with chloroform and UV treated. Stirring with chloroform removed all nucleating capabilities of the polymeric collagen, whist fumigating decreased it from both the control and UV treated, (this was significant in batches 1 and 3 but not batch 2) (statistical significance assessed by Kruskal-Wallis and Dunn's multiple comparisons test. (* = p=0.018, *** = p = 0.0003) 190

7.6 Raman spectra of A the calf tendon from which the collagen was extracted, B batches 1 and 2 of polymeric collagen both treated and untreated with chloroform, C Ungelled polymeric collagen batch 1 194

7.7 Oil red O staining of the differentiated bone marrow stem cells, showing positive staining for lipid indicated by the arrows. On the left the cells are in 2D cell culture on the right the image is of the cell within the collagen hydrogel, indicating that the lipid is retained when cells are transferred to the hydrogel 195

7.8 Nucleation of bubbles within monomeric collagen hydrogels containing 45,000 Adipose cells/ml. No statistically significant differences (N=4) 196

7.9 Showing the relations of depth, rate of compression, rate of decompression and time at depth for polymeric collagen doped samples. R^2 values for linear regression shown with p values for significance from 0 gradient line given. The open circle denotes a data point that was excluded as an outlier as a large bubble between the base of the gel and the glass of the chamber failed to dissolve on compression and grew rapidly during decompression. 199

7.10 Experimental results, showing the effect of changing two dive parameters at once. Both the depth and the decompression rate were simultaneously changed. It is shown that the multi-linear regression is not simply the additive affect of both parameters indicating that there is interaction. 201

7.11 Showing the supersaturation of the midpoint of each gel as modelled solely by diffusion without bubble nucleation 202

7.12 Showing the time of nucleation onset for changes in the decompression rate only, (green circles) and the variation in both decompression rate and depth (pink squares), values for the depth only were not recorded . 203

8.1 Left- pressure profile used for all cellular decompressions; right - the set up for the oxygen monitoring with relevant distances given. 210

8.2 Oxygen monitoring of collagen hydrogels with 5000, 50,000 or 500,000 HDF cells/ml. Atmospheric concentration is shown for reference. Statistically significant difference between 500,000/ml vs. 5,000/ml and 500,000/ml vs 50,000/ml as assessed by two way repeated measures using ANOVA (Tukey's multiple comparison correction) $p \leq 0.0003$ 212

8.3 Modelled oxygen consumptions for set up seen in Figure 8.1. The parameters used were $k_h = 1.397x10^{-9}$ mol ml^{-1}mmHg, $D = 2.5x10^{-9}$m^{2}s^{-1},
$V_{max} = 3x10^{-17}$mol cell^{-1} s^{-1} , $K_m = 5.6$mmHg, cell densities were 5,000 cells/ml, 50,000 cells/ml, and 500,000 cells/ml, $\pm$ 10%, error bars are from repeated simulations (3 per cell density) with variation in the cell density between max and min estimates, in addition to error caused by averaging over the sensor area. 212

8.4 Modelled dissolved oxygen concentrations at the mid-cross section of the gel for the three different cell densities just prior to start of the pressure profile. Concentrations have been non-dimensionalised on the ambient pressure colour scale shown on the right side. The parameters used were $k_h^{O_2} = 1.397x10^{-9}$ mol ml^{-1}mmHg, $D = 2.5x10^{-9}$m^{2}s^{-1}, $V_{max} = 3x10^{-17}$mol cell^{-1} s^{-1} , $K_m = 5.6$mmHg, cell densities were 5,000 cells/ml, 50,000 cells/ml, and 500,000 cells/ml, ... 213

8.5 Nucleation of bubbles within blended monomeric-polymeric collagen hydrogels containing 5,000, 50,000 or 500,000 HDF cells/ml. Left - the maximum number of bubbles which nucleated, statistical significance was found between 500,000 vs. 5,000 cells/ml and 500,000 vs. 50,000 cells/ml as assessed by one way ANOVA (Tukey's multiple comparison correction). Right - the number of bubbles in the field of view over time. N=3 gels per cellular density. 214

8.6 Left - relationship between bubble half life and cell density, right - relationship between bubble plateau radius and cell density, mean and SD shown for points a linear regression fit with 95% CI is also shown. R^2 and p-values of the linear regression given on each graph. No statistical dependence was found for either measured variable with varying cell density 215

8.7 Showing the dissolved oxygen concentration during the pressure profile just prior to decompression (at 1880secs) and at 2hrs after the start of the profile, (A) - where cellular metabolism continues at the same rate as pre profile. (B) - where all cellular metabolism stops when pressure profile begins. Concentrations for all plots use the scale shown in the scale bar on the right-hand side, where all concentrations have been non-dimensionalised to atmospheric pressure 217

8.8 Comparison of the live dead cell population in collagen hydrogels with 50,000 HDF cells/ml. Statistically significant differences are shown between the pre and post exposure as well as the sham and post exposure. Significance assessed by ANOVA (Tukey's multiple comparison correction) *** - p = 0.0007, * - p = 0.0116, below the graph are representative images of the 3 conditions scale bars are 200 nm, N=6 . . . 218

8.9 The result of the post exposure live dead measurement spilt according to the orientation of the gel. Diagram of the orientation is shown to the right of the graph as is an image taken through the side of the gel post decompression. A statistically significant difference is found between the two orientation as assessed by a paired t-test 219

9.1 Images taken side on showing the change in bubble distribution with changes in the max depth and decompression rate. scale bars are 2mm length. 234

List of Tables

4.1 Parameter units and values used in derivation of the radial change equation . . . 113

5.1 Estimations of diffusion coefficients in various biological media 133
5.2 Estimations of μ in various biological soft tissues and tissue mimics . . 134
5.3 Estimations of L in various biological tissues 135
5.4 Estimations of γ in various biological tissues 136

6.1 The initial radii of the paired bubble data with the pressure difference between the bubble pair shown and the mean of the pair for use in the computational simulations 145
6.2 Dive parameters used in the experimental sensitivity analysis 154
6.3 Summary of results of experimental sensitivity analysis, (+/-) indicates the sign of the gradient (and hence the nature of the correlation) and ** indicates statistical significance. 157

7.1 Bubble nucleation in monomeric COL1 gels with the addition of various dopants to investigate possible nucleation sites. 500nm mesoporous Carbon Activated Charcoal were intended to serve as positive controls, on the basis of preliminary gelatin experiments and literature. Other dopants were considered potential biological nucleation sites, all gels were 0.5ml volume 183
7.2 Dive parameters used to assess nucleation in polymeric collagen 197

Chapter 1

Introduction

1.1 Decompression sickness (DCS)

Decompression sickness (DCS) is a pathophysiology that may affect any organism exposed to rapid reduction in ambient pressure. The research effort to prevent and understand the condition is driven by the commercial and recreational diving industries as well as the construction, aeronautical and space industries. The primary cause of DCS is the formation of bubbles of inert gas within the body and the inflammatory response that follows. Bubbles are formed as a result of decompression following a period of gas saturation at a higher ambient pressure. For self-contained underwater breathing apparatus (SCUBA) divers, increasing pressure is exerted on the body as he or she descends through the water. In order for a diver's lungs to function, the pressure of inhaled gas must be close to the ambient pressure, thus as a diver descends gas is deliver to the lungs at a higher pressure via a regulator. All gases breathed into the lungs dissolve into, and/or chemically react with the blood. Metabolic gases, such as oxygen and carbon dioxide, bind to haemoglobin to form complexes. Inert gases, such as nitrogen or helium, dissolve into the blood as it passes through the lungs in proportion to their partial pressures. This is known as Henry's Law. Therefore, as a diver descends and stays at higher pressure, the concentration of inert gas dissolved in the blood will increase, and over time will equilibrate with all tissues in the body. Once a diver begins to ascend, the ambient pressure decreases and the dissolved gas is forced out of solution forming bubbles. When in the blood stream, bubbles may be transported to the lungs which can trap and filter them in the small alveoli capillaries. Bubbles which form in tissues and cannot translate into the blood stream, will eventually dissolve as the tissue

gas concentration drops with time. DCS is not a newly discovered condition, it was first described in the eye of a viper by Boyle in 1670 [7]. The first medically recorded observations in humans came in 1841 during the first caisson work in France [8]. It was not until the work of Haldane and Boycott in 1908 [9] that systematic research into the avoidance of DCS through control of the ascent speed began in earnest [10].

1.1.1 Symptoms, treatment and prevention

DCS affects many systems of the body, and there is thought to be a predilection of certain symptoms with certain types of dive [11]. The onset of DCS is entirely diagnosed by clinical manifestation, and the three most common of these are musculoskeletal pain, numbness or parenthesis, and constitutional (such as fatigue, nausea, headache etc.) [11]. These symptoms often resolve with the administration of 100% oxygen, but recompression is recommended in most cases as DCS is a progressive condition with more severe symptoms often only manifesting after several hours [12]. These later onset symptoms tend to be associated with more severe DCS, and include neurological manifestations such as motor problems, paralysis, altered mental state loss of consciousness and seizures [10], pulmonary manifestations more commonly seen in aviation related DCS [13] include dyspnoea and coughing [11]. The treatment for all DCS is the same, recompression therapy and 100% oxygen. This combined approach aims to reduce the size and number of bubbles within the patient by increasing the gradient for gas to dissolve from bubbles into the blood stream. Despite the effectiveness of recompression, residual symptoms are relatively common, with a delay in treatment increasing their likelihood [13]. In addition possible long term effects of repeated DCS are unknown and so it is always preferrable to prevent rather than treat their occurrence. Prevention has predominantly been focused on dive profiles, i.e. the length of time at depth, the depth of the dive and the ascent rate. Tables or dive computers which calculate safe profiles are often based on models of the underlying tissue gas kinetics or in some cases, on basic bubble dynamics [14].

1.1.2 Gas kinetics

The gas kinetics of human bodies can be described through a series of concepts and gas laws.

Three terms are used ubiquitously within the DCS field, under saturation, satu-

ration and supersaturation. These terms are used to describe the dissolved gas concentration of tissues relative to the ambient pressure. In each case, the dissolved gas concentration is described in relation to the equilibrium pressure for the current ambient pressure. Thus, undersaturation indicates lower dissolved gas concentration in tissues than the equilibrium pressure for the current ambient pressure. Saturation is the equilibrium condition and supersaturation (P_{ss}) is the case where the dissolved gas in the tissue or blood is higher than the equilibrium pressure for the current ambient pressure.

There are three stages to gas kinetics in the body:

1. dissolution of gas into the blood stream from air in the lungs,

2. transport in the blood stream,

3. diffusion from the blood into the tissue,

As previously mentioned, Henry's law governs the amount of gas that will dissolve into the blood at a given pressure excluding any chemical reactions.

$$C^g = k_h^g pp_g \tag{1.1}$$

Where C^g is the concentration the gth gas, k_h^g is Henry's solubility constant and pp_g is the partial pressure of gas g. Often the dimensionless solubility coefficient L is used rather than Henry's constant where $L = k_h/\mathscr{R}T$, ($\mathscr{R}$ is the universal gas constant and T the temprature).

Transport of gas in the blood stream and its diffusion into tissues is generally modelled by Fick-Fourier kinetics [13],

$$\frac{dC^g}{dt} = \nabla(D \cdot \nabla C^g) + \frac{\dot{Q}}{V_t}.(C_{a,g} - C_{v,g}) - Z'_{met,g} - Z'_{b,g} \tag{1.2}$$

Where D is the diffusion coefficient, $\dot{Q}$ is the blood flow rate (ml of blood per min). V_t is the tissue volume, $C_{a,g}$ and $C_{v,g}$ are the arterial and venous gas concentrations and $Z'_{met,g}$ and $Z'_{met,b}$ are the respective rates of gas consumption by metabolism and bubble growth respectively.

In general within the DCS literature tissues are modelled as either perfusion or diffusion limited. For a perfusion limited tissue the first term on the RHS of (1.2) is neglected. It is often described as the tissue being 'well stirred', that is where all points within the tissue have the same gas concentration and there are no internal gradients. In this case the amount of dissolved gas within a tissue is limited only by the rate of blood flow and the difference between the arterial and venous gas concentrations. The venous gases, are considered to be in perfect equilibrium with the tissue gas concentration. This formulation is often written in terms of the tissue gas tensions p_t rather than the gas concentrations C. Diffusion limited tissues, by comparison, are assumed to be dominated by the first term on the RHS of (1.2) [13].

In the perfusion limited case of a tissue with no bubbles, the change in the inert gas concentration with time can be described as

$$\frac{dp_{t,g}}{dt} = \frac{p_{a,g} - p_{t,g}}{\tau_t} \tag{1.3}$$

where τ_t is the tissue half time, and $p_{t,g}$ is the tissue tension assumed to be equal to the venous gas tension.

$$\tau_t = \frac{L_{t,g}}{\dot{Q}L_{b,t}}, \tag{1.4}$$

where $L_{t,g}$ and $L_{t,b}$ are the solubilities of the gth gas in the tissue and blood respectively. The tissue half time is a parameter specific to a particular tissue.

1.1.3 Bubble dynamics

In order to explain bubble dynamics two key processes must be understood, nucleation and diffusion controlled bubble growth.

Nucleation is the phase transition of a portion of a bulk liquid to a vapour (or liquid to solid in the case of crystallisation). The process can be described by classical nucleation theory which states that two Gibbs free energies are associated with the phase change: a volume energy and a surface energy. For a spherical bubble this can be written as

$$\Delta G = -\frac{4}{3}\pi R^3 G_v + 4\pi R^2 G_s \tag{1.5}$$

where G is the Gibbs free energy and subscripts v and s denote the surface and volume respectively. As can be seen the energy associated with the formation of a volume

phase reduces the overall free energy whilst the formation of a phase boundary (a surface) increases it. These two opposing terms lead to an energy barrier to nucleation depending on the radius of the nucleus [15]. The volume and surface energies depend on the surface tension and supersaturation of the surrounding liquid respectively, for a bubble in a supersaturated solution the critical radius (R_{crit}), at which the energy barrier is overcome can be found from the maximum of the energy function (1.5) with G_v equal to the supersaturation of the tissue (P_{ss}) and G_s equal to the Laplace pressure:

$$R_{crit} = \frac{2\gamma}{(P_B + P_v) - P_{amb}} = \frac{2\gamma}{P_{ss}} \tag{1.6}$$

where P_B is the pressure inside the bubble, P_v is the vapour pressure of the liquid in which the bubble forms, γ is the surface tension, P_{amb} is the ambient pressure. Nuclei which are larger than the critical radius will expand rapidly to form bubbles as the diffusion of gas into the bubble caused by the supersaturation is greater than the tendency of the bubble to shrink due to the surface tension. From this the steady state nucleation rate can be described by

$$J_{ss} = J_0 e^{Gk_bT} \tag{1.7}$$

where J_{ss} is the number of critical nuclei generated per unit time and per unit volume, J_0 is the kinetic factor, G is the reversible work for the formation of a critical nucleus, k_B and T are the Boltzmann constant and temperature respectively. The energy at the critical radius (G_{crit}) can be described by

$$G_{crit} = \frac{16\gamma^3}{3P_{ss}^2}. \tag{1.8}$$

It can be seen that the value of γ is raised to a power of three and is in the exponent of the steady state nucleation expression. It is therefore crucial for this to be accurately described.

There are three types of nucleation: homogeneous, heterogeneous and tribonucleation. Homogeneous nucleation occurs when there is no free gas phase initially in the liquid phase. Thus, nucleation occurs only due to random molecular fluctuations within the liquid. This type of nucleation is generally thought to require very high supersaturation, far higher than those experienced in SCUBA diving [16].

Heterogeneous nucleation occurs when a solid surface within the liquid lowers the surface energy required to form a bubble. In this case the value of G is altered through the presence of the surface [17]. The change in G can be described by

$$G_{het} = \frac{G}{4}(2\cos\theta)(1-\cos\theta)^2 \tag{1.9}$$

where θ is the contact angle. This type of nucleation essentially requires impurities within the liquid which lower the surface energy barrier to nucleation.

Tribonucleation or viscous adhesion, is nucleation caused as two solid surfaces immersed in a liquid and in contact are moved apart. It is thought to occur due to the local low pressure cause by the movement of the solid surfaces in the viscous fluid [18]. This type of nucleation has been hypothesised to occur at joints and muscle facia [16].

The dissolution and growth of bubbles is predominately controlled by the mass transfer through the bubble surface, which in turn is dependent on the concentration of gas within the bubble and that in the immediately surrounding tissue. By assuming that the concentration of gas a the bubble surface is in equilibrium with the bubble, the concentration of gas at the bubble surface can be described by Henry's law. At equilibrium the pressure of gas within a bubble is described by the Laplace equation

$$P_B = P_{amb} - P_v + \frac{2\gamma}{R_B} \tag{1.10}$$

where R_B is the bubble radius. As the radius of curvature is always positive for a spherical bubble the pressure in the bubble will be higher than the ambient pressure and hence bubbles will tend to dissolve unless within a supersaturated solution.

1.2 Thesis aims and outline

The aim of this thesis is to use a combined computational modelling and experimental system to develop new understanding and provide insight into the formation and growth of bubbles within tissues. By creating an experimental system that is sufficiently controllable and comparable to a computational model, the development of current understanding about how material and pressure parameters control bubble dynamics will be possible. The aim is for the computational model to be validated and developed by results and observations from the experimental system, and for the computational sys-

tem to generate hypotheses that can be tested in the experimental system. Throughout this work continuous efforts have been made to ensure that simplifying and engineering the experimental system, has not eliminated the biological relevance of the work to understanding DCS.

1.2.1 Chapter outlines

Chapter 2 provides a literature review to motivate the investigation of extravascular bubbles with the combined approaches of *in vitro* experiements and numerical simulations. Chapters 3 and 4 describe the development and testing of the experimental system and of the governing equations of the computational model. Chapter 5 outlines the numerical implementation and parameterisation of the computational model. Chapter 6 is a validation and comparison of the computational model and the experimental system. A comparative sensitivity analysis of the impact material and dive parameters have on bubble dynamics is undertaken. Multi-bubble dynamics are introduced to the model and their impact is assessed and used to interpret results from the experimental system. Chapter 7 investigates the nature of nucleation in the experimental system. The effect of both dive parameters and material parameters are explored, and their implications for computational modelling discussed. The final chapter is an investigation into the effect cells have on bubble dynamics and the impact bubbles may have on cell viability. This constitutes an extension the the current uses of *in vitro* models within the DCS literature.

Chapter 2

The use of *in vitro* models in DCS

The aim of this chapter is to motivate the investigation of extravascular bubbles via a reductionist in vitro *methodology.* To provide this motivation two arguments are needed: the first to show the importance of extravascular bubbles in the aetiology of DCS and the second to establish that *in vitro* models are particularly suited to investigation of these bubbles. The chapter is broken into 3 parts: The first section details the mechanisms through which both extra and intravascular bubbles are thought to cause DCS. The second section focuses on current measurement techniques of both intra and extravascular bubbles.The final section is a summary of existing computational models of DCS and how these models have been conceptualised and validated in light of experimental evidence.

2.1 Decompression sickness

DCS as described in the previous chapter is a collection of symptoms seen after a rapid reduction in ambient pressure and broadly categorised into two types. Despite observations of bubble formation in decompressed animals by Boyle in 1670, it was not until the seminal work of Paul Bert [19] motivated by the death of many caisson workers in the 1800's, that indicated nitrogen bubbles were the cause of the deaths. Hills and Mcleod [20] repeated much of Bert's work in 1903, observing bubble formation *in vivo* in the wings of bats and the webbing of frogs legs during decompression. Following this work Haldane and Boycott used goats to test dive profiles and produce the first decompression tables for the British Navy [9]. Throughout the early 1900's it was widely believed that bubble formation and DCS were synonymous; bubble formation in the various tissues of the body was thought cause DCS through mechanical distortion

and embolitic effects. The wide range of symptoms and susceptibility was attributed to variation in the location of bubble formation caused primarily, by anatomical differences. However, as research techniques progressed, it became clear that bubbles could cause biochemical as well as mechanical insult. Current understanding regarding the pathophysiology of DCS is that bubbles which evolve during decompression, cause both biophysical and biochemical insults which may result in immediate local symptoms, a systemic inflammatory response and long term damage. The exact causal chain, and complex feed back loops amongst these mechanisms as well as the variation in individual susceptibility remain important areas of research.

2.2 How bubbles cause DCS

The injuries which bubbles cause are often split into two categories: biophysical and biochemical. Biophysical actions are those caused by the mechanical forces bubbles have on tissues and vasculature; biochemical actions are the consequences of the blood/tissue-air interface on molecules within the body. Although this distinction is useful in many ways, most mechanisms believed to lead to symptomatic DCS are caused by the feedback between both types of injury: The majority of mechanical insults will result in a biochemical response, as many cells and systems within the body are mechanosensitive. In this section the various theories and mechanisms by which bubbles cause insult are discussed.

2.2.1 Immediate mechanical action

The term 'immediate' is used here to denote the deleterious effects of bubbles on surrounding tissues and vasculature independent of downstream biochemical reactions. Bubbles within the vasculature become lodged within sufficiently small vessels, eventually occluding blood flow. In the arterial system this leads to an arterial gas embolism (AGE), a condition with severe neurological and cardiac results. Bubbles due to DCS are not routinely observed in the arterial system and hence AGE resulting from decompression, occurs only when there is a route for bubbles to pass from the venous to the arterial circulation. Pulmonary barotrauma, patent foramen ovale (PFO) or overload of the pulmonary lung filter are mechanism by which this has been observed to happen [12]. In general the mechanical effect of vascular bubbles is restricted to the venous

system where the majority of DCS bubbles remain. Infarction of the venous system may lead to various pathologies depending on the region in which it forms[13].

One widely researched hypothesis is that blockage of the epidural vertebral venous plexus (EVVP), the system of veins which drain the spinal cord, is the cause of spinal cord DCS. This type of DCS is characterised by early onset (normally within 1-2hrs), and by ascending parenthesis and paralysis[13]. Infarction of the EVVP is a very rare pathology [21], largely because of the extent of the plexus particularly in humans. In order to block the system a very high bubble load would be needed. Evidence for this mechanism is found in the work of Hallenbeck [22] where decompression of dogs which had been laminaectomized (exposure of the EVVP) revealed extensive bubble formation and blockage of the EVVP. Of the 33 dogs used in the study, 23 showed blocked EVVP and associated spinal cord lesions, in 10 which did not have EVVP blockage, spinal cord damage was not found. Despite this evidence, the venous infarction hypothesis has been widely criticised, due to the pattern of spinal cord lesions reported. The distribution of lesions found over a wide range of similar studies [23, 24, 25, 26, 27] showed discrete white matter lesions and haemorrage with a large degree of grey matter sparing (the pattern was less pronounced in the swine model[26]). The grey matter sparing does not correspond with venous infarction injuries reported by Taylor and Byrnes (monkey) [28] and Kato [13] or by Hughes[21] where venous infarction produced massive haemorrhage equally affecting the white and grey matter. In addition, as noted by Hills [29], the improvement of spinal cord symptoms on recompression, but their subsequent reoccurrence often seen at decompression is indicative of bubbles dissolving and reforming in the same location. This is argued to be far more likely if bubbles are forming extravascularly around local nucleation points, as opposed to forming a vascular obstruction.

The formation of extravascular bubbles is more likely to occur in lipid rich poorly perfused tissues. Nitrogen is five times more soluble in lipid than water increasing the tissue tension whilst poor perfusion will increase gas wash out times. Tissues which fulfil this criteria and have been particularly investigated are the bone marrow, spinal cord and connective tissues. The alternative to the EVVP mechanism of spinal cord DCS is the extravascular bubble formation, as proposed by Francis. Francis proposes that bubble formation in white matter could result in loss of axonal conduction through

mechanical distortion [23]. In addition Francis notes that venous infarction may still be caused by extravascular bubbles, owing to the high compliance of white matter. Evidence for this hypothesis exists in the lesion distribution discussed above but also in the disruption and structural changes in myline sheath that have been investigated histologically, and with X-ray diffraction [30, 31].

Bubble formation in the bone marrow and connective tissue have been researched primarily in connection with musculoskeletal DCS. Pain is the most commonly reported DCS symptom and is treated successfully by recompression therapy in the majority of cases. Two types of pain are reported, either a constant localised pain at a particular joint or else a migratory polymyalgia. It is thought that these two pains are likely due to different mechanisms, although extravascular bubble formation is considered a probable cause of both given the recompression response. Formation of bubbles within tendons has been observed by Gersh [32, 33] in the rabbit and guinea pig models, distension to nerve endings within these tissues could lead to the joint specific pain. Nerve ending distension by bubble formation within bone marrow could also cause the joint specific pain. Bubble formation within bone marrow has been reported in many studies [13, 34, 35, 36], it is thought that the more non-localised pain may be caused by an increase in intramedullary pressure. There has also been a suggested link between the formation of bubbles in the bone marrow and long term damage resulting in dysbaric osteonecrosis although the evidence is not conclusive[34] .

Finally it has also been hypothesised that bubble formation in the lymphatic system may be the cause of skin bends and tissue swelling, although there is very minimal evidence to support or disprove this hypothesis [13].

Despite the wide range of immediate mechanical mechanisms discussed above, a-symtomatic bubbles, individual susceptibility and the time course of symptom development are all indicative of additional downstream effects. Biochemical mechanisms are thought to provide a better explanation for these findings.

2.2.2 Proinflammatory

The presence of bubbles in the blood steam creates an abnormal air liquid interface at the blood bubble barrier. This interface has been has been shown to trigger biochemical changes in the blood which may lead to a pro inflammatory response. One

mechanism for these changes is through hydrophobic interactions, causing the adsorption of proteins onto the interface. Adsorbed proteins may undergo conformational changes, which in turn can render them non-functional and cause the exposure of lipids or active sites[13, 37, 38]. Such changes have been found to stimulate the coagulation cascade, with platelet aggregation now being a widely recognised result of decompression [39, 40, 41, 42, 43, 44, 45, 46, 47, 48]. Other pro inflammatory responses, including leukocyte increase and aggregation [49, 50] and cytokine release, [51, 52] have also been associated with decompression. Activation of the complement system, was suggested by Ward [53] to be the source of the inter subject variability and depletion of complement proteins [54] to be the source of the the acclimatisation response to diving that has been found in both humans and animals [41, 55, 56]. However, work by Nossum et al. and Hjelde at al. [57, 58] in which an anti-C5a antibody was used to suppress the complement system, failed to show any protective affect.

2.2.3 The Endothelium

Endothelial dysfunction and activation are a well researched systemic consequence of decompression thought to be caused by both mechanical and biochemical responses to bubbles and oxidative stress. The vascular endothelium consists of a mono layer of endothelial cells lining all vessels, it releases vasoactive substances, to maintain hemostasis, control fluid filtering, maintain hormone trafficking and control neutrophil recruitment. The most important vasodialator, endothelium-derived nitric oxide (NO), is a small free radical molecule the production of which is catalysed by the endothelial constitutive form of NO synthase (eNOS). The release of NO by endothelial cells is modulated by shear force from blood flow and signalling molecules released into the blood. Endothelial dysfunction is a pathology defined as the impairment of endothelial vasodilation caused by a lack of NO synthesis or bioavaliability. It is considered a prognostic marker for cardiovascular disease[59]. Endothelial activation is a related process:- Endothelial cells become activated in response to pro-inflammatory cytokines within the blood, producing the cell surface adhesion molecules VCAM1, ICAM1 and E-selectin that attract circulating leukocytes to the vessel walls. Endothelial dysfunction and endothelial activation are linked through a feedback loop; activated endothelial cells inhibit eNOS expression, whilst NO suppresses VCAM1, ICAM1 and

E-selectin expression [60]. Endothelial activation is a normal inflammatory response that if chronic may lead to atherosclerosis, whereas endothelial dysfunction is a pathology in which the endothelium is unable to produce proper vasodilatation in response to appropriate stimulus. Both endothelial dysfunction and endothelial activation are widely reported in human divers and animal studies, leading to concerns regarding the long term health implications for divers [61, 62, 63, 59].

Oxidative stress is known to produce endothelial dysfunction through stimulating the production of reactive oxidative species (ROS) which inhibit the bioavailability of NO[64]. The increased production of ROS by endothelial mitochondria has been reported *in vitro* in response to simulated dives with increased oxygen partial pressure [65]. Thus by production of ROS as a result of the increased oxygen partial pressure, the bioavailabiltiy of NO is limited leading to both endothelial dysfunction, and potentially stimulating endothelial activation.

The extent to which bubbles cause or exacerbate endothelial dysfunction and activation is less clear. A dose dependent reduction in endothelial function with venous gas embolism (VGE) grade is reported in several studies [66, 67]. This may occur through direct mechanical interaction of bubbles with endothelial cells; which has been shown to cause cell death [68] and strip cells from the vessel walls [69]. In addition, alterations in the viscosity of blood due to bubble presence may result in turbulent flow and changes in blood pressure[13], all of which are causes of endothelial activation and NO supression.

Another particularly interesting link to bubble formation, is the finding that administering NO-donors pre-dive decreases bubble numbers in the right heart of both large animals and humans[70, 71]. This can be explained due to the vasodilation caused by NO donors which facilitates inert gas wash out leading to lower supersaturation and hence less bubble formation. However, use of short-lifetime NO donors, where vasodialtion can be measured for only 15mins [70, 71] suggests that additional mechanisms may be involved. Both studies discuss the idea that NO may lead to changes in the hydrophobicity of the endothelial cells, specifically of calveolae. It is thought that calveolae, which have a high concentration of sphingolipids [72], may be the nucleation sites for bubbles detected in the vasculature. By decreasing the hydrophobicity, the nucleating propensity of such sites is decreased. This is a theory which will be

discussed in greater detail in Chapter 7.

2.3 Measuring bubbles

2.3.1 Venous gas embolism measurement

In the 1960's the use of doppler to non-invasively measure venous and arterial gas emboli (VGE and AGE) became possible [73]. This provided the means to monitor the time course of bubble formation post dive and to quantify the relationship between bubbles and DCS. Current technology allows measurement of VGE either by Doppler ultrasound, 2D echocardiogram or Transesophageal Echocardiography (TEE). Standardised measurement protocols and quantification methods have become used widely in the field, typically measurements begin as soon as possible post dive and are taken at intervals of 15-60 min for at least 2hrs. The sites at which the measurements are taken for doppler are varied, the pulmonary artery outflow from the right ventricle or subclavian veins are most commonly used [13]. Both resting bubble count and bubble count post movement are normally measured as a shower of bubbles is typically observed following movement.

The bubble echoes or images are analysed via grading scales: The Spencer and Efterdal-Brukakk scales grade bubbles from 0-IV and I-V respectively, based on descriptions of the bubble frequency (number of bubbles per cardiac cycle). They are the two most widely used scales. The Kisman Masurel (KM) scale is a doppler grading scale in which bubbles are graded on a 0-4 scale for 3 separate parameters: frequency (number of bubbles per cardiac cycle) , percentage/duration (number of cardiac cycles in which bubbles are heard), and the amplitude of the bubble sounds as compared to background cardiac sounds. These three are combined to give a single grade. [74]

In order to estimate the risk a particular dive has resulted in, bubble grade data across the time course is transformed to a single number; either the highest bubble grade, or the Kisman integrated severity score (KISS)-: the integral of the bubble grade over the whole experimental time course [13].

The use of such a measurement procedure and the subsequent analysis is a complex procedure that requires specialist technicians to grade subjects. This increases the cost of trials and reduces the number of subjects that can be measured. The grading scales have also been criticised on the basis of their subjectivity, coarseness (particu-

larly at high bubble grades) and in the loss of raw bubble data (i.e. bubbles/ml) which would enable better validation of computational models[18, 74]. Some automated grading scales have been created [75], but are not widely used.

2.3.2 Correlation of VGE and DCS

From the first usage of VGE measurements, it became clear that bubble grades could provide vital insight into the mechanisms of DCS. The routine presence of asymptomatic bubbles post dive [73, 76] and that of high bubble grades with no clinical symptoms of DCS [77]; led to much of research into the pro-inflammatory and endothelial disfunction mechanisms discussed above [37]. It has also provided a means to test pharmacological interventions into DCS, with a more objective measure of DCS stress.

Despite its obvious utility as an non-invasive method of measurement; many large scale studies using doppler and echocardiograms, show an unclear relationship between VGE and DCS [13].

Large studies of sub saturation diving include Swatzky's analysis of 3234 human dives [78]; this found a predictive value of only 0.07% for symptomatic DCS given a high doppler grade. Similarly, altitude diving experiments [74] showed a positive correlation coefficient R^2 of only of 0.39 for DCS with bubble grade. Despite the poor predictive power some studies do show increased risk of DCS with higher bubble grades. Spencer and Johanson and Neuman's trials [79, 80] which had high incidence of DCS, 80% and 32% respectively, showed a statistically significant increase in DCS risk between low and high bubble grades (1% with Grade 0 which rose to 80% with Grade IV [79]). Similarly a study by Vann [81] reported a 3- 50% increase in DCS risk between grades 0-IV. [82]. More recently a study to investigate the VGE-DCS correlation introduced the term AED, "adverse effects of decompression" [83]. They hypothesised that by including often un-reported mild symptoms of decompression, such as fatigue or minor transient pain, a clearer correlation would emerge. The study concluded that VGE was a highly sensitive but poorly specific measure even with the inclusion of AED. Similarly the Sawatzky thesis [78] reports a negative predictive values of 0.999 and the altitude study [74] an R^2 of 0.98 between low bubble grades and no symptoms.

Subsaturation dives are the largest data sets and show the best correlation of VGE with DCS. In such exposures the prevailing manifestation of DCS is neurological, whereas for compressed air workers and saturation divers it is musculoskeletal. Although trials for saturation dives tend to be smaller, there is no evidence to support a correlation between VGE and risk of musculoskeletal DCS[82].

It has been argued that the lack of correlation in the available DCS data is due to the necessarily low occurrence of DCS in most trials. Trials which aim to investigate a correlation between high bubble grades and DCS symptoms, would need to use provocative profiles and would therefore be unethical to perform on human subjects [84, 85]. In the studies outlined above, in which there is a higher incidence of DCS there appears to be stronger evidence of correlation. It is widely agreed that whilst VGE may be an indicator for closer observation of a diver, it cannot be used to predict DCS.

2.3.3 Measurement techniques for extravascular bubbles

Doppler/echocardiograms measure only a small sub population of the total bubble load. Bubbles which never reach the measurement site will not be counted, this means the extravascular and stationary vascular population are not considered. Although this recording of only a subset of total bubble load is mentioned in the literature[86], what is not widely discussed, is whether this measured subpopulation is a representative or a skewed distribution; specifically, over-representative of asymptomatic bubbles. Bubbles which grow too large to escape the vasculature, becoming lodged as they grow, are likely to cause damage and symptomatic DCS through ischemia injuries and haemorrhage. Dives which cause fast bubble growth are more likely to lead to bubbles becoming lodged in the microvasculature, and could be measured to have a lower VGE grade than a milder dive during bubbles grow more slowly. This is in fact reported in the work of Daniels [73], where both stationary and mobile bubbles were monitored in a guinea pig using pulsed ultrasound. Fewer mobile bubbles were recorded in the more provocative profile than the milder one; only by considering the stationary bubbles did the bubble load reflect the severity of the dive profile. A particularly strong inflammatory reaction to bubbles may also cause a lower VGE grade, for example where bubbles cause greater platelet aggregation and endothelial activation, they are more

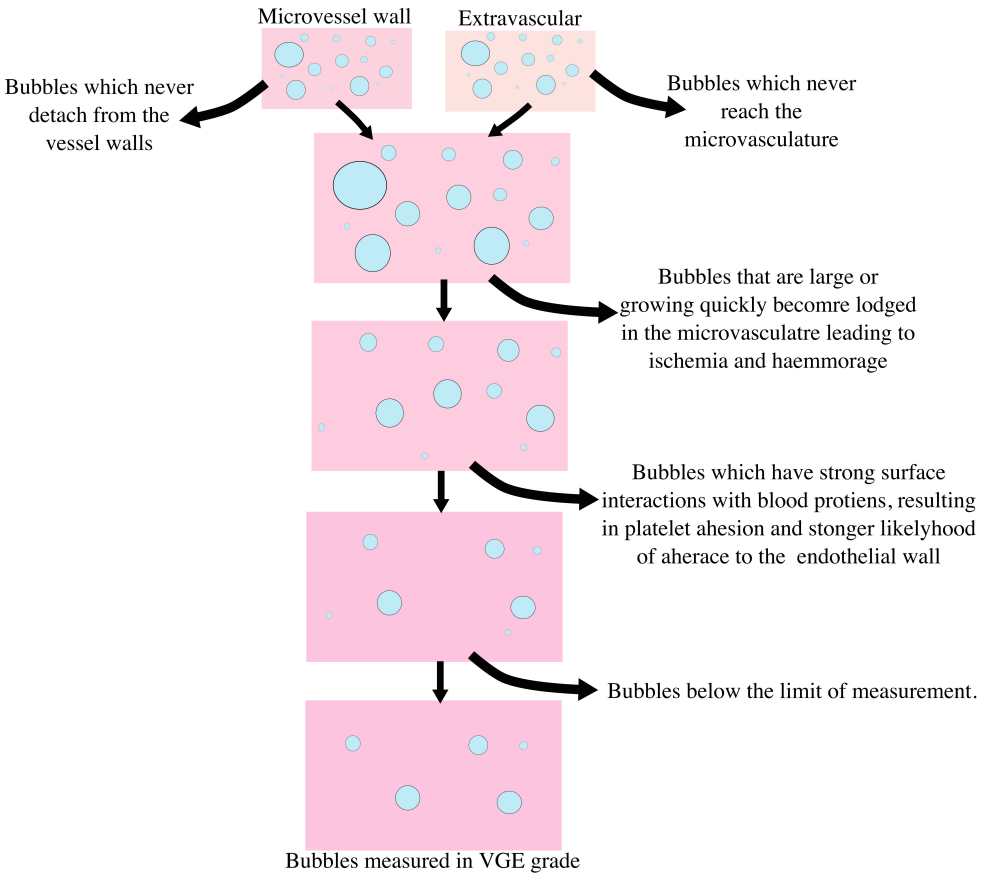

Figure 2.1: Diagram representing the subpopulation of bubbles that VGE measures

likely to reattach to the vessel walls, this could lead to a lower VGE grade where there is stronger inflammatory response. Figure 2.1 depicts how doppler/echocardiogram may lead to measurement of a bias subpopulation of the total bubble load. This is another argument for the importance of understanding extravascular bubble dynamics in DCS. What proportion of the total bubble load extravascular bubbles contribute to and how their growth affects the measured venous bubble load, could help better predict DCS risk on the bases of VGE grade. To be able to model this effectively experimental data are required to parameterise extravascular bubble models and also to validate the results. To provide such data quantitative measurement of extravascular bubbles is needed.

A systematic literature search in to the techniques used to investigate extravascular bubbles was performed. Google scholar was used with search term *Bubble AND (Decompression sickness or decompression illness OR decompression) AND (extravascular OR vitro OR phantom OR gelatin OR agarose OR autochthonous OR "tissue bubble" OR "tissue bubbles")* , date range of 1945-current day was used.

Returned results- 3300, first pass- 184 (exclusion criteria- review articles, computational modelling articles.) Second pass- 107 (exclusion criteria- articles which only reported results of venous gas bubbles)

Seven additional of papers found from the references of those in the search were included as they were deemed of interest and had not been found in the initial search.

These papers were categorised into five methods of investigation:

- Non- invasive methods, Pulsed or dual frequency ultrasound and MRI
- *In vivo* decompression of mammalian species, with invasive observation
- *In vivo* decompression of (non-mammalian) animal models with non-invasive observation
- *Ex vivo* tissue
- *In vitro* models

In addition papers were grouped into those which reported only qualitative or observational bubble results, and those which reported quantitative results suitable for either validation or parameterisation of a computational model. Figure 2.2 shows the distribution. There were a group of papers which this search excludes though it could be argued they are of relevance. These papers are those which take measurements of blood or breathing gas mixture [87]. Such studies are useful in parameterising computational models as they provide data for saturation times and tissue gas wash out. They have not been considered here as the initial search results would have become prohibitively large. Instead we have chosen to consider only those studies which may provide parameter information regarding size or spacial bubble distribution and growth or dissolution rates.

The most widely used technique is the invasive observations of *in vivo* decompressed mammals. This technique is separated in Figure 2.2 into those which use fixation and histology, or those which expose tissue of interest to image directly using light microscopy. The primary advantage of both these techniques is their obvious physiological relevance. Animals with similar physiology to human divers are needed for correlation of DCS symptoms with quantified bubble findings and are essential for

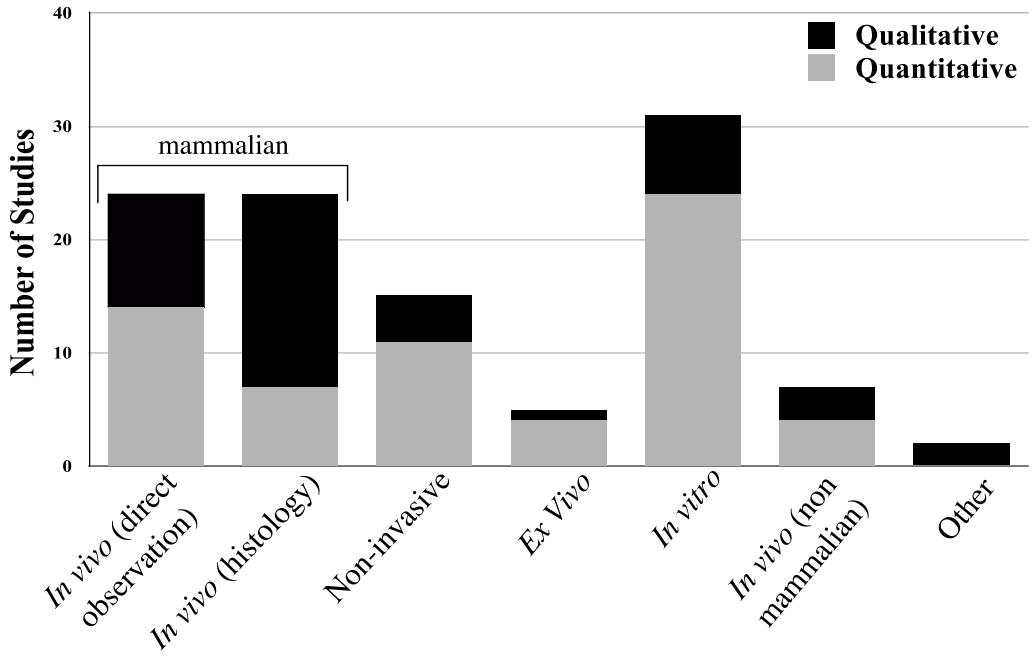

Figure 2.2: Chart showing the distributions of techniques used to investigate extravascsular bubbles

the assessment of pharmacological interventions. Other biological measurements including blood samples, blood pressure, endothelial dysfunction, VGE etc. can also be monitored.

Within the two invasive *in vivo* techniques, histological examination allows bubbles within opaque tissues to be imaged and staining may reveal additional information regarding the surrounding tissue structure. However, fixation and staining can only ever give a single time point for what is a dynamic process. Direct microscopy may overcome this by allowing bubbles within exposed tissues of interest to be monitored throughout the experimental time course. However by exposing internal organs either before the dive or post-mortem, some of the biological relevance of the system is disrupted, and visualisation of bubbles within many tissues will still be impossible due to their opacity. In addition to this, two disadvantages of such studies are the cost and ethical considerations. Another disadvantage of these techniques for monitoring extravascular bubbles is the difficulty in obtaining quantitative data. As shown in Figure 2.2 the proportion of quantitative data for these two techniques is the lowest. This is due to the complexity of a holistic mammalian model; with so many possible physiological measurements which may be made of the whole system, few studies report

histology or light microscopy as their primary findings. Often histology is performed only at the end point of the experiment, after other measures have been taken for some time post dive [58, 88]. Given that dissection or fixation would prevent or interfere with other possible measurements, decompression of large animal groups solely for dissection limits the scope and the cost/ethical justification for such investigation. However, unless light microscopy or fixation is done immediately at a number of different time points, the results are not of use quantitatively. Another difficulty with animal models is the variation in animal susceptibility [89]. Although it can be argued that this is an important biological feature of DCS which should be replicated in a model; it vastly complicates the understanding of how individual factors may affect bubble dynamics. Without a more reductionist approach the number of possible variables is too large to parameterise or validate current mathematical models of DCS [90].

The other two *in vivo* techniques shown in Figure 2.2 are the non-invasive ultrasound and the non-invasive observation of bubbles in non-mammalian animals (primarily marine or aquatic animals). Extravasular and vascular bubbles may often be observed in aquatic animals due to the transparency of their tissues. These systems have provided a relatively high proportion of quantitative results due to the simplicity with which bubbles can be observed. In addition such models retain some of the complexity of the mammalian models but such animals often have a simpler physiology, and more practical to decompress owing to the lower costs and fewer ethical issue surrounding their use [91]. Although a full animal model coupled with tissue transparency appears to make this an ideal model, they are not widely used in the literature. This is mostly due to their physiological dissimilarity to human divers. Given that these animals are primarily marine organisms, it is not unlikely to suppose that they have evolved physiological mechanisms which make them more resistant to DCS or bubble formation. As far less is known about their normal physiology, it is unclear whether such adaptations exist. How applicable results from such animals are to parameterising models intended for human use, is the main criticism of their utility. Additionally such animals are mostly too small for monitoring physiological markers other than some behavioural indications of DCS [91].

Non-invasive techniques which are capable of monitoring bubbles within opaque tissues include MRI, pulsed and dual frequency ultrasound (DFU) [92, 93]. These

methods show a high proportion of quantitative results but are amongst the most complex and expensive to implement. The MRI experiments of Hansen et al. [92] for instance, required the construction of a pressure chamber compatible with an MRI machine. Technological development of such techniques to reduce cost and increase ease of use, will make them an improvement on and potential replacement for the invasive *in vivo* techniques.

Ex vivo tissues have provided a very high proportion of the available quantitative data, however they are one of the least utilised models. *Ex vivo* tissue lacks the complexity of a full animal system, but still does not give the variable control control of an *in vitro* model. Bubbles within the tissue are still often impossible to visualise, and hence the data for these techniques largely reports bubble formation on the surface of the tissue.

The second most commonly used technique is *in vitro* models. This includes cell cultures and tissue phantoms such as gelatine and agarose. These models have also provided a high proportion of quantitative data. This is largely due to the control with which such systems can be manipulated and the ease of bubble observation. For example the gelatin models of Yount et al. [94] have been instrumental in the field of DCS, and resulted in development of the Varying Permeability Model (VPM) [95] and subsequent Reduced Bubble Gradient Model (RGBM) [96], The use of *in vitro* cell models has been important in understanding the role of ROS in endothelial dysfunction [65]. This wide ranging utility is due to the specificity with which hypotheses can be tested, a function of the control an experimenter has over the system. In addition such models are relatively cheap to use and hence study design can be optimised and run with large sample numbers. What is interesting within the *in vitro* category, is the lack of models which are able to combine cellular responses and bubble dynamics during simulated dives. Models tend to use either 2D cell cultures [97] in which case bubble formation is not considered, or they involve monitoring bubble production in 3D but without any cellular component, e.g. the gelatin models [94]. The main argument against *in vitro* models is, as with marine animals, the unknown biological relevance. It is not clear whether bubble models parameterised from such data are an accurate representation of the *in vivo* diver. Such criticism although valid to a certain degree, fails to understand that much greater simplifications are currently made in the computational modelling of

bubbles used in dive algorithms. *in vitro* models bridge the gap between current computational bubble models and predictions of DCS in whole animals. The utility of such models lies in the reductionism that they enable. This provides the ability to validate specific assumptions made in computational models and to probe specific interactions of interest whilst providing far greater control over other variables in the system. Thus through careful selection of the hypothesis to be tested and the specific *in vitro* model used; data from these models is useful and important in the development of DCS understanding and prevention.

The following sections will overview only the quantitative experimental data found in the literature search.

2.3.3.1 Published Data

The original pioneer of the doppler technique Daniels, recognised the importance of monitoring the stationary as well as mobile bubble population and used a pulsed doppler technique to measure stationary bubbles [73]. Using this technique. Decompression of guinea pigs from 0.69 and 0.83MPa indicated that stationary bubbles occurred before mobile bubbles were noted at ≈3min following a 0.83 MPa dive but only 17min following a 0.69MPa dive. From their work it was calculated that mobile intravascular bubbles accounted for only 0.01 to 0.9% for 0.69MPa of gas elimination and 0.06-6% in 0.83MPa. Interestingly they noted that if only mobile bubbles had been considered the 0.69MPa dive would have been reported as more severe than the 0.83MPa dive. Despite these findings pulsed doppler has not been widely used as a method after this original work.

In recent years the development of a dual frequency ultrasound system has been pursued [98, 99, 100, 101, 102, 103]. Dual frequency ultrasound uses two ultrasound transducers to transmit a low pump frequency and an high image frequency. Extravascular bubbles of a specific size will resonate due to the pump frequency. The nonlinear resonant oscillations from the bubbles will interfere with the image frequency allowing the bubbles to be detected and sized. This technique has been validated *in vitro* with a gelatin model using injected microbubbles [99] and in *ex vivo* beef tissue [100]. It has also been used in swine models [102]. Additionally the same group showed that microbubble like signals could be detected in the legs of humans following walking

[101]. Again the finding that stationary micro bubbles appear before mobile bubbles is confirmed. A transthoratic version of the dual frequency machine was used for intravascular measurements in swine [98]. The results from these experiments report an increase in signal amplitude after decompression, however the bubble sizing was not sufficiently sensitive or of a large enough range, and hence was not reported. The device of Chahine et al. [100] showed excellent agreement between optical sizing and DFU in *ex vivo* beef, however this was for injected micro bubbles. The main difficulty for DFU is that the size of the bubbles and likely bubble density within tissue is not known. Sizing of bubbles with this device requires either large pump frequency sweeps, and or knowledge of the size distribution. More recent studies have begun to use alternative non-invasive techniques such as MRI to investigate spinal cord DCS. However these studies are in general retrospective studies of human divers [104, 105], which could not provide useful quantitative bubble data.

2.3.3.2 In vivo decompression with histology or autopsy

Of the studies which use fixation and histological staining of mammalian species, only approximately one third of the papers found give quantitative data regarding bubble number, or size. The dog model of Francis et al. [23, 106] quantified the number of bubbles per section of spinal cord as well as the area of the bubbles and the proportion of the tissue which was occupied by bubbles. These data demonstrated that bubbles were more numerous in the white matter (7.66 and 0.48 per section in white and grey respectively), and that these white matter bubbles were smaller in size $0.010mm^2$ and $0.018mm^2$ for white and grey respectively. The highest proportion of the tissue area occupied by bubbles was found to be 0.47% in the lumbar region of the spine (L4). The rat model investigated by Marzella [88, 107] reported quantification of lesions and demonstrated that fixation produced bubble like artefacts. The proportion of non-staining lesion area was found to be 0.009% in control (undived) and 0.026% in dived. The authors concluded that extravascular bubbles although present in rats with spinal DCS did not constitute a large enough portion of the spinal cord area to cause dysfunction. Work by Palmer et al. [27] used a goat model of central nervous system (CNS) DCS, where the number of so called, grossly dilated empty vessels (GVED) was qualified and the percentage of meninges with GVED were also recorded. GVED

was significantly greater for animals that were euthanised at depth and then decompressed as well as those, compressed, decompressed and then euthanised, as compared to undived controls, (those euthanised at depth were not breathing during decompression and there gas exchange was substantially altered in these animals). One particular observation of this study was that what appeared to be extravascular bubbles, showed thin endothelial staining around the edges; from this the authors conclude that many "extravascular bubbles" actually arise in small capillaries or venuoles. In swine a large study was performed by Dick [26], however lesions were not quantified, More recently Mahon[108] carried out swine protocols and describes similar lesion distribution to Dick. Quantification showed the maximum proportion of lesion area to be 1.2% of the histological section of the spinal chord.This was found in the cervical spine, as opposed to the lumbar spine reported by Francis [106]. Areas of $< 0.5\%$ were reported for the thoracic and lumbar spine. Kitano investigated DON through bubble formation in the bone marrow of rabbits[35]. Histological quantification reported only that largest bubbles sizes were 5000μm for intravascular bubbles and 500μm maximum for extravascular bubbles.

Given the possible introduction of artefacts with fixation and the knowledge that bubbles are a transient phenomenon, many investigators choose to directly observe bubble formation with light microscopy. This is either done in real time with specialist decompression chambers to view exposed organs and tissues; or with immediate autopsy post decompression. Studies which use real time observations are advantageous in that they can investigate the initial bubble formation, however they suffer from poor visualisation of extravascular bubbles and are restricted to small studies. In many cases intravascular bubbles are reported in such experiments.

Direct observation by light microscopy has a higher proportion of quantified papers than the histological approach. This is primarily due to a series of papers by Hydelgaard et al. using a rat model with a specially constructed pressure chamber which incorporated a microscope[109, 110, 111, 112, 113, 114, 115, 116, 117, 118]. Although some spontaneous extravascular bubble formation was reported in adipose tissue [112], the methodology in these works involved the injection of a known gas volume into the tissue of interest and reporting on shrinkage rates with the addition of various interventions. The data show that bubble shrinkage rates increase when a change to breathing

heliox or oxygen is administered post or pre dive, and that this is increased further with the use of perofluorocarbons. Although the data from these experiments are of a high quality; it does not provide any insight into nucleation frequency, bubble sizes, or distribution within tissue. Shupak [119], dissected the intestinal mesenterium of rats post dive and quantified results via image analysis. Bubbles were mostly reported in the fibrous tissue adjacent to capillaries. Bubble number averages ranged from 1.35 -0.02mm^{-2} and bubble sizes were grouped into $< 50\mu m$ and $> 50\mu m$. 'Pingers' (high frequency sound emitters for locating underwater objects) were shown to increase bubble size and number.

Bennett et al. [120] counted bubbles in the tear film of human divers. Counts ranged from 0-0.33 pre dive to (0-2.25) for single day divers and (0.92-3.08) in multi-day divers. Bubble counts were shown to slowly reduce over 72hrs.

2.3.3.3 *Ex vivo*

Arieli et al. investigated the nucleation of bubbles from the aorta of sheep[121, 122, 123]. Bubbles which formed following a decompression were tracked using video and image analysis. The number of bubbles per area ($\approx 1-5/cm^2$) and the time to detachment (1-18mins) were reported in the first paper [121]. A subsequent paper published further data on the detachment size and diameter evolution over time (0.7mm-1.4mm over 15mins) [122]. This paper particularly focused on characterising so called "active spots" from which repeated bubble nucleation was seen. Reported bubble sizes in both papers, were far larger than is generally used in computational models, or that are targeted in the DFU experiments[99]. Recently the addition of flow to the model was investigated [123], it was found that a flow of 234 cm/min did not produce any change in detachment size.

Papadopoulou et al. [124] compare bubble nucleation and growth from the surface of ex vivo rabbit fat and muscle. This work used a specialised decompression chamber and optical monitoring to compared growth rates of individual bubbles until they detached from the surface of either muscle or fat. Growth rate of bubbles was compared to a $R(t) = At^{0.5}$ law (where R is the bubble radius, A is a constant and t is the time), goodness of fit was high (0.98, 0.97) for muscle and fat respectively. The size of bubbles was similar to those reported by Arieli et al. [122], with most bubbles

detaching at radius of $439\mu m$ and $231\mu m$ for fat and muscle respectively. The number of bubbles which nucleated was significantly higher on fat than muscle 4.2 and $8.4cm^{-2}$. The work also commented that bubbles coalesced on muscle surface but not on fat. Although this experiment provides excellent quantitative data for comparison to experimental models, it does not observe bubbles within the tissue samples, only those nucleating from the surface, and the relation between the two is unclear.

2.3.3.4 Transparent animals

Four simple animals have been described in the literature, A tadople tail fin model [125], a crab model[126, 127] a fingerling salmon [128, 91] and a prawn[129, 130, 131, 132]

Of these models only the crab and prawn models report quantitative results of bubble dynamics. The fingerling salmon model does not provide bubble data as the salmonids were not transparent enough to image extravascular bubble formation directly. However they do have highly simplified vascular system which enables quantitative reporting of the tissue saturation times for different gases [128]. The prawn model is the most researched. Investigations into the effect of high frequency sound[129] and hyperbaric oxygen [130, 131, 132] have been conducted. 14 animals were decompressed from 205kPa to investigate the affect of pingers. In the group exposed to the pinger, higher bubble numbers which persisted for longer, in a higher proportion of the prawns were reported. Hyperbaric oxygen exposure both pre-dive and post [130, 131, 132] showed a reduction in the number and size of bubbles for decompression from between 205-810kPa. The bubble volumes and number of bubbles per prawn are reported in both studies: in the pinger study 0-14 bubble/prawn were reported whilst in the hyperbaric oxygen 0-55 bubbles/prawn, (decompressions from greater pressure tended to produce more bubbles). The size distribution of bubbles in the pinger work reported modal bubble volume of $0.7-5$ x10^{-3} μl with a max of 20x$10^{-3}\mu l$. Although both studies show some increase in bubble number with increasing depth, no trend was reported. McDonough and Hemmingsen [126, 127], used a megalopae model to investigate the hypothesise that tribonucleation (the formation of bubbles caused by the movement of two solid surfaces within a liquid) causes bubbling in more primitive animals such as crustaceans. Mean bubble numbers of between 1-5 bubbles per animal

were reported for various conditions. Inducing animal movement created the highest number of bubbles (5 bubbles in 95% of animals), and immobilised animals had the lowest bubble numbers (only 4% developed a single bubble). These results, in addition to the observed location of the bubbles (always observed in joints), led the authors to conclude that tribonucleation played a significant role in bubble formation within crustaceans.

2.3.3.5 *In vitro*

As previously mentioned, *in vitro* models can largely be split into those which investigate cellular responses to bubbles or oxidative stress, and those which investigate physical mechanisms of bubble formation. Quantitative work on endothelial cell responses to bubble has been reported using a bubble on the end of a micro pipette to characterise the likelyhood and mechanism by which bubble proximity causes endothelial cell death[133, 134, 68, 135, 1]. These studies suggest that microbubbles cause cell death in 38.3% of cells via a an intracellular calcium influx with simultaneous mitochondirial membrane depolarisation whereas micropipette contact alone causes death in only 5.3% of cells. Both cell death and mitochondria depolarisation could be reduced by exposure to Oxycyte, (a perfluorocarbon (PFC)), and the surfactants bovine serum albium or Pluronic F-127, a polymer which competes for occupation of the bubble surface. Removing calcium from the extracellular environment and use of a calcium ion channel blocker, reduced calcium influx but not mitochondrial depolarisation. The mechanosensitive syndecan-4 receptor, a member of the transient receptor potential vanilloid (TRPV) family is the mechnosensitive trigger for two intracellular pathways summarised in Fig 2.3. Introduction of the surfactants reduced the calcium response by preventing the hydrophobic interaction of the air-liquid interface with HS syndecan side chains.

Other cell culture work does not include bubble data but does show a quantified response to the increased oxygen partial pressure for both endothelial cells[97, 65] and networks of glial cells [136]. These results highlight the complexity of potential mechanisms that must be considered if cellular response or other biological responses are to be modelled in dive algorithms. The works also highlight a gap in the field for models where bubbles, increased oxidative stress and cellular response can be investigated.

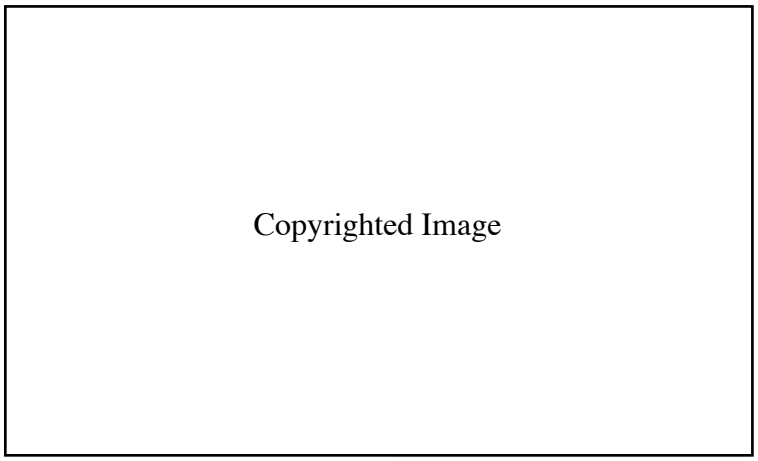

Figure 2.3: Illustration of mechanism by which air bubble contact elicits a calcium transient and mitochondrial depolarisation through two parallel mechanism. 1) the IP3 dependent Ca^{2+} influx and the PKC-α dependent mitochondrial membrane lowering pathway. [1]

Of the physical *in vitro* models, gelatine is by far the most widely used and historically important. The use of gelatine was originally conceived by LeMessurier [137] but largely developed by Yount, Strauss, Kunkle, Thomas and Beckman [2, 138, 139, 140]. The model was developed throughout the 1970's and 80's and was used to systematically investigate bubble nucleation and growth in response to variations in a wide range of dive parameters. These results formed the basis of the VPM [95] and the RBGM [96] as well as the theory of micronuclei which is now widely accepted in the field[13]. Strauss and Kunkle published two papers which tracked individual bubbles and monitored their dissolution based on gas changes [140] as well as lifetime measurements in response to recompression therapy [141]. Yount's work focused primarily on understanding the mechanism of nucleation. Yount et al. built a pressure chamber set up shown in Figure. 2.4, which utilised the transparency of gelatine to optically count the number of bubbles. Four gelatin samples could be simultaneously compressed to saturation pressure, P_s, left for a given time and rapidly decompressed to a final pressure, P_f, with the supersaturation pressure defined as $P_{ss} = P_s - P_f$. A series of experiments to test the variation in number of nucleated bubbles due to temperature, saturation times, and crushing overpressure were initially investigated [2]. Bubble numbers within the fiduciary volume (bottom 3mm of the sample chamber) were counted. Ranges of 16 - 500 per sample, 2.3-71 bubbles/ml, as a result of variation in pressure pretreatment from 300 to 150 psi were recorded. Comparison to the bubble numbers in prawns

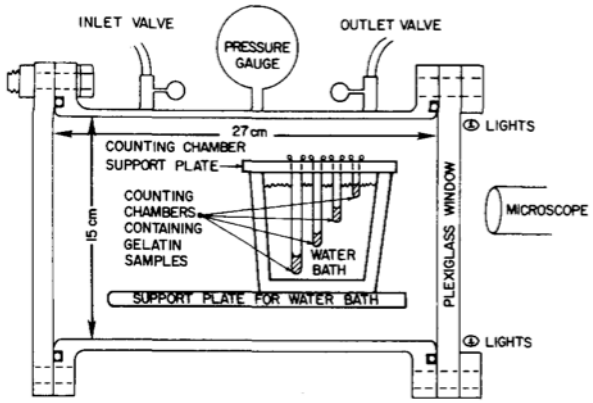

Figure 2.4: Diagram of the apparatus used in [2]

shows a similar range of values, 37 bubbles/ml (volume of prawn $\approx$ 1.2 ml bubbles per prawn= 45) when decompressed from 87 psi, following hyperbaric oxygen treatment; although it is difficult to directly compare such results as conditions and treatments were different.

Yount et al. proposed the theory of micronuclei, described below, on the basis of the gelatin experiments. This stated that decompression induced bubbles form, from gaseous nuclei stabilized by a surface-active membrane of varying gas permeability[94, 142]. Yount et al. continued to investigate the nature of these micronuclei and the hypothesised membrane in several ways [2]. Denucleation of the gelatin by centrifuging revealed that approximately 93% of the bubbles were present from the distilled water used to make the gelatine, whilst the remaining 7% were shown to form from the gelatine powder. Pressure spikes were also investigated as a means of crushing gas nuclei, these experiments showed that 75% of gas nuclei could be crushed by a short initial pressure spike of 300 psig for 1 second. Longer compression of 10mins resulted in 97% of the nuclei being crushed. Their later papers [138, 139], made a further investigation of this theory through gelatin filtering and use of stepped pressure increases. The major disadvantage of the gelatin model was the batch to batch variability [139, 143]. Numbers of bubbles produced varied by up to three orders of magnitude between different batches, with consistent results only obtained by the use of one large single batch of gelatin, frozen in aliquots and thawed before used. Using the same apparatus but with agarose gel, D'Arrigo et al. investigated the source of the batch variation and the possible surfactants which could constitute the stabilising gas

impermeable layer [144, 145, 146]. Bubble number was reported in a similar fashion to the gelatin work; purity of the agarose was found to be the factor which reduced batch variability [147]. Variation in gas type, pH (3-8) or with the addition if UO_2^+ (which would react with phospholipids) all produced no variation in bubble nucleation [146]. Much of this work focused on isolation of the molecule responsible for the stabilisation of micronuclei and will be discussed in chapter 7. Agarose gels were also used to test decompression schedules of six commercially available dive tables, including those of the French, USA, UK and Japanese navies as well as that derived by Yount for the optimum decompression of gelatin [144] [148]. It was shown that tables with slow initial ascent rates or deep stops resulted in fewer bubbles than schedules with faster initial decompression and longer shallow stops.

The agarose gel model can be criticised with the biological relevance argument discussed earlier. Gelatin is denatured collagen and therefore it can be argued that it replicates the extracellular matrix of soft tissues, however the same is not true of agarose. By using ultrapure agarose gels to ensure reproducbility, it is unclear whether the nucleation mechanism in this model is that which occurs *in vivo*. Understanding nucleation and micro bubble stabilisation are important scientific questions without reference to DCS, and hence the agarose model has utility beyond the DCS field. However, if one aims to parameterise dive algorithms with *in vitro* models, the models must be good biomimics.

Van Liew [149] specifically attempted to validate simulations of microbubbles against the dissolution of gas bubbles in saline for different gases. It was found that whilst the qualitative descriptions of the models matched, there was a systematic error whereby bubble dissolution was predicted to occur 30% faster than was measured.

2.4 Computational models

This section provides an overview of current and previous bubble models within the DCS literature, and in particular compares the methods of parameterisation and validation of each model

The section will be set out as follows: an overview of the structure and key developments of each of the reviewed models will be given with discussion of how bubble features are used and how the models validity has been assessed, a second subsection

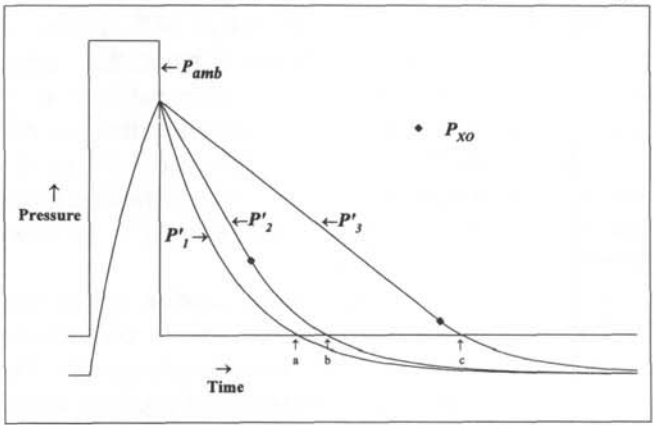

Figure 2.5: Taken from [3] showing the exponential saturation and desaturations for a mixed linear-exponential approach as used by (Thalmann).

will compare and contrast the various measures and methods used amongst the models, for parameterisation and validation.

2.4.1 How are bubbles modelled

The linear exponential Thalmann algorithm, (LE) is the algorithm implemented by the current US Navy dive computer. The algorithm describes a diver as a series of tissue compartments each characterised by a tissue half time. Each compartment absorbs gas according to an exponential gas saturation law but during decompression, tissue desaturation may follow either a linear or an exponential law, depending on whether the supersaturation of the tissue is greater than a threshold pressure denoted by P_{XO} $(P_T - P_{amb} > P_{XO})$.

The use of linear desaturation was implemented when symmetric models (exponential on and off gassing) could not provide safe decompression from long deep dives [150]. The linear desaturation regime resolved these problems and was thought to reflect the physiological change in gas kinetics created by the formation of bubbles. Bubble dynamics are not explicitly modelled in the Thalmann algorithm, as it is assumed that the bubbles are in instantaneous equilibrium with the surrounding tissue. The only output used in estimating the probability of DCS is the tissue tension, reflecting an underlying theory that this is the physiologically important measure. It is only by affecting this tissue tension that bubbles affect the probability of DCS. This probability is calculated using a maximum likelihood approach developed by Weathersby et al. [151, 152], where the probability of DCS p(DCS) in a time window $T1 - T2$ is

given by:

$$P(DCS) = e^{-\int_0^{T1} rdt} \cdot (1 - e^{-\int_{T1}^{T2} rdt}) \tag{2.1}$$

Where r is the hazard function. $T1$ is the last time the diver reported feeling normal and $T2$ is the time the diver definitely had DCS. The maximum likelihood approach with the above general expression had been used to optimise many DCS models, with the main variation being the chosen form of the hazard function. In collaboration with Thalmann, Weathersby et al. used a large dataset of over 8000 dives was used to calibrate the LE model and optimise parameters [153, 154, 3]. The hazard function was of the form:

$$r = \sum_{i=1}^{3} r_i = \sum_{i=1}^{3} A_i \left(\frac{P_{T_{IN}} + P_{FVG} - P_{amb} - Thr_i}{P_{amb}} \right) \tag{2.2}$$

Where Thr is a compartment threshold, A a constant of proportionality which sets the compartment weight, P_{FVG} is the fixed pressure contribution of the metabolic gases, P_{amb} the external pressure and $P_{T_{IN}}$ is the tissue inert gas saturation, governed by either the linear or exponential laws as discussed above. Prediction of the p(DCS) using the calibrated LE model (LE1) showed a good fit to the estimated time of DCS onset, with a three compartment version. The success of the LE1 in predicting DCS onset was taken as validation of the underling model. In addition, validation of the asymmetry in gas kinetics was independently provided in some animal and human models [155, 156, 157], which measured the exhaled gas composition during dry chamber dives. The linear desaturation kinetics, were also supported by a computational model of van Liew and Burkard [158] which will be discussed in more detail. Surprisingly, in spite of the success of the three compartment model the version in use commercially continues to utilise 9 compartments [159].

The VPM was developed by Yount et al. on the basis of the gelatin experiments [94, 160]. The premise of the model is that a population of bubble nuclei exist within tissues. These nuclei are surrounded by skins of amphiphilic molecules; which, as the bubble radius decreases, become more tightly packed eventually becoming impermeable to gas exchange. At this point the bubble is effectively stabilised against further dissolution, (the majority of the time the VPM operates in the permeable region, impermeability is only reached at $\sim$8 atm). The distribution of bubble nuclei is assumed to be exponential.

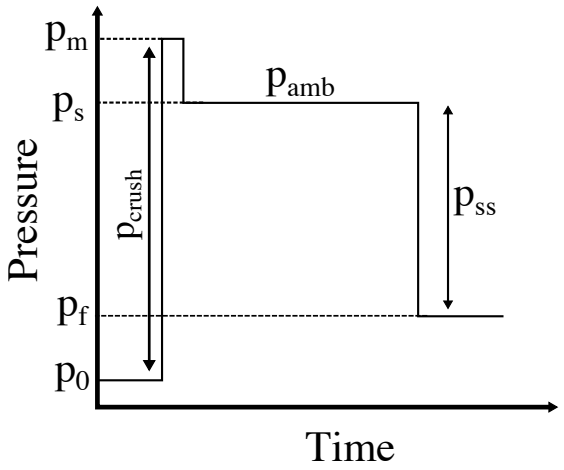

Figure 2.6: Pressure schedule with specific pressures indicated

$$N = N_0 e^{-r_{min}/\beta}, \tag{2.3}$$

where N is the number of nuclei with radius greater than or equal to r_{min}, N_0 is the total number of nuclei and β is the slope factor. When a supersaturation is applied to a distribution of bubble nuclei only bubbles with a radius greater than the critical radius r_c will grow into microscopic bubbles.

$$r_c > \frac{2\gamma}{p_{ss}} \tag{2.4}$$

where p_{ss} is the supersaturation pressure (see Figure 2.6), γ is the surface tension and r_c the critical radius. Hence, for any applied supersaturation, the number of bubbles which will nucleate into microscopic bubbles is given by.

$$N_{actual} = N_0 e^{-r_c(t)/\beta}, \tag{2.5}$$

Where $r_c(t)$ is the number of nuclei at time t to have a radius equal to or greater than the critical radius. VPM also assumes that a certain number of bubbles N_{safe} can be tolerated by a diver indefinitely, and that the number of bubbles may exceed N_{safe} for a short period of time without any ill affects. Once bubbles have nucleated their volume inflates in proportion to p_{ss}; VPM attempts to prevent DCS by keeping the volume of gas below a critical volume V_{crit}, which is calculated by

$$\int_0^t P_{ss}(t)(N_{actual} - N_{safe})dt \leq \kappa V_{crit} \tag{2.6}$$

κ is the constant of proportionality.

As can be seen, the growth dynamics of nucleated bubbles are highly simplified, most of the analytical effort is in calculating how the radial distribution of the bubble nuclei changes on the basis of the dive profiles compression and saturation pressures. To begin the algorithm values are picked for the initial minimum radius r_0^{min} ,γ ,γ_c the crumple compression of the molecular skin, the time constant τ_r over which bubble nuclei will regenerate and λ which describes the amount by which the number of bubbles N_{actual} can exceed the safe amount N_{safe}. Given a pressure increase from P_1 to P_2, where the nucleus remains in the permeable region, the new nuclear radius can be calculated by

$$\frac{1}{r_1^{min}} = \frac{1}{r_0^{min}} + \frac{P_1 - P_2}{2(\gamma_c - \gamma)} \tag{2.7}$$

Nuclear regeneration then occurs during the profile saturation time see Figure 2.6, and results in a nuclear radius $r(t_R)$. After nuclear regeneration a decrease to a pressure p_f is calculated which will just probe the originally set r_0^{min}.

$$p_{ss} = 2\left(\frac{\gamma}{\gamma_c}\right)\left(\frac{\gamma_c - \gamma}{r(t_R)}\right) \tag{2.8}$$

Given this p_{ss} ($p_{ss} = p_s - p_f$) a decompression profile is calculated, and provides a decompression time t_D. The integral in 2.6 can be re-written using t_D as

$$\kappa V_{max} = (N_{actual} - N_{safe})p_{ss}(t_D + H/ln(2)), \tag{2.9}$$

where H is the tissue half time, and V_{max} is the volume of gas evolved. A new value for p_{ss} (p_{ss}^{new}) can then be calculated from

$$p_{ss}^{new} = \frac{\kappa V_{crit}}{(N_{actual} - N_{safe})(t_D + H/ln(2))}, \tag{2.10}$$

p_{ss}^{new} will be a more aggressive decompression causing bubbles of a smaller r_0 to be excited r_0^{new}. This process is done iteratively until the volume V_{max} differs from V_{crit} by

a tolerated amount [161].

In the same way as the LE algorithm, the VPM models a diver as a series of compartments, 12 in this case, each compartment has a different tissue half time; the rate at which the tissue accumulates gas is given by the Schreiner equation [162], or an exponential Haldane equation. In contrast to the LE model the VPM uses bubble volume as the key predictor of DCS. In the originally formulated VPM this was not the case, bubble numbers were used to predict the DCS probabililty. This approach was able to predict gelatin experimental results as well as the morbidity of fingerling salmon[163], rats and humans [164] for a limited set of pressure profiles. However, when full operational dive tables were created there was seen to be a large deviation from current diving practice, with many profiles having overly conservative decompression times. This led to the development of the critical volume criterion [161] as well as the inclusion of a Boyle's law contribution to the bubble growth [162]. This updated VPM, (VPM-B) produced total decompression times more in keeping with tables calculated from the LE algorithm but with a shift towards deep stops [14].

Models which explicitly simulate bubble dynamics within tissues have also been of significance in the DCS literature. These models have been generalised to either two or three region models [4], depending on how a tissue with a bubble is described. As shown in Figure2.7 a two region model considers only a well stirred tissue with a bubble within it, where as a three region model considers a well stirred tissue, a bubble and a diffusion limited region directly surrounding the bubble. Two region models are discussed here in the context of the van Liew model, whilst three region models are typified by the Gernhardt model [165] and later the Gerth and Srinivasan models [166].

The model of Van Liew [167, 158, 168] was developed to investigate diffusion limited bubble growth in perfused tissue with a focus on the effect bubbles would have on the off gassing of the tissue. The model assumed a single spherical bubble centred within a unit of tissue that was unstirred but had uniform perfusion; all points in the tissue were subject to a diffusion law with a sink/source term. This enabled the effects of increased perfusion to be modelled without explicitly modelling a blood region. The

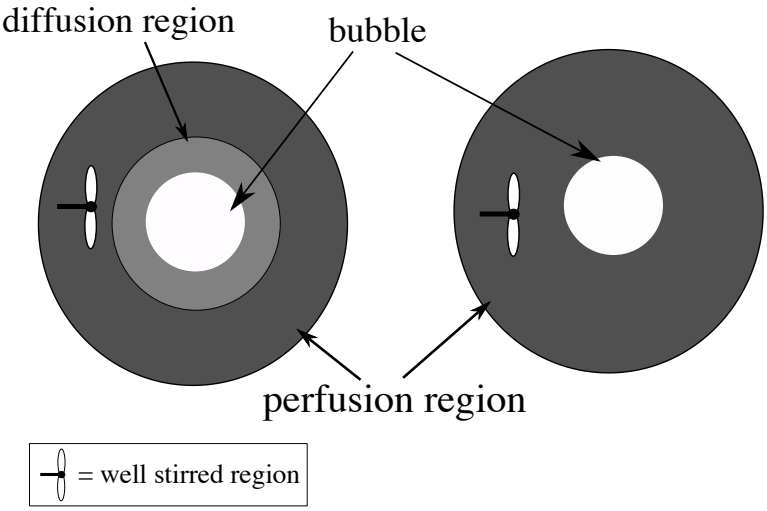

Figure 2.7: Two and three region models as described by [4]

equation of radial change for the bubble was given by

$$\frac{dR}{dt} = LtD\left(1 - \frac{p_{tissue}}{p_{bubble}}\right)(\lambda + \frac{1}{R}) \tag{2.11}$$

$$\lambda = (Lbk\dot{Q}/\alpha tD)^{\frac{1}{2}} \tag{2.12}$$

where L is the solubility of nitrogen in blood or tissue, $k\dot{Q}$ is the effective blood flow, D is the diffusion coefficient, bubble pressure is given by the Laplace equation and the pressure in the tissue was based on the rate of perfusion and the rate at which gas diffused into or out of the bubble [168]. This model could be either diffusion or perfusion controlled depending on the value of k. Van Liew used the model with a variety of tissue volumes to simulate tissues with differing bubble densities. This model produced an effect known as clamping, where bubbles stopped growing after an initial fast growth phase and tissue desaturation became approximately linear. Clamping occurred as during the initial fast growth phase a bubble will deplete the immediately surrounding tissue of gas, creating a zone of depletion which is almost in equilibrium with the bubble. When there are many bubbles in the tissue the entire tissue becomes depleted and the gradient to drive inert gas into the blood stream is greatly reduced. The effect occurred for both high bubble densities and slow gas wash out times. Through changes in the bubbles/ml and tissue half-times $t_{1/2}$, bubble dissolution time and max radius varied greatly, ($\approx$ 50 mins and $100\mu m$ for $10^5/ml$ with $t_{1/2} = 5$ mins and up to 2.5 days and $300\mu m$ for 10^2 /ml and $t_{1/2} = 360$ mins) [158]. Bubble numbers ranged from

10^2-10^6 bubbles/ml in these simulations. Estimation of the densities and initial sizes were based upon Yount's gelatin model which reported between 2-2000 bubbles/ml, crude estimates from Daniels [73] in the thousands of bubbles/ml and Kislyakov et al.[169] reported values of 10^9 bubbles/ml. Van Liew and Burkard also extended this model to multiple gases [170]. Validation of the model was done by predicting the dissolution time of bubbles in saline and for the dissolution of gas pockets injected subcutaneously in rats [171, 149]. The saline measurements found a systematic error whereby the model under estimated the dissolution time by 30%. By contrast to the maximum likelihood approach, van Liew's approach to parameterisation was to use values for solubility, blood flow, diffusivity, etc from the physiological literature and to modified them only within an accepted physiological range. Although this model was not directly used to predict DCS, the clamping effect found here was crucial in the inception of the linear desaturation mode of the LE1. Although this model described multi-bubble behaviours, bubble-bubble interaction was never considered. The tissue:bubble volume ratio is altered to simulate higher or lower bubble densities but gas transfer only occurs between tissue and bubble and tissue and blood, with no direct bubble-bubble or tissue-tissue diffusion. For high bubble densities it would be thought that bubble-bubble interaction would significantly alter overall gas transfer and bubble dynamics.

The model of Gerhart [165], described the bubble tissue system in three regions, the bubble, the perfused and well stirred tissue compartment and a well defined diffusion region surrounding the bubble. The bubble radial change is given by,

$$\frac{dR}{dt} = \frac{L_t D_b \left(\frac{1}{h} + \frac{1}{R_i}\right)(P_t - P_i) - \frac{R_i^3 dP_{amb}}{dt}}{P_{amb} + \frac{4\sigma}{3R_i} + \frac{8\pi}{R_i^3 M}} \tag{2.13}$$

Where L is is the solubility of nitrogen in the tissue, D_b is the diffusion coefficient of nitrogen through the bubble surface, h is the thickness of the bubble surface and M is the tissue bulk modulus of elasticity. The model assumed that region 3 which provides the boundary conditions for the diffusion region, was perfusion i.e. well stirred with the concentration of the entire of this region depending only on the rate of perfusion. The parameterisation of the model was based on the coincidence of the maximum bubble radius with symptomatic onset of DCS, and used logistic regression on a data set of

approximately 6500 dives to set parameter values. Major differences between this and the van Liew model were the introduction of tissue elasticity which acted on the bubble surface, as well as the concept of the diffusion shell which surrounded the bubble. In order to achieve the time delay in the onset of DCS symptoms this shell had a far smaller diffusion coefficient ($\approx 10^{-12} m^2/s$) than actual tissue ($\approx 10^{-9} m^2/s$). These two models were combined in the bubble volume model (BVM) developed by Gerth [172]. This used the two region equations of van Liew with the tissue elasticity term from Gernhardt. BVM parameters were optimised via the maximum likelihood method, on the same data subsample used to optimise the the Linear Exponential Model. It was shown that the BVM model with three compartments performed on a par with the LE1 model. However the parameter optimisation led to some non-physiological values for the diffusion coefficient and bulk modulus. The authors acknowledged that this may be indicative of an incorrect underlying model, or of mislabeling parameters, this will be discussed in more detail in Chapter 3. Although the BVM predicts similar p(DCS) and total decompression time to the Linear Exponential Model; it requires a different distribution of stop depths, with deeper stops prescribed by the BVM. During a large controlled manned trials of deeper stops profiles prescribed by the BVM a significantly higher incidence of DCS was found for the BVM compared to the LE1 (11 DCS/198 dives for deep stops, 3/192 for shallow stops) [173]. However the VPM which also prescribes similar deep stops continues to be widely used in the recreational industry, particularly by those diving using trimix gases [14].

Development of explicit bubble dynamics models has continued over recent years with much focus on the nature of Gernhardt's diffusion shell surrounding the bubble. This diffusion shell is considered to be an region of tissue immediately immediately surrounding the bubble, which is unstirred (i.e. gas transfer occurs by diffusion only), which has a very low diffusion coefficient. Investigation into differences between two and three region models were carried out in a series of papers [4, 166, 174, 175, 6].

Comparison of a three region fixed thickness diffusion shell and van Liew's two region model [4], concluded that the two region model was only mathematically appropriate for infinite tissue volumes with transformation of parameter values. The authors concluded that three region models were a preferable research avenue. Investigations into the diffusion shell were continued with diffusion region thickness and diffusion

coefficient analysis being carried out [166, 174]. These showed that use of a constant thickness diffusion region violated Henry's law. A further paper on the model examined the extension of the model to multi bubble simulations where competition for dissolved gas occurred but no mechanical interaction of bubbles could take place [175]. These models have no direct experimental validation, and are not commercially used to predict DCS risk through any hazard function.

The most recent tissue bubble model has been that of Hugon et al. [176], who developed a model of bubble dynamics within a joint. The joint was modelled as two compartments both of which are well stirred and therefore perfusion limited. These two compartments exchange gas by diffusion and perfusion. In the model only one of the compartments is considered to generate microbubbles which nucleate according to Yount's nucleation model. Their growth is governed by dynamics similar to van Liew and Srinivansan. Parameterisation of the model was a particular focus and again total gas phase volume was used as the model output which indicated DCS risk. Using risk data base from COMEX, parameter optimisation led to two parameters sets both of which were within a realistic physiological range. The authors conclude that this was a validation of the underlying mechanical model.

In addition to extravascular tissue bubble models, vasculature bubble models are also found in the DCS literature. Chappell and Payne's model [177, 178, 179, 180, 181], focused on nucleation of bubbles from crevices in the endothelium wall and their subsequent growth and detachment. The effect of the crevice geometry was investigated as a means of bubble stabilisation. The interaction between vascular and extravascular bubbles was also considered in the model with diffusion between the tissue to the crevice bubble occurring. The tissue gas saturation was modelled using the three region extravascular tissue modelled of Srinivansan and Gerth [4]. Parameterisation of the model was hampered due to the lack of experimental evidence particularly regarding contact angles. In general physiologically realistic parameter values were used however low surface tensions were needed for consistent bubble release at moderate dive profiles [178, 177]. This work is of particular interest with regard to validation as it offers the possibility of a direct validation of the model output against vascular bubble load measured with ultrasound.

2.4.2 Parameterisation and validation

Several validation and parameterisation techniques have been discussed in the models above, these can broadly be categorised as models with validation against DCS symptoms and time of onset, or direct validation of model outputs. Parameterisation is a problem bound with validation as parameter values whether fixed or optimised may give an indication of the model's validity.

Prediction of DCS and validation against data from human divers is clearly essential for any operational dive algorithm, and represents the ultimate goal of any DCS model, however there are certain disadvantages to this method, particularly if it is applied prematurely to a complex bubble model. Prediction of DCS incidence is normally done via the maximum likelihood approach with a hazard function discussed previously. Although this approach is immensely powerful given that the mechanism(s) by which bubbles cause DCS are unknown, the form of the hazard function is not a trivial decision. Tikuisis and Gault considered various forms of the risk function [182] with discussion regarding the mechanisms of bubble injury suggested by each. A volumetric hazard function is indicative of tissue displacement being the cause of DCS, whereas a biochemical mechanism is more appropriately modelled by an R^2 hazard function. Interestingly the authors found an R^4 risk function gave the best fit to the same dive data used to optimise the LE1. This is not readily interpretable but could suggest a combination of mechanisms contributing to DCS. One of the key problems of the hazard function is that it may confound validation of the underlying model. If a model fits poorly with the data set or the optimised parameter values are far outside physiological limits, it cannot be known with certainty if the underlying model is incorrect or the hazard function has been formulated on an inappropriate model output. This is a particular problem if there is no independent validation of the underlying mechanistic model. The second problem for such an approach is that the model optimisation is highly dependent on the data set used to calibrate the model. Such data sets rely on the careful collection of dive profiles and on precise recording of the DCS incidence. Such data sets are difficult to acquire and are largely held by various military bodies. This inevitably skews the data as individuals will come from a much more restricted population in terms of age, sex and physical fitness than the entire recreational diving community. In addition how such data is subsetted can have a great impact on the p(DCS) calculated. In a

re-analysis of the LE1 model and the dataset used to optimise it, van Liew and Flynn [183, 184], subdivided the data into a compendium where saturation dives, repetitive dives and non-air dives were separately considered. This analysis showed that the inclusion of even a small number of saturation dives in the data subset vastly increases the total decompression time for all dives. The report suggests that careful selection of calibration data is essential in correctly predicting the p(DCS).

Direct validation of bubble models overcomes the two problems described above. Direct validation may be in the form of *in vitro* models or in the measurement of a direct model output such as gas kinetics [185]. This type of validation allows individual aspects of a model to be validated and in the case of the *in vitro* validation creates a more controllable system. Once validity of the underlying model is demonstrated, the power of such models to provide insights into the mechanism of DCS is greatly improved, and it can be argued that this should be an essential step in the construction of any new model prior to optimisation or calibration with DCS symptoms.

The modelling and measurement of VGE provides an interesting prospect for validation. As previously discussed, there is no clear correlation between VGE and DCS, but there is a general consensus that VGE may be an indicator of decompression stress. As the technique is already widely used there are many large data sets available, with an increase in quantity and quality of the data likely as the technology progresses. Although such models have great potential, much of the vascular bubble dynamics is dependent on the tissue gas kinetics. Vascular bubble models must therefore have independently well validated extravascular bubble models, if they are to be validated against ultrasound data.

A final point to note from the above modelling review is the lack of models which incorporate biological responses. For example no immune responses, such as platelet aggregation or cellular apoptosis are modelled despite good experimental evidence of their coincidence with DCS. This is largely due to a lack of data with which to parameterise such models and an incomplete understanding of the mechanisms. This is an area in which there is great potential for DCS modelling to be applicable to therapeutic bubble usage. Such models could be used to generate new hypotheses which could in turn develop a better understanding of the field and focus experimental research.

2.4.3 Modelling summary

A variety of DCS bubble models have been discussed and their validation and parameterisation methods compared. Within the bubble models, several areas of contention and possible further research have been identified, such as the diffusion shell surrounding the bubble and the direct mechanical interaction of bubbles. In addition two approaches to parameterisation have also been seen, either to fix parameter values at known physiological values, or to allow parameters to be optimised on larger data sets. The former of these requires direct validation of the model whereas the latter is often used as a measure of validity itself. It is argued that direct validation of bubble models is an essential part of any model development. *In vitro* models provide not only this direct validation capability, but also a more controllable test system. Once a basic model is validated it may then be used as a tool to investigate the mechanisms by which bubbles may cause DCS. *In vivo* testing, potentially using VGE measurements will clearly remain an important part of commercial dive algorithm development, however, the paucity of data regarding the mechanisms by which bubbles cause DCS, and the difficulty in parameterising the underlying models remains a great challenge in this field.

2.5 Conclusion

This chapter has summarised the current understanding of the role of bubbles in causing DCS and the techniques used to investigate the underlying mechanisms.

The main challenge remains the unknown link between bubble formation and DCS. Although there is good evidence that bubbles are involved in DCS there is no simple correlation. Using bubble volume or another bubble characteristic as a means of predicting DCS risk is therefore ineffective. This in turn leads to problems with the validation of computational models. Without a mechanistically defined link between a given bubble feature and the incidence of DCS, there can be no validation of the underlying bubble models. Such a link can only be provided by quantitative experimental work that can probe bubble dynamics and cellular responses in a controlled manner. The literature review carried out here has revealed a scarcity of such evidence currently. One approach is to use a biomimetic *in vitro* system, that can provide both the cellular response and bubble dynamics; as such, this type of system thought to be a

highly worthwhile research avenue in this field.

Chapter 3

Experimental system design and build

The aim of this chapter is to descibe, justify and show the limitations of the designed experimental system. This system consists of a type I collagen hydrogel, within a small pressure chamber, which provides real time optical access to bubble dynamics within the gel. Chapter 2, highlighted the need to understand the role of extravascular bubbles in DCS and provide parameterisation for dive algorithms. The difficulties associated with these needs were partially shown to be due to the scarcity of quantitative experimental evidence. This chapter will begin by discussing the appeal of the collagen type I gel as the *in vitro* model as well as the limitations of the gels. The second half of the chapter will then describe the design and function of the pressure chamber.

3.1 Collagen gels as *in vitro* models

3.1.1 Collagen *in vivo*

All tissues within the body are made up of a cellular and an acellular component. The acellular component is known as the extracellular matrix (ECM); it provides the mechanical stability of the tissue as well as a scaffold onto and through which cells attach, migrate, signal and proliferate. The ECM is a mesh of fibrous proteins, predominately collagen of which there are 28 types; and smaller proportions of a host of other matrix components which are tissue specific. For example elastin in arterial walls, hydroxyapatite in bone and basal laminin in endothelial walls. The ECM mesh is permeated by a ground substance, which is a gelatinous mixture of water stabilised by macromolecules known as proteoglycans. These proteoglycans are highly hydrophilic allowing the retention of large amounts of water within tissues, up to as much as $\sim 70-80\%$ for

cartilage and $\sim 60-70\%$ for other connective tissues [186]. The variation of ECM proteins, macromolecules and water content amongst tissue types confers a variety of mechanical properties; for example, it is the high water content of cartilage that provides the resistance to compressive stress [187]. These mechanical properties will affect bubble dynamics through the pressure the deformed tissue exerts on the bubble as it grows. In addition, the air-liquid interface which the bubble provides acts as an attractor for hydrophobic molecules which may be present in the ECM, this can lead to conformational changes in proteins containing hydrophobic motifs. The cellular population of the tissue maintains the tissue specific ECM as well as performing many other functions. The cellular component of a tissue may effect or be affected by bubble dynamics in numerous ways: Cells exert mechanical forces on the ECM and in doing so can cause anisotropies which may mechanically affect the growth of a bubble; the metabolism of oxygen by cells creates an oxygen and carbon-dioxide gradient within the tissue known as the oxygen window, this can affect the rate of gas dissolution into and out of a bubble. Cells may also respond to the presence or nucleation of bubbles and this response may be of crucial importance in understanding the pathophysiology of DCS, in particular there is evidence that the permeability of endothelial cells is affected by the presence of bubbles [188]. With such a myriad of potential interaction it is essential to have an *in vitro* model which supports a cellular component, within a relevant ECM.

3.1.2 Collagen production, extraction and the creation of hydrogels

Collagen is the most abundant protein in the body, making up approximately 30% of the ECM. Within the superfamily, collagen type I (COL1) is the most common form [189]. COL1 is initially formed intracellularly as single collagen molecules with a triple α helical structure. These are secreted into the extracellular space and the C-N terminals are cleaved enzymatically forming tropocollagen.

Tropocollagen molecules self assemble to form collagen fibrils with a periodicity leading to distinctive D-banding. *In vivo* the molecules of the fibril are cross-linked through the hydroxylysine and lysine residues or disulphide bridges. Fibrils are further bundled into collagen fibres [190]. The mechanical properties of a tissue are affected by the length and diameter of fibrils as well as the packing and orientation of the fibres.

Collagen hydrogels are formed by extracting tropocollgen from animal tissue with high collagen content: typically tendon, skin or tail. Prior to self-assembly and cross-linking tropocollagen monomers are acid soluble and can be extracted by weak acetic acid and stored at pH 1-2 and 4 $^\circ$ C without self-assembly occurring. To form a hydrogel the pH is increased to 7 and the temperature raised. Fibrilogensis occurs as the molecules self-assemble, forming a solid gel over approximately 10-15 mins. Cells can be incorporated by the addition of a cell suspension during the small time window after neutralisation but prior to fibrilogensis.

3.1.3 Comparison to native tissue and other models

Although the *in vitro* formation of hydrogels leads to fibrils with the same D-banding seen *in vivo* [191] and excellent cellular survival and attachment; hydrogels differ from native tissues in several ways.

The most pronounced difference is in the water content; in mature tissue the proportion of acid soluble tropocollagens is $<10\%$ and this decreases with age. This low concentration limits the collagen content of a hydrogel to typical values of $<1\%$. In addition to the low collagen content, the self assembly process *in vitro* is driven entropically rather than enzymatically meaning cross-links between fibrils are not formed [191]. The combination of the low collagen content and the lack of cross links lead to the poor mechanical stability of hydrogels compared to native tissue. Techniques to address both these problems have been thoroughly researched and a number of solutions are available. Plastic compression, [192] is a technique which removes excess water from the hydrogel thereby increasing the proportion of collagen and subsequently the mechanical properties without significantly affecting cellular survival [193]. Cross links can also be formed through several mechanisms. Rich et al. [191] showed that the introduction of riboflavin to the hydrogel prior to fibrilogensis and UV-light exposure post fibrilogensis caused the formation of cross links and increased the mechanical strength [191]. A disadvantage to this technique is the cytotoxicity associated with riboflavin. A different approach which maintains biocompatibility is extraction of cross-linked collagen from the native tissue to form a blended gel [194]. The pre-crosslinked or polymeric collagen is insoluble in acetic acid but can be extracted into a stable suspension by the addition of Ethylenediaminetetraacetic acid (EDTA) which destabilises

the collagen fibril [194]. Using this technique a suspension of cross-linked polymeric collagen mixed with acetic acid dissolved monomeric collagen can be made into a hydrogel, that has been shown to have increased Young's modulus whilst maintaining biocompatibility [194].

Collagen hydrogels have been used extensively within the tissue engineering field for many years [195]. Their efficacy in this field is largely due to excellent biocompatibility, the conservation of collagen across species and the control over cellular behaviour which can be engineered. For example, endothelial cells can either migrate through a collagen gel and form sheet-like structures with apical and basal polarity; or form small capillary like networks within the gels, with the removal or addition of basal laminin [196]. Collagen gels seeded with smooth muscle cells and under uniaxial strain will remodel the collagen aligning it and forming myotubes which exert measurable contractile forces [197]. Tendon and nerve models have also been developed in which cells show significant remodelling of the surrounding matrix into more biomimetic structures [198, 199]. There is also data available on cellular metabolism, migration and proliferation, which is useful for the incorporating cellular dynamics into computational models of bubble dynamics and potentially, into dive algorithms [195, 200].

Other *in vitro* models have been used in the field of DCS as outlined in Chapter 2. Where the collagen gel improves upon these models is the increased complexity that can be achieved by comparison to gelatine or agarose models. This complexity is both in terms of the mechanical structure, by the introduction of cross-linked collagen or the plastic compression, as well as in the complex cellular structures which can be formed within the collagen gels. The major advantage of using such a model by comparison to an *in vivo* or *ex vivo model* is the level of control that can be exerted over mechanical and biological parameters. In a condition as complex as DCS it is vital to ensure that as the complexity of the computational models is increased, there is systematic validation of each step. Collagen gels provide the ability to increase the *in vitro* complexity (upto a certain limit), in line with development of computational models and thereby enable direct validation of the computational model through its development. This is a unique and incredibly important asset within the DCS field. To date there have been no models which offer this level of control coupled with the potential to bridge the gap between the

study of bubble dynamics based on physical parameters and those based on full animal scale biological parameters. It is worth mentioning that the *in vitro* modelling approach also reduces the amount of animal models that are needed, this not only reduces the cost of experimental work, it is also in line with the current government Reduction, Replacement and Refinement policy on the use of animal studies in the life science.

3.2 Approaches to chamber design

The second part of this chapter now discusses the design, development and testing of the pressure chamber system. This system must apply a preset pressure profile to a collagen gel whilst, allowing the realtime measurement of bubble dynamics. Chambers with similar design requirements have been used to investigate cellular dynamics under high pressure, as well as gels, rubbers and polymers in the DCS and industrial fields. From this literature three design approaches are apparent.

The first approach is to design a chamber which fits under a conventional microscope; the sample within the chamber is imaged through optical windows in the top and bottom of the chamber. This microscope compatible chamber, allows one to utilise a microscope of choice, and consequently benefit from the optimised optics. The chambers of Ellis et al. [201] and more recently by Nishiyama et al. [202] are of this design and both make used of high numerical aperture (NA) lenses to image cellular dynamics at high resolution. Other potential imaging modalities such as fluorescence and confocal microscopy are also possible with such a chamber design, for example the chamber of Wang et al. [97] which was designed to be compatible with a confocal microscope. Although such chambers can provide the high resolution needed for single cell dynamics, the physical dimensions of the chambers are often restricted by the microscope body and or the optical requirements. The need to have samples within the working distance of the objective lens, is often more restrictive than the need to fit the entire chamber between the microscope stage and objective lens (or stage and condenser if an inverted microscope is used). By careful selection of window material 2D cell cultures can be imaged to a high resolution in such chambers [203, 204, 205], however, to image through the depth of a moderately sized collagen gel (thickness $\sim$4mm), an objective lens with working distances $>$ 6 mm would be needed. Lenses with high NA and long working distances are difficult and expensive to obtain, increasing the build

cost of such a chamber.

The second approach is to build a chamber large enough to contain the sample or multiple samples and modify existing microscopes or create new optics to allow for imaging [124, 206]. The chamber of Yount et al. [2] allowed four samples to be simultaneously decompressed, however the resulting imaging is of much lower resolution than microscope compatible chambers. In addition if one is to take advantage of having multiple samples, optics must be arranged to capture data from all samples simultaneously.

The final approach is to use a commercially available hyperbaric chamber and put microscopy equipment within it, as has been done by D'Agostino et al. [207]. This approach is only suitable for those with access to such a facility and the cost of using such chambers makes it prohibitive to many researchers.

For this work the decision to create a microscope compatible chamber into which a single collagen gel sample could be placed and pressurised was made. The microscope available for the work was a Nikon Diaphot inverted phase contrast microscope, with the highest resolution lens being a Nikon Plan Ph2 X20/0.4 DM ELWD- WD 6 mm N.A. 0.4.

Another crucial design decision was whether perfusion of the chamber would be used. Perfusion at high hydrostatic pressure is used in several of the chambers mentioned above [203, 204, 97, 202]. Incorporating flow helps to maintain cell viability and stable temperature. For a collagen hydrogel, flow would not be needed to ensure viability of the cells over the length of a simulated dive [200]. Inclusion of such a system dramatically increases the complexity and cost of the design, and so was not included for this work. However the chamber is designed in such a way that should perfusion be required at a later date there is sufficient space in the chamber body to allow for these modifications. The final requirements for this chamber based on the literature and planned experiments were as follows:

1. A maximum pressure limit of 145 psi, equivalent to $\sim$100 m of sea water.

2. The rate of pressure increase and decrease must be controlled electronically to allow for pre-set dive profiles to be specified.

3. The ability to maintain cell viability for the duration of the experiment and be-

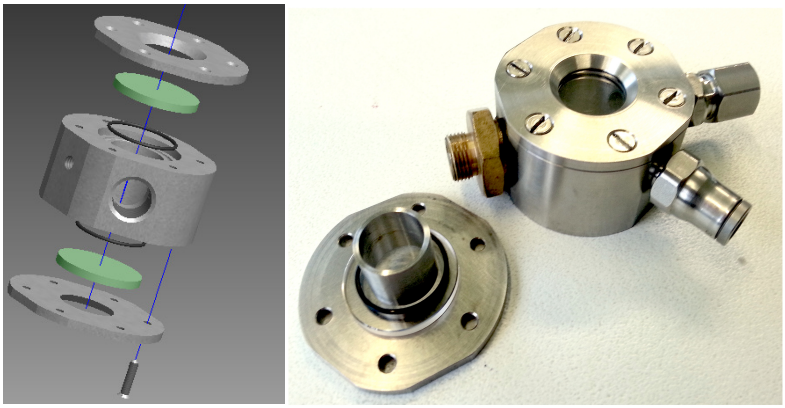

Figure 3.1: (Left) An exploded view of the pressure chamber components from the final CAD design, (Right) the final chamber with the base plate removed to show the window, o-ring and inner sample holder

yond - the chamber must permit autoclaving, have temperature control and contain a single sample surrounded by culture media.

4. Optical access during the pressure profile with an adequate level of resolution and field of view. This necessitated that the full sample should be within 6mm of the objective lens.

3.3 Pressure chamber description

3.3.1 Chamber body

With the requirements set out above and similar designs from the literature reviewed, the chamber design could proceed. Figure 3.1 shows the final designs of the chamber body and the chamber itself disassembled with an additional sample holder. Computer assisted design (CAD) software is an essential tool in the design of such a system, in this case AutoCAD inventor 2012 was used. The use of CAD software not only helps ensure accuracy but also facilitates design development. In this case exchange of CAD designs with industry enabled modifications to the chamber body to be compatible with industrially available components for the pressure and temperature control systems. Fabrication of the chamber was by the IBME workshop in the University of Oxford. The material choices for the chamber were made with both engineering and biological requirements in mind. The chamber body was fabricated in stainless steel with all other fittings selected to allow for the entire chamber to be autoclaved facilitating cell culture. As the design progressed an inner sample holder was added to allow more culture

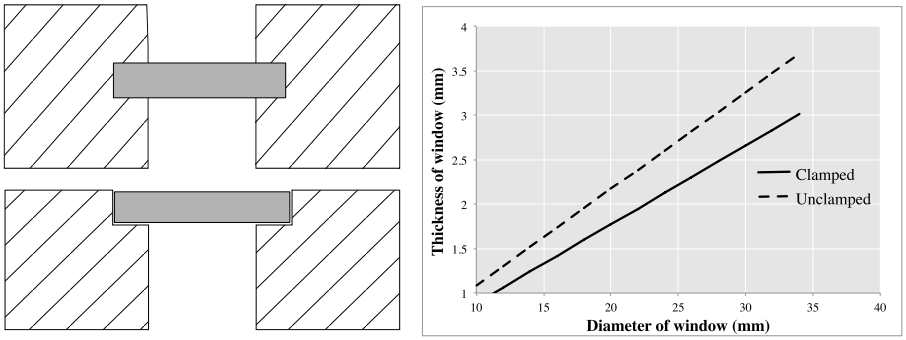

Figure 3.2: The clamped (top) and unclamped (bottom) configurations for pressure window design

media to be introduced to the chamber without damaging electrical components. This also enabled sterilisation by autoclaving only the sample holder and lower window, extending the life-time expectancy for the remaining components.

As has been discussed the main constraints on the chamber height came from the optical requirements; the outer chamber diameter was selected to ensure sufficient space for the gas inlet, pressure transducer and thermocouple. Additional space on the outer circumference also allowed for potential additions or modifications to the chamber such as additional windows, oxygen monitoring or perfusion. Designing with potential future work in mind extends possible uses of the chamber whilst keeping the initial fabrication cost lower.

3.3.2 Window design

In designing the window it is important to account for both the pressure and optical requirements of the system. The material chosen for the window was sapphire glass. Sapphire is of particular use in pressure windows as it has both a wide optical transmission range 180-4500 nm [208] and high apparent elastic modulus making it ideal for optical requirements where window thickness is crucial [201]. There are two possible configurations for windows within pressure chambers, clamped or unclamped Figure3.2. The clamped configuration requires windows to be secured without any possible motion at the clamped edges, in order to do this a glass cement or epoxy is needed. The unclamped configuration allows for a soft gasket to be used such as an o-ring, to be used to provide a seal. The pressure the window is capable of withstanding is found by [209],

$$t = D\sqrt{\frac{S_F K P}{4F_a}} \tag{3.1}$$

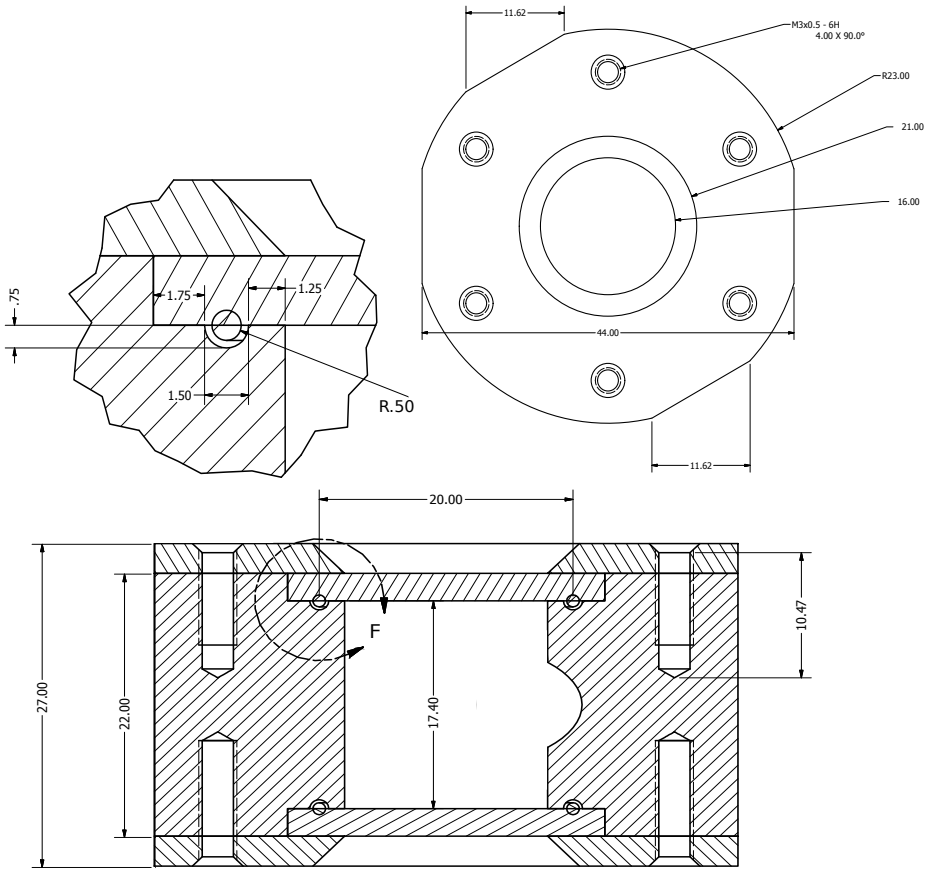

Figure 3.3: Bottom: cross-sectional view of the chamber, dimensions are shown in millimetres. Top left: Enlarged view of the O-ring seal showing the dimension of the O-ring and the groove. Top right: Plan view from the lid the six screws are used in both the top and bottom plate. The inner sample holder is not shown

where t is the thickness of the window, D is the unsupported diameter, S_F is the safety factor (13 was used), K is a constant that is either 0.75 or 1.125 depending on the mounting used [210]; P is the pressure difference across the window, and F_a is the apparent elastic modulus, (45000 psi for sapphire glass as given by Edmund optics.)

The glass used was a circular sapphire glass window, diameter 25 mm thickness 2.3 mm. This thickness allows for a maximum unsupported diameter of 25 and 21 mm for clamped and unclamped respectively.

An unclamped configuration for the chamber window was chosen to avoid the need for specialist epoxy sealing. Instead an O-ring seal was chosen, and groove dimensions were designed from industrial specification for static sealing [211] Figure 3.3 shows the dimensions of the O-ring grove in more detail. As mentioned above the unsupported diameter for this configuration was 21 mm, however this did not allow

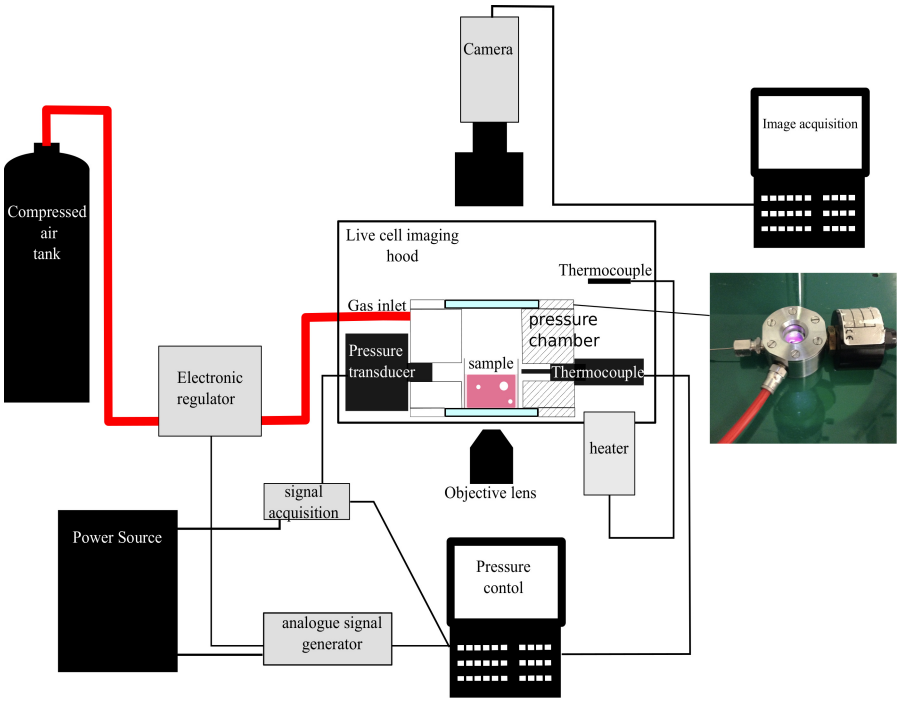

Figure 3.4: Diagram of the equipment setup

sufficient space for machining of the O-ring groove. A final size of a 16 mm window opening was chosen; this provided the required space for the O-ring groove, created inner dimensions large enough to allow the entirety of a gel made in a 48 well plate to be viewed, and allows for a theoretical pressure differential of 254 psi.

3.3.3 Temperature and pressure, control and monitoring

In addition to the chamber body, control systems for temperature, pressure and imaging were designed, Figure 3.4 shows a diagram of the complete set up.

3.3.4 Pressure control

Air pressure within the chamber was electronically controlled through Labview; either via an interface for a pre-set pressure profile or an interface which provided real time control.

The hardware used to control pressure were an electronic pressure regulator (QVP1) and separate transducer (DSX) both from Proportion-Air. The pressure regulator was calibrated from 0-145 psi $\pm 0.02\%$. A 4-20mA signal provided through a CompactDAQ Chassis and output chassis (National Instruments NI 9265, cDAQ-9171) was used to set the pressure. This particular regulator was chosen as it has a closed loop

system with its own internal pressure transducer to prevent fluctuations in pressure as a result of small leakage or temperature fluctuation. As the chamber volume was small (3.5 ml) it was suggested by the manufacturers that oscillating pressure waves within the chamber could occur affecting the specified accuracy and reliability. To monitor this potential problem a separate transducer was mounted directly to the chamber to provide an independent measure of pressure within the chamber. In the testing phase, it was shown that the chamber held pressure over a 5 hrs time period at 130 psi with no systemic loss in pressure. The low pressure limit and temporal response of the chamber were also tested. Figure 3.5 shows a pressure profile designed to test the lag time and possible oscillatory behaviour of the system. As can be seen from the lower left panel, there is an initial lag in the pressure response of the system. This is due to the initial lag time in filling the chamber and connective tubing. It can also be see that the pressure measured at the transducer is systematically slightly lower than that inputted. This was tested over a wide range of pressures and is always seen to be the case. In general this discrepancy is seen to be approx. 0.5psi. Despite further investigations, the source of the discrepancy was not determined, and given that it constituted only a maximum of 1.25% error in maximum pressure it was decided that this was within the acceptable limit.

Oscillatory behaviour can also be seen in the lower right panel of Figure 3.5. With each reduction in input pressure there is a small oscillation in the measured output which is damped in <5 seconds. It was suggested by the manufacturer that longer inlet tubing would help correct for this problem by increasing the overall chamber volume; however this would be at the expense of an increased lag time.

Although there are some limitations with the pressure control system, most of these limitations would be unimportant for the dive type profiles the chamber was designed to mimic. Indeed, despite its limitations the chamber will follow a given pressure profile far more closely than a diver would be able to. It was therefore decided not to modify the pressure control system; but for profiles where the pressure limitations could influence results, the recorded pressure profile from the transducer rather than the input profile would be used for analysis purposes.

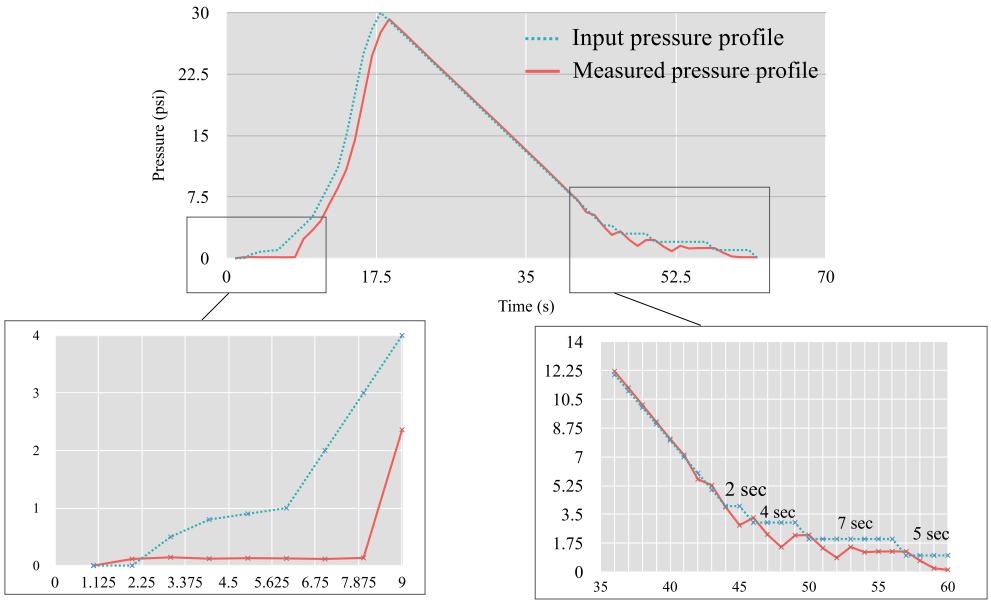

Figure 3.5: Showing a comparison of input and output pressure profiles. The bottom left shows the initial lag phase of the chamber filling.The lower right graph shows the oscillation associated with pressure changes.

3.3.5 Temperature control

The temperature control of the system was also set-up with one closed loop system controlling the temperature surrounding the chamber (Nikon) and a second system to more accurately monitor temperature within the chamber via a T-type thermocouple with Conax feed through assembly (Techni-measure UK). Samples were stored at 37°C and the chamber was heated prior to sample transfer. Once the chamber and sample were assembled temperature was continuously monitored throughout the experiment. The closed loop heating system was able to keep the ambient air pressure measured within in the chamber stable over the period of the experiments other than during fast decompressions. Figure 3.6 shows the change in the air pressure and associated temperature change within the chamber. The temperature change is approx. 0.5°C and the temperature recovers to the original pressure within 30 secs. Given this small change and the quick recovery it can be assumed that there would be no temperature variation within the gel and media which have a combined volume of 0.8 ml. Ideally the thermocouple would be used to measure the temperature of the media surrounding the gel however, in early trials it was found that bubbles tended to nucleate from the thermocouple.

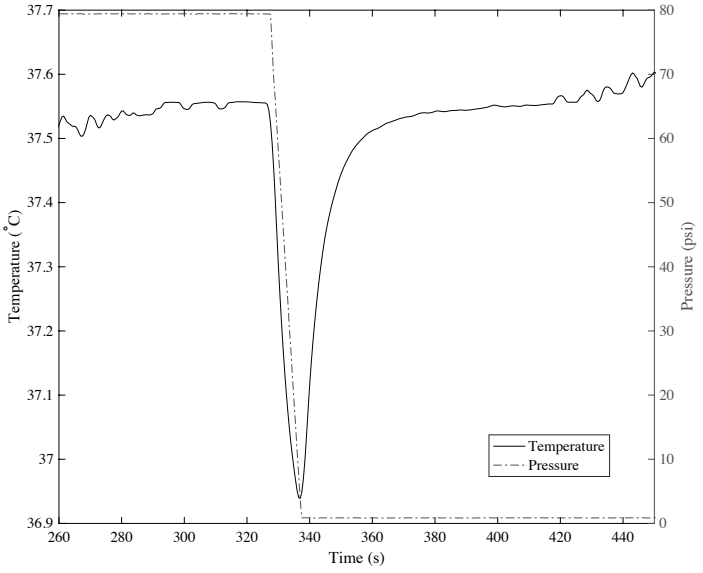

Figure 3.6: Showing the temperature fluctuation of the air inside the chamber associated with the decompression from 80 psi over

3.4 Image analysis techniques

Acquisition of time lapse images was done using a Nikon Diaphot inverted phase contrast microscope and camera (Hamamatsu C4742-95-12G04). HCL live imaging software was used to acquire images, with subsequent analysis being carried out in a combination of ImageJ and Matlab. The accuracy of the imaging was dependent upon the objective lens used in during acquisition. The lowest resolution lens enabled the largest area of gel (most bubbles) to be imaged and was therefore the most widely used. To determined the accuracy of bubble radii measurements repetitive images of the sample holder that had a known width of 1.5 mm were taken and measured manually. The standard error of the measurements was 0.005 mm, where one pixel of the image corresponded to a length of 0.007 mm. 0.007 mm constituted an absolute resolution limit for radial measurements and was also the smallest bubble that could be identified in a manual count of bubble number. However, it was found that the smallest bubble that could be reliably identified by the 'analyse particles' routine was an area of 0.001 mm^2 (radius of 0.0178 mm).

Analysis of bubble dynamics from time-lapse imaging was performed with one of three different techniques: 1) manually tracing individual bubbles in ImageJ (Fiji). 2) a semi-automated analysis using Image J to segment and find the area of well separated

bubbles, then Matlab to create time-course for each bubble. 3) counting of bubbles in sub-sectioned areas of samples.

The choice of analysis method was largely based on the quality of the image and the number and distribution of the bubbles. For samples in which a small number of bubbles nucleated and bubbles were largely well separated the semi-automated analysis could be used, and manual counting of all bubbles in the gel could be easily achieved. However, for samples in which there was a high proportion of overlapping bubbles or many were out of the plane of focus, the automated system performed poorly and manual tracing had to be used. In these cases manually counting the he number of bubbles within the entire gel lead to inaccuracies. To overcome this six rectangular areas were sub-sectioned from the image at regular points. The areas of the rectangles were chosen so that no more than 30 bubbles appeared in the area. Averaging over each of these areas produced mean bubble number per unit volume. A large amount of time was spent in trying to improve the automated bubble radius tracing algorithm. Within the literature the majority of image analysis aimed at segmentation of bubbles focuses on the circular shape [124, 212]. In the case here this could not be assured as bubbles often deviated from spherical particularly when in contact with one another. The use of machine learning segmentation as well as segmentation based on texture were used to try and improve the automation, despite some improvement many samples still required manual tracing. We suggest this would be an excellent area for potential future studies.

3.4.1 Matlab analysis

The semi-automated analysis that was used was designed as set out in Figure 3.7 briefly: The initial time-lapse stack was imported into the Fiji workspace, a Gaussian filter is applied to each image to remove uneven lighting effects. This blurred image is subtracted from each original image. A mean thresh-holding filter is applied. The *analyse particles* feature from Image J toolbox is used with the size of particle determined manually and a roundness value set to 0.4 to eliminate contaminants which can be mistaken for small bubbles.

The results of the *analyse particles* toolbox are imported into Matlab and the area plotted against slice number Figure 3.8. At this point there is no information regarding which area corresponds to which particular bubble over the entire time course. To

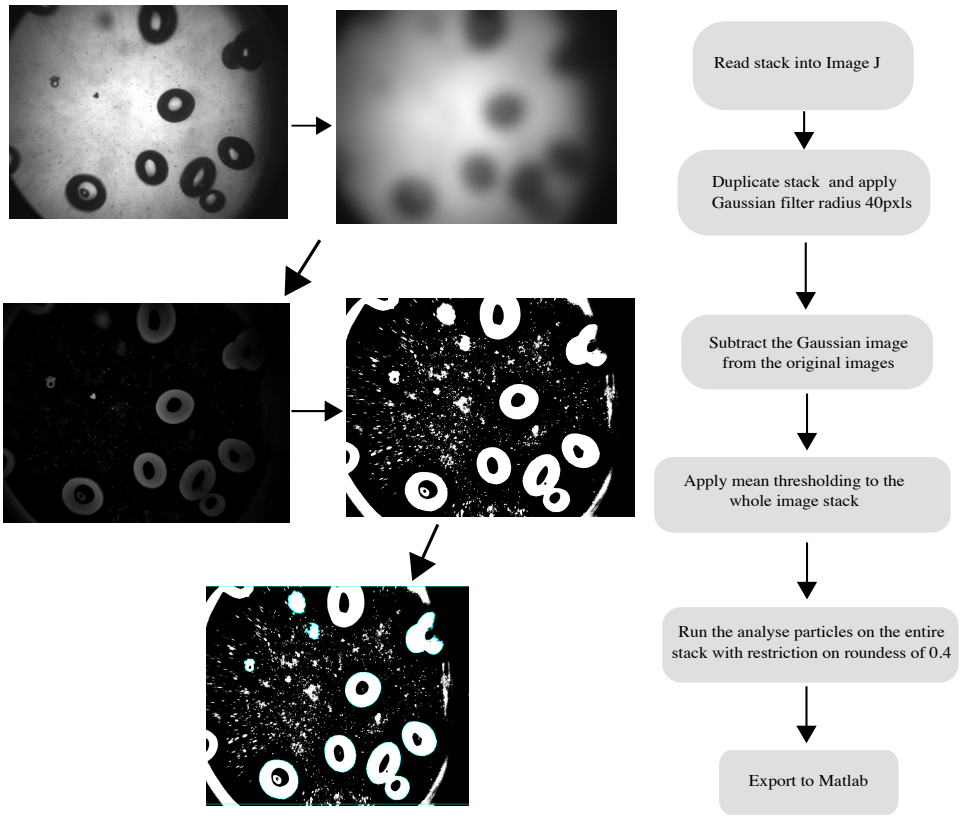

Figure 3.7: Showing the image analysis technique for the imageJ portion of the semi-automated technique

assign each area to a particular bubble trajectory the nearest neighbour for both the position of the centre and area from previous slices is compared to each particle in the current slice. If the bubble can be unambiguously assigned no user input is needed. If it cannot the two disagree the user is prompted to specify a trajectory. In instances where the number of particles changes such as where coalescence occurs a new trajectory is automatically added. Finally trajectories which do not change over the entire time course in area are eliminated as these denote mislabelled contaminant. The final result can be seen in Figure 3.8.

3.5 Basic experiment outline

The majority of experiments involved collagen hydrogels being decompressed in the pressure chamber. The basic experimental procedure is outlined here, any specific changes to the protocol will be discussed in the relevant chapters. Collagen hydrogels (0.5ml) were made as follows: 0.4ml monomeric collagen (rat tail collagen type I (First Link, UK)); was added to, 0.05 ml 10X concentration Modified Eagle's Medium

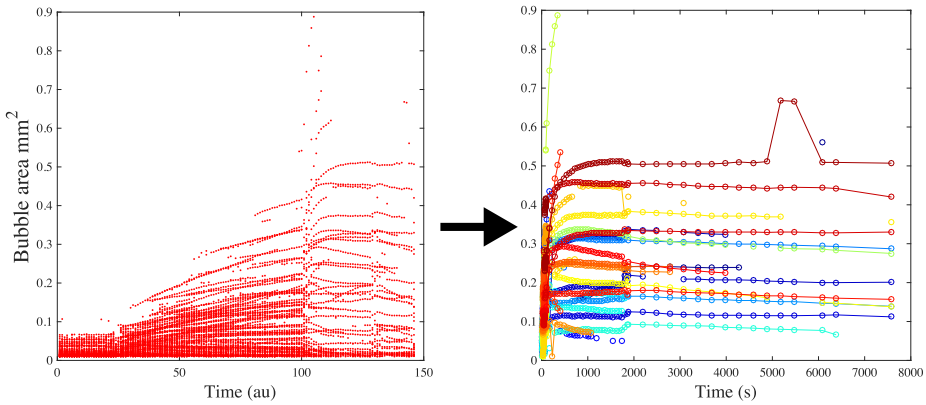

Figure 3.8: Showing the input of the raw bubble traces from the image J analysis (left) and the final output after the assignment of each data point to a specific bubble trajectory (right). In the right hand panel each coloured line represents a single bubble's growth from the start of decompression at 0 secs till 1hr 30 after the end of the profile.

(Gibco, UK). This mixture was neutralised by the drop wise addition of 5M NaOH and then stored on ice for 1hr to remove bubbles. After 1 hr 0.05 ml of either cells suspension with the required cell density, or plain Phosphate buffered saline (PBS) (Oxoid, Thermo Scientific, Loughborough, UK) or a PBS - nucleating agent suspension, was added. This was pipetted into individual wells of a 48 well plate and placed at 37°C for 15 mins for fibrilogensis to begin. After this time gels were removed from the incubator and covered in 0.6 ml Dulbeccos modified Eagles medium (DMEM), 2 mmol/l glutamine high glucose, (Sigma, UK), with 10% foetal calf serum (FCS; First Link, UK) and penicillin streptomycin (500 unit ml^{-1} and 500μml^{-1}) (ICN Biochemicals, UK)). In cases where gels were to be plastically compressed, this was done before the addition of the media. Gels were returned to 37°C for a minimium of 8-10 hrs before being used in any experiments. For use in the chamber, the entire chamber was incubated at 37° before 0.3 ml of warm DMEM was added to the sample holder. For transfer of the gels to the pressure chamber, the media covering the gels was initially removed, a 30G needle was then used to gently detach the gel from the well edge by running the needle around the edge of the gel. A small spatula was then used to lift the gel from the well to the chamber sample holder. The window and sample holder were screwed into place within the chamber and the whole chamber was placed on the

microscope table. The PID temperature system, pressure inlet hose and thermocouple were connected and the system left to equilibrate. The experimental dive profile was chosen as required via the Labview program and the time lapse imaging protocol set up as required for the experiment.

3.6 Conclusion

In this chapter a detailed description of a new experimental system for the *in vitro* study of DCS has been given. The system consists of a COL1 hydrogel and microscope compatible pressure chamber. The advantages of the COL1 as an *in vitro* model compared to others previously used in the DCS field are largely due to the interactions that are possible between, bubble dynamics, material parameters and biological functions such as cellular metabolism and viability. The controlled increase in complexity of the collagen gels and direct comparison to computational models will enable better development and validation of such models. The microscope compatible pressure chamber design was presented in light of other chambers in the field. Although the current design allows only single samples to be investigated at any one time, this is balanced against the ability to have greater resolution, which is needed for direct comparison to mathematical modelling. Some of the limitations of the chamber include the slight pressure lag between the input and measured chamber pressure however it is concluded that these sources of error are within a suitable tolerance for the type of pressure profiles that will be used. The chamber is designed with potential future alterations in mind in particular perfusion, and side windows are thought to be the most useful additions. Other further work that would improve the system would be in the automated image analysis, where dealing with overlapping bubbles and highly non-spherical bubbles would be a significant improvement to the system as a whole.

Chapter 4

Computational Model Derivation

4.1 Introduction

Models of DCS which incorporate bubble dynamics need to describe and predict a wide array of bubble behaviours. These include nucleation and stabilisation of gas micronuclei, diffusion-limited bubble growth and dissolution; as well as more complex bubble-bubble interactions such as coalescence and Otswalds ripening. As discussed in Chapter 2, an ideal bubble model of DCS should go further than this and incorporate the interaction of bubbles with cells and other biological systems. In this chapter a set of governing equations and assumptions are established for a computational model of bubble growth, dissolution and inter-bubble interactions, in the collagen gels described in chapter 3. As collagen gels themselves are good models for avascular soft tissue, it is hypothesised that such a model will provide insights into bubble dynamics *in vivo*. The use of the experimental system described in chapter 3, to validate and develop the computational model, is a novel approach in the DCS field. It provides the opportunity to investigate parameters and mechanisms in a systematic and controlled way which, in turn, can inform the development of bubble models currently used to predict and avoid DCS.

In the remainder of this chapter, the basic laws governing gas transport both through bulk tissue and over the tissue bubble boundary are discussed. The effect of tissue elasticity on bubble growth is examined, and how this has been modelled to date in the literature is analysed. The tissue mechanics analysis is presented as an exemplar of how validation of bubble models using symptoms of DCS can lead to inconsistencies in nomenclature and therefore understanding. It is particularly important that such

inconsistencies are well described and understood within the DCS field, as not doing so greatly limits the contributions other bubble research fields can make to DCS. Having analysed the elastic contribution, the full set of governing equations for the computational model is derived with non-dimensionalisation.

4.2 Gas Transfer

The model presented in this work is of bubble dynamics in collagen hydrogels due to the decompression from elevated pressure. The model considers the transport of gas through the tissue/gel during compression and the time spent at increased external pressure. During decompression, bubble growth is modelled, with gas diffusion across the tissue-bubble boundary and the external pressure change being the mechanisms of bubble radius change. Several assumptions are made regarding the behaviour and transport of gases, those which are not widely used are discussed in greater detail.

4.2.1 Gas laws

All gases are assumed to behave as perfect gases, this can be expressed as:

$$PV = \alpha m, \tag{4.1}$$

where P and m are the pressure and mass of a gas, and V is the volume occupied by it.

$$\alpha = \frac{\mathscr{R}T}{M}, \tag{4.2}$$

$\mathscr{R}$ is the universal gas constant, T is the temperature and M is the molar mass of the gas. With the assumption of perfect gas laws, Boyle's Law applies thus:

$$P_1V_1 = P_2V_2 \tag{4.3}$$

The total pressure of all is the sum of the partial pressures of the individual gases. The gases considered in this model are Oxygen and Nitrogen. The effects of water vapour, Carbon dioxide and other gases are not included.

4.2.2 Diffusive Laws

At the tissue or gel boundaries, gas is assumed to be dissolved in the surrounding media (blood in the case of a real tissue but culture media in the experimental system) in accordance with Henry's Law. Within the tissue, gases diffuse from the tissue edges according to the diffusion equation. In this model, advection is not considered [87]. Hence the governing equation can simply be written as:

$$\frac{\partial C}{\partial t} = D \bigtriangledown^2 C, \tag{4.4}$$

where C is the concentration of gas, D is the diffusion coefficient and t is the time. Boundary conditions at the tissue edge given by Henry's Law:

$$C^g = k_h^g p p^g \tag{4.5}$$

where C^g is the concentration of the gth dissolved gas, k_h^g is Henry's constant and pp^g is the partial pressure of the gth gas.

At the bubble-tissue interface, the change in mass of gas in the bubble is governed by Fick's first law of diffusion:

$$\frac{dm}{dt} = 4\pi r^2 D \frac{\partial C}{\partial r}\bigg|_{R_B} \tag{4.6}$$

$\frac{\partial C}{\partial r}\Big|_{R_B}$ is the concentration gradient at the bubble boundary. Henry's Law is used once again for the concentration of gas on the inner surface of the bubble but with P_B the pressure inside the bubble used.

$$C_B^g = k_h^g P_B^g. \tag{4.7}$$

P_B is calculated by the Young-Laplace equation

$$P_B = P_{amb} + 2\gamma/R_B + \Omega(R), \tag{4.8}$$

where $\Omega(R)$ is an additional term added to describe the pressure exerted by the surrounding tissue as a result of its deformation by the bubble and γ is the surface tension. The equations (4.1)-(4.8) are used to derive an expression for the radius change of a

bubble over the course of a dive profile. Before deriving the final equation, the elastic term $\Omega(R)$ and the possible forms it may take are analysed in depth.

4.3 Tissue mechanics

The elastic deformation term Ω was originally conceptualised by Nims and termed the 'deformation pressure' [213]. In Nims' model it was considered to describe a tissue deformation threshold; i.e when the threshold was exceeded nerve endings would be distended causing the joint pain characteristic in DCS. Nims did not give any explicit formulation for the term and there was no discussion of the possible affects this pressure could have on bubble dynamics[213]. Vann and Clarke were the first to discuss a defined elastic deformation function with reference to bubble dynamics [214]. They applied a hyperelastic strain-energy function used to describe the failure of rubbers [215, 216, 217, 218] which shall be known as "the Gent term". Vann and Clarke discussed elasticity in the context of its hypothesised effects on bubble nucleation. In the rubber field, this term predicts the growth of small spherical inclusions to occur only when the inflation pressure exceeds $5E/6 \approx 2\mu/5$ (where E is the Young's modulus and μ the small shear modulus).This prediction was validated in vulcanised rubber [219]. Vann and Clarke hypothesised that a similar effect could be responsible for the growth of bubbles in tissues, however they did not discuss incorporation of the term into a bubble growth framework. Instead, the first use of $\Omega(R)$ into a full diffusion/perfusion limited DCS bubble model was by Gernhardt [165]. In this work, the term was proposed to take a different form: $\Omega = 4/3\pi R^3 M$ where $M = K/V_{aff}$ with K =bulk modulus and V_{aff} =the affected tissue volume. This term (the Gernhardt term) was then used in the so-called Bubble Volume Model (BVM) [172]; a model which predicted the probability of DCS based on bubble volume. BVM was a three-compartment model of which three variants, BVM(1,2,3), included the $\Omega(R)$ term in either 1,2 or 3 compartments respectively. Validation of BVM was done via comparison to the then current US Navy linear exponential algorithm (LE1). BVM(3) was found to predict incidence of DCS on a par with LE1 [172], for the Navy dive database. Matching the prediction of LE1 was taken as validation for the model and, in particular, for the inclusion of tissue elasticity in the form of Gernhardt term. The problem with this analysis (which is acknowledged by the authors) is that, in order to match the LE1 outcomes, M be-

comes a free parameter which is optimised based on a subset of the database. The optimised value of M, however is unphysiological by several orders of magnitude. This suggests several possibilities: (i) that the Gernhardt term does not correctly model tissue elasticity and the M parameter relates to some other mechanical property; (ii) that their elastic term represents the combined effect of several factors which restrict bubble growth, some of which may be entirely unrelated to mechanistic affects; (iii) that the use of bubble volume for DCS prediction is not the most pertinant bubble feature. Despite these problems, the Gernhardt term and continued reference to M as the bulk modulus are found in the development of the BVM into the 3-region and multi-bubble models of [4] as well as used in the articulate joint model of [176], the 3-dimensional multi-bubble model of [220] and the joint tissue-crevice model of [178]. This is a clear example of how validation of bubble models using symptoms of DCS can confuse our understanding and intuition of the pathophysiology.

Problems with the Gernhardt term were once again highlighted by Goldman [221]. Goldman pointed out that the term is incorrectly derived with reference to either linear or non-linear elasticity. Goldman derived a new term (the Goldman term) via a more rigorous continuum mechanics approach, however the correctness of one of the boundary condition used in the derivation is disputed [6], as well as the application of linear elasticity to the problem of bubble growth in tissue. This will be discussed in detail in the following sections. In response to the work of Goldman, Srinivasan and Gerth acknowledged the incorrectness of the Gernardt term [6] but raised similar objections to the boundary conditions used in the derivation of the Goldman term. Instead Gerth and Srinivasan argue that the Gernhardt term can be seen as a reasonable one-parameter approximation to the hyperelastic Gent term[6] . Again this is disputed, in particular as the single parameter to which they refer is in-fact not a non-dimensional parameter of their model. This will be discussed in greater detail along with other non-linear elastic models within this chapter.

The final approach to tissue elasticity modelling is that taken by van Liew [158, 222]. Their models neglect tissue elasticity ($\Omega = 0$) as does the work of Chappell and Payne [178] in the crevice model. Chappell and Payne in fact, used the Gernhardt term but set $M = 0$ as it was shown that the Gernhardt term did not impact the dynamics of bubbles with radius $< 1000\,\mu m$, [178]. Although it may be the case that tissue

elasticity has a limited effect on bubble growth, given that the Gernhardt term has been recognised as mathematically incorrect it can be argued this remains to be proven. In addition, even if elasticity does not have an effect on bubble growth, there is still the question of the effect tissue distortion may have on cells and other biological systems in the vicinity of the bubble. Many cells have mechanosensitive ion channels, such channels are thought to be the mechanism behind the endothelia cell death caused by bubble proximity [134, 68].

In vitro work into the validation of tissue elasticity has been mentioned by [139]. In this work comparison of bubble nucleation in gelled vs sol (un-gelled) gelatine revealed no differences, with the conclusion that the hypothesised nucleation stabilisation as discussed in the Vann and Clark paper is disproved [214]. However, the depth of the analysis in this paper does not seem to justify their conclusion. The values for the shear modulus of the sol and gelled gelatin are not discussed and therefore it is not clear whether an inflation pressure of $2\mu/5$ was reached. Furthermore, the system did not look at the potential effect of tissue elasticity on bubble growth rate, and no cellular element was incorporated.

Finally, two constitutive approaches which might be expected to have been applied to this problem are viscoelastic and poroelastic frameworks. With reference to DCS only one application of such models [223] has been found; it describes the dissolution of large gas pockets in the subcutaneous tissue of rats using a viscoelastic constitutive equation. The dissolution of gas in polymers and other tissue-like materials is a widely researched subject and viscoelastic and poroelastic models are used in many other fields including ultrasound, soil mechanics, and polymer sciences [224, 225, 226, 227]. One of the major difficulties in the application of such models is the quasi-static approximation, which is generally used in DCS bubble models. Removing this approximation leads to a massive increase in the computational cost of such models and therefore must have a high level of justification. As the experimental evidence for extravascular bubbles is relatively scant, such justification cannot currently be made.

Having established the current state of the literature regarding tissue elasticity, the following section develops an expression to describe the stress acting on the bubble surface as a result of tissue distortion caused by a change in bubble radius. The analysis begins with the linear elastic framework, with a more detailed discussion of the

Goldman and Gernhardt terms as well as a derivation of our own linear elastic term. A general discussion regarding the validity of linear elasticity in this context follows. Hyperelastic models, in particular, the Gent model are then addressed, and evaluation of the statement that the Gernhardt term approximates the Gent term will be examined. All models are initially compared with a simple Boyle's law approach which neglects gas diffusion. Having done this, the full derivation of the diffusion limited bubble model is given.

4.3.1 Solid mechanics

The framework of solid mechanics is the basis for all the tissue elasticity terms discussed here. For any problem in solid mechanics to be well posed, three conditions must be specified:

- The conservation equation
- A constitutive equation
- Boundary conditions

The conservation equation in this work will be the Cauchy momentum equation and the constitutive equation may be linear or non-linear elasticity. In the case where the Cauchy momentum equation and linear constitutive equations are used with the assumption of electrostatics, the Navier equation is arrived at:

$$(\lambda + 2\mu)\ \text{grad div}\ \mathbf{u} - \mu \bigtriangledown^2 \mathbf{u} + \mathbf{F} = 0, \tag{4.9}$$

where μ and λ are the Lamé parameters, $\mathbf{u}$ is the material displacement and $\mathbf{F}$ the body forces.

The constitutive equation describes the relationship of stress to strain and is typically formulated in terms of several material parameters λ, μ, E, K and ν. All the parameters can be related to one another as follows.

$$\nu = \frac{\lambda}{2(\lambda+\mu)}, \tag{4.10}$$

$$\mu = \frac{E}{2(1+\nu)}, \tag{4.11}$$

$$\lambda = \frac{\nu E}{(1+\nu)(1-2\nu)}, \tag{4.12}$$

$$E = \frac{\mu(3\lambda+2\mu)}{\lambda+\mu}, \tag{4.13}$$

$$K = \lambda + \frac{2}{3}\mu, \tag{4.14}$$

Poisson's ratio, ν, describes the tendency of materials to contract along an axis perpendicular to a force exerting an extension. Many types of soft tissue are treated as incompressible ($\nu \sim 0.5$) due to their high water content [228].

Young's modulus E, is defined as the ratio of tensile stress to extensional strain. Typical tissues values range from as high as 80 GPa for bone, to $1-2$ GPa for a tendon, and $1-2$ kPa for the liver [186].

The shear modulus μ is defined as the ratio of shear stress to shear strain. μ also has a wide range of values across different tissue types, from ~ 1 Pa for the eye to $1-2$ MPa for cartilage [186].

Bulk modulus has already been introduced; it describes the resistance of a material to any change in volume caused by hydrostatic pressure (p). $p = -K\varepsilon_{kk}$ (where ε_{kk} is the volumetric strain) . K is strictly positive and is very large for almost all tissues, tending to infinity as the material approaches incompressibility. The Lamé parameter λ is closely related to the bulk modulus but is the only one of the five parameters to have no direct physical meaning. It is often understood to represent the compressibility of the material as from (4.14) it can be seen that for large $\lambda, K \approx \lambda$

Finally boundary conditions are needed to close the problem. In the case of a bubble expanding in an elastic media these boundary conditions are not straightforward. As highlighted by [229], in a standard cavity expansion problem such as that found in [230], or generally solved in soil mechanics [231], the cavity pressure is known and can therefore be used as a boundary condition. In the case of bubble expansion caused by external pressure changes, the bubble internal pressure and bubble volume and (hence

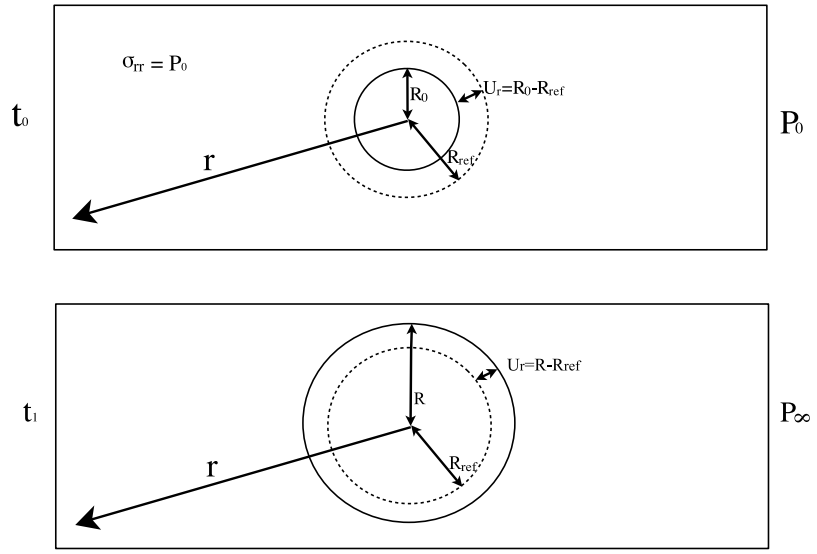

Figure 4.1: Showing how the derivation is set out with the reference configuration and the changes in bubble size depending on the change in external pressure.

radial position) are not known and must be determined.

4.3.1.1 Linear elasticity

Although as early as the 19th Century tissues were shown to have non-linear stress strain behaviours [232] the widespread use of infinitesimal strain theory and the ease of application has led to many instances of linear constitutive relations being applied to tissue mechanics. Linear elasticity crucially assumes that the strain is small and for a three-dimensional material this is essentially the same as assuming small deformations. By making this assumption, the strain tensor can be reduced in the following way:

$$\mathscr{E}_{ij} = \frac{1}{2}\left(\frac{\partial u_i}{\partial X_j} + \frac{\partial u_j}{\partial X_i} + \frac{\partial u_k}{\partial X_i}\frac{\partial u_k}{\partial X_j}\right) \approx \varepsilon_{ij} = \frac{1}{2}\left(\frac{\partial u_i}{\partial X_j} + \frac{\partial u_j}{\partial X_i}\right) \tag{4.15}$$

where X is the domain of the unstressed body and $\mathscr{E}_{ij}$ is the strain tensor. The form of the constitutive relation is also limited to a linear relation of the form, and subsitiution into Cauchy's momentum equation leads to the well know Navier equation;

$$\sigma_{ij} = \lambda \varepsilon_{kk}\delta_{ij} + 2\mu\varepsilon_{ij}. \tag{4.16}$$

To apply this to the problem of bubble growth in tissue consider the situation in Fig. 4.1. In this situation, it is assumed there is a bubble of initial size R_0 within a homogeneous, infinite tissue block. At time t_0 there is an initial external pressure of P_0

and therefore there is a constant stress throughout the tissue σ_{rr} must be equal to the external pressure P_0. At time t_1 the external pressure varies from P_0 to P_∞ and the bubble radius will change as a result. Inertial effects are ignored so that the bubble is assumed to be in static equilibrium in both situations. Diffusion of gas across the bubble-tissue interface is neglected for this formulation. The problem begins in the same way as any cavity expansion problem such as can be found in [230]. The equilibrium equation is simplified by assuming a spherically symmetric system where the displacement $\mathbf{u}$ is a function of a single vector component $\mathbf{r}$ direction only hence $\bigtriangledown^2\mathbf{u} = 0$, and body forces are neglected $\mathbf{F} = 0$. Therefore 4.9 can be reduced to:

$$\frac{d}{dR}\left(\frac{1}{r^2}\frac{d}{dr}\left(r^2 u_r\right)\right) = 0, \tag{4.17}$$

where u_r is the radial displacement. Integrating twice gives

$$u_r = ar + \frac{b}{r^2}. \tag{4.18}$$

The components of the strain tensor are given by

$$\varepsilon_{rr} = \frac{\partial u_r}{\partial r} = a - \frac{2b}{r^3}, \tag{4.19}$$

$$\varepsilon_{\theta\theta} = e_{\phi\phi} = \frac{1}{r}\left(\frac{\partial u_\theta}{\partial \theta} + u_r\right) = a + \frac{b}{r^3}. \tag{4.20}$$

Using spherical polar co-ordinates an expression for the stress within the tissue can be found from the displacement by assuming the linear elastic constitutive equation Eq.4.16.

$$\sigma_{rr} = (\lambda + 2\mu)\varepsilon_{rr} + \lambda\varepsilon_{\theta\theta} + \lambda\varepsilon_{\phi\phi} \tag{4.21}$$

$$\sigma_{rr} = 3Ka - \frac{4b\mu}{r^3} \tag{4.22}$$

At this point the boundary equations are needed and the added difficulties of this problem as compared to a standard cavity expansion problem are evident. In cavity expansion problems the bubble pressure can be used with the known external pressure as two boundary conditions to solve for the constants a and b. In the bubble problem three unknowns exist, the bubble pressure P_B, a and b

Arriving at the expression (4.22) is a simple process as is the definition of two of the boundary conditions: the force balance at the bubble surface and the force balance at the tissue edge.

$$P_B = P_0 + \frac{2\gamma}{R_0} \quad at \quad r = R_B \quad , \quad \sigma_{rr} = -P_0 \quad as \quad r- > \infty \tag{4.23}$$

Where R_B is the final bubble radius, P_0 and R_0 are the initial external pressure and radius respectively. As discussed, Goldman et al. [221] take this same linear elastic approach to the problem but use an unusual third boundary condition to close the problem, Goldman et al. apply continuity of displacement between the gas and tissue phases at the bubble surface

$$u_r^b(R_B) = u_r^t(R_B) \tag{4.24}$$

Where the superscripts (b) and (t) denote the bubble (gas phase) and tissue phase respectively. Although this approach enables a solution to be reached, the application of mechanical equilibrium and a displacement vector u_r to a gas is odd given that a gas has no solid configuration to be displaced from. The final form reached via Goldman's approach is

$$P_B = P_0 - \frac{4\mu}{3} + \frac{2\gamma}{R} \tag{4.25}$$

Where μ is the bulk modulus and γ is the surface tension. This approximation can be found in [233] and is dependent upon $\mu << K$ in an infinite elastic media.

An alternative approach to the third boundary condition, more often utilised in solid mechanics is to derive the third boundary condition based on the reference configuration.This is the configuration of the system if it were unstressed see Fig 4.1. In this case if σ_{rr} were zero throughout the tissue, there would exist a bubble with a radius of R_{ref}. The displacement u_r will always be formulated as the difference between the current radius (R_B) and this reference radius: $u_r = R_B - R_{ref}$. At time $t = 0$, $R_B = R_0$ hence $u_r = R_0 - R_{ref}$. At later times the displacement is described as the sum of the displacements at time t_0 and time t from the reference configuration. Given the two boundary conditions in (4.23) it can be seen that when $r \to \infty$ (4.18) is only valid if,

$b = 0$ and hence $a = -\frac{P_0}{3K}$; (4.18) therefore becomes

$$u_r = -\frac{P_0 r}{3K}. \tag{4.26}$$

When $R_B = R_0$ and at $r = R_{ref}$:

$$R_0 = R_{ref} - \frac{P_0}{3K} R_{ref} \tag{4.27}$$

Moving to the situation at t_1; the external pressure has changed to P_∞ and stress throughout the tissue is no longer constant. At $r = R_{ref}$, we can now define a new stress in the tissue $\sigma_{rr} = -P_{int}$, where P_{int} is the internal pressure at a point in the tissue.

$$-P_{int} = \frac{2\gamma}{R_B} - P_B \tag{4.28}$$

At $r = \infty$, $\sigma_{rr} = -P_\infty$, and from eq. 4.22 when $r = \infty$, can be used to find a,

$$a = -\frac{P_\infty}{3K} \tag{4.29}$$

Equating the two expression for σ_{rr} at $r = R_{ref}$ with the expression for a:

$$-P_\infty - \frac{4b\mu}{R_{ref}^3} = -P_{int} \tag{4.30}$$

Four simultaneous equations therefore result from the above derivation:

$$-P_\infty - \frac{4b\mu}{R_{ref}^3} = \frac{2\gamma}{R_B} - P_B, \tag{4.31}$$

$$u_r = R_B - Rref = -\frac{P_\infty}{3K} + \frac{b}{R_{ref}^2}, \tag{4.32}$$

and the ideal gas law gives

$$P_B R_B^3 = \left(P_0 + \frac{2\gamma}{R_0}\right) R_0^3, \tag{4.33}$$

$$R_0 = R_{ref}\left(1 - \frac{P_0}{3K}\right). \tag{4.34}$$

Summarising the known and unknown quantities in the above 4 equations we find:

Know	Unknown
P_∞	R_{ref}
μ	R_B
P_0	P_B
R_0	b
K	
γ	

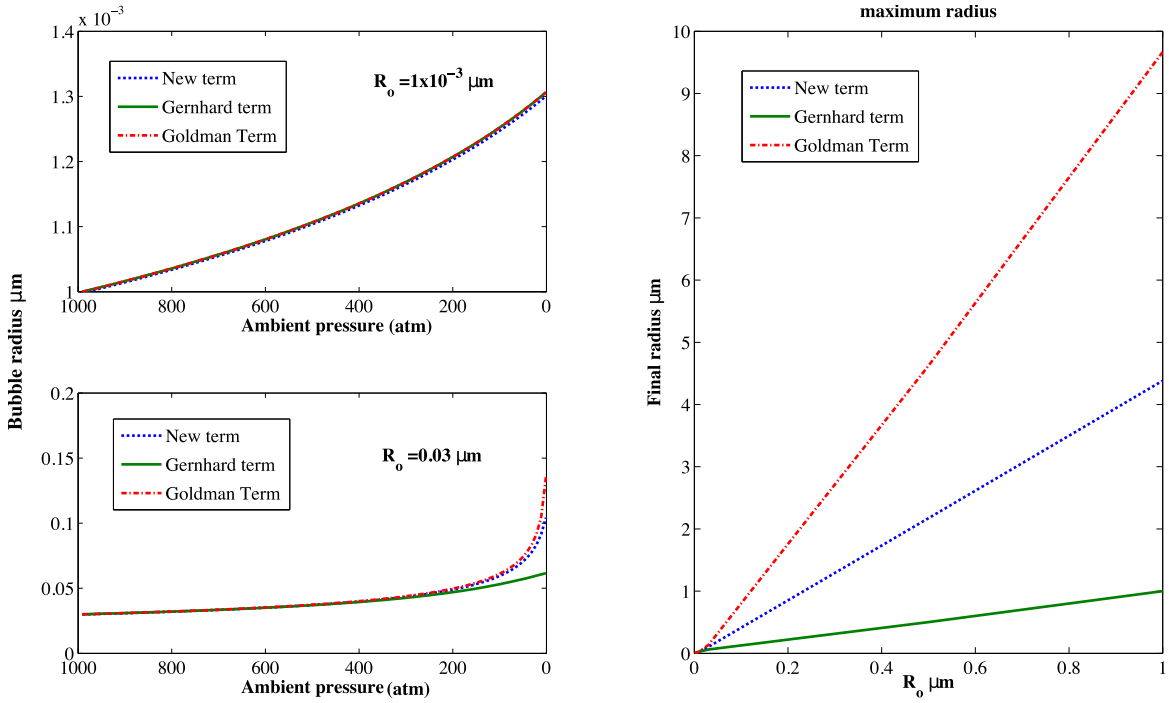

Figure 4.2: Comparison of the correct linear elastic model with the originally proposed model and with a hyperelastic model. A pressure change from 101MPa - 0.1MPa (1000-1atm) was modelled with: $\mu = 3.54kPa$, $\gamma = 0.07N/m$, $K = 2.2x10^3$ MPa [5], $M = 1x10^4$ MPa/μm^3 - Taken from [6]

These are solved to find an expression for R_B in terms of the change in external pressure P_∞. The full derivation can be found in Appendix A. The final expression is a quartic equation:

$$0 = 4\mu\left(1-\frac{P_0}{3K}\right)R_B^4 - \left(4\mu R_0\left(1-\frac{P_\infty}{3K}\right) - R_0^3 P_\infty\right)R_B^3 + 2\gamma R_0^3 R_B^2 - P_0 R_0^4 - 2\gamma R_0^3 \tag{4.35}$$

There is only a single positive real root in the above quartic equation. A comparison of our new linear elastic function, the Goldman term and the Gernhardt term can be made by a similar application of Boyle's law. Derivations of these terms can be found in Appendix 1.

Figure 4.2 compares the predicated radii by the application of Boyle's law, for

the newly derived term with the Gernhardt and Goldman terms. The left hand panels show the bubble radius profiles during a reduction in ambient pressure from 1000-1atm . At $R_0 < 1.4x10^{-3}\mu m$ (top panel), all terms result in approximately the same radius profile; whilst at larger R_0 (lower panel), differences in the radial dynamics become evident. This is due to the dominance of the surface tension term, which is common to all three models, at smaller radii. The right hand side shows the final radius after the decompression for each of the terms at varying values of R_0. The Goldman term results in the largest radii, actually enhancing bubble growth due to the negativity of the elasticity term in eq.(4.25). The newly derived term still confers elastic resistance to bubble growth but to a lesser degree than the Gernhardt term.

The parameter values chosen for this model are given in the figure caption. For the newly derived term and the Goldman terms, values of μ and K are set at physiological values, whereas the value of M for the Gernhardt term is taken from the work or Gerth et al. [175]. As mentioned earlier, the M parameter is not considered a physiological parameter. Therefore, that the use of this M value results in greater bubble restriction suggests that the term may, in fact, be approximating a combination of several mechanisms which restrict bubble growth.

Both our newly derived term and the Goldman term are restricted by the assumptions of the linear elastic limit, most notably that of small deformations. Given the sparse evidence for the range of tissue bubble size in the literature, there is little support for the small deformation assumptions. In observations of bubble formation in collagen hydrogels bubbles grow to sizes >0.5 mm diameter, which is incompatible with such an assumption. In addition, as bubble growth is thought to cause mechanical damage to certain tissues through distension of the ECM [30] a portion of bubble growth must occur in the non-linear response region of the tissue as this represents the normal physiological range or the 'toe region' shown in Figure 4.3. By virtue of this argument and by the fact that good non-linear models of tissue elasticity are available, non-linear models are considered the appropriate way to progress in developing models of DCS and, therefore, the models incorporating linear elasticity are not further pursued.

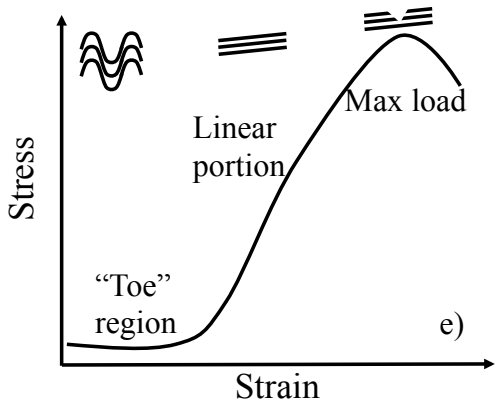

Figure 4.3: Typical stress strain curve of a tissue with the configuration of collagen fibres shown above.

4.3.1.2 Hyperelasticity

Hyperelasticity is the simplest way to introduce non-linearity into solid mechanics and hence it has been widely used to model tissue mechanics. Hyperelastic models are used to describe materials that can undergo large deformations and return to their original conformation. They assume perfect elasticity in the same way as linear models, but do not neglect higher order terms in the stress tensor and hence are not restricted to small deformations. Hyperelastic constitutive relations are described in terms of the stored elastic potential energy by a strain energy function $W(F_{ij})$, where F_{ij} is the deformation gradient (the gradient of the mapping function from the reference to deformed configuration). For any hyperelastic material a strain energy function must be given which satisfies:

$$\mathscr{T}_{ij} = \frac{\partial W}{\partial F_{ij}} \tag{4.36}$$

If $\mathscr{T}_{ij}$ is the Lagrangian stress tensor and W is formulated in terms of the same material parameters as the linear models.

Hyperelastic models were initially formulated to describe the behaviour of rubbers and other polymers and have since been applied to tissue biomechanics. The similarity in the structure of synthetic polymers and tissues, all consist of an entangled or cross-linked mesh of polymeric molecules permeated by a liquid, has meant that hyperelastic models have often been successfully applied to biomechanics. However, as made clear by Humphrey [232], there are several differences between synthetic polymers and tissues which can render the use of such models inappropriate. The assumption

of reversibility is one such problem. Energy dissipation is known to occur both in the straightening of the collagen fibres and the movement of the ground substance [234]. It can also be observed from the hysteresis in loading unloading curves of various tissues [228]. Another related problem is in the assumption of strain rate independence. Hyperelastic models assume no energy strain-rate dependence but tissue are known to exhibit both creep and stress relaxation. Despite this, the assumption of tissue hyperelasticity can often be made regardless. For instance, pre-conditioned or cyclically-loaded tissues show a steady state response in which hysteresis can be neglected. Viscous behaviours can also sometimes be neglected, depending on the relative characteristic times of the viscous and elastic responses and the experimental condition. The applicability of a hyperelastic model may also depend on the type of mechanical loading imposed. For instance, the periodontal bovine ligament is well-modelled by a hyperelastic relation in tensile extension but viscous behaviour dominates under compression [235]. Bearing in mind these considerations, three hyperelastic models are assessed with a view to their incorporation into our three-dimensional model of bubble growth in collagen hydrogels.

The Gent term is described by the strain energy function[236].

$$W = -\frac{\mu J_{lim}}{2} \ln\left(1 - \frac{J}{J_{lim}}\right) \tag{4.37}$$

where J is the first invariant of the Cauchy Green deformation tensor, $J = \lambda_\theta^2 + \lambda_\phi^2 + \lambda_r^2 - 3$, with $\lambda_\theta = \lambda_\phi$ the hoop stretch ratio and λ_r the tangential stretch ratio. J_{lim} represents a limiting stretch, at which point the stresses and strain energy become infinitely large. J_{lim} molecularly represent the limiting stretch of the individual molecules which make up the polymer, allowing the model to mimic the strain-stiffening observed in biological tissues. When $J_{lim} \to \infty$ the classical neo-Hookean strain energy function is recovered. The Gent model assumes elasticity, isotropy and incompressibility. Whist the term was originally formulated as a phenomenological model, it was later derived from molecular considerations of the elastomer structure [219]. In this derivation it is assumed that the polymer consists of a network of freely jointed polymer molecules where the end-to-end distances of the network follow a Gaussian distribution and each molecule has a linear stress-strain response.

The Gent model, although utilised widely in rubber science, has in some cases been shown to be a poor descriptor of some native tissues [237]. In a comparative study of hyperelastic models, the Gent function was shown to be a poor predictor of the stress-strain response of fatty tissues by comparison to the Neo-Hookean model ($J_{lim} \rightarrow \infty$). The neo-Hookean form has also been used as the theoretical basis of an experimental technique to measure the shear modulus of hydrogels [238, 239], *ex vivo* tissue [240] and *in vivo* shear modulus of skin [241]. A benefit of the Gent model is the ease with which it may be implemented; the mathematical formulation is simple and the two parameters have real measurable physical counterparts. This simplicity has led to its wide use in biomechanics [242] as well as its validation for bubble growth in elastomers [218]. It has also previously been suggested that its use in a DCS bubble model would be appropriate [243, 214, 6], however it has yet to be implemented in a complete diffusion or perfusion limited bubble model. Although the Gent model appears an obvious choice, there are many other hyperelastic models of tissues and hydrogels, in particular the model of Fung [228], and Holzapfel [244], are widely used. The Fung pseudoelastic model is also a relatively simple mathematical formulation, however it is not considered suitable for this work as it assumes that tissues are pre-conditioned (repeatedly loaded and unloaded), this assumption is not met by the experimental system here. The Holzapfel model should be considered due its wide application in the biomechanics field [245], The main power in this model lies in modelling a tissue as a series of layers each of which comprises a different ECM make up. Each layer contributes to an isotropic and an anisotropic component of the total tissue response. Given that the collagen hydrogel is a single layer with no orientation the Holzapfel model reduces to a single layer with only an isotropic component, which is the neo-Hookean form [244]. In future work where tissue anisotropy may be considered this model provides a good opportunity to extend the current model.

One particular criticism of hyperelastic models that should be addressed is the absence of accounting for strain-rate dependence either through a visco or poroelastic model. Given that a collagen hydrogel contains 98% water it could be argued that neglecting the viscous properties is a serious omission. The argument against the inclusion of viscoelasticity is that it comes at a high cost to the simplicity of the model, as the quasi-static approximation would no longer hold. Given that the aim of this work

is to model bubble dynamics in a way which will be relevant to DCS; it is important to remember that tissue mechanics, is only one, of a myriad of mechanism that affect bubble dynamics. Hence it is argued that the best approach to modelling tissue mechanics and all other mechanisms in the model, is to choose the simplest model which can be easily implemented with both mathematical consistency and reasonable experimental evidence. Validation of the mechanism in the experimental system should then be used to assess the model. If it is found to be a poor descriptor of the experimental data more complex additions may be added. Given that the Gent term has already been discussed in connect with DCS, has been validated in the neo-Hookean form and has measurable parameters, it was chosen to implement the the Gent term with $J_{lim} \to \infty$. Following validation the suitability of the model will be assessed.

4.3.2 Implementation

A tissue containing a spherically symmetric bubble can be described by three principle stretches in spherical polar coordinates; two equal hoop stretches $\lambda_\theta = \lambda_\phi$, and a radial stretch λ_r. Assuming incompressibility $\lambda_\theta \lambda_\phi \lambda_r = 1$, and the hoop stretch ratio can be written as $\lambda_\phi = \lambda_\theta = \lambda$. The tissue will experience two equal hoop stresses and a radial stress $(\sigma_\theta, \sigma_\theta, \sigma_r)$. Both the stress and the stretch ratios are functions of the radial position (r) in the tissue. The hoop stretch ratio at the bubble surface is given by $\lambda = (R_0/R_B)$ and the radial stress $\sigma_r(R_B) = -P_B + 2\gamma/R_B$; at other points in the tissue $\lambda = r/r_0$, where r and r_0 denote the radial position in the initial and deformed tissue respectively. As r$\to \infty$, $\lambda = 1$ and $\sigma_r(\infty) = P_{amb}$. As the tissue is considered incompressible $r^3 - R_0^3 = r_0^3 - R_B^3$. The equation of equilibrium for the system may be written as

$$\frac{d\sigma_r}{dr} + 2\frac{\sigma_r - \sigma_\theta}{r} = 0, \tag{4.38}$$

integration, using a change of variables from r to λ, and substitution into the stress at the bubble surface expression yields.

$$P_B = P_{amb} + \frac{2\gamma}{R_B} + \int_1^{R_B/R_0} \frac{2\sigma(\lambda)d\lambda}{\lambda(\lambda^3 - 1)}, \tag{4.39}$$

where $\sigma = \sigma_r - \sigma_\theta$. It is related to the strain energy function by:

$$\sigma(\lambda) = \frac{\lambda}{2}\frac{dW}{d\lambda} \tag{4.40}$$

Substituting the Gent strain energy function (4.37) this becomes

$$P_B = P_{amb} + \frac{2\gamma}{R_B} + 2\mu \int_1^{R_B/R_0} \frac{\lambda^{-2} + \lambda^{-5} d\lambda}{1 - (2\lambda^2 + \lambda^{-4} - 3)/J_{lim}} \tag{4.41}$$

The term in this form must be solved numerically, however if $J_{lim} \to \infty$ an analytical solution of the integral can be obtained thus:

$$P_B = P_{amb} + \frac{2\gamma}{R_B} + \frac{\mu}{2}\left[5 - 4\left(\frac{R_B}{R_0}\right)^{-1} - \left(\frac{R_B}{R_0}\right)^{-4}\right] \tag{4.42}$$

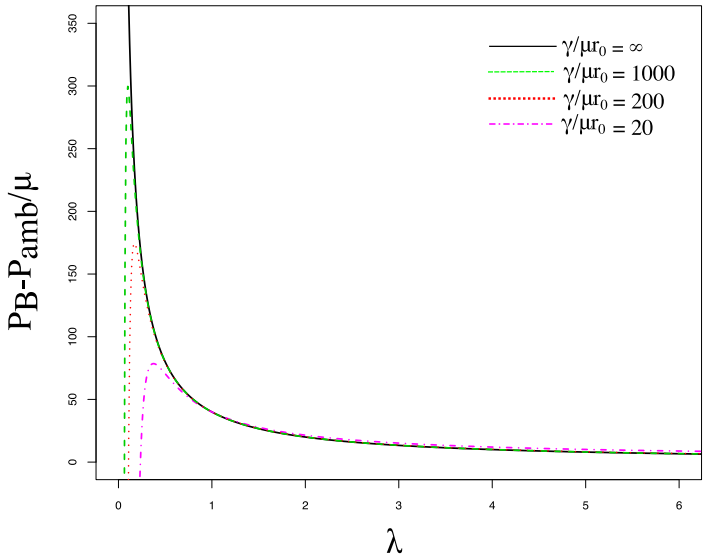

Figure 4.4: The Gent term for variations in the parameter $\frac{\gamma}{\mu r_0}$, ($J_{lim} = \infty$ for all lines)

Figure 4.4 shows the normalised bubble pressure for varying bubble radii as given by (4.42), with variations in the parameter $\frac{\gamma}{\mu r_0}$. As can be seen the Gent term behaves similarly to the Laplace equation (with no-elastic term) for large values of the parameter, and when the bubble is larger than the initial radius R_0. At smaller values of $\frac{\gamma}{\mu r_0}$, the elastic term dominates and the increase in pressure due to surface tension is balanced by the decrease in pressure due to a reduction in elastic pressure, leading to a peak in the pressure.

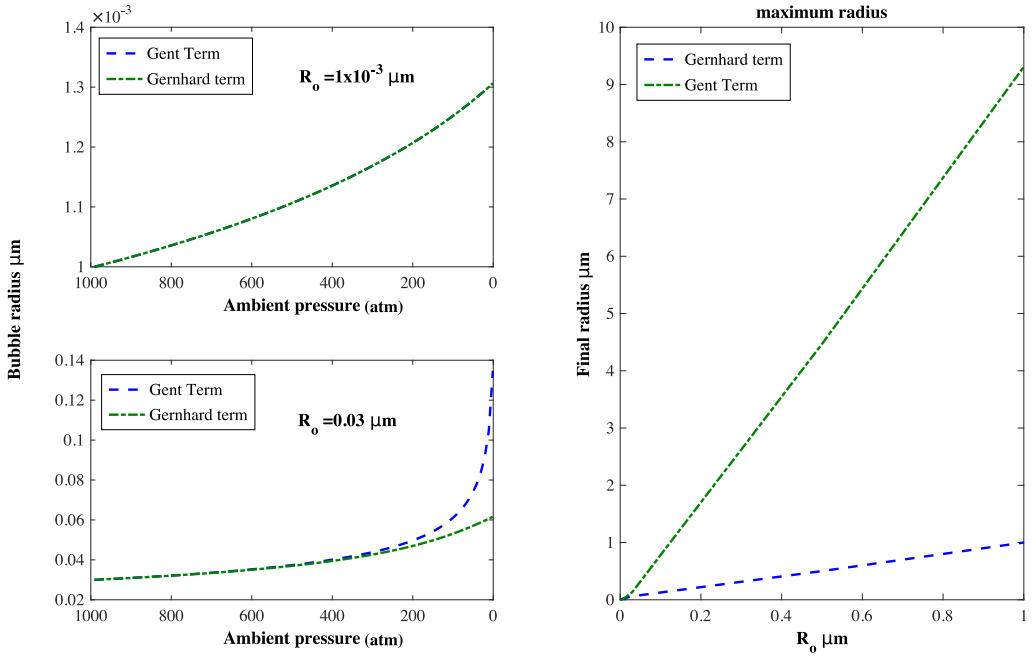

Figure 4.5: Comparison of the Gernhardt term model with the Gent hyperelastic term using the Boyle's law model. The parameters used to generate these plots are: $\mu = 3.54kPa$ (see lit search on param) atm, $\gamma = 0.7$ atm μm, $M = 1e4$ MPa/μm^3 - Taken from [6]

When the Gent and Gernhardt terms are compared using the simple Boyle's law approach (see Figure 4.5) it can be seen that the Gent term is far less restrictive of bubble growth than the Gernhardt term. This is due to setting $\lambda_{lim} - > \infty$ and hence the contribution of tissue elasticity asymptotes to a value of $5\mu/2$ for large values of λ (R_B/R_0). Gerth and Srinivasan [6] argue that the Gernhardt term is a single parameter approximation for the Gent term for a material where $\lambda\mu r_0$ is small and λ_{lim} known. However $\lambda\mu r_0$ is not a dimensionless parameter; the Gernhadt term can only be considered a fairly poor approximation for *large* values of $\frac{\gamma}{\mu r_0}$ and for finite values of J_{lim}, (see Figure 4.6).

Given that arguments have already been made as to the use of $J_{lim} \to \infty$, the Gernhardt should not be used further. Using the form of the Laplace in (4.42), the complete diffusion limited bubble model can now be derived.

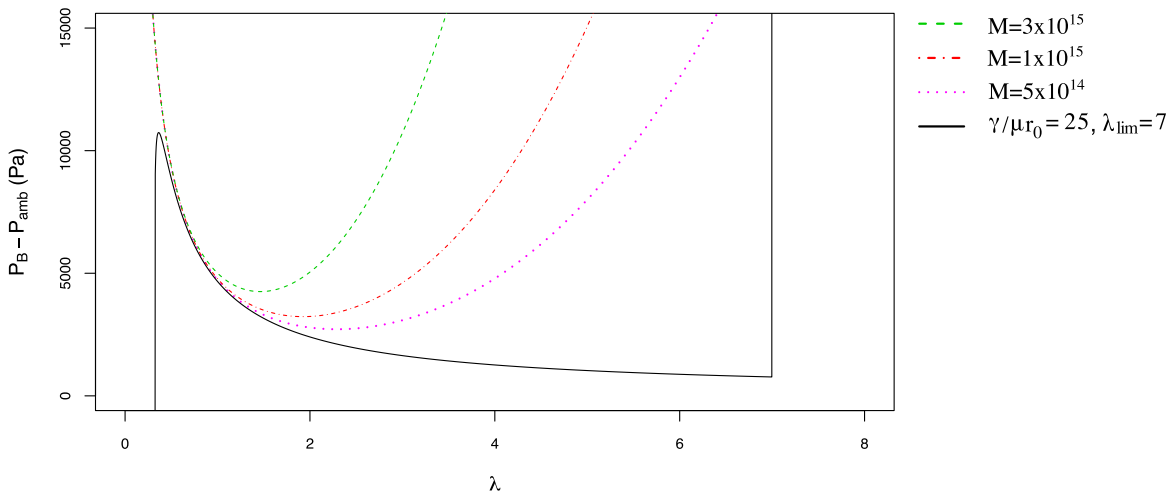

Figure 4.6: Comparison of the Gernhard and Gent terms for variations in M.

4.4 Derivation of the computational model

4.4.1 Assumptions

The assumptions made in the derivations of the diffusion-limited bubble model are as follows:

1. **Homogeneity is assumed to hold for all material properties of the gel** - these include, the diffusion coefficient, Henry's constant and the elastic moduli. This is believed to be valid to a reasonable degree given the method of gel fabrication described in chapter 2.

2. **Bubbles are assumed to be spherical** - this assumption is made to simplify the governing equations and will be dealt with more fully in chapters 5 and 6.

3. **A constant temperature of** 37° **is assumed throughout** - this has been discussed in the chapter 3.

4. **All dynamic processes are modelled as quasi-static** - this assumption vastly simplifies the governing equations and their consequent implementation. The validity of this assumption is established through its use across several research fields including DCS [158, 246].

5. **Gas micronuclei of a size R_0 are initialised within the tissue block as starting point for the growth model** - these can be considered to be the gas micronuclei which were of a size greater than the critical radius. This assumption is the same as that used in [220] and will be discussed in detail in Chapter 7

Derivation of an expression for dR_B/dt is given by substituting the bubble mass in (4.6), with the perfect gas law:

$$\frac{d}{dt}\left(\frac{PV}{\alpha}\right) = 4\pi R_B^2 D \frac{\partial C}{\partial r}\bigg|_{R_B} \tag{4.43}$$

Expanding the LHS of using the product rule and including the separate effects of a mixture of N_2 and O_2 gases, we find:

$$\frac{d}{dt}\left(\left(\frac{P_B^{N_2}}{\alpha_{N_2}} + \frac{P_B^{O_2}}{\alpha_{O_2}}\right) V_B\right) = 4\pi R_B^2 D \frac{\partial (C_B^{N_2} + C_B^{O_2})}{\partial r}\bigg|_{R_B} \tag{4.44}$$

The model can be generalised to as many gases as one wishes. For simplicity, only Oxygen and Nitrogen are shown as these make up 99.9% of the gas mix used in the experimental work. Introducing m_f^g as the constant mole fraction of gas g and substituting in the Gent form of the Young-Laplace equation to the LHS of the above equation we find:

$$\left(\frac{m_f^{N_2}}{\alpha_{N_2}} + \frac{m_f^{O_2}}{\alpha_{O_2}}\right)\left(P_B R_B^2 \frac{dR_B}{dt} + \frac{R_B^3}{3}\left(\frac{dP_{amb}}{dt} + \left(-\frac{2\gamma}{R_B^2} + \frac{2\mu R_0}{R_B^2} + \frac{2\mu R_0^4}{R_B^5}\right)\frac{dR_B}{dt}\right)\right) = R_B^2 D \frac{\partial (C_B^{N_2} + C_B^{O_2})}{\partial r}\bigg|_{R_B} \tag{4.45}$$

Rearranging for dR_B/dt

$$\frac{dR_B}{dt} = \frac{\frac{\alpha_{O_2}\alpha N_2}{m_f^{N_2}\alpha_{O_2} + m_f^{O_2}\alpha_{N_2}} D \frac{\partial C_{tot}}{\partial r}|_{R_B} - \frac{R_B}{3}\frac{dP_{amb}}{dt}}{P_{amb} - \frac{4\gamma}{3R_B} + \frac{5\mu}{2} - \frac{4\mu}{3}\left(\frac{R_B}{R_0}\right)^{-1} + \frac{mu}{6}\left(\frac{R_B}{R_0}\right)^{-4}} \tag{4.46}$$

This is the final equation to describe bubble growth. It is very similar to the derivations of [4] differing only in the form of the Young-Laplace equation and in the $\partial C_{tot}/\partial r$ term. The equations of the model were recast into pseudo non-dimesionalisation form

Parameter	Description	unit	Values in collagen gels	Source
γ	Surface tension	m/bar	0.07	Chapt. 5
μ	Shear modulus	bar	0 - 4	Chapt. 5
α_{N_2}	Gas const. N_2	$m^3.bar/kg$	0.9201	[247]
α_{O_2}	Gas const. O_2	$m^3.bar/kg$	0.8054	[247]
$k_h^{N_2}$	Henry's const.N_2	$kg/bar.m^3$	0.0152	Chapt. 5
$k_h^{O_2}$	Henry's const. O_2	$kg/bar.m^3$	0.0335	Chapt. 5
D	Diffusion coeff.	m^2/s	2.5×10^{-9} - 1.7×10^{-9}	Chapt. 5
m_f	mole fraction	[-]	$N_2 = 0.8$, $O_2 = 0.2$	[-]

Table 4.1: Parameter units and values used in derivation of the radial change equation

where only the time dimension of the model is retainied. This is done to avoid numerical errors during computation. A characteristic pressure $\bar{P} = 1$bar and length $\bar{r} = R_0/2$ were introduced and a characteristic concentration and mass derived from these. $P' = \frac{P}{\bar{P}}$, $r' = \frac{r}{\bar{r}}$, $\bar{C} = k_h^{N_2}\bar{P}$, $\bar{m} = k_h^{N_2}\bar{P}\bar{r}^3$. The parameters can then be re-cast in pseudo non-dimensional form,

$$\gamma' = \frac{\gamma}{\bar{R}\bar{P}}\,, \quad \mu' = \frac{\mu}{\bar{P}} \quad , \quad \tau = \frac{k_h^{N_2} D\alpha_{N_2}\alpha_{O_2}}{(m_f^{N_2}\alpha_{O_2} + m_f^{O_2}\alpha_{N_2})\bar{R}^2} \tag{4.47}$$

The radial change equation can then be rewritten as:

$$\frac{dR'_B}{dt} = \frac{\tau\frac{\partial C'_{tot}}{\partial R'}|_{R'_B} - \frac{R'}{3}\frac{dP'_{amb}}{dt}}{P'_{amb} - \frac{4\gamma'}{3R'} + \frac{5\mu'}{2} - \frac{4\mu'}{3}\left(\frac{R'}{R'_0}\right)^{-1} + \frac{\mu'}{6}\left(\frac{R'}{R'_0}\right)^{-4}}. \tag{4.48}$$

Table 4.1 presents a summary of the parameters used in Eq. 4.46.

4.5 Summary and Conclusion

In this chapter the governing equations for a diffusion-limited model of bubble dynamics in collagen hydrogels has been derived. There has been a particular focus on the term used to describe the tissues mechanical response to deformation by the bubble. This focus was due, in part, to the controversy that surrounds the term in the literature. A term originally derived by Gernhardt, describes the elastic tissue response to be equal to the product of the bubble volume and the parameter M, which was originally considered to be a function of the bulk modulus. Optimisation of the BVM with the Gerhardt term increased the accuracy of the Bubble Volume Model in predicting the onset of

DCS, however the optimised parameter value was far outside the physiological range of the bulk modulus. Despite the authors of the BVM model discussing this problem in their original work, in later works they continue to use the term and describe the parameter M as a function of the bulk modulus, which led to the incorrect interpretation and use of the term in other models. In fact, the term has never been rigorously derived and is mathematically inconsistent with linear elasticity. Given that the parameter value was so far outside the physiological range, this should have been an indication of the inconsistency. This chapter provides two versions of the term using the frameworks of both linear and non-linear elasticity. The newly-derived linear term is appropriate for small deformations of a soft elastic material containing a bubble with varying external pressure. The non-linear term taken from the work of Gent is more appropriate for the deformation of hydrogels caused by bubble growth. Comparison of the term to the Gernhardt term shows it to provide less restriction to bubble growth. The use the Gent term with a simplification where $J_{lim} \rightarrow \infty$ was decided to be the most appropriate model for this work due to its simplicity, robustness, previous validation. Assumptions regarding derivation of the final bubble model were discussed and the final equation derived in pseudo non-dimensional form.

Chapter 5

Code implementation and Sensitivity analysis

5.1 Introduction

This chapter details the numerical implementation, parameterisation and sensitivity analysis of the 3D diffusion-limited bubble growth model. The first section of this chapter describes the numerical implementation of the model, with particular discussion of how the phase change at the bubble tissue interface is treated, and the stability of the finite difference scheme. The following section is an analysis of the material parameters of the model, this is done via a literature search to establish the parameter limits followed by a feature sensitivity analysis of the computational model for a single bubble. The diffusion coefficient D and shear modulus μ are shown to be the most sensitive and widest ranging parameters respectively.

5.2 Numerical Implementation

5.2.1 Structure of the code

The computational model is written in C++, an open access programming language with an object oriented coding style. Using C++ allows for code transferability and the use of external resources such as the 'boost' library for more efficient computing. The object orientation of this language also allows for a more natural treatment of bubble objects, particularly when dealing with more complex behaviours such as coalescence.

The model describes a block of collagen gel as a 3-dimensional Cartesian grid of points and is executed as described by Figure 5.1: The code can be considered in

3 separate sections: The initialisation section creates a tissue block as an object with eight properties: 2 grids to store the gas concentration of every point for both O_2 and N_2, spatial and temporal step sizes, a vector of bubble objects, two masks termed the phase and boundary masks and the total mass of gas. All grid values are initialised to zero. A value for the time step is then chosen and used to interpolate a prescribed pressure profile of the correct length from a txt file. The bubbles in the block are then assigned locations, initial radii, bubble pressure, mass, and concentration gradient vectors. The final stage in the initialisation is to assign the initial conditions from the pressure profile to the concentration grids.

The dive portion of the code consists of a time loop. At each time step the boundary values of the concentration grid are updated from the pressure profile via Henry's Law. The diffusion equation is numerically solved at each grid point using one of two finite difference schemes. This grid is then used to calculate the concentration gradient at each bubble surface via a second-order accurate forward-difference scheme. This value is used in (4.46) to solve for the radius of each bubble at this new time step. Mass conservation at the bubble boundary is ensured by comparing the total mass of the bubble bounding box at the mid-point of the calculation, i.e. when the tissue concentration grid has been updated to reflect the new time point but the bubble radius has yet to be changed; to the final time point when both have been updated. The new bubble radii are then checked for bubble coalescence and grid edge proximity before being stored in the appropriate bubble radii vectors. The old concentration grid is overwritten with the new grid and a new grid with the current bubble radii is re-initalised for the next time step.

Once the time loop has ended the bubble radii, and bubble concentration vectors are written to a .txt file, and the bubble and tissue block objects deleted from the memory.

This code can be described as a Cartesian grid method with sharp immersed boundaries, meaning that the grid does not conform to the bubble surface so that the surface of the bubble cuts the grid without necessarily intersecting grid nodes and thus the interface is considered a discontinuity in the concentration field. This type of method was originally described by Peskin [248] to model cardiac movement and has been greatly developed in recent years [249, 250]. The main advantage of such methods are

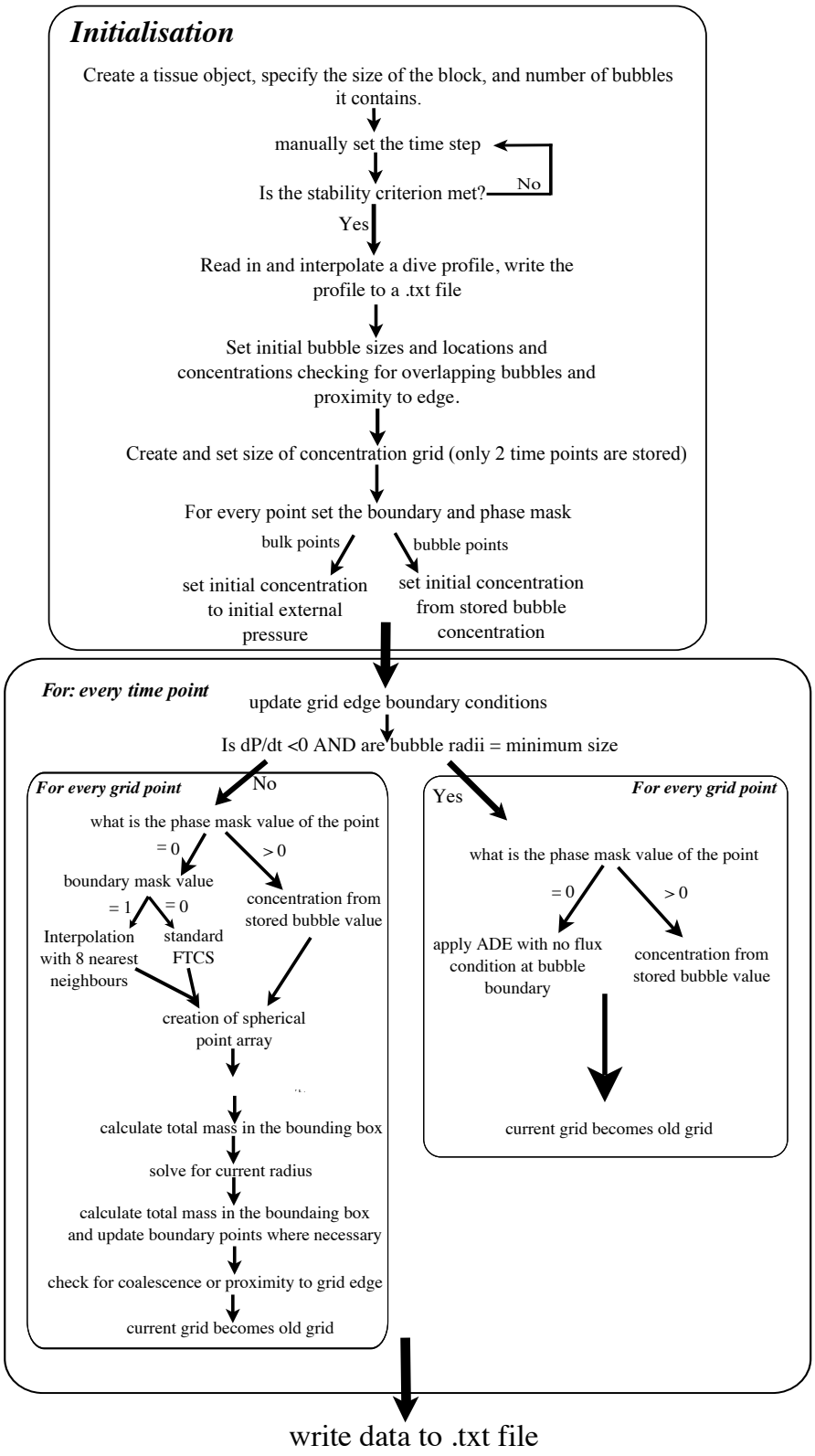

Figure 5.1: Diagram representing the execution of the code

that computationally expensive re-gridding at every time step can be avoided, whilst still enabling solutions for highly complex geometries and moving boundaries [251].

Although the complexities associated with re-gridding are avoided by the immersed boundary method, more careful application of boundary conditions is required and will be discussed in detail in this chapter. It may seem that the use of such a method is unnecessary given the initial focus on the simple geometry of single spherical bubbles; however, modelling multiple bubbles and allowing for the simulation of non spherical bubbles makes the model more applicable for future work.

5.2.1.1 Numerical forms of the governing equations

The governing equations of the model were described in chapter 4. To solve the system of equations numerically, both time and space are discretised as Δt and $\Delta x, \Delta y, \Delta z$, and denoted by the subscripts s, i, j and k respectively. The LHS of (4.48) is approximated by a forward difference approximation as.

$$\frac{dR}{dt} \approx \frac{R_{s+1} - R_s}{\Delta t} \tag{5.1}$$

likewise ambient pressure and concentration can also be written as.

$$\begin{array}{lcl} \frac{dP_{amb}}{dt} & \approx & \frac{P^{s+1}_{amb} - P^{s}_{amb}}{\Delta t} \\ \frac{\partial C}{\partial t} & \approx & \frac{C_{i,j,k,s+1} - C_{i,j,k,s}}{\delta t} \end{array} \tag{5.2}$$

The diffusion equation is given by:

$$\frac{\partial C}{\partial t} = D\left(\frac{\partial^2 C}{\partial x^2} + \frac{\partial^2 C}{\partial y^2} + \frac{\partial^2 C}{\partial z^2}\right) \tag{5.3}$$

applying the forward time and centre space approximations leads to the second order accurate forward time centred space (FTCS) approximation.

$$\begin{aligned} \frac{c_{i,j,k,s+1} - c_{i,j,k,s}}{\delta t} =& D\Big(\frac{c_{i+1,j,k,s} - 2c_{i,j,k,s} + c_{i-1,j,k,s}}{\delta x^2} + \\ & \frac{c_{i,j+1,k,s} - 2c_{i,j,k,s} + c_{i,j-1,k,s}}{\delta y^2} + \\ & \frac{c_{i,j,k+1,s} - 2c_{i,j,k,s} + c_{i,j,k-1,s}}{\delta z^2}\Big) \end{aligned} \tag{5.4}$$

which is used to calculate the concentration at each grid point. Each gas will have a separate concentration grid.

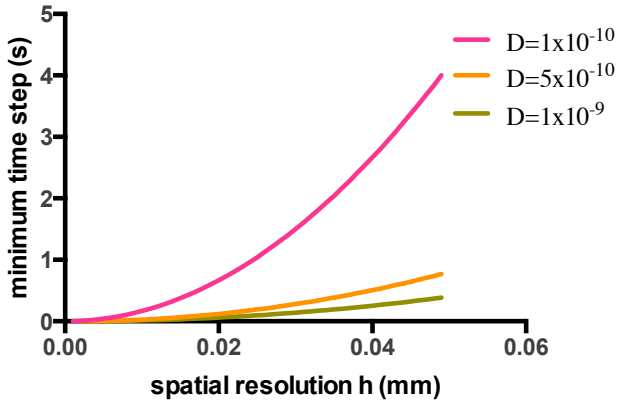

Figure 5.2: The time step size requirements for various spatial resolutions h to meet the stability criteria.

5.2.2 Stability and Simulation length

When using numerical schemes stability must be considered. Stability of the FTCS is notoriously poor and can result in large inaccuracies if the criteria for a stable solution are not met [252]. The condition for the FTCS is given by the stability criterion:

$$\frac{D\Delta t}{\Delta x^2}+\frac{D\Delta t}{\Delta y^2}+\frac{D\Delta t}{\Delta z^2}\leq\frac{1}{2}. \tag{5.5}$$

If $\Delta x^2=\Delta y^2=\Delta z^2=h^2$, this is simplified to

$$h\leq\sqrt{6D\Delta t}. \tag{5.6}$$

This requirement limits the size of the temporal step allowed for a given spatial resolution as shown in Figure 5.2. In any numerical code there will be a compromise between resolution of the simulation and the total run time. A fine spatial grid would give better bubble surface resolution but would dramatically increase simulation time as both the number of time steps and the calculation time per step would increase. The FTCS suffers from a very stringent stability requirement but, as it is an explicit scheme, the calculation at each time step is simple and hence the time per step is short. Use of more stable schemes such as the unconditionally stable Crank-Nicholson scheme would reduce the number of time steps required, but as this solution is implicit i.e. the concentration at the new time point $C^{s+1}_{i,j,k}$ does not depend explicitly on the concentrations at the current time points $C^{s}_{i,j,k}$, it requires the solution of a system of linear equations at each time step. This is more computationally expensive and consequently the length of

time for each step increases. The ideal solution is to maintain the speed and simplicity of an explicit scheme at each step whilst benefiting from larger step sizes possible in an unconditionally stable scheme. One such scheme is the Alternating direction explicit scheme (ADE) developed by Sal'yev [253] and used within the financial computing sector [254] and, though not so widely, in solution to both the heat and convection diffusion equations[255, 256, 257]. The ADE uses the average of an upwind (calculated from 1 to total node number) and a downwind sweep (calculated from total node number to 1), to approximate the concentration at each grid node.

$$C^{s+1}_{i,j,k} = \frac{Cu^{s+1}_{i,j,k} + Cd^{s+1}_{i,j,k}}{2} \tag{5.7}$$

where Cu is the upwind sweep and Cd the downwind. Each sweep is calculated thus:

$$\begin{aligned}\frac{Cu^{s+1}_{i,j,k} - Cu^{s}_{i,j,k}}{\Delta t} =& \frac{Cu^{s+1}_{i-1,j,k} - Cu^{s+1}_{i,j,k} - Cu^{s}_{i,j,k} + Cu^{s}_{i+1,j,k}}{\Delta x^2} + \\ & \frac{Cu^{s+1}_{i,j-1,k} - Cu^{s+1}_{i,j,k} - Cu^{s}_{i,j,k} + Cu^{s}_{i,j+1,k}}{\Delta y^2} + \\ & \frac{Cu^{s+1}_{i,j,k-1} - Cu^{s+1}_{i,j,k} - Cu^{s}_{i,j,k} + Cu^{s}_{i,j,k+1}}{\Delta z^2}\end{aligned} \tag{5.8}$$

$$\begin{aligned}\frac{Cd^{s+1}_{i,j,k} - Cd^{s}_{i,j,k}}{\Delta t} =& \frac{Cd^{s}_{i-1,j,k} - Cd^{s+1}_{i,j,k} - Cd^{s}_{i} + Cd^{s+1}_{i+1,j,k}}{\Delta x^2} \\ & + \frac{Cd^{s}_{i,j-1,k} - Cd^{s+1}_{i,j,k} - Cd^{s}_{i,j,k} + Cd^{s+1}_{i,j+1,k}}{\Delta y^2} \\ & + \frac{Cd^{s}_{i,j,k-1} - Cd^{s+1}_{i,j,k} - Cd^{s}_{i,j,k} + Cd^{s+1}_{i,j,k+1}}{\Delta z^2}\end{aligned} \tag{5.9}$$

By using the boundary conditions in this way the terms $Cu^{s+1}_{i-1,j,k}$ and $Cd^{s+1}_{i+1,j,k}$ (and equivalent terms in the y and z directions) are known explicitly (see Figure 5.3).

Despite this scheme appearing to offer all the advantages discussed above, it is not applicable to problems with moving boundaries such as those of the growing bubbles [254]. This limits the use of the scheme to times at which there is no bubble radius change namely times when the bubble is at a minimum radius and the external pressure is either increasing (during descent) or unchanging (during bottom time). At this time the bubbles are treated as micronuclei with a no flux boundary condition and hence they have a fixed radius. The ADE scheme is therefore implemented where these criteria are

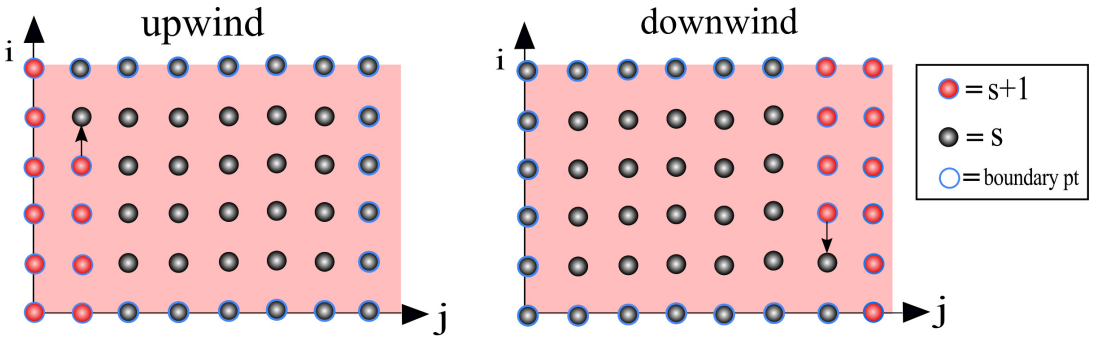

Figure 5.3: representation of the upwind and downwind sweeps in a 2-dimensional ADE scheme, the red points show points calculated in the previous spacial step

met and with a larger time step than the FTCS permits. In this way the ADE scheme decreases the overall simulation time, particularly for simulations with long bottom times.

In the future development of this code it would be ideal to implement a highly optimised implicit scheme with a refined mesh at the bubble tissue interface.

5.2.3 Bubble boundary

Diffusion at the bubble boundary requires consideration of how to calculate concentration gradients at the phase boundary. This problem arises in many fields and there are two broad approaches: diffuse or sharp interface techniques. A diffuse interface technique assumes the phase boundary to have a finite thickness over which there is a smooth change in physical properties such as concentration. By comparison, sharp interface techniques model the boundary as a surface over which a discontinuous change in physical properties occurs, (see Figure 5.4). The diffuse interface technique has been used to model several bubble behaviours including growth, coarsening and coalescence [258]. The diffuse interface approach can avoid the need to explicitly track the position of the interface relative to the finite difference grid, as the interface is implicitly tracked via the value of a phase field, (a field which takes a value of 1 in one phase and 0 in the other, with a smooth change over the interface). This makes the diffuse interface approach more suited to modelling coalescence and small scale events in which there are large changes in interface topology [259]. Despite these advantages diffuse interface methods have two important disadvantages. Firstly a parameter related to interface thickness is required. This parameter cannot be easily measured and it's value may have a significant affect on bubble dynamics, as investigated by Srinivasan et al. [166]. Sec-

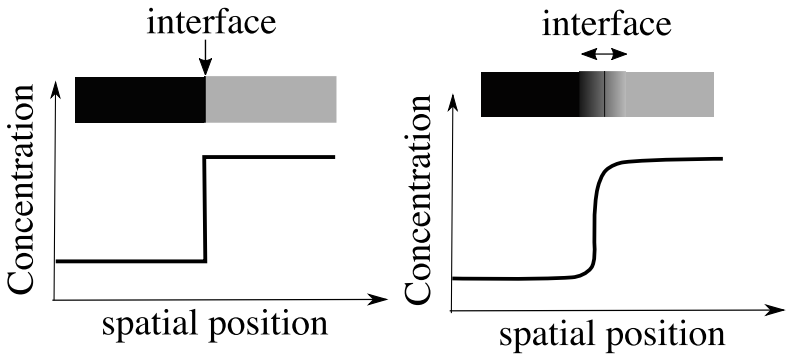

Figure 5.4: diagram of sharp (left) and diffuse (right) interfaces

ondly and relatedly; in order to compute the phase field at the interface, a very fine grid $h_i/4$ where h_i is the interface thickness is needed. This makes the technique unsuitable for computational domains far larger than the interface thickness without employing an adaptive mesh scheme, which itself is computationally challenging [260].

The sharp interface technique avoids the mesh refinement problem and was therefore chosen for implementation in this work. A method as detailed in [261, 262, 263], formed the basis of the implementation in this work.

One of the key difficulties associated with the sharp interface technique is the need to track the interface position. There are several distinct methods to achieve this including the Level-set-Method [264] and front tracking [265]. In this model, boundary tracking is greatly simplified as bubbles initially are assumed to be spherical and stationary, hence the boundary can be simply defined with the co-ordinates of the bubble centre and radius. The location of the boundary points (grid nodes which lie on the bubble boundary) are defined and stored at each time point by two masks; a phase and boundary mask. Points not in the vicinity of a bubble are assigned zero in both masks, points within a bubble are assigned an integer corresponding to the bubble number in the phase mask and a zero in the boundary mask. Points adjacent to a bubble (where the neighbouring point has a different phase), are assigned a zero in the phase mask and integer corresponding to the bubble number, in the boundary mask. Figure 5.5 shows a 2D representation of this scheme.

5.2.3.1 Bulk diffusion

During the decompression the standard FTCS explicit scheme with the imposed stability scheme must be used. For point in the bulk of the gel/tissue, the boundary mask and

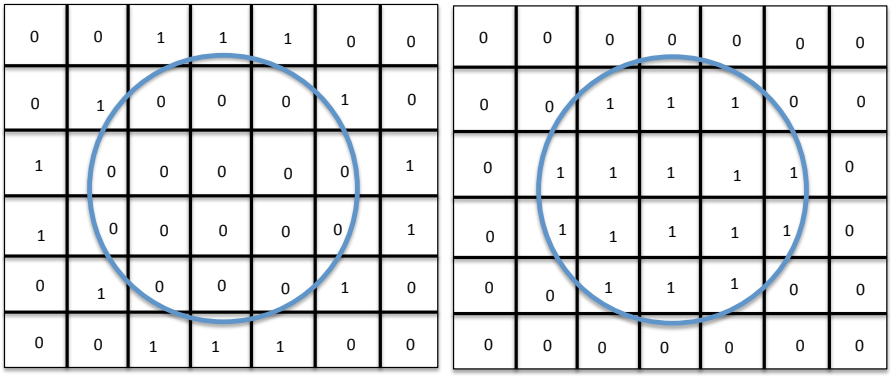

Figure 5.5: Diagram showing the masks, Left boundary mask, Right phase mask

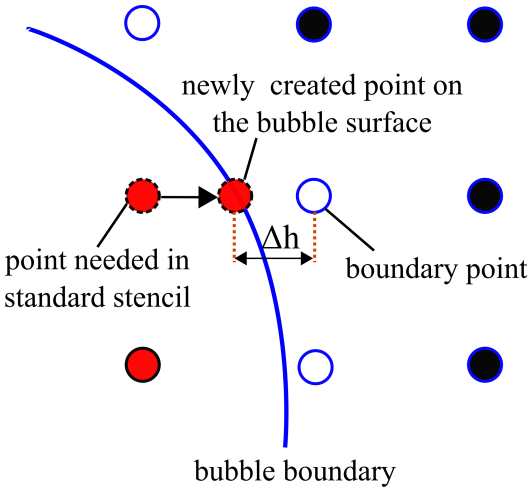

Figure 5.6: Diagram showing the case where a boundary point is reached in the FTSC bulk diffusion calculation (only a 2D representation is shown). Boundary points are shown as open circles, points inside the bubble are shown in red and bulk points as filled black. Consider the point marked 'boundary point': for the standard FTSC stencil one of the points lies within the bubble (red point). This is replaced by a point on the bubble surface and Δh shows the reduced distance between the boundary point and bubble edge. The reduced distance necessitates the use of inverse distance weighted interpolation, rather than the a space centred approximation

phase masks will both have a value of zero and an the standard scheme can be used with a 7 point stencil. For points with a boundary mask value greater than zero; at least one of the 7 points in the standard FTCS stencil would lie within the bubble, (see Figure 5.6). In this case the point within the bubble must be replaced by one at the bubble surface with concentration equal to C_B, and the stencil becomes asymmetrical. If the finite difference were calculated with this new stencil the stability criteria would be violated and spurious concentration values would be assigned to the boundary points. Instead, the value of the boundary point is found by interpolation from the surrounding neighbours including the point on the bubble surface.

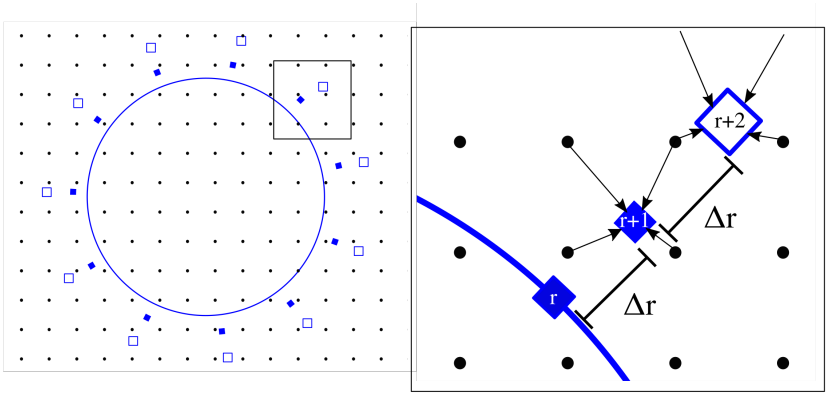

Figure 5.7: 2D Diagram showing the spherical points (squares) surrounding the bubble used to calculate the concentration gradient. The concentration of the radial points are given by interpolation from the surrounding cartesian mesh points as indicated by the arrows in the right hand panel.

5.2.3.2 Gradient at the bubble tissue interface

The expression for the gradient at the bubble surface $\frac{\partial C_{tot}}{\partial R}|_{R_B}$ is needed to calculate the flux of gas into and out of the bubble. As a sharp interface method is used, the interface width cannot be used to calculate the gradient as done in other models [175]. Instead it is calculated using a normal probe method described in [264]. A set of spherically symmetrical points around each bubble is created as shown in Figure 5.7. The concentration of these points is found using inverse distance weighting interpolation of the 6 nearest neighbours.

$$C_{new} = \frac{\sum_{i=1}^{N}(w_i(\mathbf{x}C_i))}{\sum_{i=1}^{N}(w_i(\mathbf{x})} \tag{5.10}$$

where $w(i)$ is the weighting function described by:

$$w_i(\mathbf{x}) = \frac{1}{d(\mathbf{x},\mathbf{x_i})^p} \tag{5.11}$$

$d(\mathbf{x},\mathbf{x_i})$ is the euclidean distance between the two points $\mathbf{x}$ and $\mathbf{x_i}$ and p is the power parameter.

Using the new array of spherical points a 1D forward difference approximation with 2nd order accuracy can be constructed in terms of the radial co-ordinate.

$$\frac{\partial C}{\partial R} = \frac{1}{2\Delta r}(-C_{r+2} + 4C_{r+1} - 3C_B) \tag{5.12}$$

where C_{r+2} and C_{r+1} are the concentrations at points $r+1$ and $r+2$, and Δr is the

radial distance between points shown in Figure 5.7. C_B is the concentration of gas at the bubble surface as given by Henry's law, in all simulations $\Delta r = h$

5.2.4 Mass conservation

Mass conservation is of particular importance for sharp interface Cartesian grid methods. Such methods are particularly prone to local violation of mass conservation due to the movement of the boundary over grid points (nodes), creating so called fresh and dead cells which may act as spurious sources and sinks, as well as the potential surface area discrepancy between the gas and tissue phase[266]. In order to ensure mass conservation the calculation of the mass of gas within the tissue is required for which the partial volume of cells cut by the bubble boundary must be calculated. As the bubbles are always spherical, the volume of gas can easily be calculated using the perfect gas law and the current bubble radius.

$$m_{O_2} + m_{N_2} = \frac{P_B V_B (m_f^{N_2} Mr_{N_2} + m_f^{O_2} Mr_{O_2})}{\mathscr{R}T} \tag{5.13}$$

where m_g is the mass of gas, m_f^g is the mole fraction, Mr is the molar mass of the gas and $\mathscr{R}$ is the universal gas constant. For the tissue, mass is calculated by summing the contribution from each cell in the tissue grid:

$$m_{O_2} + m_{N_2} = \sum_{n=1}^{n} V_n (C_{N2}^n + C_{O_2}^n) \tag{5.14}$$

where n is the number of tissue nodes V_n is the volume of the cube the node is centred within. For the majority of nodes in the grid the volume is simply the spatial step cubed h^3; however cubes which contain the bubble tissue interface, have only a partial volume, these are referred to as cut cells. If the partial volume of cut cells is not accounted for then discontinuous jumps in the total tissue gas mass are seen as nodes pass into and out of the tissue grid (see Figure 5.8).

In order to calculate the mass of such cells an estimation of the volume is needed. This is calculated as follows, Firstly boundary nodes which are cut cells are identified. Then the cut cell node position is converted to spherical polar co-ordinates where θ is the incline and ϕ the azimuth, the radial distance between the node and the bubble surface is calculated, (see Figure 5.9). At this point an estimate of the volume fraction

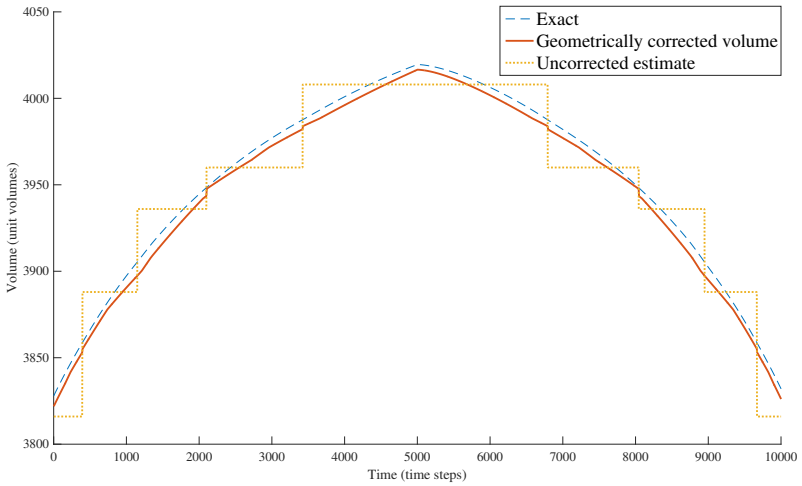

Figure 5.8: Showing the jumps in the total tissue gas mass as the number of nodes in the tissue changes

is made by assuming the surface of the bubble within the cell can approximated by a plane rather than a portion of a spherical cap. This assumption becomes more accurate as the bubble becomes larger. This assumptions results in the volume portion of bubble within the grid cube being defined by a polyhedron, the volume of which can be calculated using ray tracing algorithms. However, this is a computationally intensive task requiring all the cube plane intersection point to be calculated in the correct order. Given that the plane is already an approximation of a spherical cap, a further approximation is made whereby the volume fraction of the cell is estimated by finding the fraction of the line, which passes though the cube and is normal to the bubble surface, which is inside the bubble (see Figure 5.10). The fraction is defined as $(l-p)/l$. The length l can be calculated a coordinate system local to each cube from the azimuth and incline angles and the knowledge that either $x = 0.5, y = 0.5$ or $z = 0.5$ depending on which co-ordinate axes the line l is closest to (angular distance). For example consider Figure 5.10. If the angle between each co-ordinate axis and the line l is calculated, the angular distance to the negative z axis will be the smallest, therefore it is known that the line passes though the front and back faces of the cell and consequently the distance z will be 0.5. The length of l is then calculated by $l\cos(\theta) = 0.5$. Similarly this could be done if $x = 0.5$ or $y = 0.5$ using both θ and ϕ

Cells for which the node lies in the bubble rather than the tissue, are merged with the cell that is closest in the x,y or z direction from the bubble surface, see Figure 5.9.

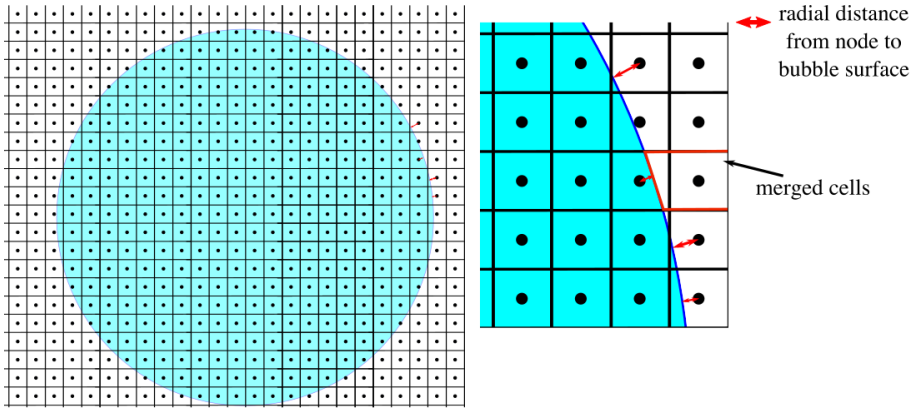

Figure 5.9: Showing the bubble imposed on the finite difference grid in 2D, the inset shows the radial distance to the bubble surface, note that the angle between the bubble surface and the line from the centre of the bubble to the node point will always be 90°

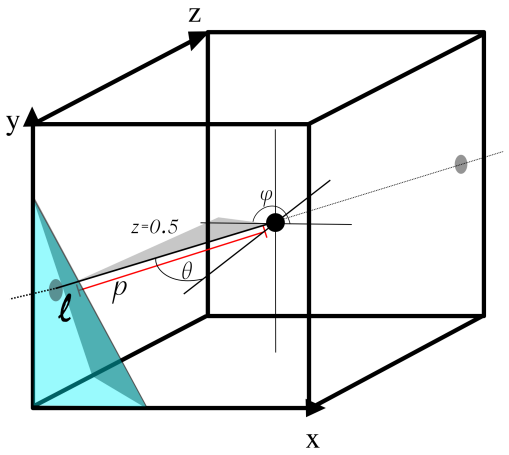

Figure 5.10: Showing a single cell with the bubble surface estimated by a plane. The line l is the total length of the line from the bubble surface to the node which lies within the cell. The line p is the distance from the node to the plane, intersecting the plane at 90°. The angles θ and ϕ are shown. In this instance it can be seen that the line l passes through the front of the cube xy plane and as such the z length of the triangle will be 0.5, from knowledge of one side and angle θ and ϕ the length l can be calculated by $lcos(\theta) = 0.5$. Similarly this could be done if $x = 0.5$ or $y = 0.5$ using both θ and ϕ

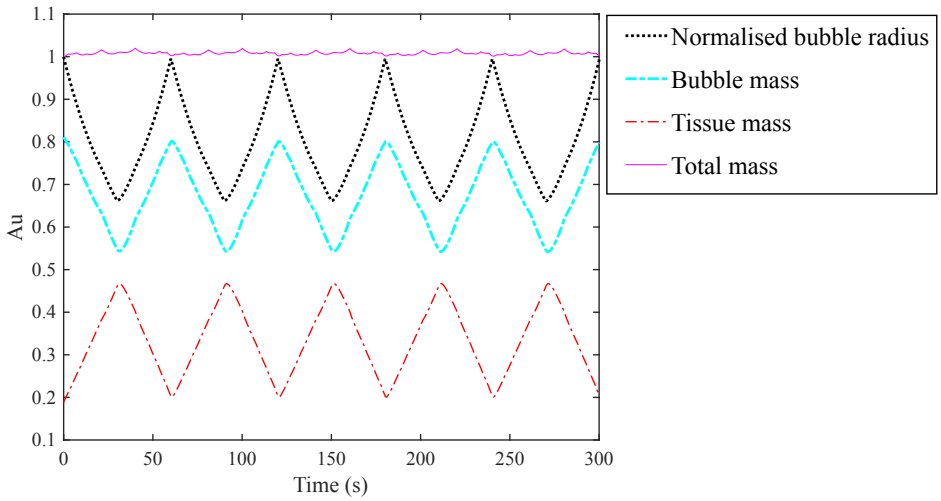

Figure 5.11: Showing the mass conservation for an oscillatory pressure profile with no flux boundary conditions at the grid edge. All masses have been non-dimensionalised to the initial total mass of the system, as can be seen there are only very small fluctuations in the total mass.

Using this new volume approximation the volume of the tissue can be seen to far more closely match the analytical value, (see Figure 5.8).

Calculation of the total mass of gas does not ensure conservation, in order to ensure local mass conservation at the bubble surface a mid-point approach similar to that of Seo at al. [266], is employed. At the point in each time step where the tissue concentration grid has been updated by the FTCS scheme, but the bubble radius has yet to be updated, the total mass of gas in a bubble bounding box must equal the total mass of gas after the radius has been updated. The mass of the bounding box at the mid point and the final point are compared. If a mass deficit is found, the mass is transferred to the surrounding tissue points in proportion to the tissue volume they contain. This method can be shown to ensure relatively good mass conservation by simulation of an oscillatory external pressure profile with no flux boundary conditions applied to the tissue edges (see Figure 5.11).

Coalescence is dealt with more extensively in the following chapter, but is discussed here briefly with reference to the computational model. Coalescence is initially modelled following the 2-dimensional implementation of O'Brien [220] i.e. when two bubbles come within one node of each other they instantly coalesce into a single bubble located at the position of the larger of the two. The new bubble is assumed to have a

mass equal to the sum of mass in the two coalescing bubbles and the volume is calculated via the perfect gas law. This model relies on the assumption that coalescence will always occur when two bubbles are in contact, and that the time over which coalescence takes place is far shorter than the time step used in the simulation. This part of the model is evaluated and developed in the following chapter.

5.3 Summary of numerical implementation

This concludes the description of the numerical implementation of the code. A link to the full code is given in the Appendix B. This section has highlighted and justified the choices made when implementing the code in particular concerning the interface techniques chosen. It has also highlighted the computational expense created by the stability requirements of the FTCS method in calculating the bulk diffusion. The introduction of the unconditionally stable ADE scheme in the descent and bottom time sections of the simulation are used to increase the efficiency of the code. Future work will include the development of a refined mesh and implicit technique.

5.4 Material Parameters sensitivity analysis

The following sections of this chapter discuss and justify the model's parameterisation. This is done through a literature search to establish physiological parameter limits and a sensitivity analysis to understand the affect each parameters has on bubble growth.

The model described thus far has many parameters (those listed in Table 4.1) in addition to the numerical parameters Δt and h as well as the overall tissue block size and the initial bubble radii R_0. The numerical parameters are chosen to ensure numerical efficiency and convergence of the solution, the initial bubble radii will be dealt with in the following chapters. This chapter is concerned with understanding the effect variations in the material parameters D, μ, γ, $k_h^{O_2}$ and $k_h^{N_2}$, have on the time course of bubble growth and dissolution. Such understanding is important as material parameter variation is seen across different tissue types in the body and also between individuals. Current models used in dive computers tend to give more consideration to dive parameters, with tissue half-time being the only variable material parameter. The tissue half-time represents the combined effects of perfusion, diffusion and solubility of gas in a given tissue. By separating material parameters, and using collagen gels in which

this parameter separation can be partially mimicked, such models can be more fully validated leading to better understanding and prevention of DCS.

Sensitivity analyses are used to investigate the influence of input parameters on model outputs. In addition to informing understanding of a model, such analyses can also be useful in generating hypotheses, checking for computational errors and focusing experimental design and protocol. There are many methodologies for performing sensitivity analyses and these can broadly be split into local and global methods. For local analyses parameters are altered one at a time whilst global analyses use probabilistic distributions of parameter values to investigate the whole parameters space. Local analyses are generally easier to implement and less computationally intensive. However, they cannot be used to investigate parameter interactions and represent only a small portion of the total parameter space [267]. Of local methods there are again many methodologies including direct and indirect methods as well as feature sensitivity. Direct and indirect methods define sensitivity as the solution to either the finite difference approximation of the following ODE or the solution to the differential of the following ODE with respect to a parameter k_j.

$$\frac{d\mathbf{y}}{dt} = f(\mathbf{y},\mathbf{k}) \ , \ \mathbf{y}(0) = \mathbf{y}^0 \tag{5.15}$$

Where $\mathbf{y}$ is the vector of variables and $\mathbf{k}$ is the vector of parameters. Feature sensitivity selects a feature in the model output and defines the parameter sensitivity as

$$S_{F,j} = \frac{F_j - F}{\Delta k_j} \tag{5.16}$$

Where F is the feature of interest and $S_{F,j}$ is the sensitivity of the parameter k_j with respect to the feature.

Feature sensitivity analysis was chosen for this work, with the maximum bubble radius and the time at which this occurs as two features that capture the time course of bubble dynamics well. The first step in such an analysis is to prescribe the parameter value space. This is done based on a literature review which aimed to provide physiological limits and collagen gel limits for all five material parameters. The literature was evaluated for mammalian tissue values, values related to collagen gels and other

similar tissue scaffolds including Agar, decellularised tissues and some synthetic polymer models where appropriate. The results are given in the form of tables for each parameter.

5.5 Parameter literature review

5.5.1 Diffusion coefficient

Values for diffusion coefficients of gases in tissues and biological fluids other than oxygen are uncommon in the literature. A meta-analysis by Lango et al. [268] reviewed 166 works on the subject and provides by far the most comprehensive review of such values. From their meta analysis [268] derive the following relation between the water content of the tissue in question and the diffusion coefficient.

$$D_{tissue} = D_{water} e^{\eta(w-1)} \tag{5.17}$$

where $\eta = 4.3$ for N_2 and $\eta = 4.4$ for O_2 and $w =$ water fraction.

In addition to this review, further literature searches for diffusion coefficients relating to collagen gels and other tissue scaffolds were done. No literature was found for diffusion coefficients of nitrogen, however diffusion of oxygen has been more widely researched in relation to the viability of such scaffolds in regenerative medicine [269]. Due to the lack of data regarding diffusion of nitrogen in collagen gels it was hypothesised that a relation such (5.17) might be applicable to collagen gels as well as tissue. The data for oxygen diffusion in collagen gels was compared to the values predicted by (5.17). Values of diffusion coefficients for oxygen in 0.1%, 0.2% , 11% and 34% collagen gels can be calculated to be. $2.3948 \times 10^{-9}, 2.29 \times 10^{-9}, 1.8 \times 10^{-9}$ and $6.7 \times 10^{-10} m^2/s$ (where the diffusion coefficient of oxygen in water is taken to be $2 \times 10 - 5 m^2/s$) These predicted values are larger than those experimentally found for high density collagen[200] and smaller or similar to those for low density collagen [270], (see Table5.1). This is possibly due to the high cell content of tissues used to fit (5.17), verses the a-cellularity of collagen gels. As (5.17) does not seem to be applicable to collagen gels in the case of oxygen, it was decided that the estimated D for nitrogen could not be derived from 5.17 and should instead be set the same as experimental values measured for oxygen.

Other DCS bubble models use a wide range of diffusion coefficient values. Srinivasan [166] and Gurmen [271] both use very small diffusion coefficients of the order of $1 \times 10^{-12} m^2/s$. This value is three orders of magnitude less than that of water and such values are not found in any of the reviewed works of [268]. Their use stems from the work of Gernhardt [165] in which a range of values from $1 \times 10^{-9} - 7 \times 10^{-15} m^2/s$ was found using a literature search based approach. The extremely low values came from the work of Hills, who argued that the diffusion coefficients for intracellular N_2 diffusion were far lower than extracellular. Gernhardt performed a sensitivity analysis on this range and found that values greater than $1 \times 10^{-10} m^2/s$ (close to that of water), lead to a peak bubble radius almost immediately after decompression, whereas values in the range of 1×10^{-11} and 2×10^{-12} lead to a delayed peak by 65-105 mins. This result was discussed in the context of the time of onset for DCS symptoms which are typically seen in in the 30-90min window post-surfacing. Gernhardt concluded that the values of 1×10^{-11} and 2×10^{-12} "predicted decompression stress patterns which were consistent with expectations for this exposure" [165]. This is again a validation of a mechanistic bubble model using symptoms of DCS. Choosing a diffusion coefficient range in this way tacitly assumes that DCS symptoms are directly caused by the increasing size of extravascular bubbles, a correlation for which there is little or no evidence. Indeed other researchers have questioned the choice of such a small diffusion coefficient. Other models such as those of Hugon and Van Liew use more biologically supported values of - $2.8 \times 10^{-9} - 7 \times 10^{-10}$ [176] and 5.35×10^{-9} [158].

Table 5.1 shows a summary of the review of [268] and additional data gathered from collagen and Agar gels. Based on the experimental data in Table 5.1 and the known percentage of collagen in the gels used an estimated range of diffusion coefficients of $2.5 \times 10^{-9} m^2/s - 9 \times 10^{-10} m^2/s$ was chosen. For comparison the range of values in the Table 5.1 is from $1.7 \times 10^{-10} m^2/s$ at smallest to $3 \times 10^{-10} m^2/s$ at largest.

5.5.2 Shear modulus

The literature values for the shear modulus of collagen hydrogels, show a large variation (see Table 5.2). This variation seems to be an intrinsic feature of the gels and it is commented upon in several of the works referenced, particularly those which measure shear modulus at small scales such as Shayegan et al. [278]. It is concluded by these

Source	Value of $D(m^2/s)$	Material	Gas	Temp $^\circ C$
[200]	4.5×10^{-10}	Collagen 11% w.t	O_2	37
[200]	1.7×10^{-10}	Collagen 34% w.t	O_2	37
[272]	1.88×10^{-9}	Water	N_2	25
[272]	2.10×10^{-9}	Water	N_2	25
[273]	1.7×10^{-9}	Water	O_2	37
[273]	$2.0 - 2.7 \times 10^{-9}$	Agar 2%	O_2	30
[274]	2.7×10^{-9}	Agar 2%	O_2	37
[275]	2.2×10^{-9}	cartilage	O_2	37
[276]	$7 \times 10^{-10} - 2 \times 10^{-9}$	Decellularized ECM	O_2	37
[270]	3×10^{-9}	Collagen (1mg/ml) 0.1%, (3mg/ml) 0.2%	O_2	30
[268]	8×10^{-10}	Aortic pig wall	N_2	37
[268]	2.9×10^{-10}	Plasma membrane cardeomyocyte	O_2	37
[277]	2.83×10^{-10}	Water	N_2	40
[277]	3.33×10^{-10}	Water	O_2	40

Table 5.1: Estimations of diffusion coefficients in various biological media

researchers that at the length scales measured by them, there is significant anisotropy in the gels leading to variation of two orders of magnitude within the same gel. Our own measurements, using a modified cavitation rheology technique, [239] similarly saw very high variability in the shear modulus measured. Owing to the large variation in results throughout our own and others work it was difficult to estimate the range of values that would be taken by the gels. The values for gels were chosen to range from 0.5-100Pa, as this covered the majority of the experimental range.

5.5.3 Solubility

The solubility coefficients of both nitrogen and oxygen were considered in the literature search. In particular the nitrogen solubility coefficient is considered important in the formation of bubble in lipid rich tissue and this is hypothesised to be a factor in the development of neurological DCS [13]. It was not clear how this parameter might vary with plastic compression of the collagen hydrogels. From the literature search, variation in tissue density did not appear to substantially affect the solubility of oxygen, and nitrogen solubility appeared to alter only where tissue lipid content varied. As none of the collagen constructs used in this portion of results had the lipid content altered, these parameters were not considered variables in experimental conditions but, their sensitivity was investigated in the computational domain. Conversion from Ostwald

Source	Value of $\mu(Pa)$	Material	Method	Temp
[279]	$6.32-318$ (aggregate modulus)	1mg/ml Collagen	confined compression	37
[280]	$10-100$	0.9mg/ml Collagen	cone plate rheology	37
[278]	$0.2-100$	0.5mg/ml-1mg/ml Collagen	optical tweezers	21
[281]	$53-40$	2.3mg/ml-1.5mg/ml Collagen	optical tweezers	37
[282]	2	$2mg/ml$ Collagen	Bholin Gemini rheometry	Unspecified
[283]	15.5	2.1mg/ml Collagen	coquette rheometry	Unspecified
[284]	$300-350$	2.4mg/ml Collagen	Bholin CVO rheometry	37
[285]	23	4mg/ml Collagen	Plate rheology	37
[286]	$0.75k-2k$	Liver	Various	*in vivo*
[287]	$0.173M-0.4M$	Articulate cartilage	Various	*in vivo*
[288]	10.6 ± 5.3	Turkey breast	Elastography	Unspecified
[288]	10.3 ± 1.5	Bovine liver	Elastography	Unspecified
[288]	7.1 ± 2.1	Agar-Gelatin	Elastography	Unspecified
[288]	46.7 ± 28.7	Poricine Fat tissue	Elastography	Unspecified

Table 5.2: Estimations of μ in various biological soft tissues and tissue mimics

coefficient (L) to Henrys constant is done via the formula from Emerson [289] pg 87. (assuming the density of biological fluid to be 1), given by

$$L^g = \frac{k_h^g}{\mathscr{R}_{spec}T} \tag{5.18}$$

where $\mathscr{R}_{spec}$ is the specific gas constant for the gth gas. Values chosen for collagen gels were 0.027 for O_2 and 0.0145 for N_2, in the modelling literature there is also agreement with these values [165, 170, 176, 271, 175, 177].

Source	Value of $k_h or L$)	Material	Gas	Temp
[268]	$0.0145(L)$	Blood Plasma	N_2	37
[268]	$0.027(L)$	Blood Plasma	O_2	37
[290]	$0.027(L)$	Water	O_2	37
[291]	$0.014520(L)$	Water	N_2	35
[268]	$0.073(L)$	Sheep bone marrow	N_2	37
[268]	$0.015(L)$	Calf Brain	N_2	37
[268]	$0.0133(L)$	Olive oil	O_2	37
[268]	$0.0261(L)$	Whole man	O_2	37

Table 5.3: Estimations of L in various biological tissues

5.5.4 Surface tension γ

The final parameter considered was surface tension. The collagen gels used in this work have a high water content, and as such the surface tension is not expected to differ greatly from that of saline. However the presence of surface active molecules and the salt concentration can affect the surface tension. The literature survey for biological tissues revealed lower values for surface tension in albumin, plasma and serum than that of water or saline. Surface tension occurs due to the hydrogen bonding between H_2O molecules. The introduction of of ionic salts or amphiphillic molecules such as phospholipids reduces surface tension by interrupting the hydrogen bonding. In biological media there are many molecules which may have this affect resulting in a lower surface tension. The addition of lipids or other surfactants may affect surface tension and this will be further discussed in chapters 6, and 7. In the modelling literature values used for surface tension tend to towards the lower end (0.05 - 0.03 N/m) of the values in Table 5.3, [165, 170, 176, 271, 175, 177]. This is consistent with the estimated surface tension for blood. For hydrogels and collagen gels made without fetal calf serum it is not clear that surface tension values will differ greatly from that of saline. This will be investigate in the following section.

5.5.5 Model sensitivity results

Figure 5.12 shows the results of the feature sensitivity analysis for all 5 material parameters. A single bubble in a tissue block exposed to a decompression from 30m in 3.75mins was modelled. The block of tissue was assumed to be saturated at the start of the decompression, hence time $t = 0$ represents the beginning of the ascent from a saturation dive. In all cases the single bubble was assumed to have an initial radius of

Source	Value of $\gamma\, mN/m$	Liquid	Method	Temp
[292]	69.8	Water	Tensiometer	37
[292]	69.8	Saline	Tensiometer	37
[292]	46.4	Albumin	Tensiometer	37
[292]	40.5	Plasma	Tensiometer	37
[292]	40.6	Serum	Tensiometer	37
[293]	73	Saline	Microscopy	Not reported
[294]	73	Polyacrylamide hydrogel	spherical harmonic of liquid drops	Room temp

Table 5.4: Estimations of γ in various biological tissues

$0.04mm$ and the tissue block a size $128 \times 128 \times 128mm$. The left-hand column shows the radius change with time for the single bubble and the right hand column shows the change in maximum bubble radius and the time of maximum bubble radius for the parameter values. For each parameter the range of values taken reflected the total possible physiological range rather than values associated with collagen gels as based on the literature survey in Tables 5.1-5.4.

From Figure 5.12 it can be seen that increases in the parameters D, μ and γ lead to a decrease in the maximum bubble size and decrease and the time taken to reach this maximum. For both L^{N_2} and L^{O_2} the increase in parameter value leads to an increase in maximum bubble size but a decrease in the time taken to reach max. This shows that bubbles are growing more quickly and to a larger size as the amount of dissolved gas in the tissue increases. In the case of tissues these results suggest that stiffer tissues will resist bubble growth to a greater degree, and that tissues which have small diffusion coefficients (denser tissues) will have larger bubbles which persist for a longer time. Tissues with low surface tensions, will also have larger bubbles, and finally more lipid rich tissues will tend to have larger bubbles.

All the right-hand panels show that there is some level of non-linearity associated with the the time to max bubble size. Some of the non-linearity is due to the effective asymptote imposed by the Boyle's law contribution. Until 225 seconds after the profile begins the ambient pressure is decreasing rapidly hence the Boyle's law term will tend to dominate. Parameters D, γ and L^{O_2} appear to have a linear relation between parameter value and maximum radius. Whereas L^{N_2} is slightly non-linear and μ

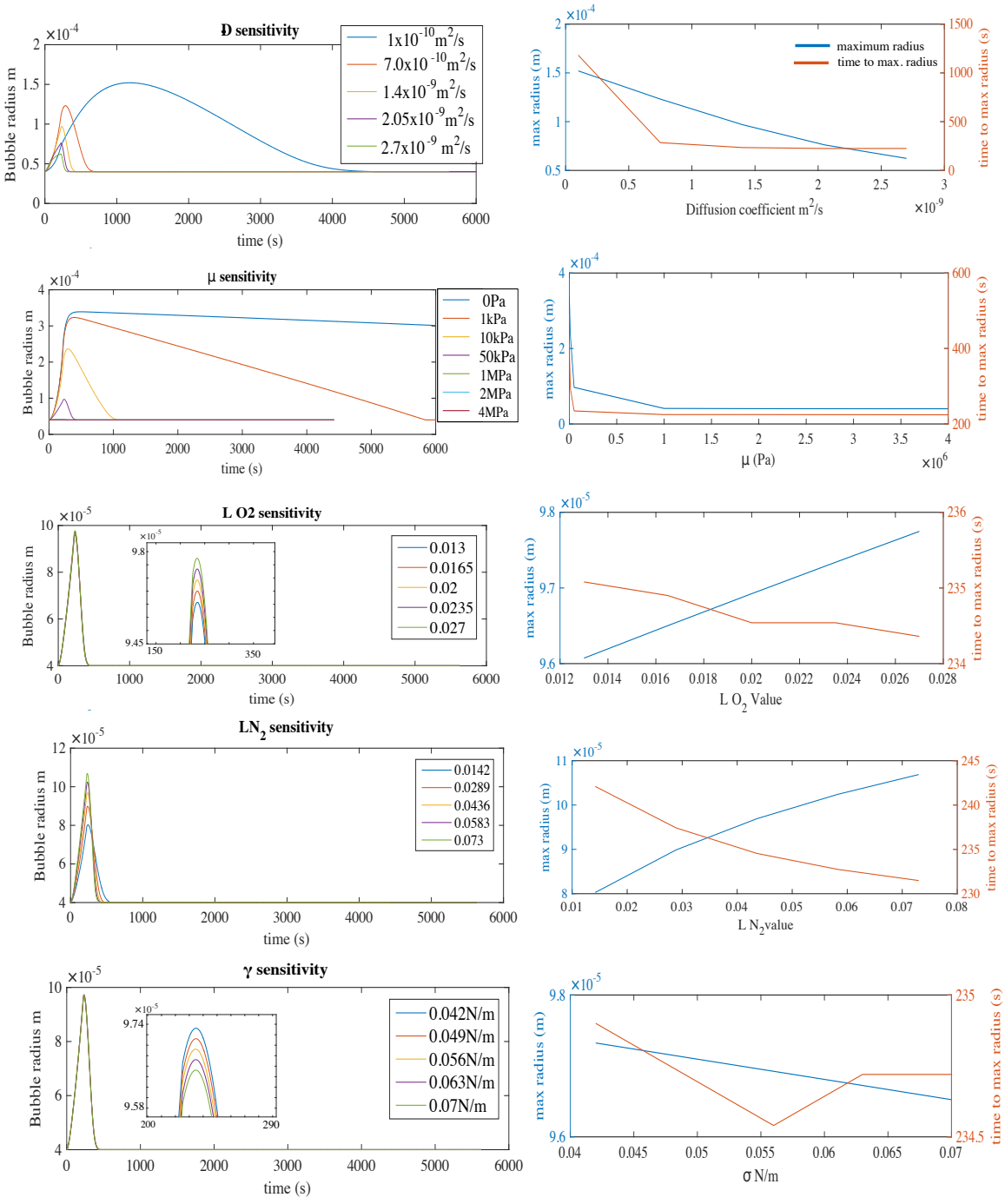

Figure 5.12: Sensitivity of the material parameters of the model for a single bubble of initial size 0.04mm. In all cases the fixed parameter values are the modal values of the range ($\gamma = 0.056$N/m, $L_{N_2} = 0.0436$, $L_{O_2} = 0.02$, $\mu = 2 \times 10^6$Pa, $D = 1.4 \times 10^{-9} m^2/s$). Left is the bubble radius profile with time, Right is the response of the two features, (bubble maximum radius and time to maximum) to changes in the parameter value. Note the y-axis scales are not even across all panels

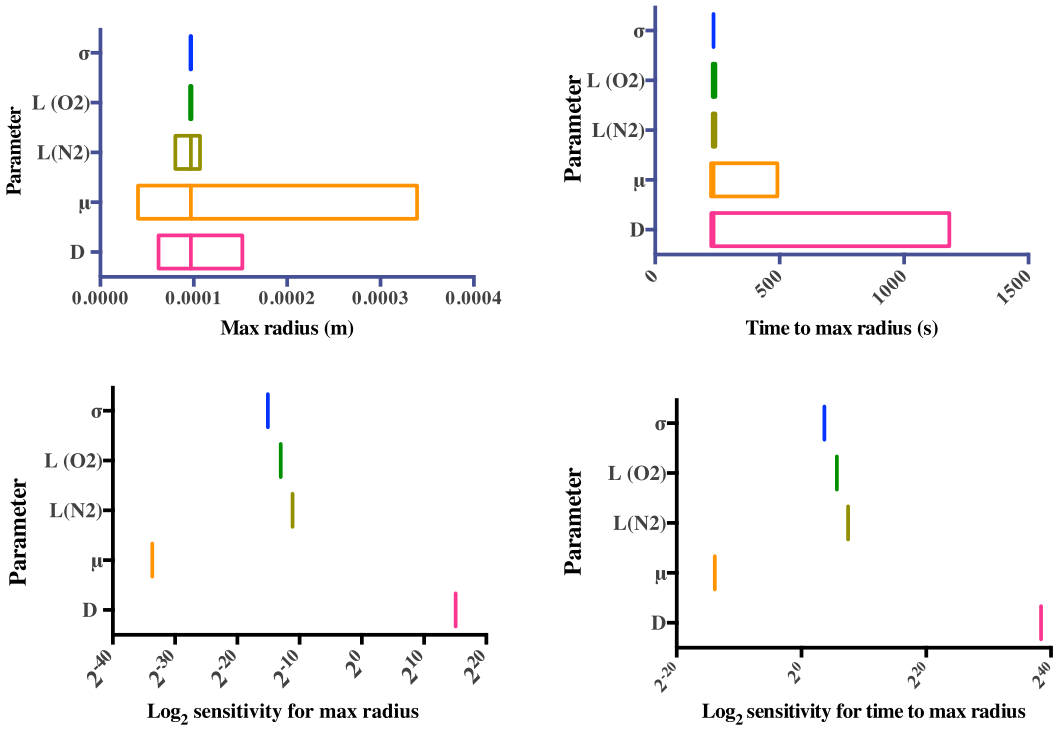

Figure 5.13: comparison of all parameters on the range of max bubble sizes (Left) and time to max bubble size (Right)

highly non-linear. In this case the largest changes in the maximum with μ appear at the low end of parameter value range. This suggests the effect of shear modulus is most pronounced in softer tissues.

Figure 5.13 shows a comparison between the relative sensitivities of all parameters. The top panel shows total effect each parameter has across its entire physiological range. From this top panel it can be seen that μ has the largest effect on maximum radius across its entire range, whilst the diffusion coefficient has the largest effect on time to max radius. The lower panel shows the sensitivity of the parameter. In this case we see that although μ has the largest affect this is due to the wide physiological range as opposed to the sensitivity of the parameter. The most sensitive parameter is D with L^{N_2}, L^{O_2} and γ having lower and relatively similar sensitivity, μ has the lowest sensitivity. The sensitivity of D is not unexpected, as it plays a role both in the transport of gas through the bulk tissue towards and away from the bubble and also in the diffusion across the bubble tissue interface. In this model the diffusion coefficient governs the rate at which gas is eliminated from the tissue and hence it is expected to have a strong influence on the rate of bubble growth. A factor which should not be ignored is that

whilst γ appears to have a low sensitivity, the initial radius of the bubble will affect the magnitude of the surface tension force. A more appropriate way to consider the surface tension sensitivity is by considering the radius at which the surface tension force begins to substantially contribute to the bubble pressure. For the lowest and highest values of surface tension ($\gamma = 0.04 and \gamma = 0.073$) the surface tension contribution to the total bubble pressure is only 2% and 3.5% at the initial radius of 0.04mm. If an initial radius of $2\mu m$ was used the proportions would be 27% and 36% for $\gamma = 0.04$ and $\gamma = 0.073$ respectively. It is therefore important to not discount the importance of surface tension.

5.6 Conclusions and Summary

This chapter has described and justified the choices made in the numerical implementation of the bubble model. The use of a Cartesian grid method with immersed sharp boundaries has been employed, as a future need to model complex geometries is anticipated. Similarly, a sharp interface method has been chosen to enable larger volume simulations. Parameterisation of the model has been addressed through a literature search for the five most crucial material parameters in the model. It is thought that values for these parameters should be restricted to physiological limits unless there is clear evidence that such limits do not apply. A comparison of the parameter limits for collagen gels to those for biological tissue reveals that, although collagen gels can mimic the physiological diffusion coefficient range, shear moduli comparable with stiffer tissues cannot be achieved. The feature sensitivity analysis showed that in the current model μ was the least sensitive parameter, this coupled with the small range of values which can be achieved in collagen gels makes this experimental system unsuitable for investigating the effect of tissue elasticity and the form of the elasticity function. Despite this, the diffusion coefficient D, which was the most sensitive parameter, is well represented in collagen gels and therefore the system is ideally suited to investigate the diffusion barrier which has been proposed in other bubble models of DCS.

for the remainder of the thesis parameter values for the less sensitive parameters are set at the values: $L^{N_2} = 0.145$, $L^{O_2} = 0.027$, $\mu = 40$Pa and $\gamma = 0.07$N/m. The diffusion coefficient for hydrogels is assumed to be the same as that of water $D = 2.5 \times 10^{-}9m^2/s$ and to reduce with gel density.

Chapter 6

Validation

6.1 Introduction

This chapter focuses on the validation of the computational model, through direct comparison of simulations to experimental data. Validation to changes in both material and dive parameters are presented. This validation stage is critical to enabling future development of the model and to assessing its current validity. As described in the previous chapters, one of the main benefits of this experimental system is the control that can be exercised over the pressure profile and the material properties of the gel. This allows validation of material parameters to be done whilst controlling dive and bubble parameters, such as bubble density. Conversely, the simulated effect of dive parameters on bubble dynamics can be validated on gels which have consistent material properties. This chapter will initially present validation of the effect change in the diffusion coefficient has on bubble dynamics. In this instance the initial computational model required development to effectively describe the experimental data. Following on from this a sensitivity analysis of dive parameters in both the computational and experimental model is presented. The complementary analyses highlight areas in which the simulations are able to describe the experimental data; instances in which the computational model aids in the interpretation of data; and areas in which the computational model is unable to predict or describe the data. In all cases the complementary approach is highly valuable. In particular areas where the model failed to predict/describe the data, attention is drawn to useful developments such as viscoelasticity and complex bubble-bubble interactions.

6.2 Diffusion coefficient validation

Of the five material parameters analysed in chapter 5, only the diffusion coefficient, and specifically the diffusive mass transfer at the bubble interface, were chosen for validation analysis. This choice was made for three reasons: i) the diffusion coefficient was found to be the most sensitive parameter computationally; ii) the diffusion coefficients for collagen gels of varying density are well characterised and fall within the range of *in vivo* values [200]; iii) there is some controversy in the modelling literature over the value the diffusion coefficient should take. As previously mentioned, some models of DCS use low diffusion coefficients in the tissue region immediately surrounding the bubble [4, 295, 271]. These values are on the order of $10^{-12}m^2/s$ and their use has been challenged, particularly by Hugon et al. [176]. Direct observation of bubble growth or dissolution to validate one or other of these views has not been widely reported in the DCS literature. Van Liew et al. investigated bubble dissolution times in saline. They reported that the experimental dissolution times were broadly in agreement with their model, which used higher diffusion coefficients ($\sim 10^{-9}m^2/s$). However, they also noted that there was a systematic error whereby bubbles persisted for 30% longer than predicted [149]. Outside the DCS field, a large body of literature on gas-liquid mass transfer exists in the chemical and bioprocessing industries. Diffusion through gas-liquid interfaces is of importance in aeration reactors such as those used for waste treatment, and fermentation [296, 297, 298, 299]. This literature is largely focused on quantifying the magnitude of the liquid-side mass transfer coefficient, (k_L) which is proportional to the diffusion coefficient (assuming diffusion across the interface is modelled by Fick's first law). This literature provides an excellent source of experimental and modelling data regarding the reduction of k_L due to the contamination of the air-liquid interface.

When seeking to quantify the effect of varying the diffusion coefficient, it should be altered whilst other material parameters are held constant. Altering the diffusion coefficient of the collagen hydrogels has been experimentally verified in previous works [200] and is done by partial plastic compression. The first hypothesis of this investigation was that plastic compression would reduce the rates of both bubble growth and dissolution. Active control of the other material parameters was not achievable as it was not possible to accurately measure the solubilities of O_2 and N_2. Likewise, sur-

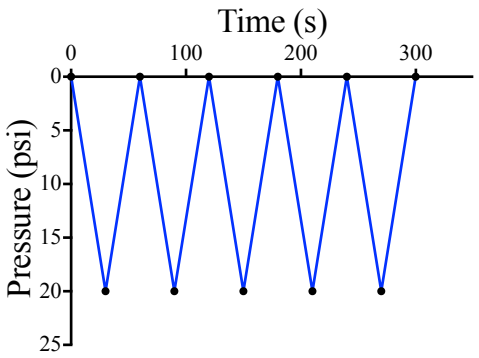

Figure 6.1: Showing the oscillatory pressure profile,

face tension was not measured in the gels, however all gels were made without FCS as this was thought to be the most likely source of contaminates that would alter the surface tension. As these parameters were shown to have low sensitivity, it was assumed that any small variation would not significantly affect the bubble dynamics. Similarly the shear modulus was shown to be a very low sensitivity parameter. As previously mentioned, measurement of the shear modulus was attempted using the method of cavitation rheology [238, 300], no significant change could be measured between partially plastically compressed (denser) gels and hydrogels. However, the technique was difficult to implement owing to the fragility of the hydrogels, resulting in poor reproducibility of the result. As the focus of this validation was diffusion through the bulk of the gel and across the bubble-gel interface, it was necessary to prevent bubble nucleation or bubble-bubble interactions from becoming dominant dynamics. To do this bubbles were introduced prior to gelling the gels by stirring the solution. In this way bubbles were seeded within the gel without decompression and adequate bubble spacing, to prevent bubble-bubble contact, could be ensured. To further restrict bubble-bubble interactions through gas exchange, short pressure profiles were used. An oscillatory pressure profile was chosen as both bubble growth and shrinkage could be investigated. The profile, shown in Figure 6.1, was applied to hydrogels and denser gels.

6.2.1 Methods

6.2.1.1 Experimental

Collagen gels were made as described in chapter 3, with a slight alteration, whereby gels were seeded with bubbles just after neutralisation by stirring with a pipette tip. After the initial fibrilogensis, samples were split into the dense gel or hydrogel group.

The hydrogel group were covered in FCS free, media and returned to 37° C. The remaining samples were removed and compressed with an absorbent plunger for 1 min. This technique, known as plastic compression, [192], removes some of the gels water content and thus increases the collagen fraction. These gels were termed the dense gel group. After plastic compression, the dense gels were covered with media returned to 37°C for 8-12hrs, before being transferred to the pressure chamber, covered in 0.3ml of FCS free media and exposed to the pressure profile in Figure 6.1. Time lapse imaging was used to track bubble radii.

6.2.1.2 Computational

Computational simulations for the dense gels and hydrogels were conducted for single bubbles, in a block of gel that measured 1.28 x 1.28 x 1.28 mm. The material parameters other than diffusion coefficient were fixed at $\mu = 40$ Pa, $\gamma = 0.07$ N/m, $L^{N_2} = 0.014$ and $L^{O_2} = 0.027$ as discussed in chapter 5. The initial bubble radius, is a key parameter of both the model and experimental system, as it dictates the relative magnitude of the surface tension pressure term. In order to interpret the effect that the change in diffusion coefficient had had, it was therefore essential that the initial radii in the dense and hydrogels were equivalent. This was done by pairwise matching of the bubbles measured in the dense gels and hydrogels. Equivalence testing using a Two One-Sided Test (TOST) was done to assess the success of the pairwise matching. The TOST test is done by comparing the 95% CI for the mean of each distribution of initial bubble radii. The difference between the lower CI for the smaller mean and the upper CI for the large mean, is compared to a defined equivalence region (ε); if the difference is less than ε the distributions are considered equivalent.

Statistical equivalence between the initial pressure distributions was found for $\varepsilon > 0.137$ (0.55 times the standard deviation of the joint distribution). Whether this is an acceptable level of equivalence must be assessed by considering the bubbles themselves. In this case the concern is that differences in the initial pressure of the bubble pairs will be larger at smaller initial radii, due to surface tension. For the twenty-three individual bubble pairs the largest difference in initial pressure was 13% as shown in Table 6.1. Although this difference seems large, removal of the pair from the data did not cause any change in the final result, it was therefore accepted that the distributions

Bubble Pair	Hydrogel initial radius (mm)	Dense gel initial radius (mm)	Rounded mean radius (simulation value) (mm)	% Pressure difference
1	0.0889	0.0988	0.09	6.09
2	0.103	0.134	0.12	13.25
3	0.133	0.141	0.14	3.11
4	0.133	0.147	0.14	4.98
5	0.140	0.150	0.15	2.88
6	0.142	0.153	0.15	3.44
7	0.147	0.157	0.15	3.09
8	0.170	0.168	0.17	0.41
9	0.193	0.172	0.18	5.08
10	0.212	0.176	0.19	7.43
11	0.216	0.180	0.2	7.71
12	0.217	0.195	0.2	4.48
13	0.225	0.201	0.21	4.42
14	0.228	0.212	0.22	2.82
15	0.237	0.228	0.23	1.51
16	0.239	0.238	0.24	0.084
17	0.244	0.238	0.24	0.90
18	0.245	0.239	0.24	0.80
19	0.250	0.2410	0.25	1.36
20	0.254	0.244	0.25	1.37
21	0.254	0.246	0.25	1.08
22	0.254	0.258	0.25	0.57
23	0.255	0.292	0.27	4.34

Table 6.1: The initial radii of the paired bubble data with the pressure difference between the bubble pair shown and the mean of the pair for use in the computational simulations

were equivalent. Analysis of both the experimental and simulated bubble radii was done using the maximum and minimum radius of the bubbles in successive pressure oscillations. Statistical comparison of the result was done based on 4 measurements: the final radial distributions at both the final minimum and maximum, and the total loss in bubble radius, again at the final maximum and minimum.

6.2.2 Diffusion coefficient validation results

6.2.2.1 Experimental results

The mean radial time course for the hydrogel and dense gels bubbles is shown in Figure 6.2, as can be seen the hydrogel shows a greater decrease in the bubble size with successive oscillations. Statistically significant differences were found between the hydrogel

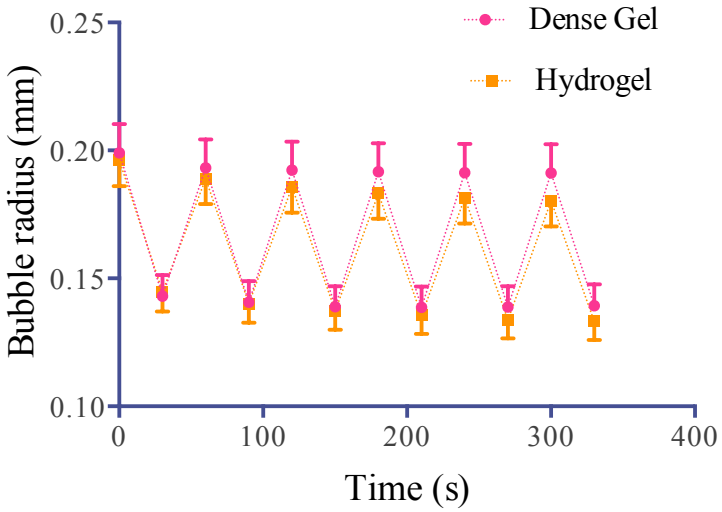

Figure 6.2: The time course of successive minima and maxima for the dense and hydrogels (n = 5) gels. Mean and standard error are shown.

and the dense gel for the change in the minimum, the change in the maximum and the final maximum as paired t-test's show in Figure 6.3. These results confirm that plastic compression can be used to effectively alter the material parameters of the collagen gels in ways which can be measured through changes in bubble dynamics. Although it has been discussed that this measured difference is primarily thought to be due to the change in diffusion coefficient, without accurate measurement of all other material parameters this cannot be definitively shown.

6.2.2.2 Computational results

Preliminary computational simulations of the oscillatory profile experiment were first conducted with a single bubble of initial radius 0.2 mm, as this was the approximate mean initial radius for both the experimental hydrogels and dense gels. Simulations were done assuming a single bubble centred in a tissue of size $1.28mm^3$ and a spatial resolution of $2x10^{-5}m$. Larger total grid size and greater spacial resolution were shown to have no affect on the final radial profile, so this grid size was used to decrease simulation time. Initial results of the simulation are shown in Figure 6.4, only successive maxima are shown for clarity. As can be seen there is a large discrepancy between the experimental results shown in dotted lines and the simulated values for the range of diffusion coefficients which were deemed plausible for collagen gels. Although the trend in successive maxima as the diffusion coefficient is decreased is the same as that

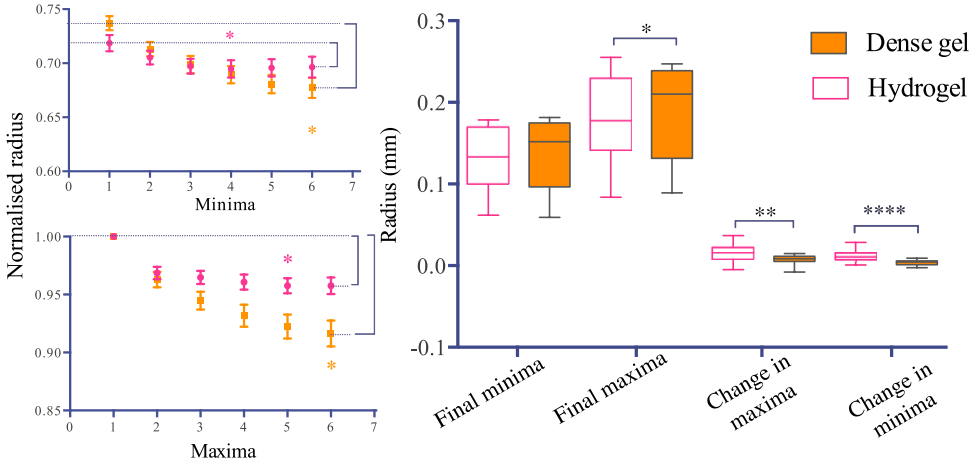

Figure 6.3: Left-hand panel- Showing the normalised radius for the dense and hydrogels where the minima and maxima have been split over two graphs for clarity (top and bottom respectively). Mean and standard error in mean are shown, the measurements, change in maxima and change in minima are indicated and the astrix denotes the oscillation at which the minimum radius was measured. Right-hand panel- showing final minima, final maxima and change in the minima and maxima, statistically significant difference between the hydrogel and dense gel can be seen for the final maximum, change in maxima and change in minima. The initial distributions (not shown) were tested for equivalence using a TOST test and found to be equivalent at $\varepsilon = 0.55$ standard deviations.

seen experimentally, the values differ greatly, with diffusion of gas out of the bubble being far too high.

In this initial version of the simulation there was no diffusion barrier, the diffusion coefficient used to characterise the bubble surface was the same as that used for diffusion through the bulk. Given the use of a diffusion barrier, in other models [166, 295, 220] and the large discrepancy between experimental and simulated results, the affect of varying the bubble surface diffusion was investigated. The approach to altering the surface diffusion coefficient was two fold. Firstly a simple decrease in the value, which was described as a fold change from the bulk diffusion coefficent, i.e. $D_{surf} = D_{bulk}/f$ where f was an integer factor. In addition to this the change in D_{surf} as a function of the bubble radius was considered. This was done as there may be several possible causes for a diffusion barrier. One possible source is the adherence of surfactants to the bubble surface. Such surfactants are known to reduce the surface diffusion by up to 15% and have a surface area or radial dependence [301, 302]. Another possible mechanism may be compaction of the collagen at the bubble surface, this

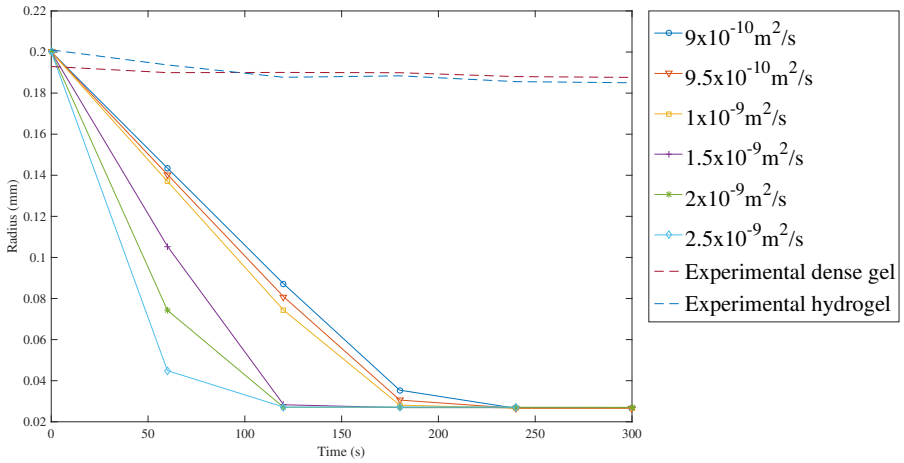

Figure 6.4: Showing the successive maxima for a computational simulation of a bubble of 0.2mm initial radius for a range of diffusion coefficients D and constant μ of 40 Pa values. Mean experimental maxima are shown in dotted lines for both hydrogel and dense gel

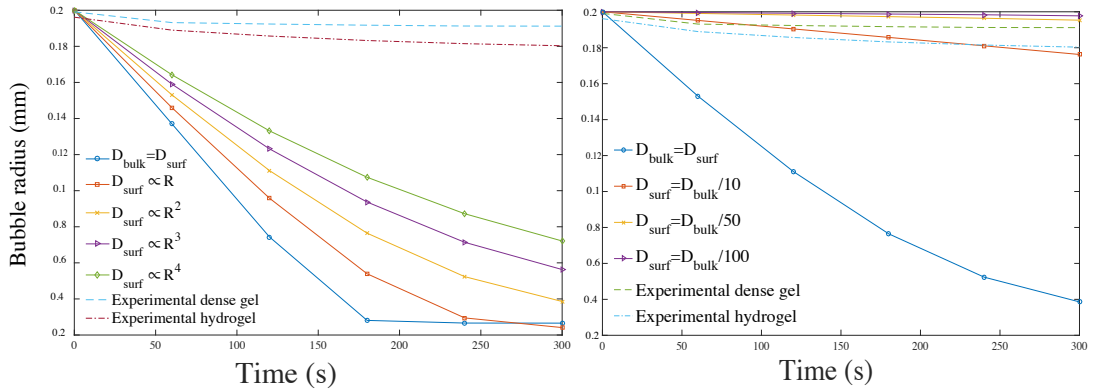

Figure 6.5: Showing the successive maxima the computational simulation of a bubble of 0.2mm initial radius for a variations in the bubble diffusion coefficent. Left: the functional relation to the radius of the bubble is varied. Right: The initial value of the bubble surface diffusion coefficient is varied in all cases the bulk diffusion coefficient was $D = 2.5 \times 10^{-9}$.

was observationally seen, shown in Figure 6.6. If this compaction leads to a diffusion barrier, the value may well depend on the bubble radius. With this in mind a diffusion barrier function was described by $D(R)_{surf} = D_0^{surf}\,(1-(R_{min}/R(t))^p)$, where R_{min} is micronuclei radius at which the bubble is impermeable and p is the power of R which was altered in this analysis. As can be seen in Figure 6.5 (RHS) the increase in D_0^{surf} has a greater change on the radial profile than variation of the dependence on R (Figure 6.5 (LHS)).

To examine this more quantitatively, both the diffusion function and D_0^{surf} were

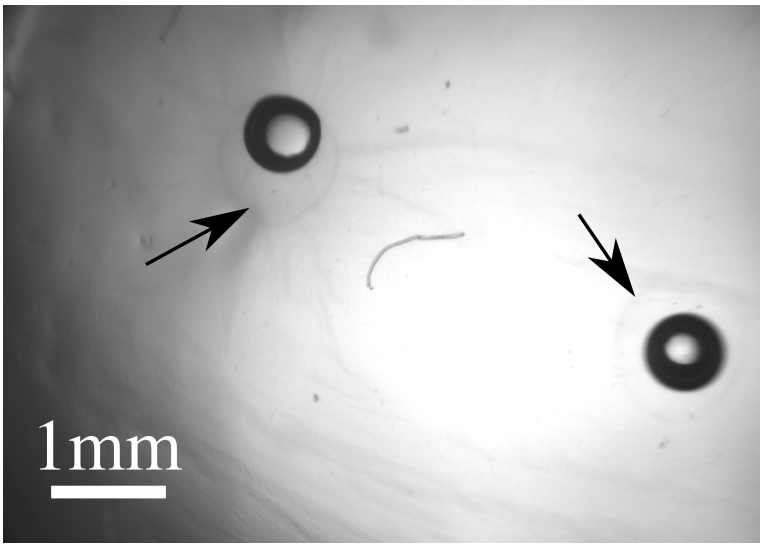

Figure 6.6: Bubbles within a compressed collagen hydrogel. Arrows indicate the outline of the bubble prior to compression these could show areas of compressed collagen and be a cause of the decreased diffusion coefficient.

optimised using the mean experimental hydrogel time course with a least squares approach. The results of this optimisation are shown in the left hand graph of Figure 6.7. This optimisation revealed that the R^2 function with a $D_0^{surf} = D_{bulk}/30$ provided the best fit to the experimental data. This function and fold change were then used to optimise for the dense gel bulk diffusion coefficient, which is shown in the right hand graph of Figure 6.7. Optimisation was done in this way as it was felt that the bulk diffusion coefficient of the hydrogel could be estimated to be the same as that of water with reasonable confidence. It was also assumed that the plastic compression of the gels would not affect the relationship between the bulk diffusion coefficient and the bubble surface diffusion coefficient. Although this is by no means a trivial assumption, there was no clear indication to suggest a difference mechanism of bubble surface diffusion in the dense gel by comparison to the hydrogel. In the absence of any evidence to the contrary the dependence of D^{surf} on D_{bulk} and R were left the same. The optimisation of the dense gel to a value of $D_{bulk} = 1.7 \times 10^9$ is within the expected range, however the sum of squares was greater in the dense gel than the hydrogel 1.7×10^{-4} compared to 0.6×10^{-4}.

Using these optimised values, simulations of the oscillatory profile for bubbles in the hydrogel and dense gel were again performed and the results are shown in Figure 6.8. The simulated hydrogel bubble fits the data better than the dense gels data which

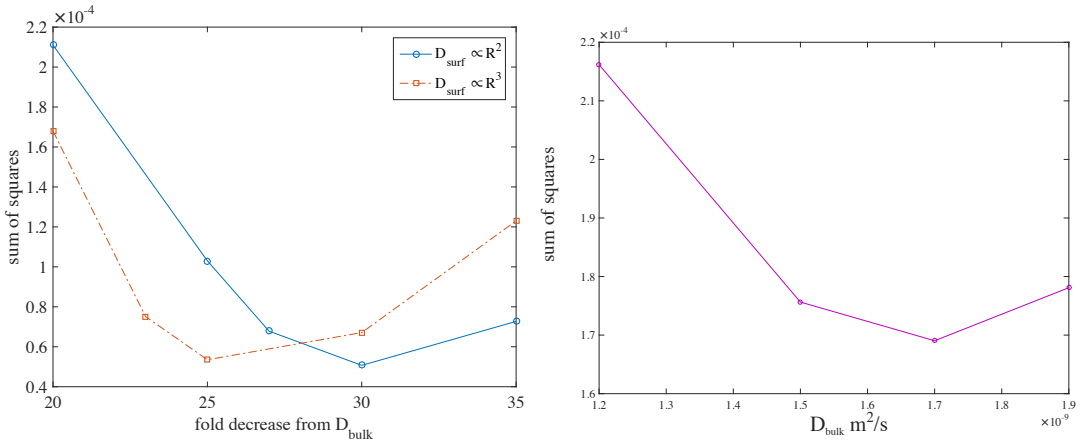

Figure 6.7: Showing the optimisation of the diffusion coefficient on a least squares comparison to the mean experimental profile. Left: The hydrogel was optimised for both the function and fold change from the bulk diffusion coefficient based radius profile. The R^2 value with a 30 fold decrease in initial bubble surface diffusion coefficient is seen to be the optimal parameter values Right: The bulk diffusion coefficient for the dense gel was optimised using the same fold change ($D_0^{surf} = D_{bulk}/30$) and function $D_{surf} \propto R^2$. The optimal value was found to be $1.7x10^{-9}$, however the dense gel is less well optimised than the hydrogel

can be seen in Figure 6.8. This may be due to the way in which the optimisation was carried out, i.e. two parameters optimised on the hydrogel and only one on the dense gel; however, it may also be due to greater variation in the dense gels. The technique of plastic compression creates a gel with anisotropic material parameters as removal of water is from a single face of the gel only and therefore leads to a gradient of collagen density through the gel. This gradient may mean that the computational model with a single bulk diffusion coefficient is less suitable for modelling gels compressed in this way. However, despite the less encouraging fit both models were carried forward for further analysis. Given the importance of the initial radius, simulations were then performed for a range of initial bubble sizes with the optimised diffusion coefficients.

The initial radial distribution for the simulated bubbles was created from the mean of each experimental bubble pair see Table 6.1. Comparison of the experimental data and the simulated results was done for the same measures as previously used in the experimental analysis. Figure 6.9 shows the comparison for the simulated hydrogel (left) and dense gel (right) to their experimental counterparts. As can be seen, the hydrogel shows no significant differences from the experimental values whereas the simulated dense gels shows some significant differences as measured by paired t-tests. It can be seen that the dense gel simulations consistently predicts a greater loss of gas

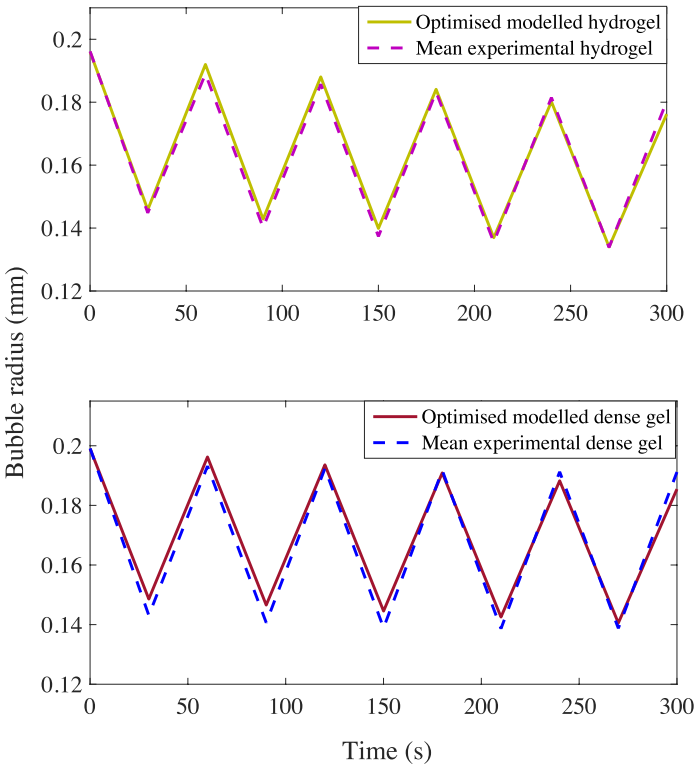

Figure 6.8: Showing the computationally optimised oscillatory simulation with the function, fold change and bulk diffusion coefficient found from the least squares analysis above. The dotted line show the mean experimental dense and hydrogel results. It can be seen that the hydrogel is better optimised than the dense gel

through the bubble surface resulting in lower final bubble sizes and larger changes in radius. This poorer description is due to what appears to be a more non-linear response in the dense gels; the decrease is not uniform under successive oscillations and the smallest radius is not seen at the final oscillation. This can be more clearly seen in the left-hand panel of Figure 6.3, where the minimum radius in each graph (minima and maxima) is denoted by an astrix. It can be seen that this is at the final value for the hydrogel but on the fourth or fifth cycle for the dense gel. This is not well captured in the model which predicts a more linear decrease in successive bubble minima and maxima, until the bubble approaches the minimum radius, (see Figure 6.5). A possible explanation for this behaviour could be that the dense gels are demonstrating some viscoelasticity, and hence the successive cycling may be leading to a preconditioned response.

Figure 6.10 shows the comparison of the simulations. From this comparison it can be seen that, similar to the experimental results (Figure 6.4), significant differences

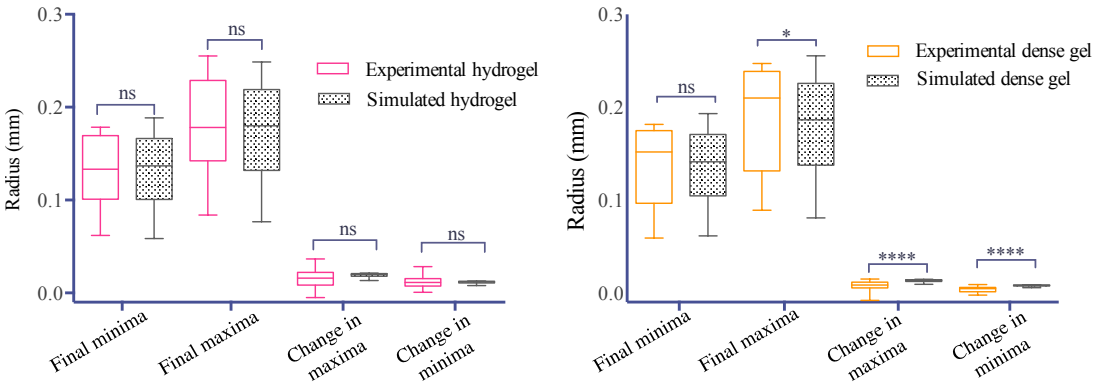

Figure 6.9: Comparison of the optimised simulated and experimental results, left- the hydrogel, right- the dense gel. The simulations used an initial radial distribution which was matched to the experimental values. For the hydrogel no significant differences were found between the simulated and experimental measures using paired T-tests in each case. For the dense gels significant differences for the change in minima and maxima was found as well as the final maximum

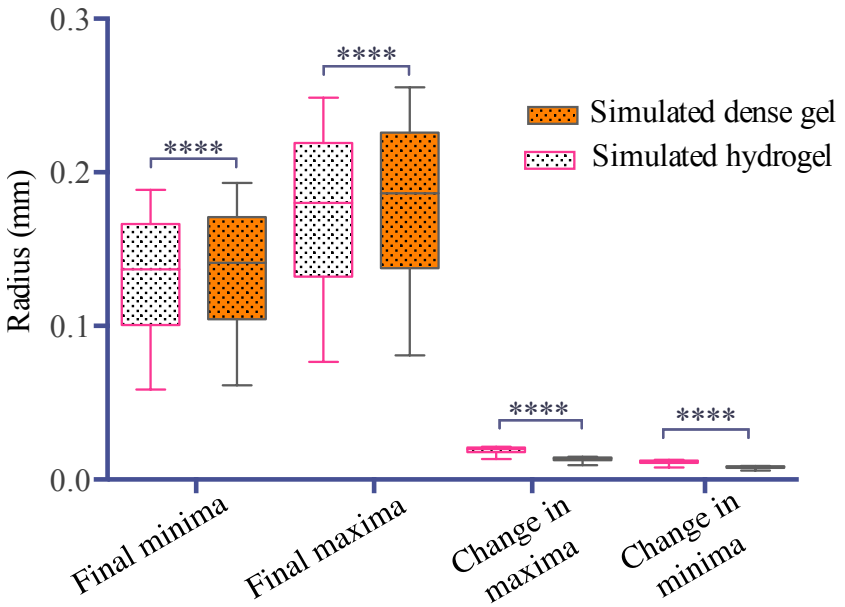

Figure 6.10: Comparison of the simulated dense gels and hydrogels. Significant differences found for all measures using paired t-tests

were found for the final maximum radius, the total change in maxima and the total change in minima. In contrast to the experimental results, the final minimum was also found to show statistically significant differences. All comparisons were done using a paired t-test.

6.3 Diffusion coefficient summary

The above experimental validation of the computational model has revealed a number of interesting findings. Firstly, it has been shown that plastic compression alters the

material parameters of the hydrogels in a way which can be significantly measured in the oscillatory response of bubbles within the gels. Secondly, it has been shown that with no diffusion barrier at the bubble surface, the computational model described in this work, is a poor descriptor of the experimental results. Using a diffusion barrier, which reduces the diffusion through the bubble's surface by thirty times compared to the bulk coefficient and has a surface area dependence, gives an optimal fit to the hydrogel data. By defining D_{surf} with the same relations for the denser gel the optimised value of bulk diffusion coefficient. This value is within the expected range for such a gel given the literature discussed in chapter 5. The diffusion barrier proposed here is most likely to be due to surface contamination of the air-liquid interface by surfactants from the collagen gel constituents. With this optimisation, the computational model is able to satisfactorily model bubble behaviour in the hydrogel. Simulations of the dense gels show a poorer fit to the experimental data, as measured by a higher sum of squares. This is primarily due to the observed more non-linear response of the dense gel bubbles, which the model does not capture. This non-linearity may be caused by several factors, including the anisotropy in collagen gel density, or possibly due to a more viscoelastic response from the denser gel. Given these findings, the hydrogel only is taken forward for dive parameter validation. Future work on the response of the dense gels would be interesting and important to discover the source of the non-linearity and investigate whether this is likely to be a feature of *in vivo* tissue.

6.4 Sensitivity to dive parameters

Given the validation above, hydrogels were used to investigate the effect of dive parameters on bubble growth. The dive parameters investigated were: the length of time at depth, the rate of decompression and the rate of compression. Time at depth and decompression rate are considered two of the most important parameters for divers undergoing decompression, and compression rate enabled some investigation of the the proposed surfactant diffusion barrier. The initial hypotheses for this investigation were: slower decompression would lead to smaller bubbles and slower growth rates, greater time spent at depth would lead to larger bubbles, increased compression rate would reduce the number of bubbles which nucleated. The decompression rate hypothesis arises as bubble growth is thought to be initially controlled by Boyle's law and if bubbles

Depth (psi)	Compression rate (psi/s)	Decompression rate (psi/s)	Time at depth (hrs)
130	1	13	0.33
130	1	13	1
130	1	13	2
130	1	13	3
130	1	13	2
130	1	8	2
130	1	4	2
130	1	2	2
130	5	13	2
130	1	13	2
130	0.5	13	2
130	0.1	13	2

Table 6.2: Dive parameters used in the experimental sensitivity analysis

reach a larger size more quickly there will be a larger surface area through which diffusion into the bubble can take place. Time at depth was thought to lead to larger bubbles as the amount of dissolved gas within the gels will increase with time at depth. If a surfactant adheres to the bubble-gel interface then as the bubble size changes, surfactant molecules will need to either be shed or recruited from the surrounding media. If the compression rate is fast there may not be sufficient time for molecular re-arrangement of the surfactant layer on the surface, making the complete dissolution of bubbles more likely. Hence it is hypothesised that if the surfactant hypothesis is correct, fewer bubbles will nucleate at high compression rates. A similar effect was observed in gelatin by Yount et al. [138]. In terms of the growth, if fewer bubbles nucleate but the total gas in the tissue remains the same, bubbles should grow to larger sizes. Hence the hypothesis is that at faster compression rates, fewer bubbles will form and they will grow to larger sizes.

6.4.1 Experimental sensitivity methods

The experimental dive profiles used are described in Table 6.2. In each case a hydrogel was transferred to the pressure chamber between 12-24 hours after it had been made by the method described previously (see chapter 2). Within each gel 1mg/ml of mesoporous carbon nanoparticles (Sigma) was also seeded. This was done to ensure bubble nucleation within each gel, (this will be discussed further in chapter 7). Once transferred to the pressure chamber, gels were covered with cell culture media (0.3ml),

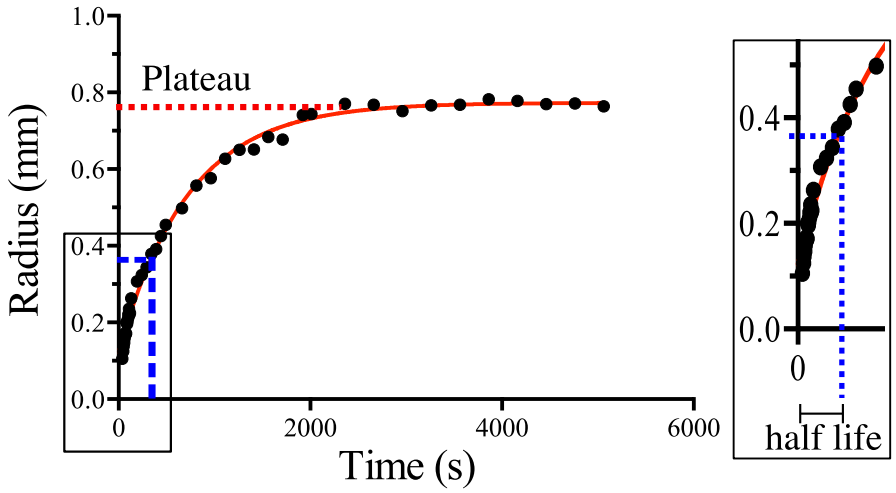

Figure 6.11: Showing an example of the non-linear regression analysis with the half-life and plateau values marked

which just covered the surface of the gel. From the start of decompression onwards images were taken of the centre of each gel, every 5 seconds until 100 images were taken and then every 30 secs for the next 50 images, then every 5 mins for a final 12 images, giving a total time of approx. 1.5hrs post decompression. The radial trajectories of the bubbles were extracted with the image analysis software described in chapter 3. The number of bubbles which nucleated within the entire gel was also recorded. Three gels per pressure profile were analysed. To compare the dive parameters each individual bubble time course was analysed via non-linear regression. The regression model chosen was a single-phase exponential decay equation described by:

$$R = (R_0 - Plateau)e^{(-t\ln(2)/\tau)} + Plateau, \tag{6.1}$$

where R is the bubble radius, R_0 the initial radius, $Plateau$ is the asymptotic value of the radius and τ is the half life of the bubble. The fit was constrained to ensure the plateau value was greater than the initial radius. A robust regression method was used as the residuals were not normally distributed even after a log transform. From the regression analysis the values of the plateau and half life were used to characterise each bubble trajectory and to compare between samples. Figure 6.11 shows an example of the non-linear regression analysis with the half life and plateau value marked.

As the bubbles will tend to dissolve with time, it may be thought that the use of a

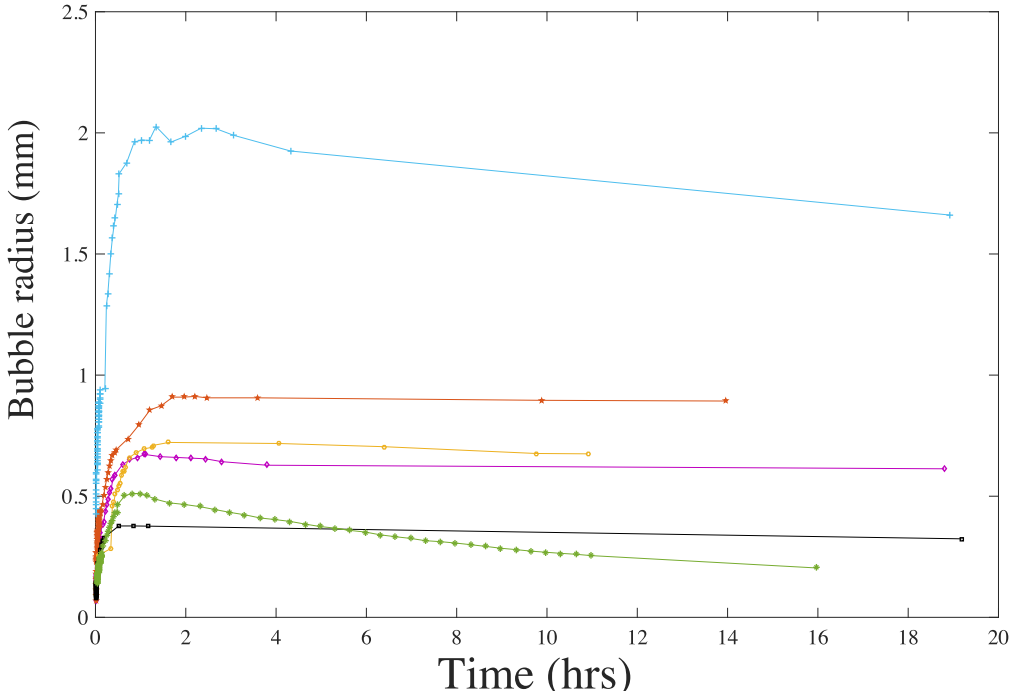

Figure 6.12: Radial trajectories over long time scales post decompression, each line is a bubble radius trajectory from a separate experiment conducted under the same conditions.

single-phase exponential decay, is not a suitable fit for the radial trajectories. An alternative approach which extracted the maximum size and the time at which this occurred, was also originally analysed but found to be inappropriate. The method was vulnerable to small local maxima which resulted from bubble-bubble contact and fluctuations in the extracted radius due to variations in light levels. In addition a study into the long term dissolution behaviour, where bubbles were followed for up to 19hrs revealed that in almost all cases bubbles were approximately stable in size even after this time, (see Figure 6.12). It was therefore decided that over 1.5hr post decompression, this fit represented the most robust approach to comparing bubble time courses.

6.5 Sensitivity results

Figure 6.13 shows the mean plateau radius and half life of the bubble as well as the number of bubbles which nucleated in each gel. Linear regression of these means reveals a significant positive linear trend between the time at depth and the plateau radius of the bubbles, as well as the number of nucleated bubbles. Also there is a significant positive correlation between the rate of compression and the plateau radius

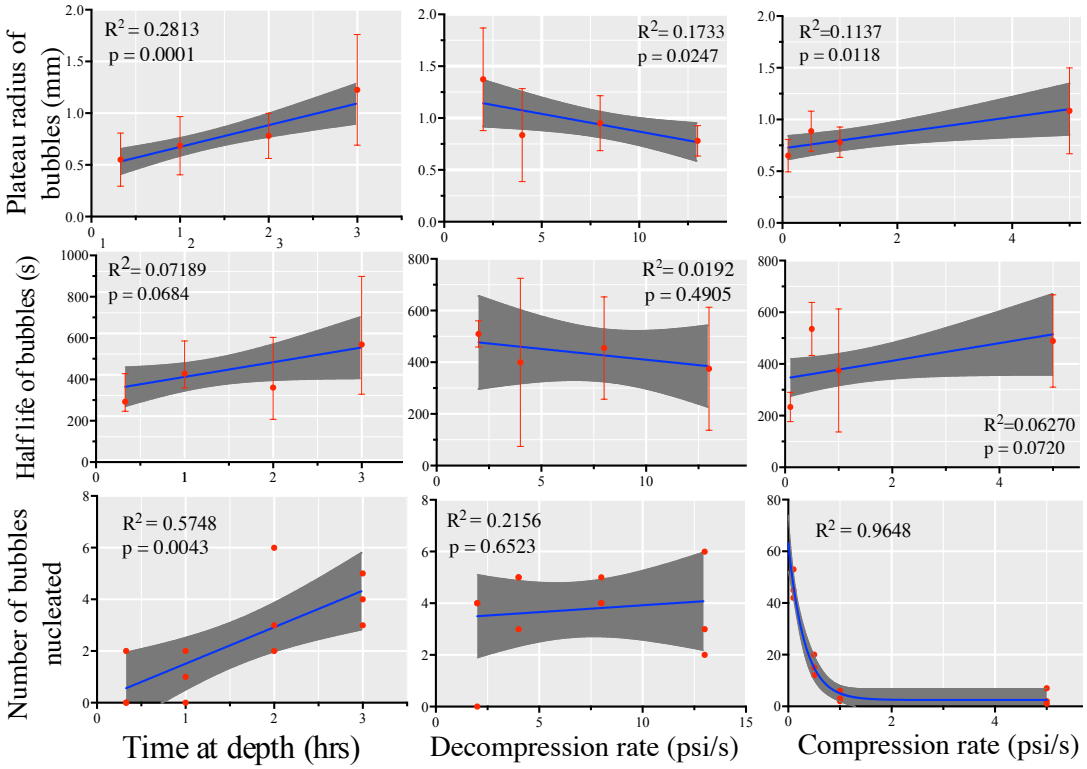

Figure 6.13: Showing the plateau values and half lives of the bubbles for each experimental condition, also the number of bubbles nucleated within in each gel, where error bars are shown the mean an 95% confidence interval is plotted. Linear regression was performed for all samples other than the number of bubbles with variation in compression rate for which non-linear regression was used. The regression R^2 values are reported for each condition and for each dive profile N=3 gels.

of the bubbles. Interestingly there is a significant **negative** correlation between the rate of decompression and the plateau radius. There is a non-linear relation between the number of bubbles which nucleate and the rate of compression. Another interesting result is the lack of significant correlation between the bubble half times and any dive parameters. These results are summarised in Table 6.3.

	Plateau radius	**Half life**	**Nucleation**
Time at depth	+ **	+	+ **
Compression rate	+ **	+	Non linear
Decompression rate	- **	-	-

Table 6.3: Summary of results of experimental sensitivity analysis, (+/-) indicates the sign of the gradient (and hence the nature of the correlation) and ** indicates statistical significance.

The apparent lack of effect that any dive parameters have on bubble half lives is an

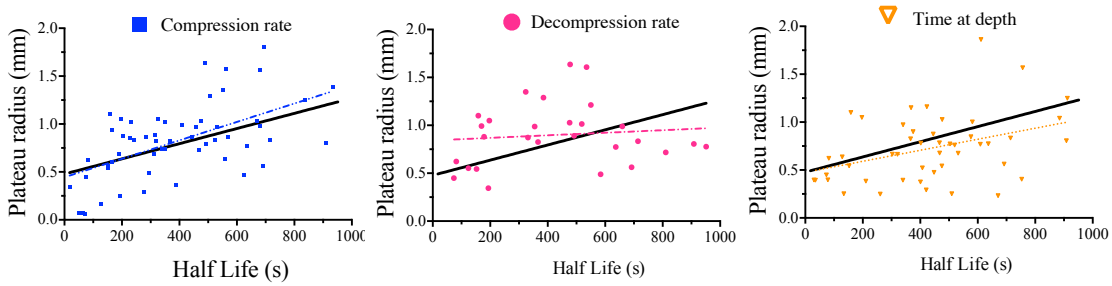

Figure 6.14: Showing a plot of the half live against the plateau radius bubbles under the various conditions. In each case the dotted line indicates the linear regression for the individual bubbles whilst the solid black line indicates the regression line for all data. A statistically significant slope is found for the decompression rate plot as compared to the total data line.

interesting result. To understand this better, the relationship between half life, plateau value and initial bubble growth rate (the amount of growth within the first half life) should be considered. Analysis of the correlation between the half lives and plateau radius shows that for the compression rate and the time at depth experiments, there is significant positive correlation, (r= 0.3857,p = 0.0074) and (r= 0.5739, $p < 0.0001$) respectively however for decompression rate variation there is no correlation (see Figure 6.14). The change in the nature of the correlation in this case, indicates that decompression rate may be affecting bubble growth in a more complex manner than previously considered. It was hypothesised that the change in correlation reflected a change in initial growth rate; Figure 6.15 shows this change in initial growth rate with rate of decompression. However it can be seen no significant trend can is detected in the initial growth rate. For the correlated cases from (Figure 6.14) radial trajectories based on this correlation are plotted for three bubbles with half lives that span the experimental data range (Figure 6.16). This shows that larger bubbles appear to be growing more slowly than smaller bubbles. Although this seems slightly counterintuitive the relationship is also shown in the computational simulation and will be discussed in the next section.

The trend in the plateau radii with variation of dive parameters supports the original hypotheses in the cases of time at depth and compression rate. For the time at depth experiment, plateau radius increases with increasing time at depth. Increased time at depth leads to a larger amount of dissolved gas within the gels and hence more gas can diffuse into the bubbles leading to larger plateau radii. For compression rate, there is a decrease in bubble plateau radius with decreasing compression rate, again as hypoth-

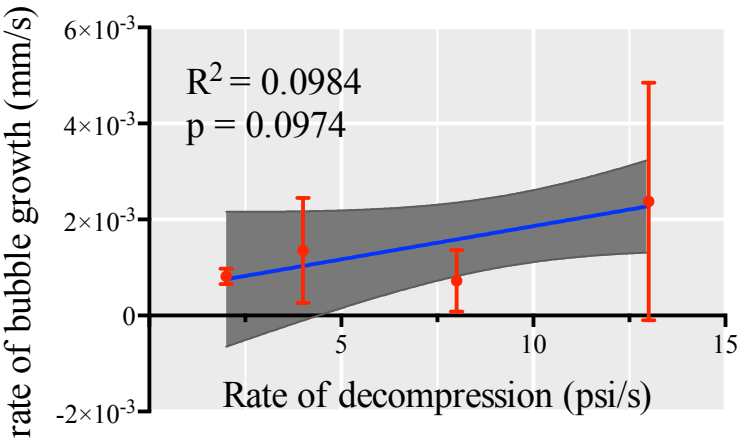

Figure 6.15: Showing the relationship between the initial rate of bubble growth and the rate of decompression - no significant correlation found p=0.0974.

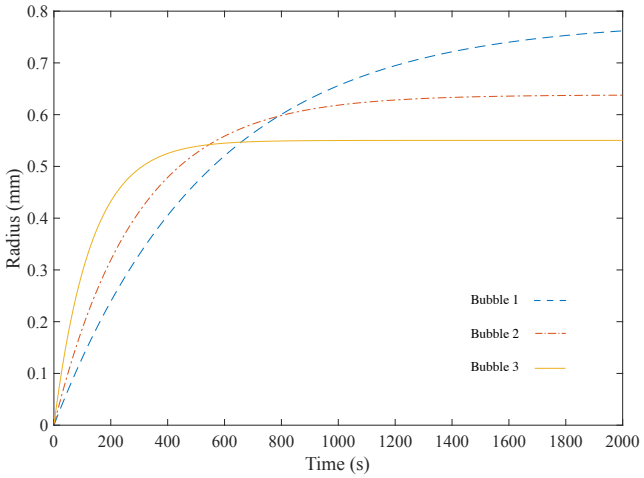

Figure 6.16: Showing the radial trajectories where tau is linearly dependent on plateau with the relation found from the linear regression of the experimental data

esised. The clear change in bubble nucleation further supports the hypothesis that the trend is caused by the competition for dissolved gas. This is a similar effect to that seen in the models of van Liew and Burkard as well as Chappell's implementation of the Gerth and Srinivasan model [158, 178, 175], where increased bubble density led to the arrest in bubble growth due to depletion of the surrounding dissolved gas. Interestingly, both Chappell and van Liew and Burkardt's models predict that the affect of competition would be seen at lower bubble densities for longer half life tissues. van Liew and Burkardt's model predicts competition to arise at 10^2 bubbles/ml for tissue half times of 360 mins; Chappell's model predicted competition at 10 bubbles/ml for tissue half times of 100 mins [158, 178]. A decrease in maximum radii with increasing

bubble number was also shown in the 2D model of O'Brien [220], where simulations used either 5 or 10 bubbles in a 2.5 m^2 tissue region. For the collagen gels, bubble competition appears to be apparent between $10^1 - 10^2$ bubbles/ml. This accords well with van Liew and Burkardt's predictions as collagen gels, having no perfusion, would be more representative of a long half life tissue. The trend for decreasing bubble radius with increasing decompression rate is somewhat harder to understand. It is very surprising to see that for slower decompression rates bubbles appear to have a larger plateau radius. Given that there is no trend in the number of bubbles which nucleate with decompression rate, this radius trend cannot be explained by similar arguments to the compression rate result. One possibility is that there is a bubble growth rate dependant resistance, such as viscosity. If bubbles with faster initial growth rates experienced more viscous resistance, this could lead to smaller final radii than their slower growing counterparts. There is little other experimental literature in the DCS field to which these results can be easily compared, the field of volcanic melts and polymer foaming again provide some experimental comparisons [303, 304, 305, 306, 307]. In the majority of cases these researchers are interested only in the initial bubble growth or foaming density and hence bubble time courses are not recorded for longer than a few minutes. In addition many of these works do not control the decompression rate only the maximum pressure and the length of time left at this pressure (typically several days to allow equilibrium to be established). The papers of Lensky et al. and Gardner et al. [305, 306] did control the decompression rate and investigated its effect on bubble growth in molten obsidean. It was shown that at faster decompression rates the bubble growth was faster, however bubbles were only recorded for 8mins and therefore a plateau radius was not seen. An interesting result from these works was that dimensionless analysis of the computational model revealed viscous resistance to be unimportant, even at the fastest decompression rate of 1MPa/s (145psi/s) from this analysis however indicated that the viscous resistance in such experiments was not significant. Similar experiments by Ohshima et al. showed increased bubble growth rate over the initial 2 seconds growth as decompression rate was increased [307]. Another possible explanation for the decompression trend in plateau radius, is that it is caused by the nucleation mechanism in these gels. It would be ideal to discover if the trend persists in denser gels and with more biologically relevant nucleating agents.

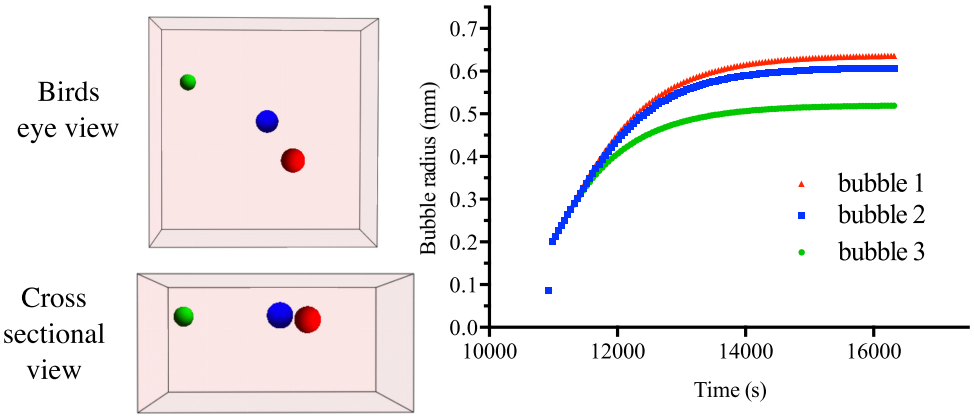

Figure 6.17: Showing the variation in radial profile caused by the position of the bubble within the gel. Left shows the birds eye view and cross section of the simulated bubbles in the left-hand panel. The size of the bubbles in the left-had panel is the final plateau radius.

The final point to note on the experimental results are that all linear regression R^2 values are relatively low. This suggests that the dive parameters are able to explain only a small proportion of the variation in the bubble dynamics. In order to explain the additional variation other variables must be important. One such variable which has not been discussed till now is the position of the bubble within the gel. With the current experimental system there is no accurate way of determining the bubble position in the gel in 3D. Although this can be done in the x-y plane relatively simply, the z calibration of the microscope stage used did not have sufficient accuracy to enable this to be determined. To investigate the affect of bubble position within the gel, multibubble simulations were done. Figure 6.17 shows a diagram of the placement of the bubbles within the gel and the corresponding radial paths. As can be seen bubble 3 (green) is the closest bubble to the tissue edge and has the smallest plateau radius. Bubbles 2 and 3 are further towards the middle of the gel and grow to similar and larger sizes. This variation is due to the diffusion of gas out of the gel post decompression-: Towards the middle of the gel gas change occurs more slowly; this means that areas towards the middle of the gel will both saturate and desaturate with dissolved gas far more slowly. Bubbles which form towards the middle of the gel will therefore have a longer exposure to high gas concentrations and would be expected to grow for longer time, resulting in a larger plateau radius.

Some evidence of this effect exists in the work or Yount et al. [2]. During the

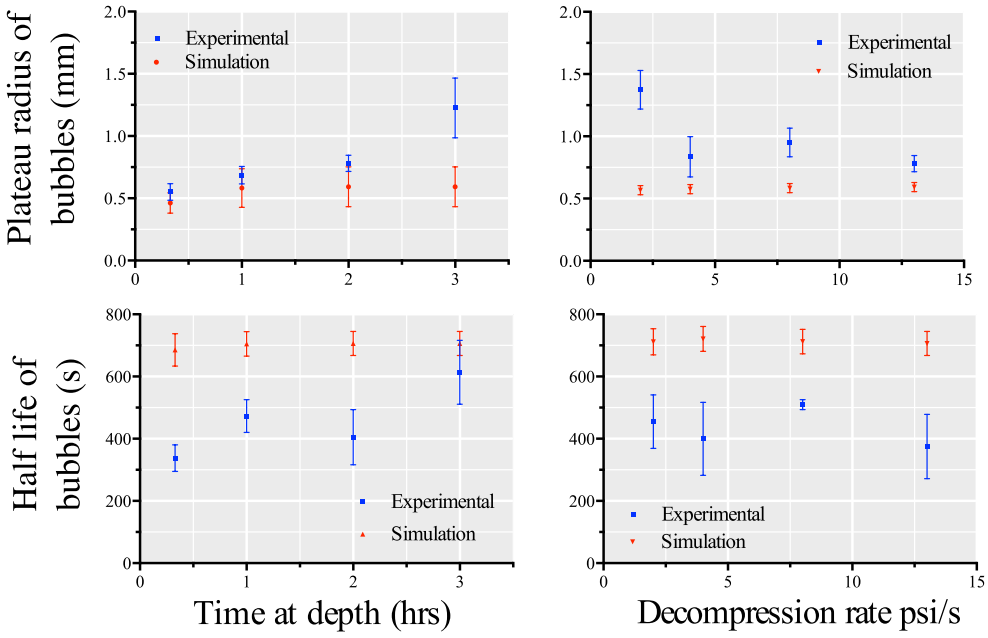

Figure 6.18: Showing a comparison of the simulated sensitivity analysis and the experimental. Mean and standard deviation shown

investigations of nucleation in gelatin by Yount et al. images of the gels were taken from a side on view. In these images it was noted that the top 1mm of the gelatin contained bubbles which were far smaller and more numerous than the remaining 3mm. The effect was apparent enough for Yount et al. to exclude this top 1 mm of the gel from their quantification of bubble numbers. The position effect can also explain the low R^2 values; if larger bubbles are closer to the centre of the gel their rate of growth may be slower due to a lower initial gas concentration in the surrounding gel, however the growth continues for longer as the gel centre does not desaturate as quickly as the edges. The position of the bubbles within the gels and any trends in bubble position with dive parameter changes would therefore be important to account for future simulations.

Simulations of a 3-bubble gel for variations in the dive parameters were also done and the same non-linear regression analysis performed. The diffusion optimisation values were used, the grid was set to reflect the actual hydrogel size and the initial bubble radii were chosen to be 0.008mm which was the smallest experimentally measured radius. The results are shown in Figure 6.18. In the case of the time at depth the plateau radius of the simulated dives follows a similar trend (increasing radius with increasing time at depth) but the values of plateau radius are somewhat below those of the experimental data and have a smaller variance. This could be explained by the chosen

spatial distribution of the bubbles. In the simulations, the bubble distribution was initially chosen randomly but then maintained throughout. However, if the distribution of bubbles in the experimental system was not randomly distributed and varied systematically with time at depth this would create additional variation and would be expected to cause an increase in the plateau radius with increasing time. For the decompression rate the simulation does not follow the same trend as the experimental values. This implies that the mechanism which causes the decrease in bubble plateau radius with increasing decompression rate is something which is not modelled. This supports the possibility that visco or poroelasticity may play a role in the bubble growth as it would explain the experimental trend and is not currently modelled. Finally the half lives of the modelled data in both cases are slightly higher than those of the experimental data and are positively correlated with the plateau radius similarly to the experimental data for time at depth.

Another potential source of variance, which has not been discussed, is the initial bubble radius. In the gels the initial bubble radius will depend on the nature and distribution of micronuclei. Variation in the initial radius of the simulated data caused relatively large variation in the plateau radius as shown in Figure 6.19. Parameterising the initial radius for the model is difficult as has been discussed. One possibility is to use an exponential distribution of micronuclei radii as done in the VPM model and used by Hugon et al. [95, 176], however this type of approach still requires parameters regarding the slope and magnitude of the distribution. In order to parameterise this part of the model a more complete understanding of micronuclei is needed. The nature of these nuclei in collagen gels will be more fully explored in the following chapter.

6.6 Summary of Dive sensitivity

The investigation into the effects dive parameters have on bubble dynamics has revealed that, of the parameters investigated here, the time at depth is the most critical parameter for explaining the variation in bubble plateau radius. The compression rate is thought to affect plateau radius by altering the nucleating density and thus changing the competition for dissolved gas. Increases in the decompression rate show a decrease in the bubble plateau radius. This is counter intuitive and is also not seen in corresponding simulations of the profile. It is thought that this decrease in plateau radius may be due

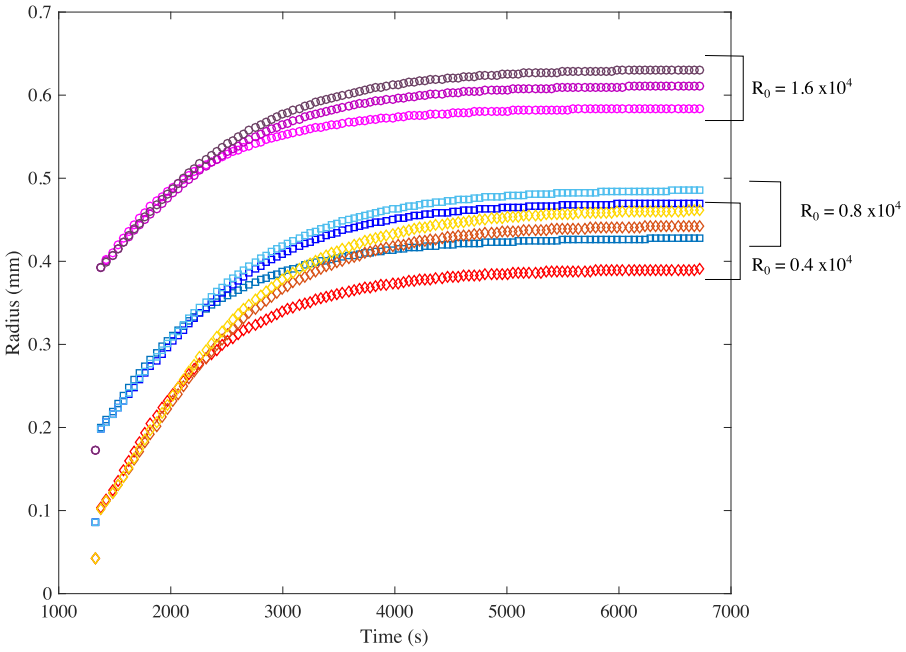

Figure 6.19: Showing the effect that initial radius has on the bubble growth. It can be seen that bubbles of larger initial radii, grow to larger plateau sizes. This effect appears non-linear with initial radius.

to viscous resistance of the gel to bubble growth which is not modelled in the simulations, or to an aspect of the nucleation mechanism. That the initial bubble growth rates are affected by varying the decompression may be interpreted from the correlations of the plateau radius and the bubble half life. For the cases where there is a positive correlation between the plateau and half life, this suggests that larger bubbles have slower growth rates. This may also be explained by understanding of how the position of a bubble within the gel alters bubble dynamics. Bubbles near the gel edge grow quickly as the concentration of gas in the surrounding tissue is high, but the desaturation of such areas also happens more quickly and therefore such bubbles stop growing sooner ending up at smaller plateau radii. For the case where there is no correlation, between half life and plateau radius, as found for the decompression rate experiments, there is no clear relation between the plateau radius and the initial growth rate as this depends both on the half life and the plateau values.

Another important feature of the experimental results was the large variance in results not explained by the dive parameters. By using model simulations the probable cause of the variation can be understood to be both the locations at which bubbles

nucleate within the gel and the initial radius from which bubbles grow. Both of these parameters will depend crucially on how nucleation is modelled. In addition, the competition for dissolved gas is also dependent on the number of bubbles and therefore the nucleation model. Overall the main result of this investigation has been to shown that although dive parameters do affect bubble dynamics, it is significant that bubble nucleation be modelled realistically as this governs several parameters which have a great impact on the subsequent bubble dynamics, independent of the dive parameters.

6.7 Bubble-Bubble interaction

The final feature of bubble dynamics that is investigated in this chapter is bubble-bubble interactions. These may be in the form of diffusion coarsening also known as Ostwald ripening or direct bubble-bubble contact which may result in coalescence. For many processes such as polymer foaming or volcanic melt dynamics, coarsening and bubble coalescence may have a significant impact on the overall bubble population dynamics [308].

Ostwald's ripening, so called as it was first described by Ostwald [309], is a process by which larger bubbles will grow at the expense of smaller ones. The mechanism is fairly simple, bubbles which are smaller have a higher pressure due to surface tension. If a large and small bubble are close together the pressure difference between the two will tend cause gas to diffuse from the smaller to the larger bubble, decreasing the size of the smaller bubble and increasing the pressure difference between the bubbles. Coalescence is a more complex process which can be described in three stages [310].

1. Two bubbles collide resulting in a liquid film between the two.

2. The thickness of the film gradually decreases as liquid drains from the film, this drainage may be governed by several mechanisms including capillary forces or further bubble growth.

3. The film reaches a critical thickness and ruptures, resulting in coalescence.

The likelihood that a bubble collision results in coalescence was described by Chesters and Hofman in terms of a balance between the film drainage time and the energy of deformation [311]. As two bubbles collide they will begin to deform. This deformation

increases the surface energy of the bubbles whilst decreasing the kinetic energy of the two bubbles. Eventually this energy transfer will lead to bubbles bouncing apart; if the film has not reached a critical thickness before this occurs then bubbles will not coalesce. The transfer between the kinetic and surface energy can be described by the Weber number (*We*)

$$We = \rho v^2 R/\gamma \tag{6.2}$$

where ρ and γ are the density and surface tension of the liquid, v is the approach velocity of the two bubbles and R is the equivalent bubble radius (the radius the bubble would be if it were spherical). Higher Weber numbers result in greater deformation upon collision. The change in thickness of the film with time when capillary forces are the driving mechanism has been modelled by Huber et al. [312] by the relation

$$t_c = C_c \ln\left(\frac{\delta_0}{\delta_{crit}}\right)\frac{\eta R}{\gamma} \tag{6.3}$$

where t_c is the critical time, C_c is a constant $\delta_0 and \delta_{crit}$ are the initial and critical film thicknesses respectively and η is the viscosity of the film liquid.

In order to have a basic estimate for the expected coalescence likelihood of bubbles in collagen gels, estimates of t_c using the ratio δ_0/δ_{crit} and the C_c constant value found by Huber et al. [312], as well as the viscosity of collagen gels, taken from Knapp et al. (6.6×10^4 Pa/s) [279], can be made. With these approximations the critical time is of the order of 10 hrs for a bubble of 0.5 mm radius. This very long drainage time is for capillary drainage only and will be reduced by the additional film thinning caused by bubble growth. Given that the pressure exerted by bubble growth will vary depending on what stage in their growth bubbles collide, it is not clear how applicable this approximation of the critical time is to our experimental system. Experimental results for bubble coalescence in collagen gels could not be found in a literature search, however experimental results of Nuguyen et al. [310], describe the film drainage time for bubbles rising to the surface of PDMS (Polydimethylsiloxane) and silica liquids. This work was the closest equivalent to our experimental system that was found. The PDMS has a viscosity lower than collagen gel by approx. ten fold and surface tension of approx. 0.02 N/m. In these experiments critical time was decreased as film thinning occurred due to both capillary drainage and gravitational forces. The drainage

times were on the order of 10^4 secs ($\sim$2.7hrs). Given this available data we may estimate that coalescence in the collagen gels would predominantly occur over a time scale of hours and would become less likely as growth slowed. This time scale and prevalence of coalescence was investigated by tracking the number of bubble-bubble interface which formed and the proportion that resulted in coalescence. Figure 6.20 shows the proportion of interfaces which resulted in coalescence over 1.5hrs, with accompanying images of an example where coalescence does occur. As can be seen the proportion of collisions which result in coalesce is very low and the case where it does occurs in the images, the top bubble was restricted in its movement by other bubbles. If the bubble density of a sample were increased the coalescence efficiency would be expected to increase also, as bubbles would be more likely to collide at earlier stages of growth when their velocities are higher. Once again having a better understanding of the bubble density and spatial distribution is key to understanding whether coalescence would be an important feature of bubble dynamics *in vivo*.

Modelling of bubble coalescence within the DCS literature is rare; the multi-bubble model O'Brien [220] is one of the few which incorporates a simple coalescence feature. This model is a two-dimensional finite difference simulation of a small diffusion controlled tissue area. Coalescence was modelled by assuming that if contact between two bubbles occurred coalescence was instantaneous and resulted in a single bubble with a volume equal to the sum of the two coalesced bubbles volumes. As seen from the estimates above, this model seems unlikely to be an accurate picture of coalescence and, indeed, when it was incorporated into the 3-dimensional model in this work, all instances of coalescence resulted in the new larger bubble having a radii too large for the simulated tissue grid. However, the introduction of more complex models of coalescence for our situation [312, 258, 313] comes with significant computational cost, and it should therefore be clear whether coalescence is an important dynamic to capture.

6.8 Conclusion

This chapter has consisted of a validation of the computational model described in chapters 4 and 5 through variation of the material properties and dive parameters of the experimental system. It has been shown that the computational model was only able

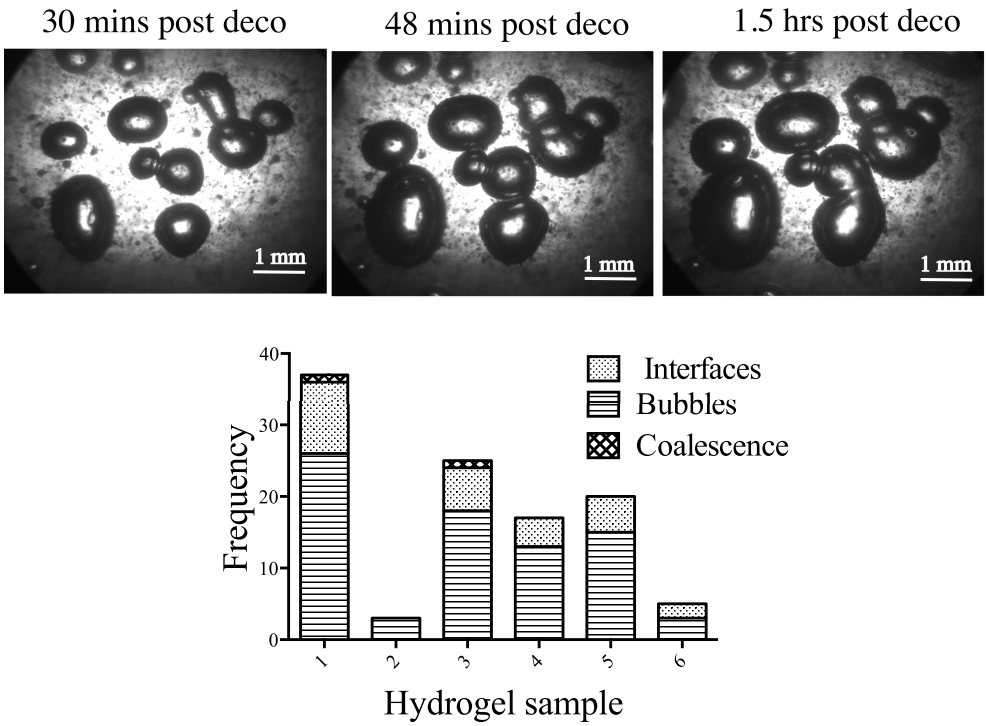

Figure 6.20: Showing the proportion of bubble-bubble contacts which result in coalescence

to satisfactorily model experimental data when a diffusion barrier at the bubble surface with bubble surface area dependency was introduced. It is thought that this diffusion barrier may be due to surfactants from the collagen solution adhering to the bubble surface. It was also seen that hydrogels were better modelled than denser gels, this may either be due to the anisotropy of the denser gels or potentially due to the importance of factors such as poroelasticity or viscoelasticity. In future work it would be important to clarify whether viscoelasticy/poroelasticity of the gels is the cause of these data, as increasing collagen density makes the gels more tissue like. The sensitivity of bubble dynamics to dive parameters has revealed several interesting results. In particular the unexpected trend of a decrease in bubble plateau radius with increasing decompression rate. This is both unintuitive and also not observed in simulations. The reason for this trend is unclear but potentially again viscosity of the gel may be restricting bubble growth during fast decompression. The computational model was also used to demonstrate how bubble position within the gels and initial radius are important parameters in bubble dynamics. Both of these parameters would be the end point of a nucleation model and therefore highlight the importance of characterising the nature and behaviour of bubble micronuclei. Finally bubble-bubble interactions were observed in the colla-

gen gels over 1.5 hrs, and the coalescence efficiency was shown to be low; this is to be expected when an estimate of the film drainage time is considered. Again the importance of bubble-bubble interactions will depend on the density of bubbles in the gel. The key conclusion that can therefore be drawn from this chapter is the importance of understanding nucleation before embarking on any further development of the growth portion of the computational model.

Chapter 7

Nucleation chapter

7.1 Introduction

Chapter 6 established bubble density as an important parameter in subsequent bubble dynamics. As bubble density is dependent on the distribution and nature of nucleation sites, this chapter focuses on the mechanisms of nucleation and nature of micronuclei in collagen hydrogels. Theoretical mechanisms of nucleation and the literature regarding these mechanisms *in vivo* and *in vitro* are outlined, followed by a comparison of modelling approaches from the DCS and polymer foaming fields. The experimental work presented in this chapter consists of a material and dive parameter investigation into the nature of nucleation sites in collagen hydrogels. Particular attention is given to biologically plausible possible nucleation sites, including bone, cell surfaces and extracellular matrix proteins. This is followed by an exploration of the impact dive parameters have on the most potent biological nucleating agent, polymeric collagen.

7.1.1 Nucleation mechanisms

Nucleation is one of the most poorly understood areas of bubble dynamics. This is because nucleation is inherently a stochastic process which begins at a molecular length scale and quickly transitions to the nano or micro scale. As such experimental investigations are fraught with difficulties and mathematical models must content with the difficulties surrounding multi-scale dynamics. As discussed in the introduction there are three types of nucleation, two of which are governed by classical nucleation theory (CNT). This chapter focuses primarily on heterogenous nucleation. Classical heterogeneous nucleation, is nucleation mediated by a surface. The presence of a surface

reduces the Gibbs surface energy barrier thus lowering the total energy required for nucleation to occur. Within the DCS field the definition of heterogeneous nucleation has been somewhat expanded to include nucleation from pre-existing stable gas nuclei [16]. This broader definition of heterogeneous nucleation is discussed in a review by Jones et al. in which heterogenous nucleation is further subdivided into three types: Classical heterogeneous nucleation is defined by Jone et al. as type II (type I being homogeneous), nucleation from micronuclei stabilised below critical radius is type III, and type IV is the case where micronuclei are stabilised above the critical radius [314]. Only in type IV is there no energy barrier to nucleation.

There have been many experiments both *in vitro* and *in vivo*, over the previous decades which have shown that a short exposure to very high pressure prior to a 'normal' dive profile, decreases the number of bubbles produced and incidence of DCS [16, 315, 316, 317]. These experiments support the hypothesis that the bubbles which cause DCS, nucleate from stabilised micronuclei that can be crushed by a short high pressure exposure. As such, much research effort has been directed at elucidating the nature of the stabilisation mechanism.

Surface active molecules which adsorb onto the bubble surface from either the blood or extracellular matrix are thought to be one possible stabilisation mechanism. Such 'skins' confer mechanical stability to the bubble, may reduce the permeability of the bubble surface and lower the surface tension. Fox and Herzfeld considered a skin of organic molecules that were impermeable until a threshold pressure 'cracked' the skin at which point diffusion could once again occur [318]. These skins were not widely accepted however as experiments using cyclic pressure conflicted with theoretical predictions [18, 319]. Yount et al. [94], considered skins of variable permeability. In this theory skins were formed of surface active molecules which diffused between the bubble surface and a reservoir surrounding the bubble. Normally such skins were permeable however at high pressures >8 atm these skins became impermeable. The actual nature of the surface active molecules was never definitively demonstrated, and the gelatin experiments which provided the foundations of the theory were plagued by significant variability [142]. In an attempt to resolve this variability and identify the surface active molecule in question, D'Arrigo conducted further investigations into the source of the gelatin variability [143]. D'Arrigo proposed that the source of the vari-

ability was the gelatin itself and conducted a study with a more chemically inert gel, agarose [143]. In a series of experiments, D'Arrigo, comparing commercially available agarose sources of varying purity, found that purer forms of agarose gave more consistent results, (purity was described as lower sulphate and ash [143]). No differences in bubble nucleation were reported for different gases, for changes in the pH or with the addition if UO_2^+ (which would react with phospholipids). From these collective results D'Arrigo concluded that nonionic surfactants were responsible for the stabilising layer [146]. This work demonstrates some of the experimental problems and also highlights the difficuties in using *in vitro* systems for such work. As the *in vitro* system is simplified further and further to attain a controllable system, the biological relevance of the system diminishes. In the end it is difficult to relate D'Arrigo's conclusions back to nucleation in a human body following a SCUBA dive. However, without such simplification data is often conflicting and irreproducible, *in vivo* experiments with the aim of identifying possible skin surfactants have thus far been inconclusive [320, 12, 18].

The second method of stabilisation proposed in the literature, is by hydrophobic crevices. If gas is located within a hydrophobic cavity, it will adopt a negative radius of curvature due to the hydrophobicity of the surface and the angle of incline. A negative radius of curvature will mean that the Laplace pressure in the bubble is lower than that of the dissolved gas within the bulk liquid and thus the bubble will be stabilised against dissolution. Crevice nucleation was first proposed by Harvey based on observations of bubble formation from glass surfaces in supersaturated water [316]. A mathematical model of crevice nucleation was proposed by Harvey and later developed by Atchley and Prosperetti and Tikuisus [316, 321, 322]. Most recently this has been further extended by the works of Chappell and Payne [180, 179, 181, 177]. In these works a model was developed in which gas micronuceli within crevices grew as a result of a decompression. Bubbles initially grew within the crevice, advancing up the walls, and then external to the crevice, before ultimately detaching from the surface. Gas diffusion through the crevice walls from the tissue was included in this model and a joint tissue crevice bubble model was described. Analysis of the model revealed that the geometry of the cavity was important for modelling the initial bubble growth up the walls of the crevice, but was less important once the bubble emerged into the blood stream. In addition it was found that the formation of tissue bubbles resulted in the decreased

production of crevice bubbles as the tissue bubbles stored the inert gas, and increased gas wash out times. One of the difficulties highlighted in these works is the lack of information regarding the crevice sites *in vivo*. Without their identification both the geometry and likely density cannot be known. Several hypotheses exist as to the source of these cavities, with the majority focusing on areas of the body where lipids accumulate. Hills proposed that lamellar bodies composed of phospholipids in the spinal cord could provide nucleation sites [29]. In addition Hills identified areas of hydrophobicity in the lumen of certain ovine blood vessels thought to be due, again to phospholipid surfactants. In the same work an oligolamellar lining was also found bridging the tight cell-cell junctions of endothelial cells in the cerebral vasculature [323], which had previously been suggested as a nucleation source by Tikuisus [322]. More recently Arieli et al. have investigated bubble formation from large ovine vessels [121, 122]. 'Active spots' were described by the group as points on the vessels from which bubbles repeatedly nucleate, however the hydrophobic/hydrophilic nature of such spots was not detailed. Caveolae, small invaginations on the surface of most mammalian cells, which contain a high proportion of sphingolipids and phospholipids have most recently been suggested as a candidate nucleation site [324]. Caveolae are found on the surface of most cells but are not uniformly distributed in the body, with greater numbers identified in endothelial and certain epithelial cells, as well as adipocytes [325, 72, 326].

Observation of bubble density *in vivo* was discussed in chapter 2. The use of these data to understand or parameterise models of nucleation is somewhat frustrated by the variations in the type of bubbles being measured, and the lack of systematic comparison of tissue type and bubble number. Some experiments which provide such comparisons are available. The works of Gersh et al. are some of the most useful in understanding systematic differences in bubble formation between various tissue. Gersh at al. reported a comparative study into the distribution of bubbles for various tissues in a guinea pig model [327, 32]. Raw bubble numbers and the bubble volume/tissue volume were reported. These results found that the numbers of bubbles in fatty tissues including, adipose fat, myelin sheaths, adrenal gland and bone marrow was much higher than that of skeletal muscle or liver. Bubble numbers ranged from 116 bubbles (146 bubble volume/ tissue volume) to zero for leaner animals. A low number of extravascular bubbles was also found in tendons. Gersh et al. noted that bubbles were predominantly lo-

cated in regions of tissue dominated by fat cells, and bubbles were often noted within fat cells. The findings of Gersh et al. support the hypothesis that the distribution of bubbles within various tissues in the body is closely correlated to their fat content and the increased solubility of nitrogen this fat confers. The work of Papadopoulou et al. compared bubble nucleation from the surface of fat and muscle, finding that fat had significantly higher bubble nucleation than muscle (8.4 bubbles/cm^2 and 4.2 bubbles/cm^2 respectively) [124]. This work is particularly interesting as the tissue was not saturated with dissolved gas, only the surrounding water, therefore the increased nucleation in this instance cannot be attributed to the greater solubility of nitrogen in the fatty tissue. One theory is that the hydrophobicity of fatty tissues in addition to the increased nitrogen solubility, causes higher levels of bubble nucleation in such tissues [18]. The prawn experiments of Arieli et al. and the crustacean work of McDonough and Hemmingsen reported that bubbles were seen to preferentially form between muscle strata in the prawn and in the joints of crustaceans [126, 132]. The authors observed that tribonucleation would explain this distribution of bubbles.

7.1.2 Models of nucleation

The two main models of nucleation within the DCS literature are the crevice model of which the most recent development is that of Chappell and Payne [180] and the VPM model of Yount et al. [94]. As discussed above, the model of Chappell and Payne requires parameterisation of the crevice geometry, and, for use on a larger scale, the density of crevices also needs to be known. The VPM model, described in chapter 2, models an exponential distribution of nuclei which have a surface permeability dependent on the external pressure. The slope parameter (β) for the exponential distribution and the total number of bubbles (N_0) need to be parameterised in this model. Hugon et al. used the VPM model of nucleation with parameter values of $N_0 = 5000ml^{-1}$ and $\beta = 5 \times 10^6 m^{-1}$ [176]. These values were used to successfully predict the incidence of DCS in the COMEX database set, however it is not clear on what the parameter values were based.

Nucleation models are of particular interest in the field of polymer foaming. In the current foaming processes nucleation is initiated with a rapid pressure reduction after saturation with a gas, typically CO_2. In many instances nucleating particles are

introduced to the molten polymer to control bubble density [17]. Classical nucleation theory (CNT) is often used to predict bubble density, but it has been known to under predict bubble nucleation in the foaming process by several orders of magnitude, in cases both with and without nucleating agents [328]. Improvement in CNT predictions for cases which use nucleating agents have been made through the use of crevice models similar to that of Chappell and Payne [329, 330]. However, this type of model is still fundamentally based on CNT. Investigations into the poor predictive power of CNT show that the essential flaw in the model lies in the treatment of the gas liquid interfacial tension. As discussed in the introduction to this thesis, the interfacial tension in CNT is described by the large scale surface tension, γ, and appears in the exponent of the expression for steady state nucleation raised to a third power (1.8). In most implementations of CNT the value of this interfacial tension is set to the same value as the flat interface surface tension γ_∞. This approximation is widely known to be problematic as it is strictly only applicable where the thickness of the interface is negligible by comparison to the nucleus size [331]. Approaches to correctly approximating the interface tension largely revolve around describing a scaling function between γ_∞ and the nucleus interfacial tension. One way in which this scaling function is derived is through the use of the diffuse interface techniques, that were discussed in chapter 5 (section 5.2.3) [332, 333, 334, 331]. This method parameterises the entropy and enthalpy in the two bulk phases (liquid and gas) and results in a characteristic interface thickness and corresponding interface free energy dependent on the radius of a cluster of gas molecules [334, 331]. Applying this interfacial tension model provides far more accurate bubble density predictions for homogeneous nucleation within polymer foams [332, 333, 335]. The utility of these models lies in their depiction of the gas liquid interface at small length scales. At larger length scales the interfacial tension is closer to the γ_∞ and CNT becomes a better predictor of bubble density. Thus, the need to apply a diffuse interface technique is largely dependent on the size of the micronuclei in question. For DCS the micronuclei size distribution *in vivo* is not known but calculation of the critical radius can provide estimates: Given a decompression from 33fsw (10m depth), minimum stable nuclei would be approx. 0.8 μm this decreases with increased depth [336]. Stable nano-bubbles of 100nm have been reported by Arieli et al. in water [337], as have 1 micron bubbles in gelatin by Yount et al. [338]. The theroetical work of Gold-

man regarding the formulation of the Gibbs free energy supports this. The calculations in this work suggest nuclei would be on the order of $\approx 5 \times 10^3$ molecules for an N_2 in H_2O system [339]. At these sizes the need for diffuse interface techniques or similar methods less crucial for predicting *in vivo* bubble nucleation. However, these models are still of interest as they aid in numerical implementations of nucleation models and inform the theoretical understanding of gas-liquid interfaces.

Before developing DCS models of nucleation further, a better understanding of the distribution of nucleation sites *in vivo* and the nature of the stabilisation mechanism must be attained. We argue that nucleation in collagen hydrogels provides an adequately biomimetic model to achieve this aim. Collagen hydrogels are more biomimetic in their composition than either water or gelatin and have the advantage of being able to support cellular populations. As current nucleation theory is largely based on observations in water made by Harvey et al. [316], or gelatin by Yount et al. [338]; collagen hydrogels represent a progression in this research.

7.2 Overview

To the best of the author's knowledge no previous experimental work investigating nucleation in collagen hydrogels exists, therefore this work was highly exploratory in its initial stages. Initial decompressions of the monomeric type I collagen hydrogels or gelatin were unable to produce bubble nucleation, even under the most provocative decompression profiles that could be applied. These early results were unexpected in light of the gelatin work conducted by Yount et al. [95]. In order to conduct systematic investigations into bubble growth such as those discussed in Chapter 6, establishing control and reliability of bubble nucleation was essential. A trial and error approach was adopted in a preliminary study which aimed to produced bubbles within the gels through the addition of dopants. A range of dopants were chosen, some of which are used to commercially control foaming processes (carbon black) and others that were deemed possible *in vivo* nucleation sites based upon the literature. The results of these experiments are discussed in section 7.5. The wide range of substances tested in this trial precluded high n numbers for any single dopant. Dopants that were deemed of particular interest from this study were taken forward for further investigation. The commercial agents were found to be reliable nucleating agents and were used to in-

vestigate the effects of dive parameter variation (as presented in Chapter 6). Further investigation of these dopants with particular focus on possible batch variation was undertaken, as this had been identified as a potential source of error from the work of Yount et al. and D'Arrigo [144, 142]. The biological dopants were more extensively investigated given their relevance to the problem of DCS. Of the four biological dopants only one (polymeric collagen) produced a clear and striking increase in nucleation. Investigation into the lack of nucleation that appeared from both bone/mineral as well as from cellular surfaces were carried out. The preliminary cellular results were of particular interest as there is a good rational for cells providing nucleation sites, and a growing preference in the literature for this theory [59, 69]. In addition to the small preliminary study using Hacat cells, two further studies using adipose cells and human dermal fibroblasts (HDF) were conducted. The HDF results are presented in chapter 8 with additional cell-bubble interaction data. The choice of adipocytes was hypothesis driven, based on data concurrently acquired from the investigations of polymeric collagen. These data had revealed that removal of non-polar molecules via chloroform fumigation (a standard sterilisation process for monomeric collagen) reduced or entirely negated the nucleating propensity of untreated polymeric gels. Such a treatment is able to sterilise collagen because the chloroform acts as a solvent for fats which comprise cell membranes. The method is also used to estimate the fat content of certain tissues [340]. Thus, the hypothesis was formed that nucleation in the case of polymeric collagen was due to the presence of lipid from cellular debris. Adipocytes produced intracellular lipid droplets, it was therefore hypothesised that monomeric collagen gels containing adipocytes would have a nucleating propensity similar to polymeric collagen. In addition this hypothesis was supported by literature [316, 124] and from the known hydrophobic nature of lipid droplets. In a separate analysis confirmation of the presence of lipid in the polymeric collagen was attempted via Raman spectroscopy. The results of the polymeric and cell surface studies are presented in section 7.5.3.2 and 7.5.3.3 respectively. Following the dopant study, a systematic investigation of the effect dive parameters had on nucleation in polymeric collagen was conducted. The hypothesis of this study was that polymeric collagen would produce the same nucleation trends as the non-biological dopants (chapter 6). The rational for this was that nucleation in both cases was believed to be driven by the gel's supersaturation with the threshold of

nucleation for polymeric collagen being lower than that of the non-biological dopants. The data was also used to develop strategies for modelling such nucleation.

7.3 Types of dopant

Initial results of nucleation within collagen hydrogels were surprising, no bubbles could be formed within the gels even under the most aggressive of decompression profiles. In order to understand this, attempts to replicate the gelatin experiments of Yount et al. [139] were undertaken. Using bovine skin gelatin (Sigma), no decompression profiles and no variation in the concentration of gelatin was able to produce any bubble nucleation. This was again a surprising result given the work of Yount et al. [139]. It was hypothesised that the gelatin was too pure and did not contain the nonionic surfactants which D'Arrigo had identified to be the cause of the nucleation. To test this hypothesis the gelatin was doped with various impurities, these included charcoal, talc, sodium dodecyl sulphate, and glass. With the addition of any of these dopants bubble nucleation was seen. This simple preliminary study indicated that the purified collagen in the Sigma gelatin, did not contain the impurities required for heterogeneous nucleation. A more rigorous dopant study into the nucleation within the First link type I collagen using a range of both biologically relevant and synthetic dopants, was used undertaken following the gelatin findings. The selection of dopants used in the preliminary collagen study are outlined below with the rational for each choice:

1. Activated charcoal (Sigma)- This had worked well in the preliminary gelatin study and was therefore tested in the collagen hyrogels. Activating carbon usually involves heating and oxidising the carbon to increase the porosity and results in a hydrophilic surface.

2. 500nm mesoporous carbon nano particles (Sigma), were used as carbon black (a similar preparation) is used in industrial foaming processes. The particles used here are graphized and therefore hydrophobic and have a better characterised, size distribution.

3. Crushed bone - This was included as one of the plausible *in vivo* dopants. Fragments of bone are found in joint capsule due to the joint rubbing and the calcified cartilage zone has mineralised portions.

4. 200nm Hydroxyapatite nano particles (HANPs)- hydroxyapatite is the main mineral component of bone and these were used as they were considered to provide a similar surface to the bone but with a better characterised shape, surface topography and chemical composition.

5. Spontaneously immortalized human keratinocytes (HaCat) cells were used as a dopant. These cells are an epithelial cell line which grow with ease in collagen hydrogel, can form tight cell-cell junctions and have calveolae [341].

6. Plain collagen which had already been shown to have little or no nucleating propensity.

7. Polymeric collagen, this was extracted as described in the methodology, from calf tendon.

Each of these dopants was incorporated into a collagen hydrogel and decompressed to evaluate its nucleating potency. On the basis of the preliminary results, further investigations were made of the dopants physical and chemical properties.

7.4 Experimental Methods

7.4.1 Prep of powder samples

Crushed bone powder was prepared from sheep femur by initial crushing in a pestle and mortar to obtain a rough powder. This powder was then transferred to the Mikro-Dismembrator (Sartorius) where it underwent a 1 min milling process. The powder was then added to PBS at 1 mg/ml, 5 mg/ml and 10 mg/ml. Hydroxyapatite particles (200 nm) [342] were added to PBS at the same concentrations as above. Activated charcoal and 500nm mesoporous carbon nanoparticles were also added to PBS at 1 mg/ml. All PBS powder suspensions were sonicated for 15 mins to disperse powders evenly. For use in hydrogels, 0.01 ml of the powder-PBS suspension was added after the gel had been neutralised and left on ice for 1 hr. Good dispersal of the powders throughout the gels were seen in all cases.

7.4.2 Transmission electron microscopy (TEM)

Powdered samples were prepared for TEM by the dropwise addition of the powder PBS suspension to carbon film TEM grids (Agar scientific) and allowed to dry in a

fume hood. TEM images were taken using a Philips CM 12 TEM.

7.4.3 Polymeric collagen extraction

Polymeric collagen was extracted from calf tendon as per the method of Wong et al. [194]. Samples of calf tendon ($\approx$ 1 cm^3) were frozen and weighed. Each sample was placed in a pestle and mortar with a small amount of liquid nitrogen and crushed to break up the tendon, until a powder was produced. The tendon powder was then placed into 0.5 M EDTA (Gibco) (100 ml/g of tendon) and stirred overnight at 4°C. This process destabilises the cross-links. The solution was then centrifuged at 200 rmp for 2 mins and the supernatant removed. The 0.5 M EDTA was replaced and the mixture stirred for 4 hrs at 4°C. The solution was washed with distilled water twice. Acetic acid 0.5 M (100 ml/g of tendon) was then added to expand the collagen. This was stirred overnight at 4°C. To purify the polymeric collagen, 0.1 ml of MEM per 1 ml of solution was added to the acetic acid collagen mix, and 1M NaOH used to neutralise the mixture whilst simultaneously stirring with a cold glass or metal rod. The unidirectional shearing created by the stirring, caused polymeric collagen to accumulate on the rod. The polymeric collagen was then transferred to fresh acetic acid (0.5 M) and stirred overnight at 4°C. The purification process was repeated twice. Finally to assess the polymeric collagen concentration a wet weight dry weight method was used as described in [197]. Briefly this involves weighing a sample of the final collagen acetic acid solution, then freezing and freeze drying the sample before re-weighing. Once the sample has been freeze dried the vast majority of the remaining solid portion of the sample is collagen. This polymeric collagen solution is then blended with the rat tail monomeric collagen (First link), and a collagen hydrogel can be made in the usual manner.

7.4.4 Cell culture, differentiation and staining

Spontaneously immortalized human keratinocytes line (Hacat cells) were used in this work. Cells between passage 13-30 were cultured in tissue culture flasks (T 75 or T225) (Corning) Dulbeccos modified Eagles medium (DMEM), 2 mmol/l glutamine high glucose, (Sigma, UK), with 10% foetal calf serum (FCS; First Link, UK) and penicillin - streptomycin (500 unit ml^{-1} and 500μml^{-1}) (ICN Biochemicals, UK). When confluent (approx. every 2-3 days) cells were passaged. Cell culture media was

removed and the flask washed gently with PBS (Oxoid, Thermo Scientific). A 10% Trypsin/solution (Gibco, Paisley, UK) was applied to the cells and incubated at 37°C for 1-2mins (until cells visibly became detached) equal amounts of DMEM were added to block the action of the tripsin. The cell suspension was transferred to universal tubes and centrifuged for 2mins at 2000 rpm. The supernatant was poured away and fresh DMEM added. Cells were split down at a 1:4 ratio. If cells were to be added to collagen hyrogels a small amount of the cell suspension was pipetted into a clean eppendorf and added in either a 1:1, 2:1 or 4:1 ratio to trypan blue (Sigma); 10 μl of this mixture was introduced to a haemocytometer and cells counted manually with a dissecting microscope. Two counts were made for each cell density and the number averaged. Cells were then spun down again and DMEM added to make the desired cellular concentration. These were then added to the collagen gels after they had been neutralised

Bone marrow stem cells (BMSCs) from 4-6 weeks old wistar female rats were kindly cultured and differentiated into adipocytes by Anita Sanghani and Liza Osagie. Briefly cells were seeded at 1×10^4 cells/cm2 followed by 14 days of culture in adipogenic induction media (MEM, 10% serum, 1 μM dexamethasone, 10 μg/ml human insulin, 100 μM indomethacin and 25 μM IBMX). Assessment of adipogenic differentiation was by oil red O staining. Cells were fixed for 4-5 mins in paraformaldehyde (Sigma), this was then removed and cells washed with PBS, 60% isopropanol was added for 15 mins followed by oil red O stain. Stain was washed off with PBS after 15 mins, the same protocol was used for cells within the collagen gel with longer initial fixing time (10 mins) and three washes to remove the stain. Imaging was done on an inverted fluorescence microscope (Apotome Zeiss).

7.4.5 Raman spectroscopy

Raman spectra of collagen samples were taken with a Renishaw inVia (Renishaw plc, Gloucestershire, UK) Raman microscope (x50 objective) equipped with an 830 nm laser (laser power at the sample was 10 mW). 20 accumulations of 1 min. Two sample preparations were used. Either, fully set hydrogels were frozen at -80°C then freeze dried overnight; or 0.5 ml of polymeric collagen solution was dropped directly onto a clean metal well and allowed to dry in the fume hood overnight.

Dopants	no. bubbles in 0.5ml gel (mean)	SD	N
500nm mesoporous carbon nps	40.857	63.164	14
Activated charcoal	8.208	10.413	24
HA nano particles	0.000	0.000	7
Bone fragments	0.000	0.000	5
Hacat cells	0.000	0.000	3
None	0.250	0.500	4
Polymeric collagen	766.667	404.145	3

Table 7.1: Bubble nucleation in monomeric COL1 gels with the addition of various dopants to investigate possible nucleation sites. 500nm mesoporous Carbon Activated Charcoal were intended to serve as positive controls, on the basis of preliminary gelatin experiments and literature. Other dopants were considered potential biological nucleation sites, all gels were 0.5ml volume

7.5 Results

7.5.1 Preliminary investigations

The results of the preliminary collagen investigation are shown in Table 7.1. The dopants were incorporated into the gel as per the methodologies previously above. A pressure profile of 130psi for 4hrs with 130psi/s decompression and 1psi/s compression was used on all samples. The number of bubbles that nucleated in the each 0.5ml hydrogel were counted. As can be seen no nucleation was observed in the crushed bone, hydroxyapatite, Hacat cell samples and only one incidence of nucleation in the plain monomeric collagen. Some nucleation was observed in the carbon and the charcoal samples, a result which matched the preliminary trials in gelatin. Polymeric collagen provided a striking increase in nucleation. The large standard deviation in the case of the polymeric collagen samples was primarily due to the difficulties associated with accurate manual counting of the bubbles. Following this experiment the segregated area method of counting, described in chapter 3 was used.

7.5.2 Non-biological dopants

Both types of carbon particle had relatively similar nucleating propensities. This is interesting given the differences in the surface properties of the two. Carbon is inherently non-polar and therefore hydrophobic. Activated charcoal is a treatment which heats charcoal in the presence of an oxidising catalyst. This process increases the porosity of the carbon and also renders the surface hydrophilic [343]. The mesoporous carbon by

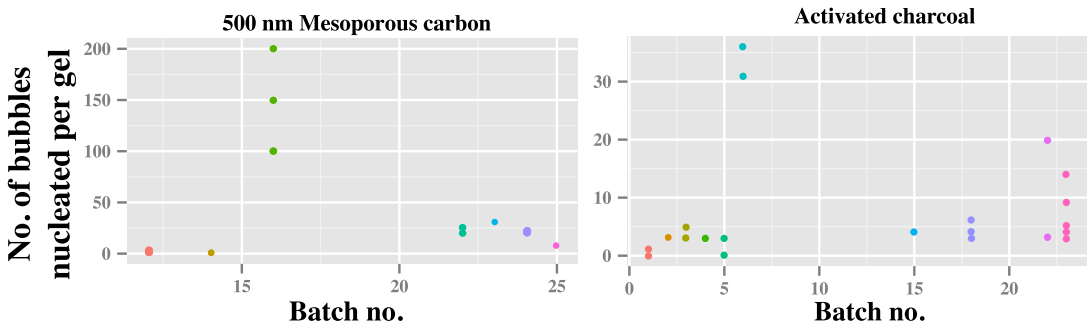

Figure 7.1: A study into the variation amongst batches of 500nm carbon and activated charcoal. As can be seen the charcoal does not show particular variation however the carbon shows one batch (batch 16) with very high nucleating power by comparison to other batches. Kruskal-wallis test finds that there are no significant differences between batches (p-value = 0.058 for activated charcoal, p-value = 0.052 for 500nm carbon). Even though there was not a significant difference, batch number was maintained going forward.

contrast, retains the hydrophobic surface of graphite. A more detailed comparison of the two samples was undertaken to investigate this further. Given the previous results in the literature regarding batch variability, a batch study of the carbon and charcoal was undertaken, Figure 7.1 shows the results. Comparison of the various batches of carbon and charcoal revealed an unexpected level of variation. Although the results were not significantly different, there was an indication that one of the batches of carbon (batch 16) produced greater number of bubbles than other batches. This was the batch that had been used in the previous bubble dynamics study of chapter 5. Whilst not affecting the analysis regarding correlations of bubble growth to dive parameters or bubble growth to bubble nucleation any results regarding bubble nucleation as a result of dive parameter variation were somewhat undermined. In particular the change in compression rate relation, (an experiment specifically used to test for the bubble surface contaminants) [142], was of importance to investigate further.

Repetition with a more typical batch of the carbon (batch 17) did not show the same trend as the previous. Figure 7.2 shows the difference in the trend of the two batches, batch 17, when fit with the same regression as batch 16 had an R^2 of only 0.1044 compared to the 0.9648 of batch 16.

The difference between these two behaviours was strongly suggestive of contamination of batch 16 at some point during the methodology. Despite efforts to reduce the possibility of such contamination through the use of aseptic culture hoods, and washing of the chamber in water, ethanol and acetone before each use; avoiding contamination

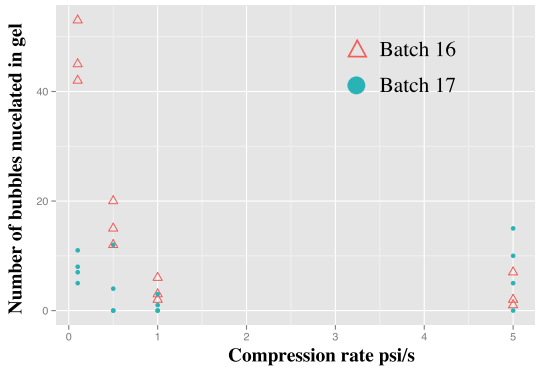

Figure 7.2: Showing the relation between compression rate and nucleation in 500nm carbon with two different batches of carbon batch 16 is one suspected of contamination

could only be assured through use of a clean room. It is also interesting to note that the contamination appeared to be confined solely to the powdered carbon and possibly charcoal as the PBS used was the same across all solutions. Although these results were of great interest it was felt that the various forms of carbon were not of sufficient biological relevance to merit further investigation in light of the bone, cell and polymeric collagen results.

7.5.3 Biological dopants

7.5.3.1 Bone and HANPs

Of the powdered biological dopants both HANPs and crushed bone showed no nucleating propensity. This may be unsurprising given that they are both hydrophilic, however the nucleation seen in the activated charcoal and with talc in the preliminary study (both of these are hydrophilic), suggested that hydrophobicity was not necessary [344]. In addition bone contains small amounts of lipid [345] and therefore may have areas of hydrophobicity. TEM of the two powders was done to assess the surface morphology for suitable crevices. The TEM images are shown in Figure 7.3. A clear difference in the topology of the two particles can be seen, however, due to the agglomerates of the HANPs which form, crevices within the agglomerates are of very varied angles. Measurements of crevice angles using the line tool in image J, were made from the TEM data. These cannot provide a full 3-dimensional understanding of crevice geometries and as such can only be treated as an indication of suitable crevice morphology. What is revealed by these images, particularly in the crushed bone, is the presences of many potential crevice angles and geometries. It may be concluded, therefore that it is the

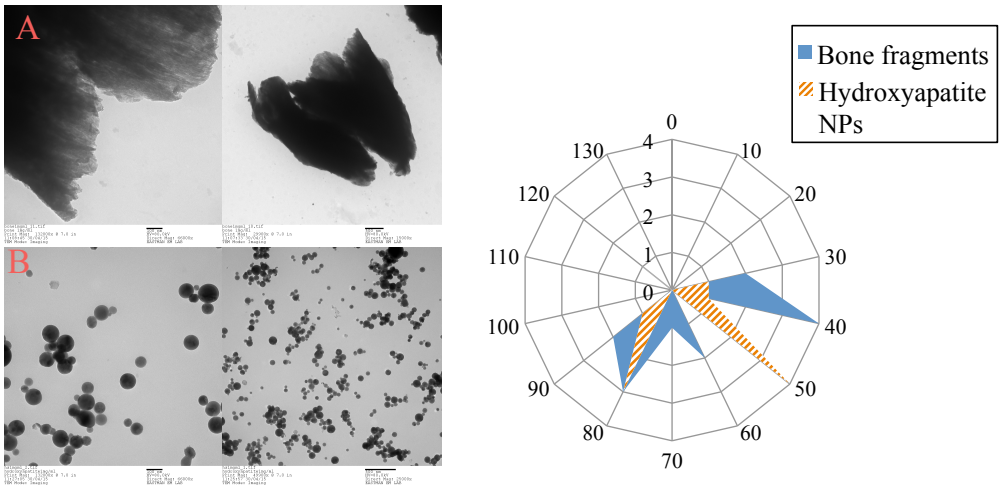

Figure 7.3: representative TEM images for the comparison of (A) bone fragments and (B) hydroxyapatite particles, the radar plot shows the distribution of crevice angles from all images.

surface properties of the bone i.e. its hydrophilicity which prevent nucleation.

7.5.3.2 Polymeric collagen

Of all the dopants used in the initial study, polymeric collagen was by far the most successful nucleating agent, with over a 20 fold increase in nucleation compared to the carbon or charcoal. The effect of increasing the polymeric collagen concentration on bubble nucleation showed significant positive correlation as shown in Figure 7.4. Polymeric collagen is the mature form of collagen where enzymatic and non-enzymatic cross links have formed in the ECM. In tendon, these cross links are predominately trivalent intermolecular pyridinoline cross-links and lysyl pyridinoline [346]. As the tendon ages the amount of non-enzymatic cross-links formed by glycation will increase [347]. Cross-links render such collagen insoluble in acetic acid thus making its extraction from tissue more difficult. The monomeric collagen, used up till now in this work, is tropocollagen. This type of collagen is far less abundant in the ECM as it represents only that fraction which has yet to be cross linked. The amount of monomeric to polymeric collagen in tissues will vary depending on the rate of collagen production by cells and the rate of enzymatic cross linking extracellularly. In general collagen cross linking increases with age or high glucose levels [348, 349]. In order to extract polymeric collagen the covalent cross-links must be destabilised before it can be extracted. An extraction method based on calf tendon was previously optimised by Cheema et al. and Wong et al. [197, 194], and it has been demonstrated that blended

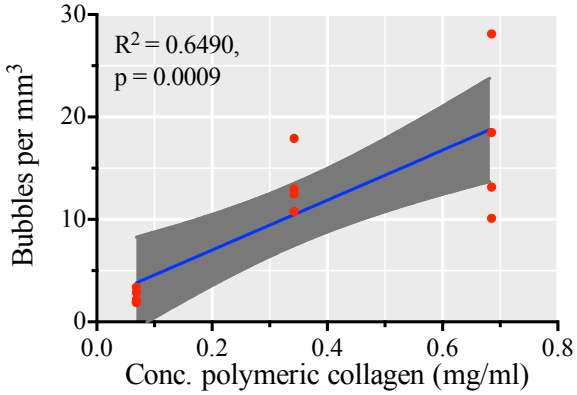

Figure 7.4: Changes in nucleation as a result of variation in the concentration of polymeric collagen. Linear regression reformed r^2 value reported with p-value.

polymeric-monomeric gels are biocompatible and have an increased Young's modulus [194]. Such gels may be considered more biomimetic than the previous monomeric collagen gels as, *in vivo* the majority of collagen (>90%) is cross-linked [194]. To the best of our knowledge, the nucleating propensity of polymeric collagen has never been investigated. Its efficacy is surprising, as it is not clear that polymeric collagen would contain crevices, and, although cross-linking may increase or amplify areas of hydrophobicity, uncrosslinked collagen also has areas of hydrophobicity, these are the drivers of its self assembly into fibrils [350]. Another possibility is that particulate debris from the tendon could be mechanically caught in the highly viscous collagen when it is extracted, (collagen cannot be filtered for such particles as it is too viscous), such particles may have appropriate crevices. Another alternative is that the polymeric collagen was contaminated as suspected in the case of the carbon. However three separate batches were extracted at different times from different tendons and all had similar nucleating propensity. The final possibility is that an amphiphilic molecule possibly a neutral lipid was extracted from the tendon with the collagen.

The discovery of this nucleating propensity may be highly significant for decompression sickness and for ultrasound induced cavitation. The ECM as a possible source of nucleation sites is not an area that has received much attention. However, this matrix is rich in many proteins and molecules which could provide sources of nucleation. Furthermore the amount of extracellular matrix and its composition differs throughout tissues in the body. If a particular constituent of the ECM can be found to be a primary cause of bubble nucleation, tissue matrices rich in this component would be at higher

risk. If the source is a wide spread matrix constituent, tissues with a high proportion of ECM such as connective tissue would be at higher risk of bubble formation. The general pattern of DCS injury, although by no means conclusive, does fit this idea [12]. Interestingly bubble nucleation in tendon was noted by Gersh et al. but the amount of bubble formation was lower than that of the fatty tissues [32, 327]. This suggests that the extraction of polymeric collagen from tendon may be specifically selecting for a strong nucleating agent, or that the mechanical breaking up of the tendon releases nucleating particles, possibly components that were previously intracellular. A final and more concerning possibility is that the process of polymeric collagen extraction introduces contamination by its nature. An indication against this is that the stages of the process where contamination seems most likely, the breaking up of the tendon, are the same as those used on the bone fragments.

The drastically different nucleation behaviour of the monomeric and polymeric collagen provided some ideas as to the likely source of the nucleation. The previous commercially extracted monomeric collagen was from rat tail whereas the polymeric was extracted from calf tendon. Both the animal source and the tissue from which the collagen was extracted were different. Different animals are know to have a different predisposition to DCS, however this is largely thought to be due to the size of the animal [89]. Collagen is a highly conserved molecule across species and therefore the animal source was thought unlikely to be the cause [192]. The difference in the tissue of extraction was considered a more likely source of the variation, as there may be differences in the amount of lipid in each tissue. However, tendon is generally though to have a very low lipid content [351] and as rat tail is a poorer source of polymeric collagen than calf tendon, this was not easily investigated. The hypothesis thought most likely was that the treatment used to sterilise the commercial monomeric collagen affected the nucleating behaviour. This treatment is chloroform fumigation. The collagen solution is pipetted onto a layer of chloroform (the two are immiscible) and left for several hours for the chloroform to evaporate through the collagen. Chloroform is used as a sterilisation method as it is a non-polar solvent and therefore disrupts the cell membranes of any bacteria or other cells within the collagen. In addition to this fumigation method a chloroform agitation method was also investigated. In this method the chloroform and collagen solution were continuously mixed together for 2hrs as previous work had

shown that fumigation was not always effective at sterilising polymeric collagen due to its higher viscosity than monomeric collagen. In addition to this treatment UV sterilisation and a hexane mixing protocol were also used to contrast. Hexane is again a non-polar solvent, and it was used in the same way as the chloroform (stirred with collagen for 2hrs). All treatments other than the hexane treatment allowed hydrogel gels to be made in the usual way after the process (hexane treated gels would not undergo fibrilogenesis). The nucleating propensity of the remaining four groups was examined and the results are shown in Figure 7.5. As can be seen, the chloroform fumigation slightly reduced the nucleating propensity and the chloroform agitation entirely eliminated it bringing it to the same level as the monomeric collagen. The UV treatment did not affect the nucleating propensity. All three batches of polymeric collagen were included in this study and all showed the same trend of results.

These results are strongly suggestive that non-polar molecules in the ECM are responsible for the nucleation of bubbles. The previous data from the addition of adipocytes to the monomeric collagen initially appears to contradict this. However it may be reconciled if all the available literature is considered. In all cases where bubbles were seen in fatty tissue or in adipose cells, these tissues had been mechanically deformed. In the works of Harvey, the deliberate mechanical deformation of tissue and cells was specifically shown to induce bubble nucleation [206]. In the same work it was also noted that bubble formation at the cut edges of the tissue was profuse, and was thought to be due to contamination of the cut edges with micronuclei. In addition inducing crush injuries to the limbs of animals also increased the number of bubbles after decompression [352]. In the works of Gersh et al. the samples in which bubbles were identified had been surgically removed and fixed [327, 32]. In the work of Papadopolou et al. again tissue was dissected from the animal prior to its use [18]. The cutting of such samples is likely to mechanically disrupt cells within the tissue and contaminate the cut edges with micronuclei. If the mechanical disruption either kills the cells or disrupts the cell membrane, intracellular debris may be expelled into the ECM. This intracellular debris could be the cause of nucleation with certain cell types such as adipose cells having intracellular components which favour nucleation more than others (such as muscle cells). In the adipocyte work conducted for this thesis, cells were not specifically mechanically disrupted prior to seeding in the gels. The

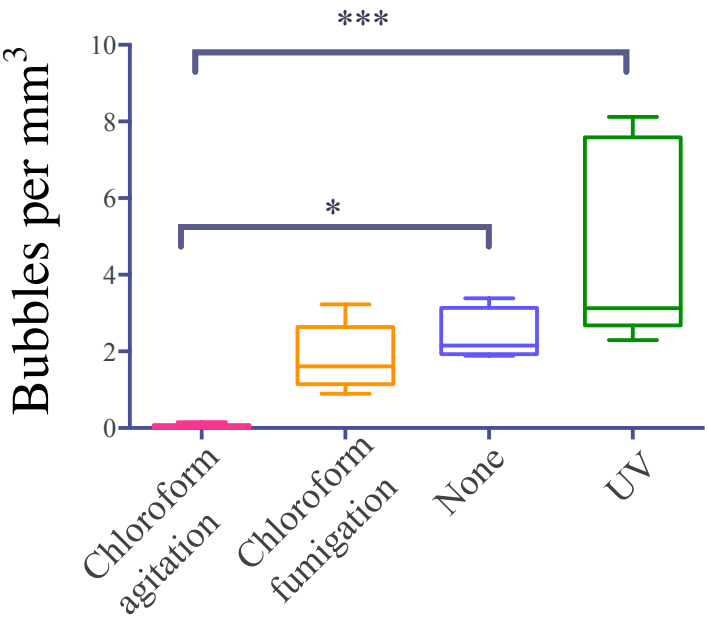

Figure 7.5: Treatment of polymeric collagen in order to sterilise it and use in cellular gels was done via three methods. Vigorously stirred with chloroform, fumigated with chloroform and UV treated. Stirring with chloroform removed all nucleating capabilities of the polymeric collagen, whist fumigating decreased it from both the control and UV treated, (this was significant in batches 1 and 3 but not batch 2) (statistical significance assessed by Kruskal-Wallis and Dunn's multiple comparisons test. (* = p=0.018, *** = p = 0.0003)

O-oil red stain additionally confirmed that lipid droplets were not obviously present in the ECM. This would suggest that it is not the polymeric collagen itself which caused the nucleation in these experiments, but the cellular debris which is extracted with the collagen from the tendon.

To investigate the presence of the suspected non-polar molecules in the polymeric collagen, Raman spectroscopy was used. Raman spectra of freeze dried gels that had been treated or untreated with chloroform agitation were taken in addition to a spectrum of calf tendon prior to the extraction. Raman spectroscopy measures the frequency shift of incident photons, caused by the inelastic scattering of these photons as they interact with the vibrational modes of the sample molecules. The technique has become widely used in biological investigations owing to the limited sample prep required, and the quantitative results that can be extracted [353].

Figure 7.6 shows the raman spectrum of the calf tendon from which the polymeric collagen was extracted, the blended collagen gels when fully gelled, and the ungelled

polymeric collagen solution. Identifying changes in molecular structure from Raman spectra is not straightforward. Raman spectroscopy provides information regarding both the primary and secondary structures (such as beta sheets or alpha helices) of biological molecules. Secondary structures are observed as broader bands whilst the primary structure is denoted by the vibrational energies of specific skeletal structures such as the C−C stretching or aliphatic ring vibrations. Of particular importance in Raman spectra of biological tissues are the amide I and amide III bands. These bands arise due to two different vibrational modes of the peptide bond and are sensitive to the secondary structure of the protein. These bands are found at 1600-1685 cm^{-1} for Amide I and 1225-1310 cm^{-1} for Amide III, the range denotes the shift which is dependent on the secondary structure. Vibrations arising from amino acids originate either from the CH_2 or CH_3 groups, or from the aromatic rings of the phenylalanin, tryosine and tryptophan. These occur in the lower region of the spectrum from $\sim$ 1100 - 500 cm^{-1}. Both types of features must be considered when analysing spectra.

Examination of Figure 7.6A shows the initial tendon sample, within the spectra the Amide I (1627 cm^{-1}) and Amide III (1253 cm^{-1}) peaks can be clearly identified, and a number of peaks in the skeletal region corresponding to various aliphatic rings. This spectra is almost identical to spectra of turkey tendon [354]. When comparing this spectra to the gelled polymeric collagen samples Figure 7.6B a several of the peaks have been changed and some lost. The clearest difference are the prominence of the peaks at 1001.1 cm^{-1} and 1031 cm^{-1} in the gelled collagen. These are attributed to the Phenylalanine, and are sometimes used to quantify the amount of collagen within a sample [353, 355, 356, 357]. In addition the amide I and amide III bands are still evident with the double peaks of the amide III band (α-helix and β pleated sheet at 1268 cm^{-1} and 1241cm^{-1} respectively) clearly distinguishable in the gelled collagen. In addition the peak at 1448.3 cm^{-1} can be attributed to the CH_2 bending [353, 355, 356, 357]. The region below the Phenylalanine peak is more complex to distinguish.

To understand the effect of the chloroform treatment, Figures 7.6 B and C should be considered. For the gelled collagen samples the peaks already identified appear to show no differences between samples or treatment conditions. When looking at the 933.4 cm^{-1} peak it appears there may be a very slight difference. In batch 1 untreated there appears to be a double peak, this is reduced in the untreated batch two and does

not appear to be present in the chloroform treated samples of both batches. This peak is slightly contentious in the literature with some assigning it to a proline ring stretch [356, 357], whilst in other literature it is assigned to the skeletal C−C stretch in the α- helix configuration [353, 355]. A further insight into this difference was provided by taking the raman spectra of the gels without gelling the samples. It was thought that this may provide spectra with less potential interference from other solutions used in the gelling process and possibly higher concentration of the polymeric collagen. Only Batch 1 was investigated and the spectra is shown in Figure 7.6C. As can be seen there does indeed appear to be a loss of the 933.4 cm^{-1} peak in the sample agitated with chloroform. In addition it can be seen that the Amide III band (area marked in red bracket) has also been greatly diminished or removed. That the two bands appear to have some basic correlation supports the assigning of the band to the C−C stretch in the α- helix configuration rather than the proline ring stretch, however it is far from clear how or whether this is the cause of the change in nucleation behaviour. In addition a spectra difference in the 738.8 cm^{-1} peak can also be seen where this peak is evident only in the untreated samples. Unfortunately this peak was not discussed in any literature found regarding collagen or ECM, this is largely because the convention of Raman spectroscopy is to focus on the 800-1800 cm^{-1} region. By searching Raman databases for molecules with peaks at 735-742 cm^{-1}, but no other strong peaks between this and 801cm^{-1}, a possible candidate molecule is identified to be Thymine, one of the nucleic acids found in DNA [358]. Although this could be present as the tendons were not decellularised, the comparison of the spectra of individual pure molecules from a database to the spectra obtain from mixtures such as the samples here is often misleading.

Assessment of non-polar molecules with raman is dependent on the behaviour of the long acyl chains which causes the hydrophobicity of lipids. Normally this is done in two regions, the finger print region 1500-1050 cm^{-1} and the higher wave numbers 2700-3100 cm^{-1} [359]. In the current set up only spectra in the finger print region could be recorded and not the high wave numbers. This lower region is associated with CC, CH_2 and CH_3 vibrations whereas the higher region is associated with CH. As the finger print region already contains many peaks from amino acids and collagen it is particularly difficult to associate peaks in this region with lipid in a mixed sample such

as these gels. One peak which is associated with a CH_2 vibration only within lipids is a peak at 1297 cm^{-1}. This peak is not seen in any of the samples.

Although the raman data are difficult to interpret, there is no strong evidence to suggest that there is a large amount of lipid in the treated verses untreated samples as the region from 1100-1200 cm^{-1} do not appear to have peak variation between the treated and untreated samples. Investigating higher wavenumbers would be of use in strengthening this conclusion. In addition there does seem to be a difference in the skeletal C-C vibration in the α-helix configuration as well as an absence of the amid III band. The 738.8 cm^{-1} peak could not be assigned but is worth further investigation. One feature that would greatly improve this characterisation is development of better sample holders for the ungelled collagen, this would increase the concentration of collagen left as a residue after evaporation and would greatly improve the quality of the spectra attained.

7.5.3.3 Cellular surfaces

Nucleation from cells is a contentious area of DCS research, on the one hand there are several theories that bubbles may nucleate from the cell junctions on endothelial linings [16], or from the caveolae on cell surfaces [70]; on the other hand the body of experimental evidence opposes this. Both Harvey et al. and Hemmingsen et al. investigated the nucleation of bubbles in single cells [360, 352]. Both found resistance to bubble formation for a wide range of cells, (Amoebae: Chaos chaos and Amoebra sp. Paramecium Arbacia eggs, Asterias eggs and Nitella,Tetrahymena). It was even shown by Hemmingsen et al. that particles which were successful nucleating agents in water, lost all nucleating potential once ingested by Tetrahymena [16]. Harvey showed that nucleation was possible in cells which died spontaneously or were mechanically deformed. Bubbles were also seen to be present within fat cells and in general much higher levels of bubbles were seen in fatty tissues [352]. The work of Gersh et al. also found evidence of bubble nucleation within and in the vicinity of fat cells [32, 327]. The lack of nucleation from Hacat cells seen in the initial dopant study, adds to the evidence against nucleation from cell surfaces or intracellular structures. However, the effect of chloroform treatment on polymeric collagen, strongly suggest that lipids, trapped within the gels, are the sites of nucleation. Given that lipid presence could not

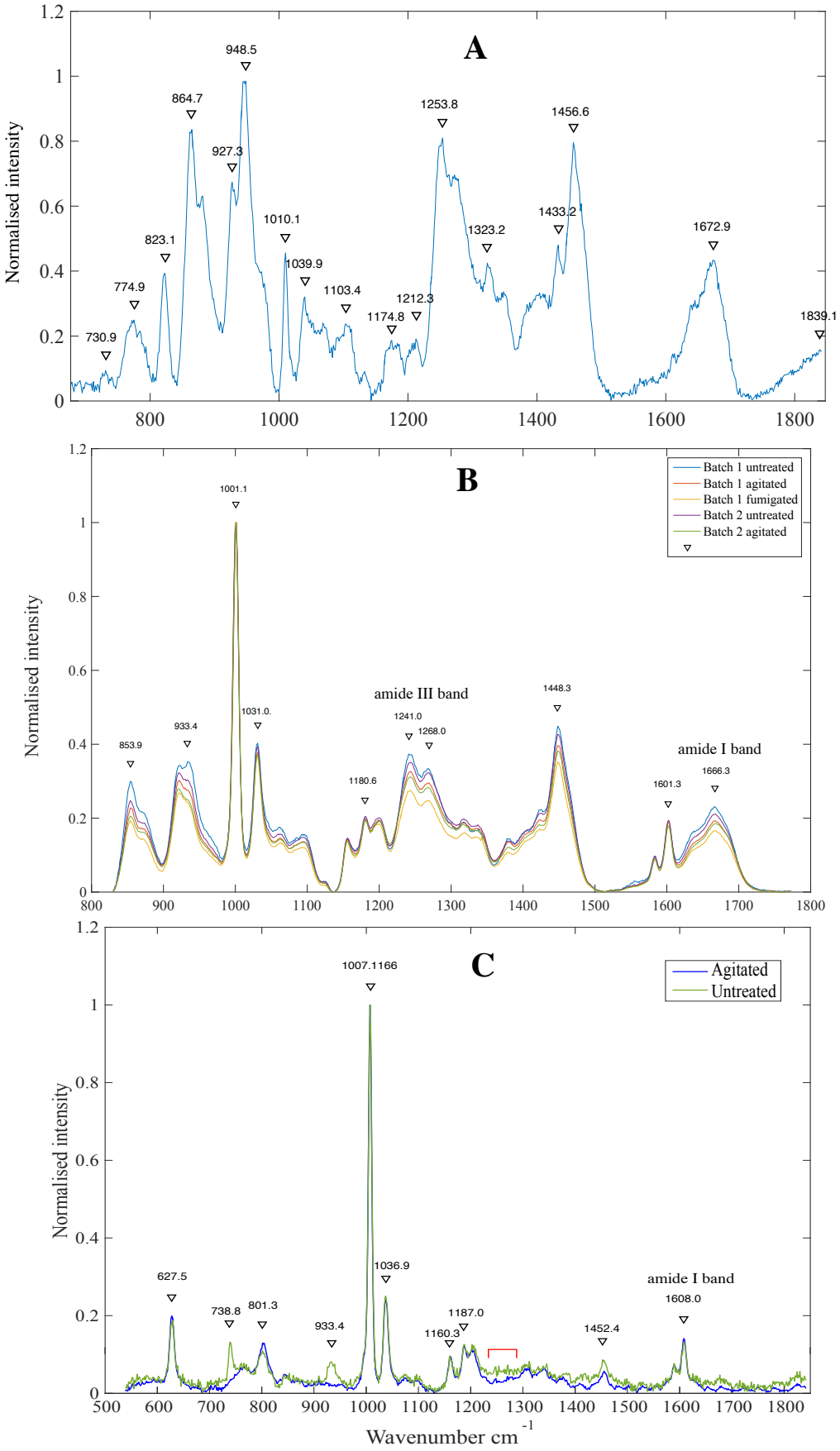

Figure 7.6: Raman spectra of A the calf tendon from which the collagen was extracted, B batches 1 and 2 of polymeric collagen both treated and untreated with chloroform, C Ungelled polymeric collagen batch 1

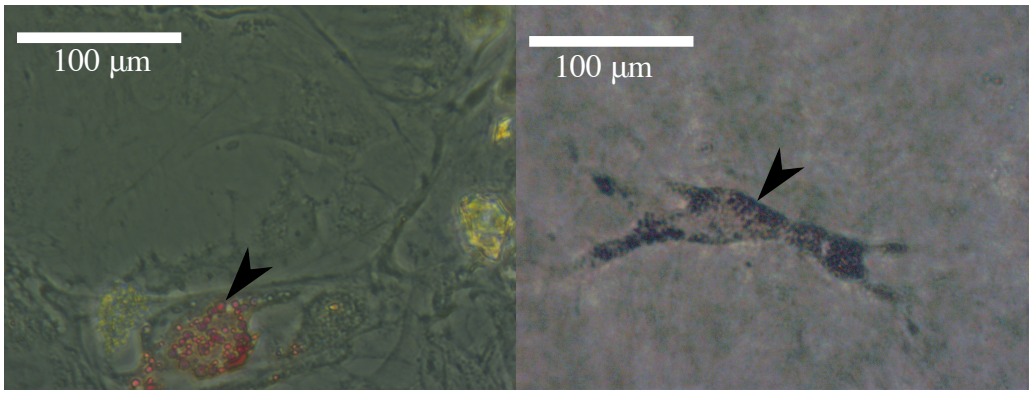

Figure 7.7: Oil red O staining of the differentiated bone marrow stem cells, showing positive staining for lipid indicated by the arrows. On the left the cells are in 2D cell culture on the right the image is of the cell within the collagen hydrogel, indicating that the lipid is retained when cells are transferred to the hydrogel

be found by Raman spectroscopy and nucleation from Hacat cells was not noticeable, it was hypothesised that very low lipid concentration might be producing a large variation in nucleation. To test this hypothesis the nucleating potential of adipocytes was also investigated. Bone marrow stem cells from rats were differentiated into adipocytes as described in the methodology. O-Oil red stain was used to show the presence of lipid droplets within the cells and confirm their differentiation. Stained images of the cells both in 2D tissue culture and in the 3D collagen gel show lipid droplets to be present, (see Figure 7.7). Lipid droplets are organelles and within adipocytes, are composed largely of triglycerides and free cholesterol with a phospholipid layer [361]. They are important in the regulation of lipid metabolism.

Despite the clear presence of lipid droplets, there was no significant change in bubble formation for gels containing 45,000 adipocytes/ml, (see Figure 7.8). A slight increase in bubble nucleation was seen but this was not statistically significant. Although the n numbers for this study were low (n=4), it can be said that intracellular lipid droplets do not cause a striking change in nucleation such as was observed with even the lowest concentrations of polymeric collagen. These data in conjunction with the HaCat data of the preliminary study (and HDF data presented in chapter 8) collectively add to a the evidence that lipid droplets and caveolae in live cells do not provide highly effective nucleation site. This conclusion accords with Hemmingsen's results [360], where hydrophobic particles ceased to nucleate once internalised by cells; but conflicts with those of Havey et al. and Gersh et al. [352, 32, 327]. One possibil-

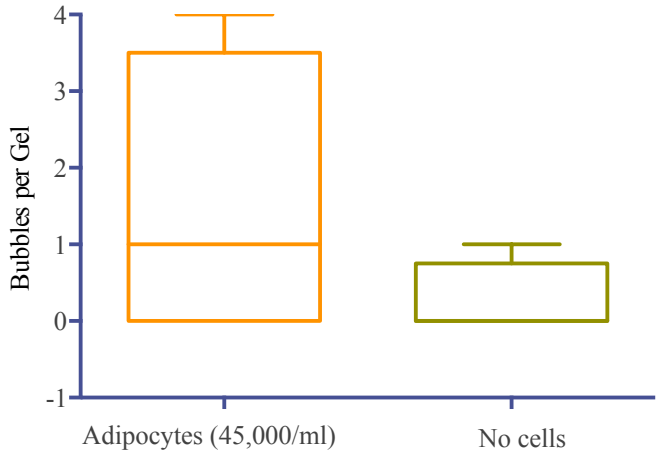

Figure 7.8: Nucleation of bubbles within monomeric collagen hydrogels containing 45,000 Adipose cells/ml. No statistically significant differences (N=4)

ity is that the bubbles may occur in adipocytes but only when the cell is dead or the membrane is compromised. An additional experiment that may be able to disprove this hypothesis, would be to lyse or mechanically deform the adipocytes within the collagen hydrogels and then observe subsequent nucleation. Another possibility is that tight cell-cell junctions are needed to provide nucleation sites. This could also be tested in such a system if cellular gels were allowed to mature to the stage where such junctions formed.

7.5.4 Summary of dopant nucleation

From the range of dopants investigated, the non-biological dopants nucleated bubbles reliably in response to decompression. However, it was found that batch variation appeared to confound the results. The batch variation is an important finding to stress as batches varied in both the magnitude of nucleation, as well as in the trend between nucleation and response to changed in compression rate. Batch variation is also reported in the literature on gelatin [139] and it is therefore an important parameter to consider in any future works. Biological crystalline dopants such as crushed bone or HANPs do not show a high nucleating propensity, this is most likely due to their surface hydrophilicity. Polymeric collagen had very striking nucleation propensity that has not been previously reported. The reduction of this nucleating propensity with chloroform treatment indicates that it may be due to lipids physically trapped within the gel. How-

Depth (psi)	Compression rate (psi/s)	Decompression rate (psi/s)	Time at depth (hrs)
130	1	13	0.5
130	1	13	1
130	1	13	2
130	1	13	2
130	1	8	2
130	1	4	2
130	5	13	2
130	1	13	2
130	0.5	13	2
130	0.1	13	2
130	1	13	2
80	1	13	2
40	1	13	2
40	1	4	2
80	1	8	2
130	1	13	2

Table 7.2: Dive parameters used to assess nucleation in polymeric collagen

ever, Raman spectroscopy was unable to detect lipids and incorporation of Hacat cells or adipocytes into the hydrogels, did not produce nucleation of a similar magnitude. These findings appear somewhat in tension with one another but could be interpreted as adding to existing evidence that intracellular lipid, (the normal mechanism of fat storage in the body [362]), or caveolae, from intact cells are not suitable nucleation sites. Further testing of dead cells and cellular debris may be a fruitful research avenue.

7.5.5 Dive parameter sensitivity

In addition to analysing the nature of the nucleation sites, changes in nucleation for polymeric collagen gels, as a result of dive parameter variation were also investigated. This type of investigation is important as the current experimental DCS literature regarding dive parameter variations, consists only of the works of Yount et al. and Kunkle et al. [139, 2, 141]. All these works used the same gelatin model and experimental system. This experimental system did not have control over the decompression rate and the time of nucleation is not reported. The works of Yount et al. and Kunkle et al. supported the hypothesis that nucleation is dependent only on the level of supersaturation. This hypothesis can be more fully investigated in the current set up as greater control of dive parameters is possible and higher resolution imaging available.

In similar experiments to the previous chapter, gels were decompressed for various dive profiles and the number of bubbles nucleated quantified. As the number of bubbles was much higher in the polymeric samples as compared to the carbon; the number of bubbles was analysed after the experiment via manual image analysis. Just prior to, and for 70 secs during the decompression images in the centre of the gel were taken every second. Onto this set of images 6 rectangular areas were imposed, (5 evenly radially distributed and one in the centre), the number of bubbles in each area was counted and the size of the area recorded. The areas were sized so that no more than $\approx$25 bubbles were present in each area. These counts were converted to the number of bubbles per unit volume by establishing that the imaging system could capture a depth of $\approx$ 3mm with clarity. This is slightly subject to the clarity of the gels and also the size of the bubbles (very small bubbles at the maximum depth may not be resolved). Due to this, direct comparison of raw bubble numbers to the carbon results, cannot be made, however trends between polymeric and carbon can be compared and raw numbers across all polymeric collagen samples can also be compared.

Dive profiles which varied in: time at depth, decompression rate, compression rate, maximum depth and decompression rate and depth simultaneously were used, and are summarised in Table 7.2. Results for the four single parameter variations are shown in Figure 7.9.

As can be seen there is significant positive linear correlation for time at depth, decompression rate and max depth. No correlation was found for the compression rate. The trends for the 3 positive correlations are in line with expected results for nucleation occurring from stabilised micronuclei. The fact that nucleation occurred even at relatively low maximum pressure and for short bottom times (40 psi $\approx$ 27 msw for 30 mins) suggests that the micronuceli are stabilised at relatively large sizes (on the order of 1 μm). Increasing the time at depth, the maximum depth or the decompression rate will increase the supersaturation upon decompression. These results differ from those of carbon, which did not a significant affect of dive parameters on nucleation for most parameters. One interesting feature of the results that was observed is from the point which was excluded from the time at depth study indicated by the open circle. In this case a large bubble was trapped between the bottom of the gel and the glass base of the chamber. This bubble failed to dissolve during the compression and bottom

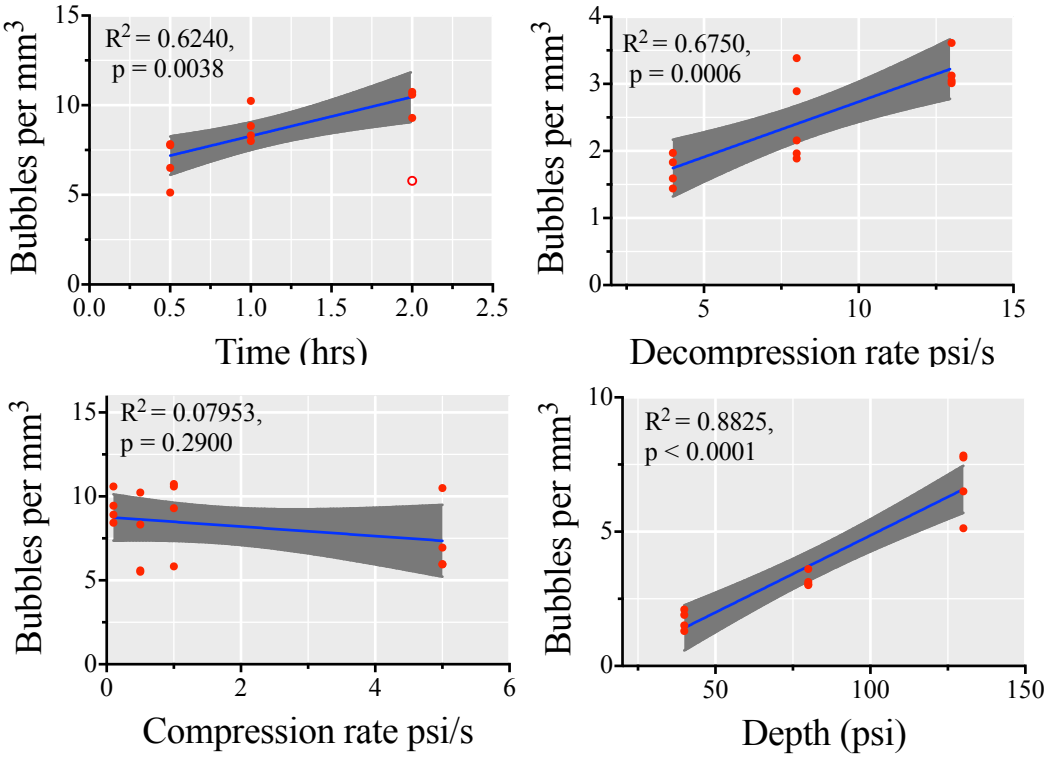

Figure 7.9: Showing the relations of depth, rate of compression, rate of decompression and time at depth for polymeric collagen doped samples. R^2 values for linear regression shown with p values for significance from 0 gradient line given. The open circle denotes a data point that was excluded as an outlier as a large bubble between the base of the gel and the glass of the chamber failed to dissolve on compression and grew rapidly during decompression.

time and upon decompression grew rapidly and apparently at the expense of nucleation within the gel. This result is of interest as it shows that pre-existing bubbles within the system may have significant effects on the nucleation of bubbles due to decompression. This would be of particular interest in repetitive diving situations. By comparison to the works of Yount and Kunkle these data show a generally higher level of bubble nucleation than the gelatin work. Gelatin samples decompressed from a saturation of 2.5 atm ($\approx$ 37 psi) produced 12.5-25 bubbles/ml in the fiducial volume [2, 94]. The bubbles per ml in the collagen hydrogels is of the order of several thousand. In the experiments of Yount et al. the upper 1 mm of the gelatin was not included in the bubble count. This area of the gel was believed to be disturbed by the meniscus of the gelatin [2] and bubbles within the area were reported to be far smaller and more numerous. No such consideration was necessary for the collagen gels, as no meniscus was present. This may account for the a proportion of the additional bubbles measured

in the collagen system.

The lack of correlation with compression rate may be in conflict with a surfactant stabilisation hypothesis. A surfactant stabilisation hypothesis also requires a surfactant absorbance and shedding mechanism. Surfactant molecules will be absorbed on to the bubble from the immediate surrounding or shed from the surface depending on whether the bubble is growing or shrinking. The rate at which this occurs will be dependent on the adhesive interactions of the surfactant molecules and their concentrations in the bulk liquid and on the bubble surface. There will be rates associated with both these processes. The relative rates of bubble shrinkage gas diffusion and surfactant absorption and shedding, dictate the stability of the bubble [220]. If the bubble radius change is far faster than the rate of surfactant shedding, abrupt changes in the bubble radius may be seen. This is observed in lipid stabilised bubbles within an ultrasound field [220]. When a large amount of surfactant is shed abruptly, there is a large increase in the Laplace pressure of the bubble as the surface tension increases, the radius decreases and the permeability of the surface increases. This drives faster dissolution of the bubble and leads to a prediction that nuclei would be more likely to be crushed by faster compression rates. That this is may be taken as evidence that surfactant stabalistion is not occuring in the gels. This could be seen as evidence in favour of a crevice based nucleation hypothesis [179, 322] rather than a surfactant skin model [95]. Alternatively this result could also be interpreted to show the rates of surfactant shedding and absorption are on a far faster time scale than the compression rates used in this work.

The variation of multiple dive parameters seen in Figure 7.10, shows that the effects of each individual dive parameter on nucleation are not additive. This supports the hypothesis, that nucleation is driven only by supersaturation. Although this may not surprising given the widespread acceptance of the theory; it provides interesting data for the validation of any nucleation models.

Computational modelling of the concentration of dissolved gas distributions was used to further understand the causal relations of dive parameters to nucleation. As already discussed, the critical radius is the threshold size above which micronuclei will grow to become bubbles. This radius depends on the surface tension and the supersaturation of the gel. Using the computational model of the previous chapters with no bubbles seeded, the supersaturation of the gels in response to changes of dive parame-

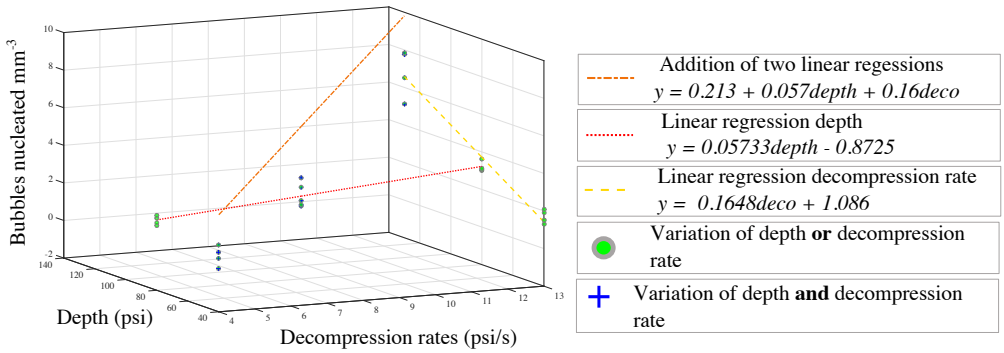

Figure 7.10: Experimental results, showing the effect of changing two dive parameters at once. Both the depth and the decompression rate were simultaneously changed. It is shown that the multi-linear regression is not simply the additive affect of both parameters indicating that there is interaction.

ters was investigated. To facilitate comparison between the profiles, the supersaturation of the central unit grid cube of each gel was plotted over time. Figure 7.11 shows that the change in supersaturation for the middle of the gel is greater in gels where greater bubble nucleation was seen. In addition this analysis suggested that if nuclei were all of a uniform distribution, there would be a threshold supersaturation pressure that would be the same for all bubbles. If an arbitrary supersaturation threshold of 0.02 bar is considered, Figure 7.11 shows that this threshold will be approached at different times for the different dive conditions. As decompression rate is decreased and depth increased bubble nucleation is expected to occur at later times. For the variation of both parameters it is predicted that the 40psi and 4psi/s profile will have the longest time before nucleation with 80psi and 8psi/s the next longest and 130psi and 13psi/s the shortest. The gradient of this trend is expected to be shallower than that of the other two single parameter variations. These predictions were tested for the decompression rate, and the depth and decompression rate experiments by extracting the time of nucleation onset from the time lapse images. These data, shown in Figure 7.12, revealed the expected trends in the time of nucleation as well as the relative gradients of the single and double parameter variation. This could have implications for the time of onset of DCS. Variations in supersaturation occur between different tissues and gradients of supersaturation will also exist within tissues. Tissues or tissue regions of higher supersaturation will nucleate bubbles earlier during decompression than tissues with lower supersaturation and may significantly deplete the dissolved gas within that tissue through competition

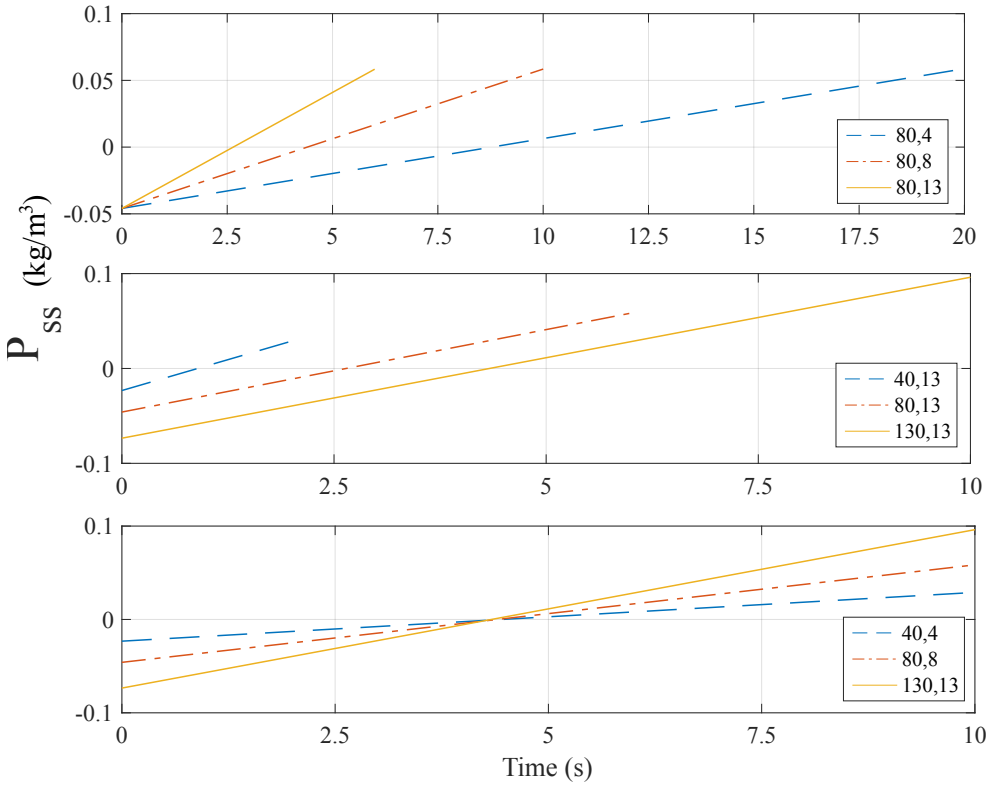

Figure 7.11: Showing the supersaturation of the midpoint of each gel as modelled solely by diffusion without bubble nucleation

for dissolved gas. This means that tissue with high supersaturations could become dominant controlling tissues in a way far more pronounced than is currently accounted for in most DCS bubble models.

7.6 Conclusions and Summary

This chapter has been an investigation into the nature of nucleation sites in collagen hydrogels. Initially the focus was on identifying the types of material which may cause nucleation. A selection of both biologically relevant and synthetic dopants were added to the collagen hydrogels and their nucleating propensity tested. Investigations into the synthetic dopants, charcoal and carbon revealed batch to batch variability, presumably due to contamination. This variability affected not only the levels of nucleation, but also the relation between nucleation and rate of compression. This highlights the importance in batch testing and in reporting any such variations when they are found. Of the biologically relevant dopants, bone fragments, HANPs, Hacat cells and adipose cells were found to produce no significant increase in nucleation. In the case of the bone and HANP's this was thought to be due to the hydrophilicity of the surfaces. For

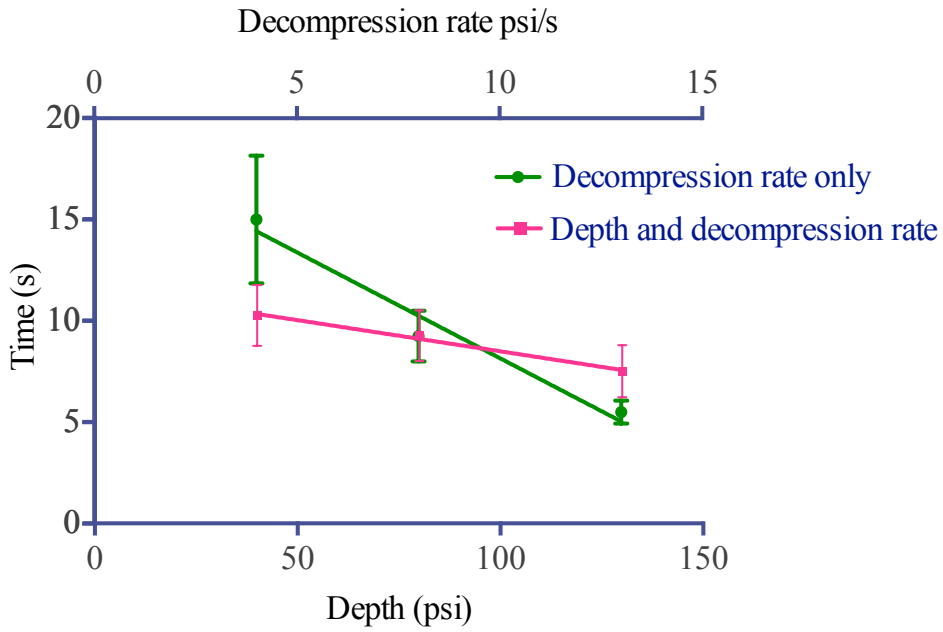

Figure 7.12: Showing the time of nucleation onset for changes in the decompression rate only, (green circles) and the variation in both decompression rate and depth (pink squares), values for the depth only were not recorded

the two cell types these results further add to the body of work which suggest cells caveolae or intracellular lipid droplets are not likely nucleation sites. This suggests that nucleation sites should be sought within the ECM. The nucleating propensity of polymeric collagen which has been shown in this chapter, is an interesting and novel finding for the DCS and ultrasound cavitation fields. It further strengthens the idea that the ECM should be more carefully considered as a nucleation site and mediator of bubble dynamics. The nucleating propensity of this mature form of cross linked collagen is 20 fold greater than that of the carbon or charcoal. Investigation into the source of this nucleation revealed that treatment of the polymeric collagen with chloroform eliminated the nucleation almost entirely. As chloroform is a solvent for non-polar molecules, this was strongly indicative that extracellular lipids may be the source, however, raman spectroscopy of the samples failed to shown the presence of any lipid in the original tendon, the gelled samples or the ungelled solution. It is possible that raman spectroscopy in the higher wavenumber region would be able to further elucidate the source of the nucleation, however it was seen that a change in the C-C vibrational energy in an α- helix secondary structure were removed by the chloroform treatment.

In addition another change in an unassignable peak was also seen.

Moving on from the material causes of the nucleating behaviour to the effect tissue supersaturation has on nucleation; it was seen that increasing the gel supersaturation by varying dive parameters resulted in increased nucleation. This result is as expected if nucleation is considered to occur from a population of stabilised micronuclei. In addition, the effect of dive parameters on the time of nucleation could be predicted by considering the supersaturation of a single point in the centre of the gel. This shows that the most obvious way to incorporate nucleation into computational models is to either seed bubbles dependent on the concentration of gas within a tissue, or to seed micronuclei of various sizes throughout the gel and only those which exceed the critical radius will grow. The advantage of the former method is that only the initial number of bubbles needs to be parameterised rather than the distribution of radii. The final preliminary investigation in this chapter has highlighted the data that may be gathered by three dimensional imaging of bubble formation in *in vitro* models.

Chapter 8

Cell-bubble interactions

This chapter investigates the effect cells have on bubble dynamics in terms of nucleation and growth, in addition to the effect that bubble nucleation has on cellular function.

8.1 Introduction

Cell-bubble interactions were an area, highlighted in chapter 2, in which *in vitro* models are lacking. No models were found in the literature that were able to measure the responses of cells to bubble formation, growth as well as high ppO_2, whilst also being able to monitor the changes in bubble dynamics. *In vitro* models which investigated only cell-bubble interactions but did not provide data on high ppO_2 can be found in the ultrasound literature and focus primarily on endothelial cells [363]. Much of this work may be applicable to the DCS field, as the interaction of bubbles with endothelial cells has been found to increase endothelial permeability, which is used to aid drug delivery in the therapeutic ultrasound case [188], and thought to be a mechanism of injury in the DCS case [65]. However, the effects that extracellular bubbles may have on the stromal cell population and vice versa have been largely overlooked, as has the added possible injury caused by the high ppO_2, which is specific to the DCS case. This is an interesting oversight as stromal cells are the majority of the cell population within tissue in the body [364]. That bubbles may effect or be affected by this cell population seems clear, but what the effects and affects may be, have not been quantified.

One area in which *in vitro* cell models have been used, is in investigating nucleation. One feature of this nucleation work, is that often the investigations use rather unusual cell types such as single cell organism. Although information on these cells adds to the body of work, the direct physiological relevance to human divers is more

tenuous. When designing an *in vitro* cell bubble model the choice of cell is important [363]. For the model to be as relevant as possible, the choice of cell should ideally be from the species in question, (human) or, at least, a mammalian cell type would be preferable. It is important to balance this against the difficulty of obtaining and culturing the cells. Cells which are particularly sensitive, require specialist culture conditions or have slow doubling times. This will lead to less reliability in experiments and ultimately limit the numbers of experiments that can be performed. This is particularly the case for 3D culture where the numbers of cells needed is generally much higher than 2D culture. The ideal cell type is therefore a human derived cell that is relatively robust and widely present within the body. It should be simple to culture and have a fast cell doubling time. Such requirements are very well fulfilled by the human dermal fibroblast (HDF). Fibroblasts are the most widely abundant cells in connective tissue producing much of the ground substance of the ECM; HDFs are a subpopulation found in the dermis of the skin. The cells used in this work were primary dermal fibroblasts. Their culture is very simple, and the cells are extremely robust to many cell culture stresses.

Cells and bubbles may interact through several mechanisms which will be of importance in DCS pathogenesis and modelling of bubble dynamics. The one most commonly described in the literature and incorporated into some computational models of DCS is the metabolism of oxygen.

8.1.1 Cellular metabolism of oxygen and the oxygen window

One way in which cells may impact on bubble dynamics is through altering the dissolved gas concentrations via the metabolism of oxygen. Oxygen is needed for respiration, during which, it is combined with glucose to produce CO_2 and water: $C_6H_{12}O_{16} + 6O_2 \longrightarrow 6CO_2 + 6H_2O$. As can be seen, the ratio of oxygen consumption to CO_2 production is 1:1, however there is a large difference in the partial pressure exerted by 1 molecule of O_2 by comparison to 1 CO_2 molecule in solution. This difference is due to the differences in solubilities; the solubility of oxygen is relatively low ($\sim$20x less than CO_2). If a concentration of 1mol/ml of O_2 is considered, by Henry's law this exerts a partial pressure of $1/k_h^{O_2}$, when metabolised and converted to 1 mol of CO_2 the new partial pressure exerted is $1/k_h^{CO_2}$ where $k_h^{CO_2}$ is $20k_h^{O_2}$. This decrease in

partial pressure leads to a decrease in total pressure (sum of all partial pressures) and thus increases the fraction of N_2 in the total dissolved gas. This creates a greater gradient for N_2 to diffuse out at the alveoli and hence be eliminated from the body. This is known as the oxygen window and is exploited in diving by breathing high oxygen content gas mixtures pre, during and post dive [13].

Modelling of the oxygen window is generally done via assuming that the contribution of metabolic gases is of a fixed partial pressure. In The Linear Exponential model the venous partial pressure of oxygen, $P_V O_2$ is considered the same for all compartments (46mmHg) [365]. The same is true for Hugon's joint model, where both compartments are assumed to have the same fixed partial pressure of metabolic gases [176]. In the work of O'Brien [220], which investigated only extravascular bubbles with a spatially explicit model, the metabolism of O_2 was modelled as fixed at 50%. Whilst a fixed $P_V O_2$ may make sense in the major vessels i.e. the superior vena cava, in general the venous dissolved gas concentration will depend on the dissolved gas concentration of the tissue it is passing through and hence on the metabolic rate of that tissue. Different tissues metabolise different amounts of O_2 and therefore the magnitude of the oxygen window will vary throughout the body. These various levels of tissue saturation would be expected to affect bubble nucleation as well as the subsequent growth dynamics.

Oxygen metabolism within cells is the result of three reactions, glycolysis, the Krebs cycle and the electron transport chain, The last of which is where the majority of the oxygen is consumed. These reactions are fact well modelled by a single expression, Michaelis-Menten kinetics. This is a relation to describe reactions which are enzymatically catalysed, and can be written as:

$$\mathrm{E} + \mathrm{S} \underset{k_r}{\overset{k_f}{\rightleftharpoons}} \mathrm{ES} \xrightarrow{k_{cat}} \mathrm{P} + \mathrm{E}, \tag{8.1}$$

where E is the enzyme, S is the substrate, P the product and k denotes a rate constant. K_m, the Michaelis rate constant, can be written as $K_m = \frac{k_r + k_{cat}}{k_f}$. From this the rate of oxygen consumption (R_{O_2}) can be derived as:

$$R_{O_2}(C) = \frac{V_{max} C^{O_2}}{C^{O_2} + K_m}, \tag{8.2}$$

where K_m is described as the half-maximal oxygen concentration and V_{max} is the maximum rate of oxygen consumption. Modelling of oxygen metabolism with this equation is widely accepted [366, 367, 368]. Of particular interest are the parameter values for K_m and V_{max}, the half maximal concentration and the maximum rate of oxygen metabolism respectively. These are values that will be cell specific, and to a large part dependent on the number of mitochondria within the cell; they may also vary for a specific cell type depending on the state of the cell e.g. quiescent, differentiating or proliferating [369]. To model the spatial distribution of oxygen within a cellular tissue or collagen gel, the Michaelis-Menten approximation can be incorporated into the diffusion equation:

$$\frac{\partial c}{\partial t} = D \bigtriangledown^2 \frac{\partial c}{\partial x} - \frac{V_{max} c}{c + K_m} \tag{8.3}$$

In this work, the diffusion equation with Michaelis-Menten kinetics is implemented numerically using the ADE finite difference approximation, described in chapter 5, to investigate the spatially explicit dissolved oxygen concentration in collagen gels of differing cell densities.

8.1.2 Mechanism of cell damage during diving and decompression

The above section describes how cellular metabolism may affect bubble dynamics. The effect that bubbles and increased oxygen partial pressure have on cells is also of importance to divers, however this is not something which is currently incorporated into any dive algorithms. Inclusion of such mechanisms in dive algorithms in a simple manner may enable a more precise prediction of the impact bubble dynamics will have on specific tissues in the body.

8.1.2.1 Increased oxygen partial pressure ($pp\mathrm{O}_2$)

Although oxygen is required for respiration, high concentrations of oxygen may have toxic effects on the body. At a cellular level, increased $pp\mathrm{O}_2$ increases the production of reactive oxygen species (ROS) such as the superoxides $\mathrm{H}_2\mathrm{O}_2$ and $\mathrm{O}_2\dot{-}$, which are a product of the electron transport chain. Under normal conditions these ROS are prevented from further reacting either through enzymatic action or via direct reactions with antioxidants. However, increased levels of ROS can overwhelm the antioxidant defences, allowing the ROS to further react within the cell [13]. An area particularly

prone to damage by the reactions of ROS are plasma membranes, and with mitochondria being one of the greatest producers of ROS, increased $pp\mathrm{O}_2$ will often lead to mitochondrial membrane damage, or depolarisation. Membrane depolarisation is a linked will apoptosis, and works of Wang et al.[65], have shown that for bovine endothelial cells, increased $pp\mathrm{O}_2$ leads to membrane depolarisation and death.

8.1.2.2 Mechano-sensitive responses of cells

The effect of bubbles on cell function and viability is less clearly understood. There are a variety of ways which bubbles may affect cellular function, some of which were discussed in chapter 2. Most cells within the body are mechanosensitive, that is they contain transmembrane ion channels or receptors that can trigger intracellular biochemical signals in response to extracellular mechanical stimulus. One particular mechanosensitive pathway that has been investigated in relation to bubble proximity is that of the syndecan IV ion channel. This channel is activated by bubble proximity, and results in a large calcium influx into the cell, ultimately resulting in cell death in $\sim$ 30% of endothelial cells [68]. This effect is in fact a combination of a hydrophobic attraction and a mechanosensitive response. The heparan sulfate side chains of the syndecan IV channels are attracted to the air liquid interface of the bubble and as the bubble is moved the mechanical tension on the side chains displaces the syndecan IV which in turn activates a calcium specific transient receptor potential channel (TRPV) resulting in a calcium influx [133]. This response has only been investigated in endothelial cells, however the syndecan IV and TRPV channels are found widely in most cell membranes and hence the effect may be expected to occur in a wide range of cell types.

8.2 Methods

Human dermal Fibroblast (HDF) cells (primary cells obtained with full consent and ethical approval; passages 5-12) were cultured in Dulbeccos modified Eagles medium (DMEM), 2 mmol/l glutamine high glucose (25mM/L), (Sigma, UK), with 10% foetal calf serum (FCS; First Link, UK) and penicillin streptomycin (500 unit ml^{-1} and $500\mu ml^{-1}$) (ICN Biochemicals, UK). Collagen hydrogel gels (0.5 ml) were made up of 0.4 ml blended collagen (0.1:10) polymeric collagen, extracted as previously described to monomeric collagen (rat tail collagen type I (First Link, UK)); added to this was, 0.05 ml 10X concentration Modified Eagle's Medium (Gibco, UK). This mixture was

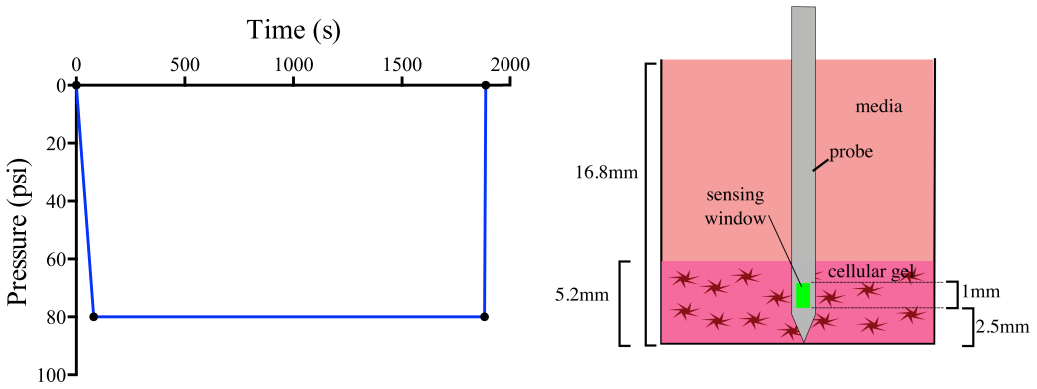

Figure 8.1: Left- pressure profile used for all cellular decompressions; right - the set up for the oxygen monitoring with relevant distances given.

neutralised by the drop wise addition of 5 M NaOH and then stored on ice for 1 hr to remove excess bubbles. After 1 hr 0.05 ml of cell suspension with the required cell density was added. Cellular densities were calculated by adding in a ratio of 1:1 2:1 or 4:1, Trypan blue to cell suspension; 10μl of this mixture were introduced to the haemocytometer and cells counted manually with a dissecting microscope. Two counts were made for each cell density and the number averaged. Gels were then pipetted into a 48 well plate (0.5 ml per well) and allowed to set at 37°C for 15mins. After this a further 0.5 ml of culture media was added to the top of the gels and these were left for 8-12 hrs at 37°C.

For oxygen monitoring, the 48 well plate was placed in a jig onto which oxygen probes were attached to ensure placement of probes was consistent. An oxygen probe (NX-NP/O/E Oxford Optronix) was inserted into the centre of the gel vertically until the tip of the gel contacted the well plate base (see Figure 8.1). Oxygen measurements were taken every 80secs for ∼8hrs or until there was an obvious error with a probe at which time the experiment was terminated.

For bubble growth and nucleation experiments, cellular gels were transferred to the pressure chamber under aseptic conditions. The pressure profile shown in Figure 8.1 was applied and gels were imaged following protocol previously described. Cell viability measurements were made on cellular gels which had either undergone the profile in Figure 8.1 or a sham dive, where the gel was transferred to the chamber for the same total time with no pressure applied. Following the profile end, gels were immediately transferred to a 7 ml Bijou tube containing 17 μl ethidium homodimer (2 mM; Invitrogen) and 20 μ calce- in-AM (4 mM; Fluka Analytical) diluted in 5ml

PBS, and incubated for 35 mins. Gels were then imaged on an inverted fluorescence microscope (Apotome Zeiss). 6 images of each gel were then taken: 3 on each side at 0, 120 and 240°. In each case 200 um total depth was imaged in slices of $6\mu m$ thickness. Live dead cell proportions were manually counted for all samples.

8.3 Results and discussion

8.3.1 Effect of cellular metabolism on bubble nucleation and growth

This section of the chapter details the results of the investigation into the affect cellular oxygen consumption has on bubble dynamics. If all cells within a collagen gel are assumed to consume the same amount of oxygen, it can be deduced that a greater cell density will lead to a decreased dissolved oxygen concentration. Given that the previous chapter concluded that cell surfaces do not increase nucleation, increased cell density was hypothesised to decrease the amount of bubble nucleation. It was also hypothesised that increasing the cell density would result in smaller bubbles with shorter half lives. These hypotheses were again due to the overall reduced dissolved gas concentration at the start of the pressure profile, as well as the effect continued oxygen metabolism would have on bubble growth post decompression.

To initially assess the magnitude of the oxygen consumption for varying cell densities, the concentration of dissolved oxygen within the gels was measured. Using the set-up configuration shown on the right hand side of Figure 8.1, the dissolved oxygen concentration for the gels at varying cell densities are shown in Figure 8.2. It can be seen that only 500,000 cells/ml showed a significant difference over the time measured. This was interesting as the cells at 50,000 cells/ml and 5,000 cells/ml could be observed to be alive from their morphology under a dissecting microscope. To understand whether this result was to be expected, simulations using the V_{max} and K_m found by Cheema and Streeter [370], were used to perform simulations of the experimental set up. Figure 8.3 shows the results of these simulations. As can be seen there is good agreement between the measured and simulated values for all cellular densities. There is some additional measurement error in the experimental samples by comparison to the modelled data, this is likely due to a slightly inhomogeneous distribution of the

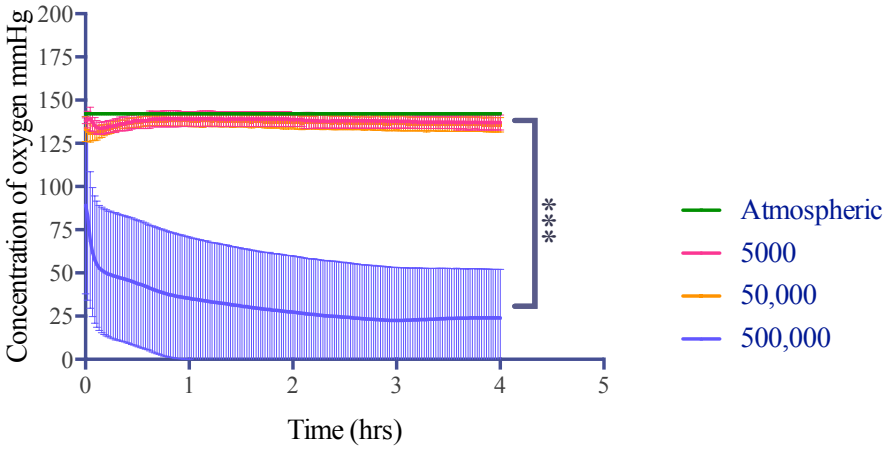

Figure 8.2: Oxygen monitoring of collagen hydrogels with 5000, 50,000 or 500,000 HDF cells/ml. Atmospheric concentration is shown for reference. Statistically significant difference between 500,000/ml vs. 5,000/ml and 500,000/ml vs 50,000/ml as assessed by two way repeated measures using ANOVA (Tukey's multiple comparison correction) $p \leq 0.0003$

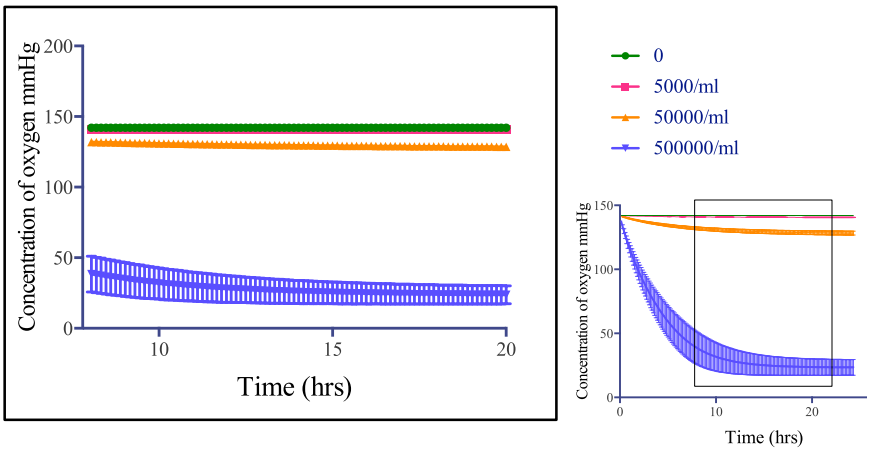

Figure 8.3: Modelled oxygen consumptions for set up seen in Figure 8.1. The parameters used were $k_h = 1.397x10^{-9}$ mol ml^{-1}mmHg, $D = 2.5x10^{-9}$m^{2}s^{-1}, $V_{max} = 3x10^{-17}$mol cell^{-1} s^{-1} , $K_m = 5.6$mmHg, cell densities were 5,000 cells/ml, 50,000 cells/ml, and 500,000 cells/ml, $\pm$ 10%, error bars are from repeated simulations (3 per cell density) with variation in the cell density between max and min estimates, in addition to error caused by averaging over the sensor area.

cells within the gel and the relative position of the probe, as well as small movements in the probe within the gel.

To understand how this dissolved gas was distributed within the gels, the simulation results were also plotted as a cross sectional view through the centre, see Figure 8.4. Interestingly there is not a large gradient within the gels by comparison to the differences between them.

For samples that were exposed to pressure profiles, a transfer from the 48 well

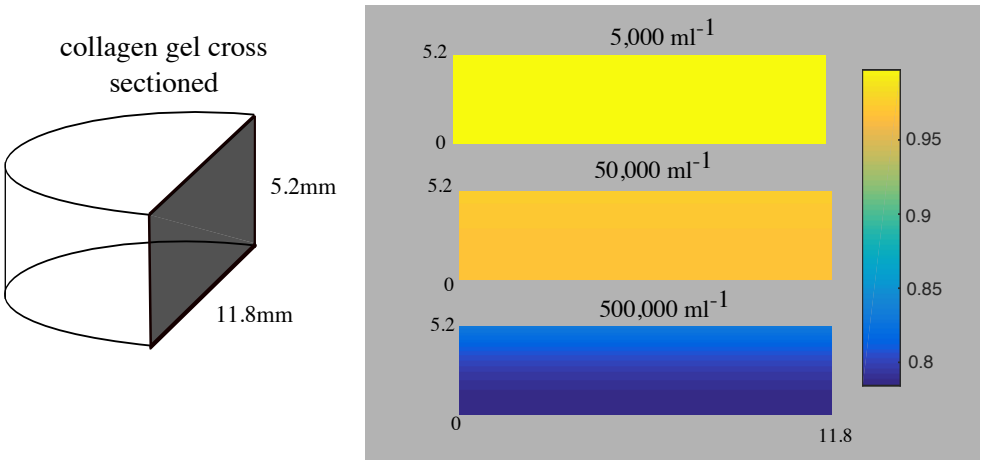

Figure 8.4: Modelled dissolved oxygen concentrations at the mid-cross section of the gel for the three different cell densities just prior to start of the pressure profile. Concentrations have been non-dimensionalised on the ambient pressure colour scale shown on the right side. The parameters used were $k_h^{O_2} = 1.397x10^{-9}$ mol ml^{-1}mmHg, $D = 2.5x10^{-9}$m^{2}s^{-1}, $V_{max} = 3x10^{-17}$mol cell^{-1} s^{-1} , $K_m = 5.6$mmHg, cell densities were 5,000 cells/ml, 50,000 cells/ml, and 500,000 cells/ml,

plate where the gels were gelled, to the chamber was necessary. This occurred at 10 hrs after the gels had been set i.e. at time = 0 hrs on Figure 8.2. This transfer will have altered the dissolved oxygen distribution of these gels by comparison to their pre-transfer state. To ensure that the differences found in Figure 8.2 were preserved for the decompressions, transfer time was minimised as far as possible. It was assumed that this preserved the differences between gels. For simulation purposes, the initial dissolved gas concentration prior to compression, was the same as the state just prior to transfer from the 48 well plate to the chamber. The key change for the simulations before and after gel transfer was in the geometry of the system. Whilst in the 48 well plate the edges of the gels were considered to have no-flux boundaries (they were against tissue culture plastic), and there was 11 mm of media on top of the gel. Once transferred to the chamber all edges other than the bottom face were modelled to be in equilibrium with the external ambient pressure (media was added to only just cover the gel surface).

Having established the differences in dissolved gas concentrations within the gels at the beginning of the dive profile, the effect this had on the final bubble dynamics was investigated. The differences in the nucleation within the gels is shown in Figure 8.5. As can be seen, there is a significant decrease in the number of bubbles which nucleated between the 5,000 cells/ml and 50,000 cells/ml and the 5,000 cells/ml and 500,000

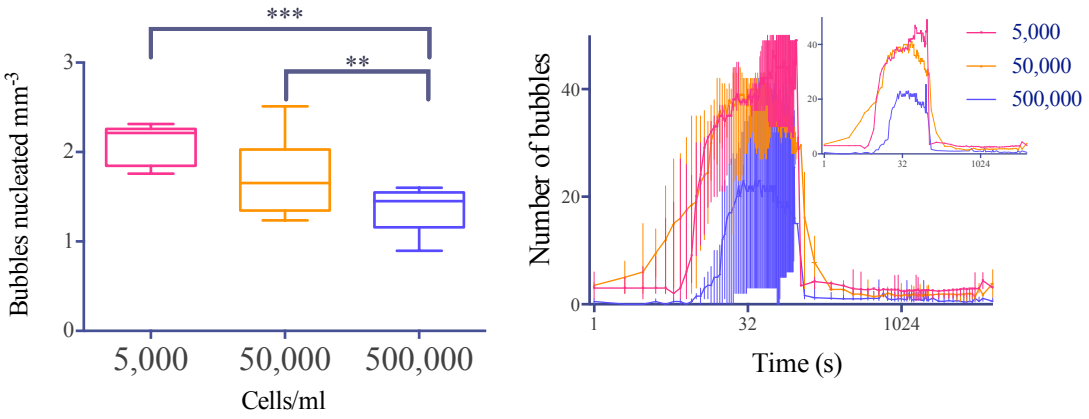

Figure 8.5: Nucleation of bubbles within blended monomeric-polymeric collagen hydrogels containing 5,000, 50,000 or 500,000 HDF cells/ml. Left - the maximum number of bubbles which nucleated, statistical significance was found between 500,000 vs. 5,000 cells/ml and 500,000 vs. 50,000 cells/ml as assessed by one way ANOVA (Tukey's multiple comparison correction). Right - the number of bubbles in the field of view over time. N=3 gels per cellular density.

cells/ml. This concords with the measured dissolved oxygen concentration prior to the dive (Figure 8.2). The nucleation data supports the original hypotheses that the consumption of oxygen by cells decreases the nucleation of bubbles. For human divers, this suggests that tissue with high cellular content and or high metabolic demands, are at lower risk from decompression induced bubble formation. Cells within collagen hydrogels are at a lower concentration than would normally be found within the body. For instance, the cellular density of articulate cartilage is estimated at between 2.5^6 - 10^6cells/ml [364] and for cortical bone 400,000-900,000 cells/ml, [364] both of which are cell sparse tissues within the body. Although it would be preferable to use higher cell densities closer to those found *in vivo*, higher cell densities lead to significant contraction of the gel within 10 hrs of fibrilogenesis and also increase the opacity of the gels making it more difficult to obtain good quality images.

Having investigated the first hypothesis, analysis of bubble growth for the same experiments was used to assess whether the cell density in the gel caused a decrease in the bubbles plateau radii and half lives. Figure 8.6 shows the results of both the plateau radius and half life analysis, which was conducted in the same way as that in chapter 6. Note that the cellular density is plotted on a log axis for clarity. This analysis suggests that the cell density had minimal effect on the bubble plateau radius or bubble half life, which is in conflict with the original hypothesis. There are several possible reasons for

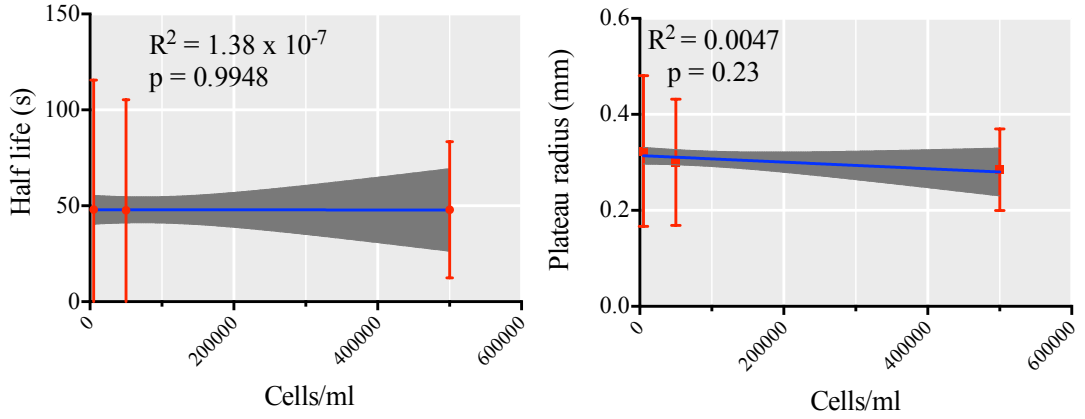

Figure 8.6: Left - relationship between bubble half life and cell density, right - relationship between bubble plateau radius and cell density, mean and SD shown for points a linear regression fit with 95% CI is also shown. R^2 and p-values of the linear regression given on each graph. No statistical dependence was found for either measured variable with varying cell density

this. The first is the combination of trend in bubble radius with number of bubbles that nucleate, and the reduced dissolved gas concentration. As was shown in chapter 6, for gels in which a higher number of bubbles nucleate, the plateau radii will be smaller and the half life shorter. Given the nucleation data shown above, this effect would act to increase the size of bubbles in the 500,000 cell/ml and potentially cancel out the reduction in radius due to the lower dissolved gas concentration. Another factor which may be responsible is a change in the level of cellular metabolism during the pressure profile.

Long term maintenance of the reduced dissolved oxygen concentration in the gels post dive is dependent on continued metabolism of oxygen. However, as discussed in the introduction to this chapter, there is evidence to suggest that increased $pp\mathrm{O}_2$ interferes with cellular metabolism and may even cause cell death. If this is the case it cannot be assumed that the rate of oxygen consumption will continue at the same level when the $pp\mathrm{O}_2$ is increased, or, that it will recover to its original value after the decompression. If the rate of oxygen consumption falls, the dissolved gas concentration in the gels will rise and hence the growth of bubbles after the decompression may be increased. The effect that this change in metabolism could have on the dissolved oxygen concentration was examined by simulating the total gas concentrations in the three gels for the case where the Michaelis-Menten kinetics were applied with the same V_{max} and K_m throughout the simulation, and the case where oxygen metabolism stopped entirely

during and post dive. This is the most extreme case, and was not expected to occur in the experiments performed here. However very little information could be found in the literature on how V_{max} and K_m would be altered by the increased $pp\mathrm{O}_2$, and decompression, and hence simulation of the two most extreme possibilities was investigated. It should be made clear that these simulations did not include bubble formation, which will of course alter the dissolved gas concentration. Inclusion of Michaelis-Menten kinetics into the full 3D bubble model was not achieved within this project but is a key aim of future work. Figure 8.7 shows the cross-sectional gas concentrations for simulations of each of the three cellular densities at 1800 secs (just prior to decompression) (left) and at 2 hrs after the start of the profile (right); the top and bottom panels show the cases where oxygen metabolism continues, and where it is zero after the start of the profile. As can be seen, the levels of cellular density lead to only small differences in the dissolved gas concentrations just prior to decompression in both the top and bottom panels. There also appears to be no differences between the two extremes of metabolic behaviour, at any time or for any cellular density. In fact, for the 500,000 cells/ml simulations at 2hrs (bottom right heat map in panels A and B), there are very small differences, a maximum of 0.003 greater concentration in panel B - no metabolism than A - normal metabolism. These results indicate that the initial dissolved gas concentration prior to the pressure profile, dictates the dissolved gas concentration 2hrs after the profile regardless of any changes in cellular metabolism caused by increased $pp\mathrm{O}_2$. This shows that the dissolved gas concentration at the start of the profile (Figure 8.4) will determine the number of bubbles which nucleate, and it is this bubble density which will predominately control bubble dynamics in the short to medium term after the dive. *In vivo*, where tissues generally have a higher cellular content, the effect of cellular metabolism on bubble growth may be more pronounced and hence, whether or not cellular metabolism is changed by exposure to a pressure profile is still important to investigate.

8.3.2 Effect of bubbles on cell viability

The final section of this chapter is an investigation into the effect dive profiles may have on cell viability. The effects will be due to both the increased $pp\mathrm{O}_2$, as well as bubble formation and growth. The hypothesis of this investigation was that cell death would be

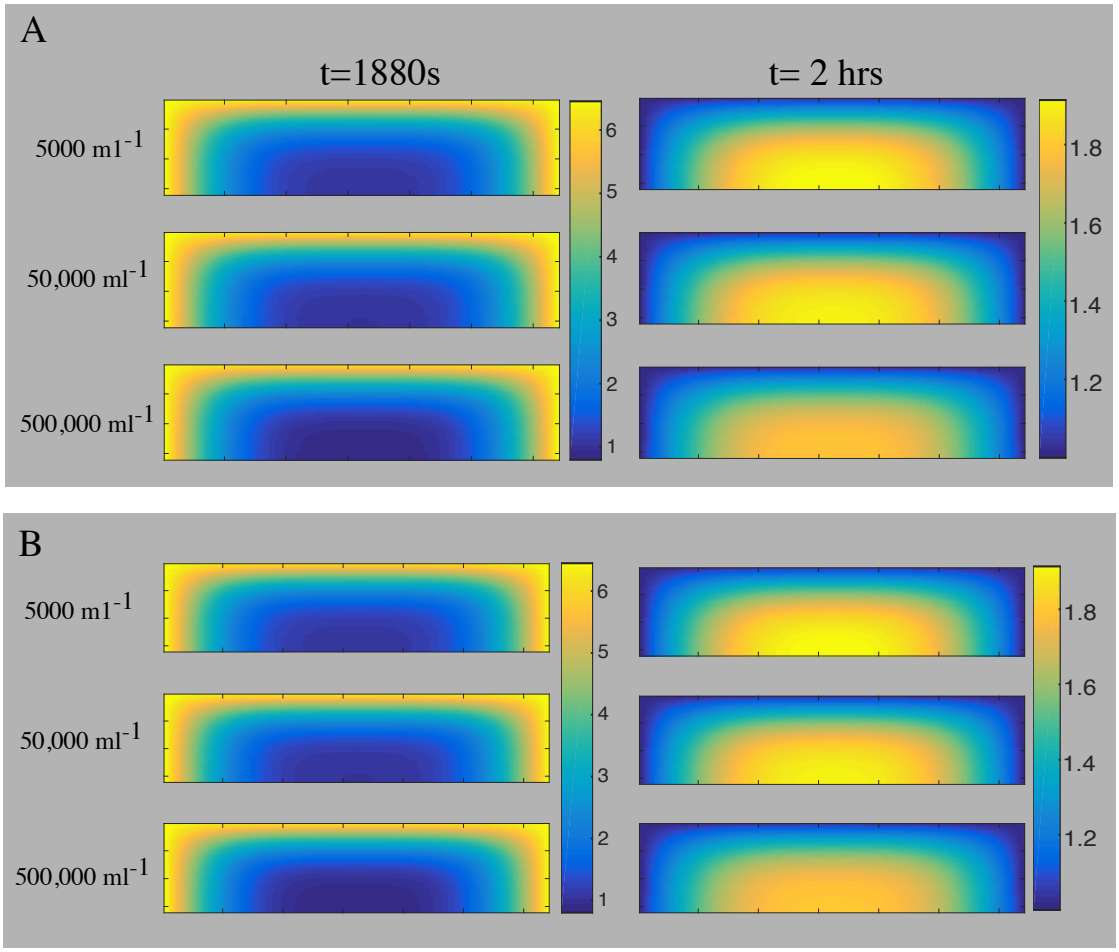

Figure 8.7: Showing the dissolved oxygen concentration during the pressure profile just prior to decompression (at 1880secs) and at 2hrs after the start of the profile, (A) - where cellular metabolism continues at the same rate as pre profile. (B) - where all cellular metabolism stops when pressure profile begins. Concentrations for all plots use the scale shown in the scale bar on the right-hand side, where all concentrations have been non-dimensionalised to atmospheric pressure

seen following a decompression profile. Of particular interest was to assess the magnitude of the response. Previous works looked at cell viability following increased ppO2 *or* bubble proximity alone [133, 65], whereas the experimental setup in this work theoretically allows both mechanisms to act simultaneously. In addition, the previous works were done on 2D cultures of endothelial cells, in this work, 3D cultures of fibroblast cells were chosen. Although the choice of cell may affect the magnitude of cell death somewhat, the mechanisms proposed for both the bio-mechanical (bubble proximity) induced cell death and the ppO_2 cell death, should not be unique to endothelial cells. Fibroblasts have both the syndecan IV ion channels as well as the TRPV family of calcium channels, and mitochondria in fibroblasts should be susceptible to membrane

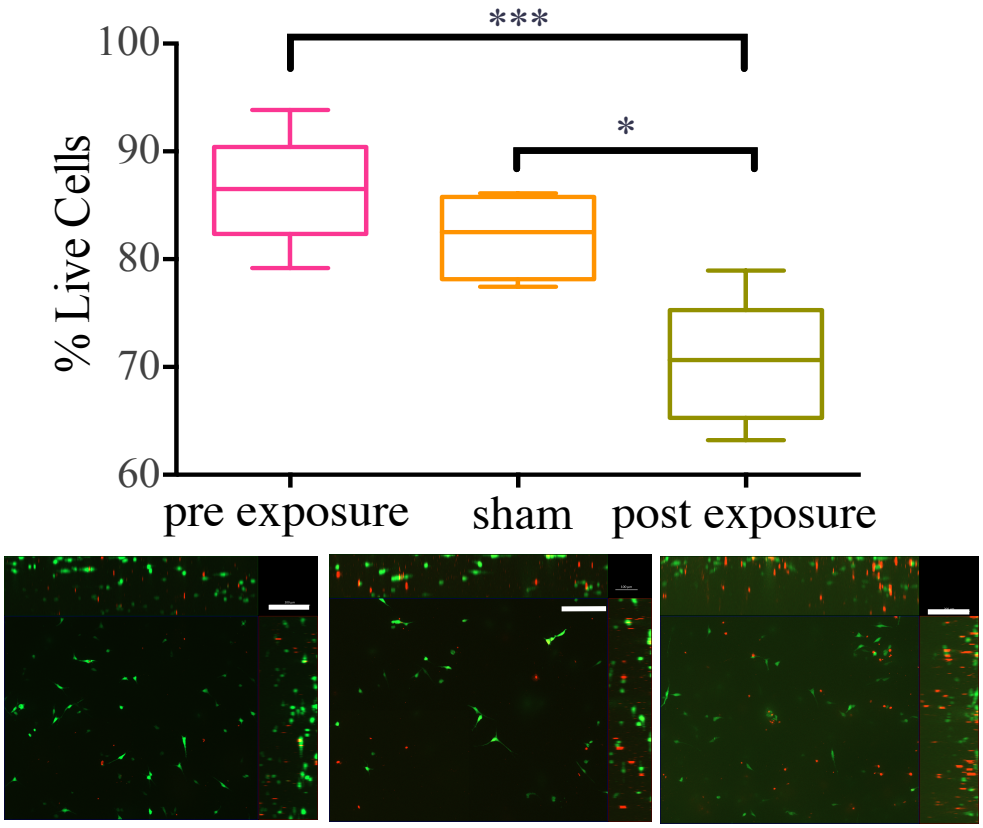

Figure 8.8: Comparison of the live dead cell population in collagen hydrogels with 50,000 HDF cells/ml. Statistically significant differences are shown between the pre and post exposure as well as the sham and post exposure. Significance assessed by ANOVA (Tukey's multiple comparison correction) *** - p = 0.0007, * - p = 0.0116, below the graph are representative images of the 3 conditions scale bars are 200 nm, N=6

depolarisation and damage by ROS.

The pressure profile used for this experiment was a 1psi/s compression to 80 psi for 30 mins followed by an 8 psi/s decompression, which has already been demonstrated to cause bubble formation. In this experiment only gels containing 50,000 cells/ml were used, which did strongly inhibit bubble formation previously but provides enough cells for accurate live dead analysis. Figure 8.8 shows the results of the fluorescent live dead analysis with comparison of the live cell percentage pre-pressure profile, post sham profile and post actual pressure profile. As can be seen there is a significant reduction in the proportion of live cells following the dive profile, which supports the original hypothesis. The magnitude of the reductions were 11.56% and 15.82% from the sham and pre-dive respectively. These reductions are less than the 30% found by Sobolewski et al. for the bubble proximity experiments and the $\sim$ 40% reported by Wang et al. for

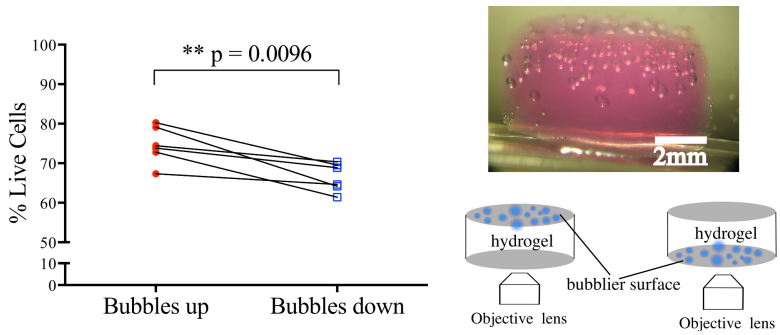

Figure 8.9: The result of the post exposure live dead measurement spilt according to the orientation of the gel. Diagram of the orientation is shown to the right of the graph as is an image taken through the side of the gel post decompression. A statistically significant difference is found between the two orientation as assessed by a paired t-test

high $pp\mathrm{O}_2$ mediated cell death [65, 68] .

To understand this magnitude difference we must consider both the geometry of the 3D culture and the pressure profiles used. It has already been discussed in chapter 7 that bubbles do not form uniformly throughout the collagen gels, but follow the gradient of supersaturation. In the works of Sobolewski et al. 30% of endothelial cells which came into contact with bubbles died; as such only a proportion of the cells within the collagen gel are likely to die by this mechanism [68]. The same is true for the $pp\mathrm{O}_2$, as seen in Figure 8.7, there will be a gradient of $pp\mathrm{O}_2$ in the gel with again only a small proportion of the cells exposed to the higher concentrations. If this gradient is taken into account, it is understandable that the mean cell death measured for both the top and bottom portions of the gel is lower than the 2D works. To provide a more direct comparison to the other works, the live dead measurements of the post exposure gels were subdivided depending on the orientation in which the images were taken, see Figure 8.9. It can be seen that there is a significant decrease in the percentage of live cells for samples with bubbles nearest the objective lens, i.e. those exposed to the higher $pp\mathrm{O}_2$ and a higher likelihood of bubble proximity. The increase in % cell death for the bubbles down samples are 19.8% and 15.6% as compared to the pre-exposure and sham exposure groups respectively. This value is closer to the literature but still below any combination of the two effects. To understand this we must consider the 3D geometry. Both the $pp\mathrm{O}_2$ gradient and non-homogeneous bubble distribution (see Figure 8.9) mean that the proportion of cells exposed to the maximum $pp\mathrm{O}_2$ and those likely to experience bubble contact is far lower than in either of the 2D cell culture

experiments. Estimating the number of cells that contact a bubble is not possible with the current imaging setup however if one were to estimated that 50% of cells were in contact with a bubble, predicted cell death based on the 2D results for the 3D system would be 15%. The magnitude and duration of the ppO_2 exposure in the 3D geometry must also be considered. In the work of Wang et al., endothelial cells were exposed to a ppO_2 ten times that of atmospheric oxygen for 52 mins. In this experiment, the external ppO_2 was six times that of ambient air pressure and the time of exposure was only 30 mins. Cell death at 30 mins in the Wang et al. study was reported as $\sim$20%. If one now considers the ppO_2, as seen in Figure 8.7. it can be seen that only cells towards the edge of the collagen gel are exposed to the highest increased ppO_2. If an estimate that 20% of cells are exposed levels of ppO2 comparable to the 2D experiment only a 4% increase in cell death would be expected. Thus if the ppO2 gradient and bubble distribution are taken into account, it may be argued that cell death measured for the top of the gel greater than either of the 2D studies. This suggests that the level of cell death seen in our experiments is higher than that caused by high ppO_2 only or bubble cell contact only. Although one explanation of this is that the increased cell death is due to the combined effects of high ppO_2 and bubble contact, it may also be the case that fibroblasts are more susceptible to ppO_2 and/or bubble contact than endothelial cells. It could also be the case that all cell types are more vulnerable to ppO_2 and/or bubble contact mediated cell death when in 3D culture. Further investigation would be required to understand the separate affects of ppO_2 and bubble-cell proximity. Use of HUVEC cells in the 3D culture would be of particular interest to provide a direct comparison to the 2D experiments. In addition, the amount of bubble caused death and ppO_2 caused death could be separated by using either dive parameters (such as decompression rate), or nucleation material parameters (such as chloroform treatment) to control the number of bubbles produced in a given profile. Furthermore time lapse fluorescent imaging during the dive could be used to separate these two effects. This would require either modification to the chamber for the use of a thinner optical window, or the alteration of the inverted fluorescent microscope table to allow the objective lens to be brought closer to the sample.

8.4 Conclusions

This chapter has been an investigation into various cell bubble interactions. In particular, this chapter has sought to provide evidence which is lacking in the literature regarding the interaction between stromal cells, bubbles and increased $pp\mathrm{O}_2$. In the first section of the chapter it was shown that bubble nucleation is lowered by the metabolism of oxygen. This finding suggests that tissues with high cell densities may be protected from bubble formation by their inherent undersaturation. It was then shown that the bubbles which did nucleate within the varying cell density gels, reached similar plateau radii and had similar half lives. Given the lower initial supersaturation confirmed by the measurements, modelling and nucleation results; this plateau radius result was not predicted. It was originally hypothesised that bubbles would be both less numerous and smaller in the higher cell density gels. This result could be due to the relationship, shown in chapter 6, where lower numbers of bubbles have higher plateau radii and longer half lives. This highlights the importance for models of bubble dynamics to include competition for dissolved gases.

The second hypothesis concerned the effect of dive profiles on cell viability. Cell viability may be affected by both increased $pp\mathrm{O}_2$, and by bubble contact. To investigate the effect of both these mechanisms, the viability of HDF cells within collagen gels were measured following a prescribed pressure profile. Cell death following the pressure profile was higher than that following the sham exposure, indicating that cell death may be caused by one or both of the high $pp\mathrm{O}_2$ and bubble contact mechanisms. The magnitude of the cell death initially appeared lower than the data reported for either bubble contact or increased $pp\mathrm{O}_2$ alone. However, when geometry of the 3D culture was taken into consideration as well as the length and magnitude of the $pp\mathrm{O}_2$ exposure, it appears that there is higher cell death than found for the $pp\mathrm{O}_2$ response alone. This is suggestive that either both mechanisms are contributing to cell death; or that the change in either cell type or 3D culture are the cause. This could be determined in the current system with additional experiments.

Cell death may also be important for modelling tissue gas kinetics *in vivo*. If increased ambient pressure and decompression disrupts cellular metabolism of oxygen, undersaturation of cell rich tissues will diminish. For the first ”dive” and in the short to mid term after this ”dive” possible variation in cellular metabolism does not appear to

affect bubble nucleation or growth as measured in collagen gels. However, for the cell densities more typically found *in vivo*, and over longer time periods, this effect could become important. This would be of particular importance for dive algorithms which aim to be used for repetitive exposures over several days and for commercial divers undertaking saturation dives.

Chapter 9

General Conclusions

DCS is a complex condition, with many variables influencing its development, and the causal mechanisms of injury not clearly described. In particular, the role of extravascular bubble formation and growth is poorly understood [25, 13]. One of the major difficulties in understanding the role of these bubbles is the lack of quantitative evidence about their distribution within the body and their growth dynamics. The main obstacle to obtaining such evidence is the difficulty in observing or measuring extravascular bubble formation, subsequent dynamics and interactions with biological structures *in vivo*. A review of the available literature revealed several different measurement techniques which aim to over come this obstacle. Techniques for extravascular bubble measurement are far less developed than those of vascular bubbles, where ultrasound is routinely used to assess bubble density in human divers [74]. Traditionally extravascular bubble formation has been assessed via histological sectioning or invasive light microscopy. These methods have informed much of the understanding regarding the distribution of bubbles in the body. One of the drawbacks of such data however, is that the majority is not quantitative. That which is, generally represents only a single time point post dive. Thus the utility of such data for understanding the time course of bubble nucleation, growth and dissolution is limited.

Current dive algorithms aim to prevent DCS by limiting the growth of bubbles through controlling dive parameters, specifically the ascent rate. The algorithms tend to model divers as a series of compartments, which are loosely intended to model different tissue types within the body [371]. Parameterisation and validation of such models with the current experimental data is a problem within the DCS field [87]. The current most widely used procedure relies on a maximum likelihood method developed

by Weathersby et al. [151]. The procedure can be summarised as follows: a bubble dynamics model is run with an initial set of parameters. A bubble output, usually total free gas volume, is used to infer the risk of DCS using a risk function. The risk for the particular simulation is compared to the incidence of DCS reported for that dive in large databases of DCS incidences, either with or without time of onset and type of symptoms. The input parameters are then adjusted to attempt to better match this symptoms database. If the final optimal parameter set is within physiological limits, this is used as proof of validation of the mechanistic model [14, 165, 172]. However as a validation methodology this has serious flaws. The risk function tacitly assumes the form of the relationship between bubble formation and the probability of DCS. As discussed by Tikuisus et al. the selection of the bubble feature, (i.e. surface area, volume, number etc) will affect the final prediction of DCS risk [182]. Not only is there scant evidence regarding this relationship, there is positive evidence that the vascular bubble grade does not correlate with the risk of DCS [78]. By using this validation technique, it cannot be known whether the mechanistic model of bubble formation and growth is valid.

These problems may be addressed by the use of a joint *in vitro* and computational modelling approach. An *in vitro* system may allow detailed quantitative data to be more easily extracted, and the system itself can be made more similar to a computational model. By using this joint approach appropriately, the reduction of the systems complexity enables isolated testing of the effects material and dive parameters may have on bubble dynamics. The similarity of the computational and experimental system also allows hypotheses, generated by the computational model, to be tested in the experimental system, and enables observations from the experimental system to be used to develop the complexity of the computational model. An important pitfall to avoid with such a system, and a criticism that has been made of their use, is the loss of biological relevance [16]. It should always be kept in mind that the overall aim is not to build a very good predictor for bubble dynamics in this specific *in vitro* system, but to use the *in vitro* system and computational model to increase understanding of DCS and ultimately improve the tools to help avoid its occurrence.

Chapters 3-5 of this work outline the development and testing of a novel experimental system with a complementary computational model: an experimental system

consisting of a collagen gel within a miniature pressure chamber; and a 3-dimensional spatially explicit multi-bubble computational model. The experimental chamber system provides control over the temperature, and pressure of the sample, as well as providing real-time data on bubble formation and dynamics over the course of a preset pressure profile. The collagen gel has been shown to be a good tissue mimic in many instances and is widely used throughout the tissue engineering field [195]. The computational model created simultaneously with the experimental system, enables simulations of multiple bubbles within a 3-dimensional gel. The model is novel within the DCS field in providing both 3-dimensional spatially explicit dissolved gas distributions and multi-bubble dynamics. The derivation of the computational model highlighted the inconsistencies of a tissue elasticity term, currently widely used in the literature [174, 4, 166, 175, 176, 220], with a continuum mechanics framework. The replacement of the term with a hyperelastic neo-Hookean term used in the modelling of rubber [219] was suggested as a reasonable alternative. The initial implementation, parameterisation and sensitivity analysis of the computational model was able to show that, in the experimental system the diffusion coefficient would be the dominant material parameter. Tissue stiffness was found to be the widest ranging parameter *in vivo* and as such, may play a role in bubble dynamics. Collagen gels have a low mechanical stiffness and are therefore only able to mimic the most compliant tissues, limiting its ability to validate the entire range of mechanical parameters.

Chapter 6 demonstrated the utility of the joint experimental and computational approach. Simple control over the experimental system enabled direct validation of how mass transfer into and out of the bubble is computationally modelled. A large difference between the initial simulations and measured results, revealed that the model was a poor descriptor of this behaviour, with mass transfer out of the bubble being far too large. This was rectified by the addition of a bubble surface diffusion barrier, implemented by a lower diffusion coefficient for the bubble surface in the governing equations. This diffusion barrier has been a source of controversy in the literature. Some researchers have introduced diffusion barriers with very low diffusion coefficients in order to match the time course of bubble evolution to the time of onset of DCS [165]. Other researchers have argued that the introduction of such unphysiological values of the diffusion coefficients is unsupported and unnecessary [176]. The work in this thesis is one of the

only direct validations showing that introducing a diffusion barrier provides a better fit to actual measured bubble dynamics, indeed to the best of our knowledge, it is the only case to do so in a collagen gel. The work of van Liew et al. had previously showed that their model, which did not include any diffusion barrier, under predicted the lifetime of bubbles in saline [149]. For collagen gels, the diffusion barrier that provided an optimal fit, was based on an initial small reduction from the bulk diffusion coefficient with variation according to the surface area of the bubble. A similar surface area dependence was used in a 2-dimensional model of bubble dynamics by O'Brien [220]. The physical interpretation for such a barrier is that surfactant molecules which are present in the collagen gel, adhere to the air-liquid interface at the bubble surface, and reduce mass transfer. Experimental evidence of such mechanisms is found in the fields of ultrasound contrast agents and the modelling of aeration reactors [220, 296, 297, 299]. Although the surfactants in collagen gels may not be identical to those found *in vivo*, it is most likely that surfactants adhere to the bubble liquid interface *in vivo* and produce a similar effect. This means that models which currently do not include a diffusion barrier [176, 158] are likely to be over estimating the size of bubbles *in vivo*.

Chapter 6 also provided an investigation into the changes in bubble dynamics due to variations in the dive parameters using both the computational and *in vitro* models. Discrepancies between the computational model and the *in vitro* results were found for the changes in bubble plateau radius and half life with variation in decompression rate. The experimental data show a statistically significant trend for decreasing plateau radius with increasing decompression rate, whereas in the simulated response there was a trend for increasing bubble size with increasing decompression rate. The experimental result is somewhat counterintuitive and is contrary to the computational simulations and to the models of O'Brien et al., Gerhardt et al. and Gurmen et al. [220, 165, 271]. These data for collagen gels are either erroneous, or point to a potentially important and unaccounted for mechanism. One possibility is the role of visco- or poroelasticity. Such a mechanism could act to restrict the size of bubbles with fast initial growth, whilst slower growing bubbles would experience less viscous resistance and hence, grow to larger sizes. Viscosity was discussed in the computational models development, however it was felt that the additional mathematical and computational complexity its implementation would introduce, required experimental evidence that it

was a significant factor in bubble dynamics. These data may provide that incentive, all the more so as the viscoelasticity of tissues in the body is well established [228].

The experimental work of chapter 6 also provided evidence in support of predictions made in the literature regarding the competition for dissolved gas amongst bubbles [158, 178, 175]. The bubble densities at which competition for dissolved gas became apparent in the collagen gels was similar to that predicted by both van Liew and Burkardt as well as Chappell and Srinivasan for tissues with long half times [158, 178, 175]. This is an important phenomenon both for describing bubble dynamics and for preventing DCS. Depending on the mechanisms by which bubbles are thought to cause DCS, a large number of smaller bubbles could be less harmful than a smaller number of larger bubbles or vice versa [220, 182]. The computational model was able to show that the spatial position of the bubbles in relation to the gel edge and the initial size of the bubble nuclei were parameters that impacted significantly on subsequent bubble dynamics. These parameters could account for much of the radius and half life variation seen in the *in vitro* data, which was not predicted by the dive parameters.

The relative importance of bubble-bubble interactions, specifically coalescence, was another area in which this experimental system was able to provide new insight. The majority of previous DCS bubble models do not model direct bubble-bubble interactions [176]. In one computational model which does, coalescence is assumed to occur instantaneously [220]. This is shown to be a largely inaccurate description of the dynamics in collagen gels where the coalescence efficiency is low. The number of interfaces which form and the velocity of colliding bubbles is likely to play an important role in this efficiency.

One of the main conclusions that can be drawn from all the findings of chapter 6 is the importance of bubble density. This feature will affect much of the subsequent bubble dynamics, through dictating initial bubble size, spatial distribution, as well as the likelihood and velocity of bubble-bubble collisions. To provide bubble density estimates bubble nucleation is the key process that must be better understood and modelled.

The *in vitro* model can again be used as a powerful tool in the investigation of nucleation but it must be carefully applied. Unlike with the material parameters, where the similarity of collagen gels to tissues is well understood, how similar nucleation in collagen gels is to nucleation in tissue, is less well defined. A good argument can how-

ever be made that collagen gels are more biomimetic in their constituents and structure, than gelatin, agarose or water; three models upon which much of the current nucleation theory is ultimately based [352, 206, 2, 141, 143]. It can even be argued that nucleation within and from the surface of cells will be more accurately represented in a collagen gel than in 2D culture or suspension as previously used [360, 352].

One of the most critical problems for DCS and nucleation models is identifying possible nucleation sites *in vivo*. One of the most compelling findings of this thesis is the dependence of nucleation on the components of the ECM. It was shown that bone fragments, despite having the appropriate geometry for nucleation, did not nucleate bubbles. It was also shown that several cell types, Hacat, Adipocytes and HDF's do not significantly increase bubble nucleation when intact and alive. These findings add to the body of evidence against bubble nucleation occurring from the caveolae, cell-cell junctions or intracellular lipid droplets of live cells *in vivo*. By contrast, the ability of polymeric collagen, extracted from tendon, to nucleate bubbles was strikingly clear. This nucleation was over 20 fold greater than the synthetic dopants. This was particularly interesting given the *in vivo* findings of Gersh et al. which showed that bubble density in guinea pig tendon was far lower than fattier tissues and below the levels found in the collagen gels [327, 32]. The elimination of this nucleating propensity by agitation with chloroform suggests non-polar molecules in the extracted matrix are the source. Non-polar molecules are hydrophobic and therefore could line existing crevices or flat surfaces, or provide stabilising molecular skins. All of these mechanisms would provide micronuclei stability. The most obvious source of non-polar molecules would be neutral lipids, these are sometimes present in the ECM but are mostly stored in cells or make up the cell membrane [325, 362]. One hypothesis is that mechanical cell damage causes intracellular or cell membrane lipids to be released into the ECM where they are able to act as nucleation sites. This is supported by a large amount of experimental evidence in the literature [327, 32, 352, 124]. It is a particularly attractive hypothesis as it would explain the strong nucleating propensity of the polymeric collagen - the first stage in the extraction from calf tendon is a vigorous mechanical breakdown without prior decellularisation of the tendon. However, Raman spectroscopy of the polymeric collagen did not clearly show the presence of lipids. Chloroform treatment was found to effect the Raman spectra of the collagen solution, however the changes appeared to

be in the secondary structure of the collagen fibrils, and it is unclear how this may be causing the loss of nucleating propensity.

Quantification of the effect each dive parameter had on nucleation within polymeric collagen gels revealed that nucleation was significantly affected by the maximum depth, time of dive and decompression rate, but not by the rate of compression. In addition experimental variation of two parameters simultaneously, and time of nucleation were investigated. Simulation of the dissolved gas concentration in the gels and comparison to the two parameter variation and time of nucleation provide additional strong support for the theory that bubble nucleation can be predicted by the level of tissue supersaturation.

The final chapter in the thesis addressed the question of how does diving and specifically decompression lead to the symptoms that constitute DCS. Whilst *in vitro* models will never have the complexity of an entire animal and cannot exhibit 'symptoms' of DCS, cellular responses to bubbles and high oxygen partial pressures can be investigated in a more detailed way. The experimental system in this work provides the only model found in the literature that can monitor the combined effects bubbles have on cells, that cells have on bubble dynamics and that high $pp\mathrm{O}_2$ has on cells. Increasing the cellular density of the gels led to a decrease in the measured dissolved gas concentration and a decrease in bubble nucleation. There was no significant change in the plateau radii or half lives of the bubbles with varying cellular density of the gels. The plateau radius result was unexpected. It was originally hypothesised that bubbles would be smaller in more cell dense gels, due to the reduction in total available dissolved gas. However as shown in chapter 6, where fewer bubbles nucleate they grow larger as there is less competition for dissolved gas. In this case; gels with higher cell densities and hence lower supersaturation, nucleate fewer bubbles. This reduces the competition for dissolved gas amongst these bubbles, resulting in larger than expected plateau radii. Current bubble models do not vary the magnitude of the oxygen windows in different tissues/compartments [372, 176, 220], however, as shown here, this may have a significant impact on the bubble density and hence bubble dynamics of different tissues. This is an effect that could be easily incorporated into current dive algorithms by simply varying the venous oxygen concentration of different tissue compartments.

Finally, the impact which bubble nucleation has on cell viability was investigated.

It was shown that the combination of bubble nucleation and higher $pp\mathrm{O}_2$ led to cell death within 1 hr of the end of the dive. The amount of cell death found in this work appear to be greater than that reported by 2D cell culture studies into either bubble proximity or high $pp\mathrm{O}_2$ alone [65, 68]. This work in isolation constitutes a novel addition to the literature, however it can more interestingly be viewed as a proof of the utility of this experimental system. The use collagen gels in this type of study could be easily extended to more biologically complex structures such as neovasculature or cellularly aligned gels, for which existing techniques already exist [196, 199, 200]. In addition, more specific staining and time course analysis could be used to investigate mechanisms of cell damage more fully. Elucidating these types of mechanisms will facilitate the understanding of how different biological structures in the body respond to diving stress and decompression. Ultimately it is plausible that some of the wide ranging symptoms of DCS could be understood from such investigations.

Overall this work has developed and shown the utility in using a combined experimental and computational approach to understanding bubble dynamics in tissues. The use of a biomimetic *in vitro* model with a pressure chamber capable of providing real time bubble measurements, allows precise quantitative data to be extracted from the experimental system and thus compared to the computational model. The utility of this approach has been demonstrated through the direct validation of the computational model as well as through the use of the computational model in interpretation of experimental results. The comparison of the model and the experimental data has shown that a diffusion barrier at the bubble surface which reduces mass transfer is likely to be present and has highlighted the central importance of nucleation in modelling bubble dynamics. Assessment of suggested *in vivo* nucleation sites from the literature has revealed that intact cells are unlikely to provide nucleation sites, however the ECM and the possible cellular debris that may be found within it appear to be an important and novel site for nucleation. The effects which the metabolic activity of cells have on bubble dynamics, has been shown and the cell death caused by bubbles and high $pp\mathrm{O}_2$ have been clearly demonstrated.

9.1 Further Work

The work in this thesis has highlighted many new and interesting lines of research which merit further work. The key avenues of potential further work will be briefly outlined and data of a preliminary study designed to parameterise a model for the spatial distribution of bubble nuclei is presented.

9.1.1 Experimental set up development

The experimental set up could be improved upon and developed in many ways. Without re-building the chamber improvements could be made to the imaging system. Better automation of the image processing analysis, specifically for gels with high bubble densities where the majority of gels overlap, is needed. The use of a machine learning segmentation algorithm was tested and appeared to be a promising avenue of research. However, one of the main obstacles to a more automated analysis lies in the quality and consistency of images. Improved consistency of the imaging would be achieved by better optics, specifically an objective corrected for spherical aberrations and a more powerful light source. In addition, more accurate timing of the imaging would be greatly facilitated by using a single labview program to control both the pressure systems and camera. More significant alterations to the chamber would include the insertion of an additional window in the side of the chamber. This would allow imaging in two planes of the gels which would enable the assessment of spatial variations in bubble dynamics. Adaptation to allow for a thinner chamber window would make the chamber compatible with an inverted fluorescent microscope. The introduction of perfusion to the chamber would better reflect *in vivo* tissues. The experimental system would then include perfusion rate as a controllable parameter.

9.1.2 Tissue mechanics

The results of chapter 6 suggest that viscous or poroelastic mechanisms are impacting significantly on bubble dynamics. The inclusion of such dynamics in the governing equations of the model could be done in several ways. The effect of viscous properties on bubble dynamics is already widely modelled in the ultrasound field [373] and a poroelastic framework developed by Rice and Cleary [226], is used within the fields of soil mechanics. It would also be advisable to incorporate anisotropic material parameters into the formulation at this point. In this way more biomimetic gels such as layered

and cellularly aligned gels could be modelled [195, 198, 199, 200].

9.1.3 Numerical implementations

There are many ways in which the numerical implementation here could be furthered. The most immediately applicable would be the introduction of a refined mesh scheme. One possibility would be to apply a model currently used in a related field such as polymer foaming, volcanic eruption or metal annealing [313, 374, 258]. In particular it would be of interest to apply a phase field model which accounts for both nucleation and bubble-bubble interactions [333]. If this was done non-spherical bubbles and coalescence could be modelled; their impact on bubble dynamics could then be assessed and validated.

9.1.4 Validation

Work in developing methodologies to measure all material parameters of the gels more effectively, would improve the quality of the validation and parameterisation of the model. Methodologies to measure the rheological properties could include optical tweezers or two photon microscopy [278, 285]. A diffusion cell could be used to provide separate diffusion coefficients for various gases. In addition quantification of the solubilities of nitrogen and oxygen and how they are affected by increasing gel density would be of utility [291]. Additionally, assessment of whether the introduction of viscoelasticity into the model was able to account for the decompression rate trend in plateau radii would be of interest.

9.1.5 Nucleation

The most crucial further work is in developing both a model of nucleation and in uncovering the source of the nucleation in the polymeric collagen. One particular experiment that could be done to investigate the cellular debris hypothesis, would be to mechanically disrupt cells prior to seeding them within a collagen gel. This could be done by simply drawing the cell suspension through a fine needle several times prior to its addition into the neutralised collagen solution. This is well know to lyse cells due to the capillary pressure when forced through the needle. Varying the number of cells in the cell suspension or the gauge of the needle could be used to introduce more or less debris. An alternative experiment which could investigate this hypothesis would be to

decellularise the calf tendon prior to extracting polymeric collagen (this would require the extraction method to be altered significantly and re-optimised).

9.1.5.1 Development of a nucleation model

As discussed in chapter 6, the position of a bubble relative the surface of the gel will impact on the dynamics of the bubbles growth. In the current model micronuclei are randomly distributed within the gel, similar to that of O'Brien [220]. However, it was observed that this was not a good representation of the experimental system where there appeared to be a non-uniform distribution. It was hypothesised that bubble nucleation followed the spatially explicit supersaturation within the gels. The investigation of this spatial distribution and its incorporation into the 3D multi-bubble model was investigated in a preliminary study by Johns [375]. The spatial distribution of bubbles within hydrogels was analysed using low magnification images taken from both birds-eye and cross-sectional views. No variation in the spatial distribution of nuclei was found in the birds eye view, but the bubble distribution could be clearly seen to be inhomogeneous in the cross sectional view. As mentioned earlier in this section, in order to investigate the bubble distribution in real time, the three dimensional co-ordinates of the bubbles would need to be known. For this to be achieved a side window in the chamber and accompanying imaging system would be needed. As this was not possible, gels were instead removed from the chamber post decompression and placed in a dish containing PBS. Images from the side of the gel i.e. (cross sectional) view through the gels were taken with a stereo microscope and attached digital camera. Representative images for different dive profiles can be seen in the left-hand panels of Figure 9.1. Although these images are of reasonably good quality, image analysis was unsuccessful, largely due to the varying light conditions and orientation of the the gels. The right hand side of Figure 9.1 shows the cross sectional view through the centre of a simulated gel exposed to the same pressure profile as the experiment. Despite the lack of quantitative data, qualitative analyses and comparisons can still be made. The inhomogeneous distribution of bubbles, in the top three images, is clear, with more bubbles present towards the top of the gels. Comparison of the left and right-hand images shows that the dissolved gas concentration appears to mirror the bubble distributions. This is particularly striking when comparing the bottom of the four panels to the other three. In this gel the pro-

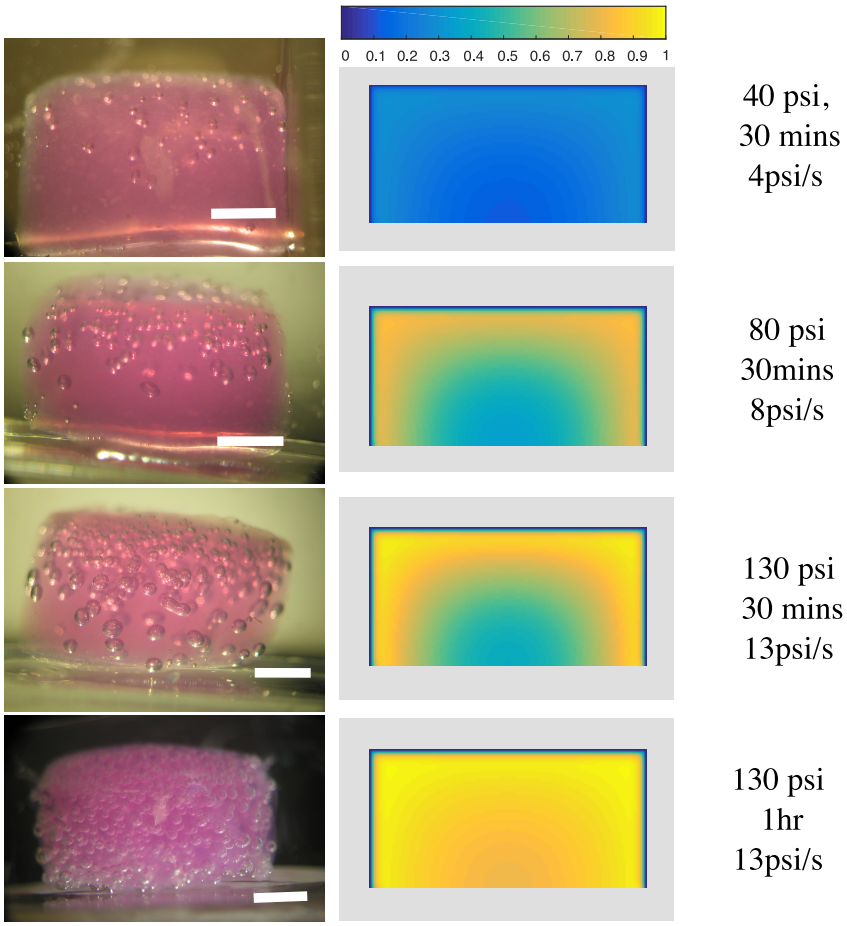

Figure 9.1: Images taken side on showing the change in bubble distribution with changes in the max depth and decompression rate. scale bars are 2mm length.

file of exposure was for a duration of 1hr; the simulated dissolved gas concentration is high and almost uniform. The corresponding gel image shows a far more homogeneous distribution of bubbles than the other images.

A Monte-Carlo method for incorporating this data into at 2-dimensional finite difference model was investigated. In this model, micronuclei were uniformly seeded throughout the finite difference grid. The micronuclei were ”activated” with a probability dependent on the supersaturation of the finite difference grid node. This method qualitatively produced the same bubble distribution seen in the gel images however, in this preliminary analysis bubble formation was not modelled. To do this it would be necessary to calculate the amount of gas in the new bubble and ensure mass was conserved during the activation process.

Appendix A

Solid mechanics

A.1 Derivation of quartic expression for the solution to the bubble expansion problem using linear elastic constitutive equations

$$R_{ref} = \frac{R_0}{1 - \frac{P_0}{3K}} \tag{A.1}$$

Subbing 4.34 into 4.32

$$R_B = \frac{\left(1 - \frac{P_\infty}{3K}\right)}{\left(1 - \frac{P_0}{3K}\right)} R_0 + \frac{b}{R_0^2}\left(1 - \frac{P_0}{3K}\right)^2 \tag{A.2}$$

rearranging 4.33

$$P_B = \left(P_0 + \frac{2\gamma}{R_0}\right)\left(\frac{R_0}{R_B}\right)^3 \tag{A.3}$$

subbing into 4.31

$$P_B - \frac{2\gamma}{R_B} - P_\infty = \frac{4b\mu}{R_{ref}^3} \tag{A.4}$$

rearranging for b:

$$b = \left(P_B - \frac{2\gamma}{R_B} - P_\infty\right)\frac{R_{ref}^3}{4\mu} \tag{A.5}$$

plugging in P_B and and 4.34

$$b = \left(\frac{P_0 R_0^3}{R_B^3} + \frac{2\gamma R_0^2}{R_B^3} - \frac{2\gamma}{R_B} - P_\infty\right)\left(\frac{R_0}{1 - \frac{P_0}{3K}}\right)^3 \frac{1}{4\mu} \tag{A.6}$$

Substitute into 4.32

$$R_B = \frac{1-\frac{P_\infty}{3K}}{1-\frac{P_0}{3K}} R_0 + \frac{b}{R_0^2}\left(1-\frac{P_0}{3K}\right)^2 \tag{A.7}$$

putting in the expression for b

$$R_B = \frac{\left(1-\frac{P_\infty}{3K}\right)}{\left(1-\frac{P_0}{3K}\right)} R_0 + \left(\frac{P_0 R_0^3}{R_B^3} + \frac{2\gamma R_0^2}{R_B^3} - \frac{2\gamma}{R_B} - P_\infty\right)\left(\frac{R_0}{4\mu\left(1-\frac{P_0}{3K}\right)}\right) \tag{A.8}$$

A.1.1 Nims term

$$P_{B_N} = P_\infty + \frac{2\alpha}{R} + \frac{4}{3}\pi R^3 M \tag{A.9}$$

Where M is the lumper parameter previously described as $K/V_{affected}$ using P1V1=P2V2

$$\left(P_0 + \frac{2\alpha}{R_0} + \frac{4}{3}\pi R_0^3 M\right) R_0^3 = \left(P_\infty + \frac{2\alpha}{R} + \frac{4}{3}\pi R^3 M\right) R^3 \tag{A.10}$$

$$0 = P_\infty R^3 + 2\sigma R^2 + \frac{4}{3}\pi M R^6 - R_0^3 P_0 - R_0^2 2\sigma - \frac{4}{3}\pi R_0^6 \tag{A.11}$$

A.1.2 Gent term

$$P_{B_G} = P_\infty + \frac{2\alpha}{R} + \frac{\mu}{2}\left[5 - 4\left(\frac{R_B}{R_0}\right)^{-1} - \left(\frac{R_B}{R_0}\right)^{-4}\right] \tag{A.12}$$

$$\left(P_0 + \frac{2\alpha}{R_0}\right) R_0^3 = \left(P_\infty + \frac{2\alpha}{R} + \frac{\mu}{2}\left[5 - 4\left(\frac{R}{R_0}\right)^{-1} - \left(\frac{R}{R_0}\right)^{-4}\right]\right) R^3 \tag{A.13}$$

$$0 = \left(-P_0 R_0^3 - 2\sigma R_0^2\right) R + \left(P_\infty + \frac{5\mu}{2}\right) R^4 + (2\sigma - 2\mu R_0) R^3 - \frac{\mu}{2} R_0^4 \tag{A.14}$$

Appendix B

Numerical Code

The full code can be downloaded from dropbox, via this link, it can be compiled and run as is in Xcode Version 6.1.1 (6A2008a), in can also be run in codeBUG.
https://www.dropbox.com/sh/bl3svmya9jinu87/AADcVesM1XQ4BGHc4sCUF5Foa?dl=0

Bibliography

[1] Alexandra L Klinger, Judith Kandel, Benjamin Pichette, and David M Eckmann. Pefluorocarbon inhibition of bubble induced ca2+ transients in an in vitro model of vascular gas embolism. *Experimental Biology and Medicine*, 239(1):116–122, 2014.

[2] David E. Yount. Bubble formation in gelatin: A model for decompression sickness. *Journal of Applied Physics*, 47(11):5081, 1976.

[3] E D Thalmann, E C Parker, S S Survanshi, and P K Weathersby. Improved probabilistic decompression model risk predictions using linear-exponential kinetics. *Undersea Hyperb Med*, 24(4):255–274, 1997.

[4] R S Srinivasan, W a Gerth, and M R Powell. Mathematical models of diffusion-limited gas bubble dynamics in tissue. *Journal of applied physiology (Bethesda, Md. : 1985)*, 86(2):732–741, February 1999.

[5] Jm Walker, Am Myers, Md Schluchter, Vm Goldberg, Ai Caplan, Ja Berilla, Jm Mansour, and Jf Welter. Nondestructive evaluation of hydrogel mechanical properties using ultrasound. *Annals of biomedical . . .* , 39(10):2521–2530, 2011.

[6] Ramachandra Gerth, Wayne A and Srinivansan. Mathematical Models of Diffusion-Limited Gas Bubble Evolution in Perfused Tissue. Technical report, Navy Experimental Diving Unit, 2013.

[7] Boyle R. New pneumatical experiments about respiration. *Philos Trans*, 5:2011–2058, 1670.

[8] Richard Moon. The natural progression of decompression illness and development of recompression procedures. *SPUMS JOURNAL*, 30(1):36–45, 2000.

[9] Arthur Edwin Boycott, GCC Damant, and John Scott Haldane. The prevention of compressed-air illness. *Journal of Hygiene*, 8(03):342–443, 1908.

[10] D Z H Levett and I L Millar. Bubble trouble: a review of diving physiology and disease. *Postgraduate medical journal*, 84(997):571–8, November 2008.

[11] Richard D. Vann, Frank K. Butler, Simon J. Mitchell, and Richard E. Moon. Decompression illness. *The Lancet*, 377(9760):153–164, 2011.

[12] Alfred A Bove. *Bove and Davis' diving medicine*. WB Saunders Philadelphia, 2004.

[13] D.H. Brubakk, A.O. and Neuman, T.S. and Elliott. *Bennett and Elliott's Physiology and Medicine of Diving*. Saunders, 4th edition, 2003.

[14] J Hugon. Decompression models: review, relevance and validation capabilities. *Undersea & hyperbaric medicine: journal of the Undersea and Hyperbaric Medical Society, Inc*, 41(6):531–556, 2013.

[15] C. Dethloff. *Modeling of Helium Bubble Nucleation and Growth in Neutron Irradiated RAFM Steels*. Schriftenreihe des Instituts für Angewandte Materialien. KIT Scientific Publ., 2014.

[16] Jean-Eric Blatteau, Jean-Baptiste Souraud, Emmanuel Gempp, and Alain Boussuges. Gas nuclei, their origin, and their role in bubble formation. *Aviation, space, and environmental medicine*, 77(10):1068–1076, 2006.

[17] Lu Feng. *Experimental Study of Nucleation in Polystyrene/CO2 System*. PhD thesis, The Ohio State University, 2012.

[18] Virginie Papadopoulou, Robert J. Eckersley, Costantino Balestra, Thodoris D. Karapantsios, and Meng Xing Tang. A critical review of physiological bubble formation in hyperbaric decompression. *Advances in Colloid and Interface Science*, 191-192:22–30, 2013.

[19] Paul Bert. *La pression barométrique*. G. Masson, 1878.

[20] Leonard Hill and JJR Macleod. Caisson illness and diver's palsy. an experimental study. *Journal of Hygiene*, 3(04):401–445, 1903.

[21] J Trevor Hughes. Venous infarction of the spinal cord. *Neurology*, 21(8):794–794, 1971.

[22] JM Hallenbeck. Cinephotomicrography of dog spinal vessels during cord-damaging decompression sickness. *Neurology*, 26(2):190–190, 1976.

[23] TJ Francis, JL Griffin, LD Homer, GH Pezeshkpour, AJ Dutka, and ET Flynn. Bubble-induced dysfunction in acute spinal cord decompression sickness. *Journal of Applied Physiology*, 68(4):1368–1375, 1990.

[24] TJ Francis, GH Pezeshkpour, and AJ Dutka. Arterial gas embolism as a pathophysiologic mechanism for spinal cord decompression sickness. Technical report, DTIC Document, 1989.

[25] Marzella Yin. Role of Extravasucular Gas Bubbles in Spinal Cord Injury Induced by Decompresssion sickness in the Rat. *Experimental and Molecular Pathology*, 61:16–23, 1994.

[26] Edward J Dick Jr, Jonathan R Broome, and Isaac J Hayward. Acute neurologic decompression illness in pigs: lesions of the spinal cord and brain. *Laboratory animal science*, 47(1):50–57, 1997.

[27] AC Palmer. Nature and incidence of bubbles in the spinal cord of decompressed goats. *Undersea & hyperbaric medicine: journal of the Undersea and Hyperbaric Medical Society, Inc*, 24(3):193–200, 1997.

[28] AR Taylor and DP Byrnes. Foramen magnum and high cervical cord compression. *Brain*, 97(1):473–480, 1974.

[29] BA Hills. Spinal decompression sickness: The occurrence of lamellar bodies in spinal tissue as potential foci for bubble formation. *Journal of the South Pacific Underwater Medicine Society*, 1992.

[30] JJ Sykes and LJ Yaffe. Light and electron microscopic alterations in spinal cord myelin sheaths after decompression sickness. *Undersea biomedical research*, 12(3):251–258, 1985.

[31] Jeremy P Bond and Daniel A Kirschner. Spinal cord myelin is vulnerable to decompression. *Molecular and chemical neuropathology*, 30(3):273–288, 1997.

[32] Isidore Gersh, Gladys E Hawkinson, and Elizabeth H Jenney. Comparison of vascular and extravascular bubbles following decompression from high pressure atmospheres of oxygen, helium-oxygen, argon-oxygen and air. *Journal of Cellular and Comparative Physiology*, 26(2):63–74, 1945.

[33] Isidore Gersh and Hubert R Catchpole. Appearance and distribution of gas bubbles in rabbits decompressed to altitude. *Journal of Cellular and Comparative Physiology*, 28(3):253–269, 1946.

[34] Emmanuel Gempp, Jean-eric Blatteau, Olivier Simon, and Eric Stephant. Musculoskeletal decompression sickness and risk of dysbaric osteonecrosis in recreational divers. *Diving and Hyperbaric Medicine Journal*, 2009.

[35] Motoo Kitano, Mahito Kawashima, Ko Hayashi, Shin-ichiro Tokufuji, Yasushi Taya, Charles E Lehner, et al. Histopathological study of the bone marrow of rabbit femora with experimentally induced acute decompression sickness: with consideration of pathogenesis of dysbaric osteonecrosis in diver's femur. *ł*, 14(2):223–231, 1994.

[36] John P Ramirez S Jone, J R and S B Doty. The pathophysiologic role of fat in dysbaric osteonecrosis. *Clinical orthopaedics and related research*, 296:256–264, 1993.

[37] D.H Elliott. Acute decompression sickness. *The Lancet*, pages 1193–1199, 1974.

[38] L Vroman, AL Adams, and M Klings. Interactions among human blood proteins at interfaces. In *Federation proceedings*, volume 30, page 1494, 1971.

[39] David M Eckmann, Stephen C Armstead, and Feras Mardini. Surfactants reduce platelet-bubble and platelet-platelet binding induced by in vitro air embolism. *Anesthesiology*, 103(6):1204–10, December 2005.

[40] R Thorsen, T Lie, R, and H Holmsen. Induction of platelet aggregation in vitro by microbubbles of nitrogen. *Undersea biomedical research*, 16(6), 1989.

[41] Jean-Michel Pontier, Nicolas Vallée, and Lionel Bourdon. Bubble-induced platelet aggregation in a rat model of decompression sickness. *Journal of applied physiology (Bethesda, Md. : 1985)*, 107(6):1825–9, December 2009.

[42] Gerardo Bosco, Zhong-jin Yang, Guglielmo Di Tano, Enrico M Camporesi, Fabio Faralli, Fabio Savini, Angelo Landolfi, Christian Doria, and Giorgio Fanò. Effect of in-water oxygen prebreathing at different depths on decompression-induced bubble formation and platelet activation. *Journal of applied physiology*, 108(5):1077–1083, 2010.

[43] J Lehtosalo, T Tervo, and L A Laitinen. Bubbles and Hematologic Alterations in Intracranial Veins During Experimental Decompression Sickness *. *Acta Neuropathologica*, pages 139–144, 1983.

[44] RF Goad, TS Neuman, and PG Linaweaver Jr. Hematologic changes in man during decompression: relations to overt decompression sickness and bubble scores. *Aviation, space, and environmental medicine*, 47(8):863–867, 1976.

[45] DM Pickles, D Ogston, and AG MacDonald. Effects of gas bubbling and other forms of convection on platelets in vitro. *Journal of Applied Physiology*, 67(3):1250–1255, 1989.

[46] Kate Lambrechts, Jean-Michel Pontier, Costantino Balestra, Aleksandra Mazur, Qiong Wang, Peter Buzzacott, Michael Theron, Jacques Mansourati, and François Guerrero. Effect of a single, open-sea, air scuba dive on human micro-and macrovascular function. *European journal of applied physiology*, 113(10):2637–2645, 2013.

[47] Kate Lambrechts, Jean-Michel Pontier, Aleksandra Mazur, Peter Buzzacott, Christelle Goanvec, Qiong Wang, Michaël Theron, Marc Belhomme, and

François Guerrero. Effect of splenectomy on platelet activation and decompression sickness outcome in a rat model of decompression. *Diving and hyperbaric medicine*, page 154, 2014.

[48] J-M Pontier and K Lambrechts. Effect of oxygen-breathing during a decompression-stop on bubble-induced platelet activation after an open-sea air dive. *European journal of applied physiology*, 114(6):1175–1181, 2014.

[49] Paul A Nyquist, Edward J Dick, Thomas B Buttolph, N Yquist Pa, D I C K Ej, and B Uttolph Tb. Detection of Leukocyte Activation in Pigs with Neurologic Decompression Sickness. *Environmental Medicine*, 75(3), 2004.

[50] Stephen R Thom, Ming Yang, Veena M Bhopale, Shaohui Huang, and Tatyana N Milovanova. Microparticles initiate decompression-induced neutrophil activation and subsequent vascular injuries. *Journal of applied physiology (Bethesda, Md. : 1985)*, 110(2):340–351, February 2011.

[51] Nancy J Bigley, Heather Perymon, Gloria C Bowman, Barbara E Hull, Harold F Stills, and Richard a Henderson. Inflammatory cytokines and cell adhesion molecules in a rat model of decompression sickness. *Journal of interferon & cytokine research : the official journal of the International Society for Interferon and Cytokine Research*, 28(2):55–63, February 2008.

[52] A Ersson, C Linder, K Ohlsson, and A Ekholm. Cytokine response after acute hyperbaric exposure in the rat. *Undersea & hyperbaric medicine*, 25(4):217, 1998.

[53] CA Ward, D McCullough, and WD Fraser. Relation between complement activation and susceptibility to decompression sickness. *Journal of Applied Physiology*, 62(3):1160–1166, 1987.

[54] P Nyquist, R Ball, and MJ Sheridan. Complement levels before and after dives with a high risk of dcs. *Undersea & Hyperbaric Medicine*, 34(3):191, 2007.

[55] KL Huang and YC Lin. Activation of complement and neutrophils increases vascular permeability during air embolism. *Aviation, space, and environmental medicine*, 68(4):300–305, 1997.

[56] Kate Lambrechts, Jean-Michel Pontier, Aleksandra Mazur, Peter Buzzacott, Jean Morin, Qiong Wang, Michael Theron, and Francois Guerrero. Effect of decompression-induced bubble formation on highly trained divers microvascular function. *Physiological reports*, 1(6):e00142, 2013.

[57] A Hjelde, K Bergh, AO Brubakk, and OJ Iversen. Complement activation in divers after repeated air/heliox dives and its possible relevance to dcs. *Journal of Applied Physiology*, 78(3):1140–1144, 1995.

[58] Vibeke Nossum, A Hjelde, K Bergh, and AO Brubakk. Lack of effect of anti-c5a monoclonal antibody on endothelial injury by gas bubbles in the rabbit after decompression. *Undersea & hyperbaric medicine*, 27(1):27, 2000.

[59] Alf O Brubakk and Andreas Mollerlokken. The role of intra-vascular bubbles and the vascular endothelium in decompression sickness. *Diving and Hyperbaric Medicine Journal*, 2009.

[60] James K Liao. Linking endothelial dysfunction with endothelial cell activation. *Journal of Clinical Investigation*, 123(2):540, 2013.

[61] Stephen R Thom, Michael Bennett, Neil D Banham, Walter Chin, Denise F Blake, Anders Rosen, Neal W Pollock, Dennis Madden, Otto Barak, Alessandro Marroni, et al. Association of microparticles and neutrophil activation with decompression sickness. *Journal of Applied Physiology*, 119(5):427–434, 2015.

[62] Stephen R. Thom, Michael Bennett, Neil D. Banham, Walter Chin, Denise F. Blake, Anders Rosen, Neal W. Pollock, Dennis Madden, Otto Barak, Alessandro Marroni, Costantino Balestra, Peter Germonpre, Massimo Pieri, Danilo Cialoni, Phi-Nga Jeannie Le, Christopher Logue, David Lambert, Kevin R. Hardy, Douglas Sward, Ming Yang, Veena B. Bhopale, and Zeljko Dujic. Association of microparticles and neutrophil activation with decompression sickness. *Journal of Applied Physiology*, 119(5):427–434, 2015.

[63] Leigh a. Madden and Gerard Laden. Gas bubbles may not be the underlying cause of decompression illness - The at-depth endothelial dysfunction hypothesis. *Medical Hypotheses*, 72(4):389–392, 2009.

[64] RJ Gryglewski, RMJ Palmer, and S Moncada. Superoxide anion is involved in the breakdown of endothelium-derived vascular relaxing factor. *Nature*, (320):454 – 456, 1986.

[65] Qiong Wang, François Guerrero, Aleksandra Mazur, Kate Lambrechts, Peter Buzzacott, MARAC Belhomme, and Michaël Theron. Reactive oxygen species, mitochondria, and endothelial cell death during in vitro simulated dives. *Medicine and science in sports and exercise*, 47(7):1362–1371, 2015.

[66] Vibeke Nossum, Astrid Hjelde, and Alf O Brubakk. Small amounts of venous gas embolism cause delayed impairment of endothelial function and increase polymorphonuclear neutrophil infiltration. *European journal of applied physiology*, 86(3):209–214, 2002.

[67] Vibeke Nossum, S Koteng, and AO Brubakk. Endothelial damage by bubbles in the pulmonary artery of the pig. *Undersea & hyperbaric medicine*, 26(1):1, 1999.

[68] Peter Sobolewski, Judith Kandel, Alexandra L Klinger, and David M Eckmann. Air bubble contact with endothelial cells in vitro induces calcium influx and IP3-dependent release of calcium stores. *American journal of physiology. Cell physiology*, 301(3):C679–86, September 2011.

[69] G Laden, L Madden, G Purdy, and J Greenman. Endothelial damage as a marker of decompression stress. In *UHMS Meeting Abstracts*, 2004.

[70] Andreas Møllerløkken, Vegard J Berge, Arve Jørgensen, Ulrik Wisløff, and Alf O Brubakk. Effect of a short-acting no donor on bubble formation from a saturation dive in pigs. *Journal of Applied Physiology*, 101(6):1541–1545, 2006.

[71] Z Dujic, I Palada, Z. Valic, D Duplacic, U Wisloff, and A Brubakk. Exogenous nitric oxide and bubble formation in divers. *Medicine & science in sports & exercise*, 2006.

[72] Radu-Virgil Stan. Structure and function of endothelial caveolae. *Microscopy research and technique*, 57(5):350–364, 2002.

[73] S Daniels, JM Davies, WD Paton, and EB Smith. The detection of gas bubbles in guinea-pigs after decompression from air saturation dives using ultrasonic imaging. *The Journal of physiology*, 308:369, 1980.

[74] Neal W Pollock. Use of ultrasound in decompression research. *Diving and Hyperbaric Medicine Journal*, 2007.

[75] Peter Germonpré, Virginie Papadopoulou, Walter Hemelryck, Georges Obeid, Pierre Lafère, Robert J Eckersley, Ming-Xing Tang, and Costantino Balestra. The use of portable 2d echocardiography and 'frame-based'bubble counting as a tool to evaluate diving decompression stress. *Diving Hyperb Med*, 44:5–13, 2014.

[76] Sealy L J Frank H C Spencer M P, Spencer C D and Lindbergh J. Experiments on decompression bubbles in the circulation using ultrasonic and electromagnetic flowmeters. *Journal of Occupational and Environmental Medicine*, 11(5):238–244, 1969.

[77] KD Sawatzky and RY Nishi. Intravascular doppler-detected bubbles and decompression sickness. *Undersea Biomedical Research*, 16(1 Supplement), 1990.

[78] Sawatzky KD. The relationship between intravascular doppler-detected gas bubbles and decompression sickness after bounce diving in humans. Master's thesis, York University, Toronto, 1991.

[79] Merrill P Spencer and David C Johanson. Investigation of new principles for human decompression schedules using doppler ultrasonic blood bubble detection. Technical report, DTIC Document, 1974.

[80] TS Neuman, DA Hall, and PG Linaweaver Jr. Gas phase separation during decompression in man: ultrasound monitoring. *Undersea biomedical research*, 3(2):121–130, 1976.

[81] RD Vann, AP Dick, and PD Barry. Doppler bubble measurements and decompression sickness. *Undersea Biomedical Research*, 9(1 Supplement), 1982.

[82] Olav Sande Eftedal. *Ultrasonic detection of decompression induced vascular microbubbles*. PhD thesis, Det medisinske fakultet, 2007.

[83] Olav Sande Eftedal, Stian Lydersen, and Alf O Brubakk. The relationship between venous gas bubbles and adverse effects of decompression after air dives. *Undersea & Hyperbaric Medicine*, 34(2):99, 2007.

[84] S Lesley Blogg and Andreas Møllerløkken. The use of venous gas emboli to validate dive computers. In *Undesignated and Unpublished Reports*. Norwegian University of Science and Technology., 2012.

[85] David J Doolette, Keith A Gault, and Christian R Gutvik. Sample size requirement for comparison of decompression outcomes using ultrasonically detected venous gas emboli (vge): power calculations using monte carlo resampling from real data. *Diving Hyperb Med*, 44(1):14–19, 2014.

[86] A Møllerløkken, SL Blogg, DJ Doolette, RY Nishi, and NW Pollock. Consensus guidelines for the use of ultrasound for diving research. *Diving and hyperbaric medicine*, 46(1):26–32, 2016.

[87] D J Doolette, R N Upton, and C Grant. Countercurrent compartmental models describe hind limb skeletal muscle helium kinetics at resting and low blood flows in sheep. *Acta physiologica Scandinavica*, 185(2):109–21, October 2005.

[88] L Marzella and A Yin. Role of extravascular gas bubbles in spinal cord injury induced by decompression sickness in the rat. *Experimental and molecular pathology*, 61(1):16–23, 1994.

[89] P Eggleton, SR Elsden, J Fegler, and CO Hebb. A study of the effects of rapid-decompression'in certain animals. *The Journal of physiology*, 104(2):129, 1945.

[90] B.G D'Aoust, L Stayton, and L.S Smith. Separation of basic parameters of decompression using fingerling salmon. *Undersea biomedical research*, 7(3):171–81, 1980.

[91] Brian G D'Aoust and Lynwood S Smith. Bends in fish. *Comparative Biochemistry and Physiology Part A: Physiology*, 49(2):311–321, 1974.

[92] Kasper Hansen, Nikolaj Schmidt, and Michael Pedersen. Ct, pet and mri in experimental barometric physiology. *The FASEB Journal*, 29(1 Supplement):678–15, 2015.

[93] B R Bollinger. *Dual-frequency ultrasound detection and sizing of microbubbles for studying decompression sickness.* PhD thesis, Dartmouth College, 2008.

[94] David E Yount. Skins of varying premeability: A stabilization mechnism for gas cavitation nuclei. *The Journal of the Acoustical Society of America*, 65(June), 1979.

[95] David E Yount. On the evolution, generation, and regeneration of gas nuclei. *The Journal of the Acoustical Society of America*, 80:1473–1481, 1982.

[96] B R Wienke. Reduced gradient bubble model. *International journal of biomedical computing*, 26(4):237–256, 1990.

[97] Qiong Wang, Marc Belhomme, François Guerrero, Aleksandra Mazur, Kate Lambrechts, and Michaël Theron. Diving under a microscope–a new simple and versatile in vitro diving device for fluorescence and confocal microscopy allowing the controls of hydrostatic pressure, gas pressures, and kinetics of gas saturation. *Microscopy and microanalysis : the official journal of Microscopy Society of America, Microbeam Analysis Society, Microscopical Society of Canada*, 19(3):608–16, June 2013.

[98] Jay C Buckey, Darin A Knaus, Donna L Alvarenga, Marc A Kenton, and Patrick J Magari. Dual-frequency ultrasound for detecting and sizing bubbles. *Acta Astronautica*, 56(9):1041–1047, 2005.

[99] B R Bollinger, J C Wilbur, T G Donoghue, S D Phillips, D A Knaus, D L Alvarenga, and J C Buckey. Dual-frequency ultrasound detection of stationary microbubbles in tissue . *Office*, 36(2):127–136, 2009.

[100] Georges L Chahine, Michel Tanguay, and Greg Loraine. Acoustic measurements bubbles in biological tiessure. *Journal of Hydrodynamics, Ser. B*, 21(1):47–64, 2009.

[101] Jed C Wilbur, Scott D Phillips, Terry G Donoghue, DL Alvarenga, Darin A Knaus, Patrick J Magari, and Jay C Buckey. Signals consistent with microbubbles detected in legs of normal human subjects after exercise. *Journal of Applied Physiology*, 108(2):240–244, 2010.

[102] J. G. Swan, B. D. Bollinger, T. G. Donoghue, J. C. Wilbur, S. D. Phillips, D. L. Alvarenga, D. a. Knaus, P. J. Magari, and J. C. Buckey. Microbubble detection following hyperbaric chamber dives using dual-frequency ultrasound. *Journal of Applied Physiology*, 111(5):1323–1328, 2011.

[103] J G Swan, J C Wilbur, K L Moodie, S A Kane, D A Knaus, S D Phillips, T L Beach, A M Fellows, P J Magari, J C Buckey, and Jacob G Swan. Microbubbles are detected prior to larger bubbles following decompression. *Journal of Applied Physiology*, 2014.

[104] E Stéphant, E Gempp, and J-E Blatteau. Role of MRI in the detection of marrow bubbles after musculoskeletal decompression sickness predictive of subsequent dysbaric osteonecrosis. *Clinical radiology*, 63(12):1380–1383, 2008.

[105] E Gempp, P Louge, T Lafolie, S Demaistre, M Hugon, and JE Blatteau. Relation between cervical and thoracic spinal canal stenosis and the development of spinal cord decompression sickness in recreational scuba divers. *Spinal cord*, 52(3):236–240, 2014.

[106] TJR Francis, GH Pezeshkpour, AJ Dutka, JM Hallenbeck, and ET Flynn. Is there a role for the autochthonous bubble in the pathogenesis of spinal cord decompression sickness? *Journal of Neuropathology & Experimental Neurology*, 47(4):475–487, 1988.

[107] L Marzella and A Yin. Role of ischemia in rats with spinal cord injury induced by decompression sickness. *Experimental and molecular pathology*, 62(1):22–27, 1995.

[108] RT Mahon, CR Auker, SG Bradley, A Mendelson, and AA Hall. The emulsified perfluorocarbon oxycyte improves spinal cord injury in a swine model of decompression sickness. *Spinal cord*, 51(3):188–192, 2013.

[109] O Hyldegaard and J Madsen. Influence of heliox, oxygen, and n2o-o2 breathing on n2 bubbles in adipose tissue. *Undersea biomedical research*, 16(3):185–193, 1989.

[110] O Hyldegaard and J Madsen. Effect of air and heliox breathing on n2 bubbles in the spinal white matter in the rat. Undersea and Hyperbaric Medical Society, Inc., 1989.

[111] Ole Hyldegaard and J Madsen. Effect of air, heliox, and oxygen breathing on air bubbles in aqueous tissues in the rat. *Undersea & hyperbaric medicine: journal of the Undersea and Hyperbaric Medical Society, Inc*, 21(4):413–424, 1994.

[112] O Hyldegaard, D Kerem, and Y Melamed. Effect of combined recompression and air, oxygen, or heliox breathing on air bubbles in rat tissues. *Journal of Applied Physiology*, 90(5):1639–1647, 2001.

[113] Ole Hyldegaard and Joop Madsen. Effect of hypobaric air, oxygen, heliox (50: 50), or heliox (80: 20) breathing on air bubbles in adipose tissue. *Journal of Applied Physiology*, 103(3):757–762, 2007.

[114] T Randsøe, Torben M Kvist, and Ole Hyldegaard. Effect of oxygen and heliox breathing on air bubbles in adipose tissue during 25-kpa altitude exposures. *Journal of Applied Physiology*, 105(5):1492–1497, 2008.

[115] T Randsoe and O Hyldegaard. Effect of oxygen breathing and perfluorocarbon emulsion treatment on air bubbles in adipose tissue during decompression sickness. *Journal of Applied Physiology*, pages 1857–1863, 2009.

[116] O Hyldegaard, D Kerem, and Y Melamed. Effect of isobaric breathing gas shifts from air to heliox mixtures on resolution of air bubbles in lipid and aqueous tissues of recompressed rats. *European journal of applied physiology*, 111(9):2183–93, September 2011.

[117] Thomas Randsoe and Ole Hyldegaard. Effect of oxygen breathing on micro oxygen bubbles in nitrogen-depleted rat adipose tissue at sea level and 25 kpa altitude exposures. *Journal of Applied Physiology*, 113(3):426–433, 2012.

[118] O Hyldegaard, D Kerem, and Y Melamed. Effect of combined recompression and air , oxygen , or heliox breathing on air bubbles in rat tissues Effect of combined recompression and air , oxygen , or heliox breathing on air bubbles in rat tissues. *Journal of Applied Physiology*, pages 1639–1647, 2013.

[119] Avi Shupak, Yehuda Arieli, Haim Bitterman, Vera Brod, Ran Arieli, and Giora Rosenhause. High-frequency sound field and bubble formation in a rat decompression model. *Ultrasound in medicine & biology*, 28(5):655–660, 2002.

[120] Michael H Bennett, David J Doolette, and N Heffernan. Ocular tear film bubble counts after recreational compressed air diving. *Undersea & hyperbaric medicine*, 28(1):1, 2001.

[121] R Arieli and a Marmur. Evolution of bubbles from gas micronuclei formed on the luminal aspect of ovine large blood vessels. *Respiratory physiology & neurobiology*, 188(1):49–55, August 2013.

[122] R Arieli and A Marmur. Ex vivo bubble production from ovine large blood vessels: Size on detachment and evidence of "active spots". *Respiratory physiology & neurobiology*, 200:110–117, 2014.

[123] Ran Arieli, Uri Arieli, and Abraham Marmur. Bubble size on detachment from the luminal aspect of ovine large blood vessels after decompression: The effect of mechanical disturbance. *Respiratory physiology & neurobiology*, 216:1–8, 2015.

[124] Virginie Papadopoulou, Sotiris Evgenidis, Robert J Eckersley, Thodoris Mesimeris, Costantino Balestra, Margaritis Kostoglou, and Meng-xing Tang. Decompression induced bubble dynamics on ex vivo fat and muscle tissue surfaces with a new experimental set up. *Colloids and Surfaces B: Biointerfaces*, 129:121–129, 2015.

[125] BA Gooden. The tadpole tail as a model for decompression studies. *The Australian journal of experimental biology and medical science.[Adelaide] University of Adelaide*, 51(1):109, 1973.

[126] P M McDonough and E a Hemmingsen. Bubble formation in crabs induced by limb motions after decompression. *Journal of applied physiology (Bethesda, Md. : 1985)*, 57(1):117–122, 1984.

[127] P M McDonough and E a Hemmingsen. Bubble formation in crustaceans following decompression from hyperbaric gas exposures. *Journal of applied physiology (Bethesda, Md. : 1985)*, 56(2):513–519, 1984.

[128] DL Beyer, BG D'aoust, and LS Smith. Decompression-induced bubble formation in salmonids: comparison to gas bubble disease. *Undersea Biomedical Research*, 3(4):321–338, 1976.

[129] Yehuda Arieli, Ran Arieli, and Avi Shupak. Can high-frequency sound affect gas-bubble dynamics? a study in the intact prawn palaemon elegans. *Ultrasound in medicine & biology*, 26(9):1511–1515, 2000.

[130] Yehuda Arieli, Ran Arieli, and Amit Marx. Hyperbaric oxygen may reduce gas bubbles in decompressed prawns by eliminating gas nuclei. *Journal of Applied Physiology*, 92(6):2596–2599, 2002.

[131] Offir Ertracht, Ran Arieli, Yehuda Arieli, Reut Ron, Zufit Erlichman, and Yochai Adir. Optimal oxygen pressure and time for reduced bubble formation in then2-saturated decompressed prawn. *Journal of Applied Physiology*, 98(4):1309–1313, 2005.

[132] Y Arieli, K Katsenelson, and R Arieli. Bubble reduction after decompression in the prawn Palaemon elegans by pretreatment with hyperbaric oxygen . *Undersea & Hyperbaric Medicine*, 34(5):369–378, 2007.

[133] Alexandra L Klinger, Benjamin Pichette, Peter Sobolewski, and David M Eckmann. Mechanotransductional basis of endothelial cell response to intravascular bubbles. *Integrative Biology*, 3(10):1033–1042, 2011.

[134] S Kobayashi, SD Crooks, and DM Eckmann. In vitro surfactant mitigation of gas bubble contact-induced endothelial cell death. *Control*, 38(1):27–39, 2011.

[135] Peter Sobolewski, Judith Kandel, and David M Eckmann. Air bubble contact with endothelial cells causes a calcium-independent loss in mitochondrial membrane potential. *Biophysical Journal*, 104(2):215a–216a, 2013.

[136] Marco Stubbe, Matthias Nissen, Jessica Schroeder, and Jan Gimsa. The effect of hyperbaric air on the electric activity of neuronal in vitro networks. *Biosensors and Bioelectronics*, 73:153–159, 2015.

[137] DM LeMessurier. Supersaturation and "preformed nuclei" in the etiology of decompression sickness paper presented at the second international meeting on aerospace medicine, 1972.

[138] David E Yount, Chick M Yeung, and Frank W Ingle. Determination of the radii of gas cavitation nuclei by filtering gelatin. *The Journal of the Acoustical Society of America*, 65(6):1440–1450, 1979.

[139] DE Yount and CM Yeung. Bubble formation in supersaturated gelatin: A further investigation of gas cavitation nuclei. *The Journal of the Acoustical Society of America*, pages 702–708, 1981.

[140] Richard H Strauss and Thomas D Kunkle. Isobaric bubble growth: a consequence of altering atmospheric gas. *Science*, 186(4162):443–444, 1974.

[141] T D Kunkle. Bubble dissolution physics and the treatment of decompression sickenss. *Medical Physics*, 10(2):184–190, 1983.

[142] DE Yount, TD Kunkle, JS D'Arrigo, FW Ingle, CM Yeung, and EL Beckman. Stabilization of gas cavitation nuclei by surface-active compounds. *Aviation, space, and environmental medicine*, 48(3):185–189, 1977.

[143] Joseph S. D'Arrigo. Physical properties of the nonionic surfactants surrounding gas cavitation nuclei. *The Journal of Chemical Physics*, 71(4):1809, 1979.

[144] JS D'Arrigo and Y Mano. Bubble production in agarose gels subjected to different decompression schedules. *Undersea biomedical research*, 6(1):93–98, 1979.

[145] Joseph S D'Arrigo. Physical properties of the nonionic surfactants surrounding gas cavitation nuclei. *The Journal of Chemical Physics*, 71(4):1809–1813, 1979.

[146] JS D'Arrigo. Improved method for studying the surface chemistry of bubble formation. *Aviation, space, and environmental medicine*, 49(2):358–361, 1978.

[147] J. D'Arrigo. *Stable Gas-in-Liquid Emulsions: Production in Natural Waters and Artificial Media*. Studies in Interface Science. Elsevier Science, 2003.

[148] Keiji Yano and Yoshihiro Mano. Evaluation of standard decompression schedule by agarose gel method. *The Bulletin of Tokyo Medical and Dental University*, 26(3):197–212, 1979.

[149] HD Van Liew, PJ Unkel, SA Conrad, ME Gervacio, and RW Schubert. In vitro measurements of to validate mathematicla simulations of bubbles which contain more than one gas. 1996.

[150] Robert W Hamilton and Ed Thalmann. Decompression Practice. In T.S. Brubakk, A.O. and Neuman, editor, *Bennett and Elliott's Physiology and medicine of diving*, chapter 10, pages 453–498. New York: Saunders, 2003.

[151] PK Weathersby, LD Homer, and ET Flynn. On the likelihood of decompression sickness. *Journal of Applied Physiology*, 57(3):815–825, 1984.

[152] P K Weathersby, S S Survanshi, L D Homer, E Parker, and E D Thalmann. Predicting the time of occurrence of decompression sickness. *Journal of applied physiology (Bethesda, Md. : 1985)*, 72(4):1541–8, 1992.

[153] S S Survanshi, Paul K Weathersby, and ED Thalmann. Statistically Based Decompression Tables X : Real-Time Decompression Algorithm Using a Probabilistic Model. Technical Report 1996, Naval Medical Research Insititute, 1996.

[154] S S Survanshi and P K Weathersby. Statistically Based Decompression Tables XI: Manned Validation of the LE Probabilistic Model for Air. Technical Report JANUARY 1999, Naval Medical Research Center, 1999.

[155] BG D'aoust, KH Smith, and HT Swanson. Decompression-induced decrease in nitrogen elimination rate in awake dogs. *Journal of applied physiology*, 41(3):348–355, 1976.

[156] BA Hills. Effect of decompression per se on nitrogen elimination. *Journal of Applied Physiology*, 45(6):916–921, 1978.

[157] EP Kindwall, A Baz, EN Lightfoot, EH Lanphier, and A Seireg. Nitrogen elimination in man during decompression. *Undersea biomedical research*, 2(4):285–297, 1975.

[158] H D Van Liew and M E Burkard. Density of decompression bubbles and competition for gas among bubbles, tissue, and blood. *Journal of applied physiology (Bethesda, Md. : 1985)*, 75(5):2293–301, November 1993.

[159] D Doolette, K Gault, W Gerth, and Greg Murphy. U . s . navy dive computer validation. Technical report, Navy Experimental dive unit, 2012.

[160] DE Yount and DC Hoffman. Decompression theory: a dynamic critical-volume hypothesis. In *Bachrach AJ, Matzen MM, eds. Underwater physiology VIII: proceedings of the eighth symposium on underwater physiology. Bethesda: Undersea Medical Society, 1984: 131-46. 22. Yount DE, Lally DA. On the use of oxygen to facilitate decompression. Aviat. Space Environ. Med. 1980; 51: 544*, volume 50, 1984.

[161] David E Yount and DC Hoffman. On the use of a bubble formation model to calculate diving tables. *Aviation, space, and environmental medicine*, 57(2):149–156, 1986.

[162] Benjamin Kuch, Giorgio Buttazzo, and Arne Sieber. Bubble model based decompression algorithm optimised for implementation on a low power microcontroller. *Underwater Technology*, 29(4):195–202, 2011.

[163] DE Yount. Application of bubble formation model to decompression sickness in fingerling salmon. *Undersea biomedical research*, 8(4):199–208, 1981.

[164] DE Yount. Application of a bubble formation model to decompression sickness in rats and humans. *Aviation, space, and environmental medicine*, 50(1):44–50, 1979.

[165] Michael Landon Gernhardt. *Development and evaluation of a decompression stress index based on tissue bubble dynamics*. PhD thesis, University of Pennsylvania, 1991.

[166] R S Srinivasan, W a Gerth, and M R Powell. A mathematical model of diffusion-limited gas bubble dynamics in tissue with varying diffusion region thickness. *Respiration physiology*, 123(1-2):153–64, October 2000.

[167] HD Van Liew. Simulation of the dynamics of decompression sickness bubbles and the generation of new bubbles. *Undersea biomedical research*, 18(4):333–345, 1991.

[168] Hugh D Van Liew and Michael P Hlastala. Influence of bubble size and blood perfusion on absorption of gas bubbles in tissues. *Respiration physiology*, 7(1):111–121, 1969.

[169] Yu Ya Kislyakov and AV Kopyltsov. The rate of gas-soluble growth in tissue under decompression. mathematical modelling. *Respiration physiology*, 71(3):299–306, 1988.

[170] M E Burkard and H D Van Liew. Simulation of exchanges of multiple gases in bubbles in the body. *Respiration physiology*, 95(2):131–45, February 1994.

[171] Hugh D Van Liew, Beverly Bishop, Pio Walder D, and Hermann Rahn. Effects of compression on composition and absorption of tissue gas pockets Effects of compression on composition and absorption of tissue gas pockets '. *Journal of Applied Physics*, 20:927–933, 1965.

[172] Gerth W. A and R.D. Vann. Probabilistic gas and bubble dynamics models of decompression sickness occurrence in air and nitrogen-oxygen diving. *Undersea & hyperbaric medecine*, 24(4):275–292, 1997.

[173] David J Doolette, Wayne a Gerth, and Keith a Gault. Redistribution of Decompression Stop Time From Shallow To Deep Stops Increases Incidence of Decompression Sickness in Air. Technical report, Navy Experimental Diving Unit (NEDU), 2011.

[174] R. Srini Srinivasan, Wayne a. Gerth, and Michael R. Powell. Mathematical Model of Diffusion-Limited Gas Bubble Dynamics in Unstirred Tissue with Finite Volume. *Annals of Biomedical Engineering*, 30(2):232–246, February 2002.

[175] R. Srini Srinivasan, Wayne a. Gerth, and Michael R. Powell. Mathematical Model of Diffusion-Limited Evolution of Multiple Gas Bubbles in Tissue. *Annals of Biomedical Engineering*, 31(4):471–481, April 2003.

[176] J Hugon, J-C Rostain, and B Gardette. A new biophysical decompression model for estimating the risk of articular bends during and after decompression. *Journal of theoretical biology*, 283(1):168–79, August 2011.

[177] M A Chappell and S J Payne. A physiological model of the interaction between tissue bubbles and the formation of blood-borne bubbles under decompression. *Physics in medicine and biology*, 51(9):2321–38, May 2006.

[178] Michael Chappell. *Modelling and Measurement of Bubbles in Decompression Sickness*. PhD thesis, University of Oxford, 2006.

[179] MA Chappell and SJ Payne. A physiological model of the release of gas bubbles from crevices under decompression. *Respiratory physiology & neurobiology*, 153(2):166–180, 2006.

[180] MA Chappell and SJ Payne. A physiological model of gas pockets in crevices and their behavior under compression. *Respiratory physiology & neurobiology*, 152(1):100–114, 2006.

[181] Michael A Chappell, Sébastien Uzel, and Stephen J Payne. Modeling the detachment and transport of bubbles from nucleation sites in small vessels. *Biomedical Engineering, IEEE Transactions on*, 54(11):2106–2108, 2007.

[182] P Tikuisis, KA Gault, and RY Nishi. Prediction of decompression illness using bubble models. *Undersea & hyperbaric medicine: journal of the Undersea and Hyperbaric Medical Society, Inc*, 21(2):129–143, 1994.

[183] H D Van Liew and E.T Flynn. Graphical Analysis:Decompression tables and Dive-Outcome Data. Technical report, Navy Experimental diving unit, 2004.

[184] H D Van Liew and E.T Flynn. Probability of Decompression sickness in no-stop air diving. Technical report, Navy Experimental dive unit, 2004.

[185] David J Doolette and Wayne A Gerth. Xval-he-4b : A maximum permissible tissue tension table for real-time thalmann algortihm support of constant 1.3 atm po2-in-helium diving to 200fsw. Technical report, Navy Experimental dive unit, 2010.

[186] Rami K Korhonen and Simo Saarakkala. *Biomechanics and modeling of skeletal soft tissues*. INTECH Open Access Publisher, 2011.

[187] S.C. Cowin and S.B. Doty. *Tissue Mechanics*. Springer, 2007.

[188] Joshua Owen, Philip Grove, Paul Rademeyer, and Eleanor Stride. The influence of blood on targeted microbubbles. *Journal of The Royal Society Interface*, 11(100):20140622, 2014.

[189] Harvey Lodish, Arnold Berk, S Lawrence Zipursky, Paul Matsudaira, David Baltimore, James Darnell, et al. *Collagen: the fibrous proteins of the matrix*, chapter 22.3. WH Freeman, 4th edition, 2000.

[190] Y.C. Fung. *Biomechanics: Mechanical Properties of Living Tissues*. Springer New York, 2010.

[191] Harvey Rich, Marianne Odlyha, Umber Cheema, Vivek Mudera, and Laurent Bozec. Effects of photochemical riboflavin-mediated crosslinks on the physical properties of collagen constructs and fibrils. *Journal of Materials Science: Materials in Medicine*, 25(1):11–21, 2014.

[192] Showan N Brown, Robert A and Wiseman, Mike and Chuo, C-B and Cheema, Umber and Nazhat. Ultrarapid Engineering of Biomimetic Materials and Tissues: Fabrication of Nano-and Microstructures by Plastic Compression. *Advanced Functional Materials*, 15(11):1762—-1770, 2005.

[193] RA Hadjipanayi, E and Mudera, V and Brown. Close dependence of fibroblast proliferation on collagen scaffold matrix stiffness. *Journal of tissue engineering and regenerative medicine*, 3(2):77–84, 2009.

[194] Josephine P.F. Wong, Danielle Baptista, and Robert a. Brown. Pre-crosslinked polymeric collagen in 3-D models of mechanically stiff tissues: Blended collagen polymer hydrogels for rapid layer fabrication. *Acta Biomaterialia*, 10(12):5005–5011, 2014.

[195] T. Alekseeva. *Introducing controllable 3D features into dense collagen constructs for tissue engineering applications*. PhD thesis, UCL (University College London), 2012.

[196] Katerina Stamati, John V Priestley, Vivek Mudera, and Umber Cheema. Laminin promotes vascular network formation in 3d in vitro collagen scaffolds by regulating vegf uptake. *Experimental cell research*, 327(1):68–77, 2014.

[197] U Cheema, S Y Yang, V Mudera, G G Goldspink, and R A Brown. 3-D in vitro model of early skeletal muscle development. *Cell Motil. Cytoskeleton*, 54:226–236, 2003.

[198] Melanie Georgiou, Stephen CJ Bunting, Heather A Davies, Alison J Loughlin, Jonathan P Golding, and James B Phillips. Engineered neural tissue for peripheral nerve repair. *Biomaterials*, 34(30):7335–7343, 2013.

[199] Prasad Sawadkar, Susan Alexander, Marten Tolk, Jason Wong, Duncan McGrouther, Laurent Bozec, and Vivek Mudera. Development of a surgically optimized graft insertion suture technique to accommodate a tissue-engineered tendon in vivo. *BioResearch open access*, 2(5):327–335, 2013.

[200] Umber Cheema, Zimei Rong, Omar Kirresh, Alexander J Macrobert, Pankaj Vadgama, and Robert A Brown. Oxygen diffusion through collagen scaffolds at defined densities : implications for cell survival in tissue models. *Tissue Engineering*, 6(1):77–84, 2012.

[201] G W Ellis and Woods Hole. A new miniature hydrostatic pressure chamber for microscopy. strain-free optical glass windows facilitate phase-contrast and polarized-light microscopy of living cells. optional fixture permits simultaneous control of pressure and temperature. *The Journal of Cell Biology*, 65, 1975.

[202] Masayoshi Nishiyama and Yoshiyuki Sowa. Microscopic analysis of bacterial motility at high pressure. *Biophysical Journal*, 102(8):1872–1880, 2012.

[203] S.R Besch and P.M Hogan. A small chamber for making optical measurements on single living cells at elevated hydrostatic pressure. *Undersea & hyperbaric medicine : journal of the Undersea and Hyperbaric Medical Society, Inc*, 23:175–184, 1996.

[204] S Koyama, T Miwa, T Sato, and M Aizawa. Optical chamber system designed for microscopic observation of living cells under extremely high hydrostatic pressure. *Extremophiles : life under extreme conditions*, 5(6):409–15, December 2001.

[205] O Friedrich, F V Wegner, M Hartmann, B Frey, K Sommer, and H Ludwig. 'In situ' high pressure confocal Ca2+ Ca2+ -fluorescence microscopy in skeletal muscle: a new method to study pressure limits in mammalian cells. *Undersea and hyperbaric Medical Society*, 33(3), 2006.

[206] E Newton Harvey. Decompression sickness and bubble formation in blood and tissues. *Bulletin of the New York Academy of Medicine*, 21(10):505, 1945.

[207] DP D'Agostino, HA McNally, and JB Dean. Development and testing of hyperbaric atomic force microscopy (afm) and fluorescence microscopy for biological applications. *Journal of microscopy*, 246(2):129–142, 2012.

[208] Daniel A Willistein. An introduction to optical window design, 2006.

[209] K Matthews. The crystran handbook of infra-red and ultra-violet optical materials. *Electric edition (Crystran Ltd., Poole, UK, 2008)*, 2014.

[210] J.H. Moore, C.C. Davis, M.A. Coplan, and S.C. Greer. *Building Scientific Apparatus*. Cambridge University Press, 2009.

[211] C. Otto Gehrckens. *O-Ring BASICS*. Cog, Seal Technology, Dichtungstechnik Gehrstuecken 9, 25421 Pinneberg, Germany, 2012.

[212] Jie-sheng Wang, Shuang Han, Na-na Shen, and Shu-xia Li. Features extraction of flotation froth images and bp neural network soft-sensor model of concentrate

grade optimized by shuffled cuckoo searching algorithm. *The Scientific World Journal*, 2014, 2014.

[213] L.F Nims. Environmental factors affecting decompression sickness. Part I: Physical theory of decompression sickness. In JF Fulton, editor, *Environmental factors affecting decompression sickness. Part I: Physical theory of decompression sickness*, pages 192–222. WB Saunders, 1951.

[214] H.G Vann, R.D and Clark. Bubble growth and mechanical properties of tissue in decompression. *Undersea Biomedical Research*, 2(3):185–194, 1975.

[215] AN Gent and AG Thomas. Forms for the stored (strain) energy function for vulcanized rubber. *Journal of Polymer Science*, 28(118):625–628, 1958.

[216] AN Gent and PB Lindley. Internal rupture of bonded rubber cylinders in tension. In *Proceedings of the Royal Society of London A: Mathematical, Physical and Engineering Sciences*, volume 249, pages 195–205. The Royal Society, 1959.

[217] a. N. Gent and D. a. Tompkins. Surface energy effects for small holes or particles in elastomers. *Journal of Polymer Science Part A-2: Polymer Physics*, 7(9):1483–1487, September 1969.

[218] a. N. Gent. Nucleation and Growth of Gas Bubbles in Elastomers. *Journal of Applied Physics*, 40(6):2520, 1969.

[219] a. N. Gent. Elastic instabilities in rubber. *International Journal of Non-Linear Mechanics*, 40(2-3):165–175, March 2005.

[220] Jean-Pierre O'Brien. *Improved characterisation and modelling of microbubbles in biomedical applications*. PhD thesis, UCL (University College London), 2013.

[221] Saul Goldman. Generalizations of the Young-Laplace equation for the pressure of a mechanically stable gas bubble in a soft elastic material. *The Journal of chemical physics*, 131(18):1–8, November 2009.

[222] H D Van Liew and E T Flynn. A simple probabilistic model for standard air dives that is focused on total decompression time. *Undersea & hyperbaric medicine*

: journal of the Undersea and Hyperbaric Medical Society, Inc, 32(4):199–213, 2005.

[223] W J Yang and C Y Liang. Dynamics of dissolution of gas bubbles or pockets in tissues. *Journal of biomechanics*, 5(4):321–32, July 1972.

[224] E Zana and L G Leal. The dynamics and dissolution of gas bubbles in a viscoelastic fluid. *Ratio*, 4(3):237–262, 1978.

[225] Evgenia a. Zabolotskaya, Yurii a. Ilinskii, G. Douglas Meegan, and Mark F. Hamilton. Modifications of the equation for gas bubble dynamics in a soft elastic medium. *The Journal of the Acoustical Society of America*, 118(4):2173, 2005.

[226] James R Rice and Michael P Cleary. Some basic stress diffusion solutions for fluid-saturated elastic porous media with compressible constituents. *Reviews of Geophysics*, 14(2):227–241, 1976.

[227] C Church. The effects of an elastic solid surface layer on the radial pulsations of gas bubbles. *The Journal of the Acoustical Society of America*, 97(3):1510–1521, 1995.

[228] Y.C. Fung. *Biomechanics: Mechanical Properties of Living Tissues*. Springer New York, 2013.

[229] Guillermo Terrones and Phillip A. Gauglitz. Deformation of a spherical bubble in soft solid media under external pressure. *The Quarterly Journal of Mechanics and Applied Mathematics*, 56(6):513–525, 2003.

[230] Lev D Landau, E M Lifshitz, J B Sykes, W H Reid, and Ellis H Dill. Theory of Elasticity: Vol. 7 of Course of Theoretical Physics, 1960.

[231] Herbert Wang. *Theory of linear poroelasticity with applications to geomechanics and hydrogeology*. Princeton University Press, 2000.

[232] Jay D. Humphrey. Continuum biomechanics of soft biological tissues: Review Paper. *Proceedings: Mathematical, Physical and Engineering Sciences*, 459(2029):3–46, 2002.

[233] J M Solano-altamirano, John D Malcolm, Saul Goldman, and Saul Solano-Altamirano, JM and Malcolm, John D and Goldman. Gas bubble dynamics in soft materials. *arXiv preprint arXiv:1409.3292*, 2014.

[234] Harvey Rich, Marianne Odlyha, Umber Cheema, Vivek Mudera, and Laurent Bozec. Effects of photochemical riboflavin-mediated crosslinks on the physical properties of collagen constructs and fibrils. *Journal of Materials Science: Materials in Medicine*, 25(1):11–21, 2014.

[235] Marzio Bergomi, Joël Cugnoni, John Botsis, Urs C. Belser, and H.W. Anselm Wiskott. The role of the fluid phase in the viscous response of bovine periodontal ligament. *Journal of Biomechanics*, 43(6):1146 – 1152, 2010.

[236] AN Gent. A new constitutive relation for rubber. *Rubber chemistry and technology*, 69(1):59–61, 1996.

[237] L. Angela Mihai, LiKang Chin, Paul A. Janmey, and Alain Goriely. A comparison of hyperelastic constitutive models applicable to brain and fat tissues. *Journal of The Royal Society Interface*, 12(110), 2015.

[238] Jessica a. Zimberlin, Naomi Sanabria-DeLong, Gregory N. Tew, and Alfred J. Crosby. Cavitation rheology for soft materials. *Soft Matter*, 3(6):763, 2007.

[239] Santanu Kundu and Alfred J Crosby. Cavitation and fracture behavior of polyacrylamide hydrogels. *Soft Matter*, 5(20):3963–3968, 2009.

[240] Jun Cui, Cheol Hee Lee, Aline Delbos, Jennifer J. McManus, and Alfred J. Crosby. Cavitation rheology of the eye lens. *Soft Matter*, 7(17):7827, 2011.

[241] MS Chin and BB Freniere. Cavitation Rheology as a Potential Method for in vivo Assessment of Skin Biomechanics. *Plastic and . . .* , 131(2):1–4, 2013.

[242] Cornelius O Horgan. The remarkable gent constitutive model for hyperelastic materials. *International Journal of Non-Linear Mechanics*, 68:9–16, 2015.

[243] Jian Zhu and Tiefeng Li. Snap-through Expansion of a Gas Bubble in an Elastomer. *The Journal of Adhesion*, 87(5):466–481, 2011.

[244] G a Holzapfel, T C Gasser, and R W Ogden. A new constitutive framework for arterial wall mechanics and a comperative study of material models. *J. Elasticity*, 61:1–48, 2000.

[245] Tom Shearer. A new strain energy function for the hyperelastic modelling of ligaments and tendons based on fascicle microstructure. *Journal of biomechanics*, 48(2):290–297, 2015.

[246] Julien Jaravel, Sylvie Castagnet, Jean-Claude Grandidier, and Mikaël Gueguen. Experimental real-time tracking and diffusion/mechanics numerical simulation of cavitation in gas-saturated elastomers. *International Journal of Solids and Structures*, 50(9):1314–1324, May 2013.

[247] The individual and universal gas constants.

[248] Charles S Peskin. Numerical analysis of blood flow in the heart. *Journal of computational physics*, 25(3):220–252, 1977.

[249] Rajat Mittal and Gianluca Iaccarino. Immersed boundary methods. *Annu. Rev. Fluid Mech.*, 37:239–261, 2005.

[250] G. Tryggvason, R. Scardovelli, and S. Zaleski. *Direct Numerical Simulations of Gas–Liquid Multiphase Flows*. Cambridge University Press, 2011.

[251] Lennart Schneiders, Daniel Hartmann, Matthias Meinke, and Wolfgang Schröder. An accurate moving boundary formulation in cut-cell methods. *Journal of Computational Physics*, 235:786–809, 2013.

[252] N. Ozisik. *Finite Difference Methods in Heat Transfer*. Heat Transfer. Taylor & Francis, 1994.

[253] Vladislav K Saul'Yev. *Integration of Equations of Parabolic Type by the Method of Nets: International Series of Monographs in Pure and Applied Mathematics*, volume 54. Elsevier, 2014.

[254] D.J. Duffy and A. Germani. *C# for Financial Markets*. The Wiley Finance Series. Wiley, 2013.

[255] A Fell and GP Willeke. Fast simulation code for heating, phase changes and dopant diffusion in silicon laser processing using the alternating direction explicit (ade) method. *Applied Physics A*, 98(2):435–440, 2010.

[256] LJ Campbell and B Yin. On the stability of alternating-direction explicit methods for advection-diffusion equations. *Numerical Methods for Partial Differential Equations*, 23(6):1429–1444, 2007.

[257] Zuzana Buckova, Matthias Ehrhardt, and Michael Günther. Alternating direction explicit methods for convection diffusion equations. *Acta Mathematica Universitatis Comenianae*, 84(2):309–325, 2015.

[258] Y Sun and C Beckermann. Phase-field modeling of bubble growth and flow in a Hele-Shaw cell. *International Journal of Heat and Mass Transfer*, 2010.

[259] RS Qin and HK Bhadeshia. Phase field method. *Materials science and technology*, 26(7):803–811, 2010.

[260] S. Gross and A. Reusken. *Numerical Methods for Two-phase Incompressible Flows*. Springer Series in Computational Mathematics. Springer Berlin Heidelberg, 2011.

[261] S. Marella, S. Krishnan, H. Liu, and H.S. Udaykumar. Sharp interface cartesian grid method i: An easily implemented technique for 3d moving boundary computations. *Journal of Computational Physics*, 210(1):1 – 31, 2005.

[262] H. Liu, S. Krishnan, S. Marella, and H.S. Udaykumar. Sharp interface cartesian grid method ii: A technique for simulating droplet interactions with surfaces of arbitrary shape. *Journal of Computational Physics*, 210(1):32 – 54, 2005.

[263] Yi Yang and H.S. Udaykumar. Sharp interface cartesian grid method iii: Solidification of pure materials and binary solutions. *Journal of Computational Physics*, 210(1):55 – 74, 2005.

[264] HS Udaykumar, L Mao, and R Mittal. A finite-volume sharp interface scheme for dendritic growth simulations: comparison with microscopic solvability theory. *Numerical Heat Transfer: Part B: Fundamentals*, 42(5):389–409, 2002.

[265] Salih Ozen Unverdi and Grétar Tryggvason. A front-tracking method for viscous, incompressible, multi-fluid flows. *Journal of computational physics*, 100(1):25–37, 1992.

[266] Jung Hee Seo and Rajat Mittal. A sharp-interface immersed boundary method with improved mass conservation and reduced spurious pressure oscillations. *Journal of computational physics*, 230(19):7347–7363, 2011.

[267] Thomas Sumner. *Sensitivity analysis in systems biology modelling and its application to a multi-scale model of blood glucose homeostasis*. PhD thesis, UCL (University College London), 2010.

[268] T Langø, T Mørland, and AO Brubakk. Diffusion coefficients and solubility coefficients for gases in biological fluids and tissues: a review. *Undersea & hyperbaric medicine: journal of the Undersea and Hyperbaric Medical Society, Inc*, 23(4):247–272, 1996.

[269] Katerina Stamati. *In vitro vasculogenesis in 3D*. PhD thesis, UCL (University College London), 2014.

[270] Adai Colom, Roland Galgoczy, Isaac Almendros, Antonio Xaubet, Ramon Farré, and Jordi Alcaraz. Oxygen diffusion and consumption in extracellular matrix gels: Implications for designing three-dimensional cultures. *Journal of Biomedical Materials Research - Part A*, 102(8):2776–2784, 2014.

[271] N M Gürmen, a J Llewellyn, R a Gilbert, and S M Egi. Simulation of dynamic bubble spectra in tissues. *IEEE transactions on bio-medical engineering*, 48(2):185–93, February 2001.

[272] E.L. Cussler. *Diffusion: Mass Transfer in Fluid Systems*. Cambridge Series in Chemical Engineering. Cambridge University Press, 2009.

[273] Estelle Chaix, Carole Guillaume, and Valérie Guillard. Oxygen and Carbon Dioxide Solubility and Diffusivity in Solid Food Matrices: A Review of Past and Current Knowledge. *Comprehensive Reviews in Food Science and Food Safety*, 13(3):261–286, 2014.

[274] Peter Vaupel. Effect of percentual water content in tissues and liquids on the diffusion coefficients of O2, CO2, N2, and H2. *Pflügers Archiv European Journal of Physiology*, 361(2):201–204, 1976.

[275] J. Malda, J. Rouwkema, D. E. Martens, E. P. le Comte, F. K. Kooy, J. Tramper, C. A. van Blitterswijk, and J. Riesle. Oxygen gradients in tissue-engineered pegt/pbt cartilaginous constructs: Measurement and modeling. *Biotechnology and Bioengineering*, 86(1):9–18, 2004.

[276] Caroline Androjna, Jorge E Gatica, Joanne M Belovich, and Kathleen A Derwin. Oxygen diffusion through natural extracellular matrices: implications for estimating "critical thickness" values in tendon tissue engineering. *Tissue Engineering Part A*, 14(4):559–569, 2008.

[277] Ralph T. Ferrell and David M. Himmelblau. Diffusion coefficients of nitrogen and oxygen in water. *Journal of Chemical & Engineering Data*, 12(1):111–115, 1967.

[278] Marjan Shayegan and Nancy R Forde. Microrheological characterization of collagen systems: from molecular solutions to fibrillar gels. *PloS one*, 8(8):e70590, January 2013.

[279] David M Knapp, Victor H Barocas, and Alice G Moon. Rheology of reconstituted type I collagen gel in confined compression. *Journal of Rheology (1978-present)*, 41(5):971–993, 1997.

[280] S Hsu, AM Jamieson, and J Blackwell. Viscoelastic studies of extracellular matrix interactions in a model native collagen gel system. *Biorheology*, 31(1):21–36, 1993.

[281] D Velegol and F Lanni. Cell traction forces on soft biomaterials. I. Microrheology of type I collagen gels. *Biophysical journal*, 81(3):1786–92, September 2001.

[282] A Basu. *Shear defomation in polymer gels and dense colloidal suspensions*. PhD thesis, University of Pennsylvania, 2012.

[283] Victor H Barocas, Alice G Moon, and Robert T Tranquillo. The fibroblast-populated collagen microsphere assay of cell traction force—part 2: Measurement of the cell traction parameter. *Journal of biomechanical engineering*, 117(2):161–170, 1995.

[284] Rheology (gel stiffness of an elastic material) of PureCol Collagen product. Technical report, advanced biomatrix, 2013.

[285] Christopher B Raub, Vinod Suresh, Tatiana Krasieva, Julia Lyubovitsky, Justin D Mih, Andrew J Putnam, Bruce J Tromberg, and Steven C George. Noninvasive assessment of collagen gel microstructure and mechanics using multiphoton microscopy. *Biophysical journal*, 92(6):2212–22, March 2007.

[286] M. L. Palmeri, M. H. Wang, J. J. Dahl, K. D. Frinkley, and K. R. Nightingale. Quantifying Hepatic Shear Modulus In Vivo Using Acoustic Radiation Force. *Ultrasound in Medicine and Biology*, 34(4):546–558, 2008.

[287] Van C Mow and X Edward Guo. Mechano-electrochemical properties of articular cartilage: their inhomogeneities and anisotropies. *Annual review of biomedical engineering*, 4:175–209, 2002.

[288] Tanya Glozman and Haim Azhari. A method for characterization of tissue elastic properties combining ultrasonic computed tomography with elastography. *Journal of Ultrasound in Medicine*, 29(3):387–398, 2010.

[289] S Emerson and J Hedges. *Chemical Oceanography and the Marine Carbon Cycle*. 2008.

[290] T.R. Rettich, Rubin Battino, and Emmerich Wilhelm. Solubility of gases in liquids. 22. high-precision determination of henry's law constants of oxygen in liquid water fromt = 274 k tot = 328 k. *The Journal of Chemical Thermodynamics*, 32(9):1145 – 1156, 2000.

[291] T. R. Rettich, Rubin Battino, and Emmerich Wilhelm. Solubility of gases in liquids. xvi. henry's law coefficients for nitrogen in water at 5 to 50°c. *Journal of Solution Chemistry*, 13(5):335–348, 1984.

[292] K Mottaghy and A Hahn. Interfacial tension of some biological fluids: a comparative study. *Clinical Chemistry and Laboratory Medicine*, 19(5):267–272, 1981.

[293] Angana Banerjee Kharge, You Wu, and Carrie E. Perlman. Sulforhodamine B interacts with albumin to lower surface tension and protect against ventilation injury of flooded alveoli. *Journal of Applied Physiology*, 118(3):355–364, 2015.

[294] Aditi Chakrabarti and Manoj K. Chaudhury. Direct measurement of the surface tension of a soft elastic hydrogel: Exploration of elastocapillary instability in adhesion. *Langmuir*, 29(23):6926–6935, 2013.

[295] BA Hills. Supersaturation by counterperfusion and diffusion of gases. *Journal of Applied Physiology*, 42(5):758–760, 1977.

[296] Mélanie Jimenez, Nicolas Dietrich, Arnaud Cockx, et al. Experimental study of o2 diffusion coefficient measurement at a planar gas–liquid interface by planar laser-induced fluorescence with inhibition. *AIChE Journal*, 59(1):325–333, 2013.

[297] Rodolphe Sardeing, Pisut Painmanakul, and Gilles Hébrard. Effect of surfactants on liquid-side mass transfer coefficients in gas–liquid systems: a first step to modeling. *Chemical Engineering Science*, 61(19):6249–6260, 2006.

[298] Marupatch Jamnongwong, Karine Loubiere, Nicolas Dietrich, and Gilles Hébrard. Experimental study of oxygen diffusion coefficients in clean water containing salt, glucose or surfactant: Consequences on the liquid-side mass transfer coefficients. *Chemical engineering journal*, 165(3):758–768, 2010.

[299] Gilles Hebrard, Jikun Zeng, and Karine Loubiere. Effect of surfactants on liquid side mass transfer coefficients: a new insight. *Chemical Engineering Journal*, 148(1):132–138, 2009.

[300] Shelby B Hutchens and Alfred J Crosby. Soft-solid deformation mechanics at the tip of an embedded needle. *Soft matter*, 10(20):3679–84, May 2014.

[301] Daniel F McGinnis and John C Little. Predicting diffused-bubble oxygen transfer rate using the discrete-bubble model. *Water research*, 36(18):4627–4635, 2002.

[302] C.E. Brennen. *Cavitation and Bubble Dynamics*. Oxford engineering science series. Oxford University Press, 1995.

[303] Vladimir Lyakhovsky, Shaul Hurwitz, and Oded Navon. Bubble growth in rhyolitic melts: experimental and numerical investigation. *Bulletin of volcanology*, 58(1):19–32, 1996.

[304] Qingping Guo, Jin Wang, Chul B Park, and Masahiro Ohshima. A microcellular foaming simulation system with a high pressure-drop rate. *Industrial & engineering chemistry research*, 45(18):6153–6161, 2006.

[305] N.G Lensky, O Navon, and V Lyakhovsky. Bubble growth during decompression of magma: experimental and theoretical investigation. *Journal of Volcanology and Geothermal Research*, 129(1-3):7–22, January 2004.

[306] James E Gardner, Matthew Hilton, and Michael R Carroll. Experimental constraints on degassing of magma: isothermal bubble growth during continuous decompression from high pressure. *Earth and Planetary Science Letters*, 168(1):201–218, 1999.

[307] Kentaro Taki, Takashi Nakayama, Taichi Yatsuzuka, and Masahiro Ohshima. Visual observations of batch and continuous foaming processes. *Journal of Cellular Plastics*, 39(2):155–169, 2003.

[308] S Lovejoy, Hélene Gaonac'h, and D Schertzer. Bubble distributions and dynamics: The expansion-coalescence equation. *Journal of Geophysical Research: Solid Earth*, 109(B11), 2004.

[309] Wilhelm Ostwald. Studien über die bildung und umwandlung fester körper. *Z. phys. Chem*, 22:289–330, 1897.

[310] CT Nguyen, HM Gonnermann, Y Chen, C Huber, AA Maiorano, A Gouldstone, and J Dufek. Film drainage and the lifetime of bubbles. *Geochemistry, Geophysics, Geosystems*, 14(9):3616–3631, 2013.

[311] AK Chesters and G Hofman. Bubble coalescence in pure liquids. In *Mechanics and Physics of Bubbles in Liquids*, pages 353–361. Springer, 1982.

[312] C Huber, Y Su, CT Nguyen, A Parmigiani, HM Gonnermann, and J Dufek. A new bubble dynamics model to study bubble growth, deformation, and coalescence. *Journal of Geophysical Research: Solid Earth*, 119(1):216–239, 2014.

[313] Julien Bruchon and Thierry Coupez. A numerical strategy for the direct 3d simulation of the expansion of bubbles into a molten polymer during a foaming process. *International journal for numerical methods in fluids*, 57(8):977–1003, 2008.

[314] S F Jones, G M Evans, and K P U Galvin. Bubble nucleation from gas cavities a review. *Advances in Colloid and Interface Science*, pages 27–50, 1999.

[315] R Arieli, E Boaron, and A Abramovich. Combined effect of denucleation and denitrogenation on the risk of decompression sickness in rats Combined effect of denucleation and denitrogenation on the risk of decompression sickness in rats. *Journal of Applied Physiology*, (February 2009):1453–1458, 2013.

[316] E Newton Harvey, AH Whiteley, WD McElroy, DC Pease, and DK Barnes. Bubble formation in animals. ii. gas nuclei and their distribution in blood and tissues. *Journal of Cellular and Comparative Physiology*, 24(1):23–34, 1944.

[317] Vann Pollard, Marsh, Fife, Smith. Ascent rate, Post-dive exerciase and decompression sickness in the rat. *Undersea & hyperbaric medicine*, 22(4):367–376, 1995.

[318] Francis E Fox and Karl F Herzfeld. Gas bubbles with organic skin as cavitation nuclei. *The Journal of the Acoustical Society of America*, 26(6):984–989, 1954.

[319] Murray Strasberg. Onset of ultrasonic cavitation in tap water. *The Journal of the Acoustical Society of America*, 28(4):801–802, 1956.

[320] N Gaskins, RD Vann, GW Hobbs, M Swingle, S Lee, and D Needham. Surface tension and bubble formation in agar gelatin. In *UHMS Meeting Abstracts*, 2001.

[321] Anthony A Atchley and Andrea Prosperetti. The crevice model of bubble nucleation. *The Journal of the Acoustical Society of America*, 86(3):1065–1084, 1989.

[322] Peter Tikuisis and William Robert Johnson. *Conditions for Heterogeneous Nucleation in the Physiological Environment*. Department of National Defence, Defence and Civil Institute of Environmental Medicine, 1983.

[323] BA Hills. A hydrophobic oligolamellar lining to the vascular lumen in some organs. *Undersea biomedical research*, 19(2):107–120, 1992.

[324] Andreas Møllerløkken. *Reduction of vascular bubbles: methods to prevent the adverse effects of decompression*. PhD thesis, Det medisinske fakultet, 2008.

[325] Paul F Pilch, Tova Meshulam, Shiying Ding, and Libin Liu. Caveolae and lipid trafficking in adipocytes. *Clin Lipidol.*, 6(1):49–58, 2011.

[326] Robert G Parton and Kai Simons. The multiple faces of caveolae. *Nature reviews Molecular cell biology*, 8(3):185–194, 2007.

[327] Isidore Gersh, Gladys E Hawkinson, and Edith N Rathbun. Tissue and vascular bubbles after decompression from high pressure atmospheres–correlation of specific gravity with morphological changes. *Journal of Cellular and Comparative Physiology*, 24(1):35–70, 1944.

[328] Yeongyoon Kim, Chul B Park, P Chen, and Russell B Thompson. Origins of the failure of classical nucleation theory for nanocellular polymer foams. *Soft Matter*, 7(16):7351–7358, 2011.

[329] James J Feng and Christopher A Bertelo. Prediction of bubble growth and size distribution in polymer foaming based on a new heterogeneous nucleation model. *Journal of Rheology (1978-present)*, 48(2):439–462, 2004.

[330] SN Leung, CB Park, and H Li. Numerical simulation of polymeric foaming processes using modified nucleation theory. *Plastics, rubber and composites*, 2013.

[331] L Gránásy. Diffuse interface approach to vapour condensation. *EPL (Europhysics Letters)*, 24(2):121, 1993.

[332] Kishore Joshi, James G Lee, Muhammad A Shafi, and Raymond W Flumerfelt. Prediction of Cellular Structure in Free Expansion of Viscoelastic Media. *Journal of applied polymer science*, 67(8):1353–1368, 1998.

[333] Aaron Naber, Chun Liu, and James J Feng. The nucleation and growth of gas bubbles in a Newtonian fluid: an energetic variational phase field approach. *Contemporary Mathematics*, 466(50390095):95–120, 2008.

[334] Adam Craig Burley. *Toward a Fundamental Understanding of Bubble Nucleation in Polymer Foaming*. PhD thesis, The Ohio State University, 2012.

[335] Zhihua Guo, Adam C Burley, Kurt W Koelling, Isamu Kusaka, L James Lee, and David L Tomasko. Co2 bubble nucleation in polystyrene: Experimental and modeling studies. *Journal of Applied Polymer Science*, 125(3):2170–2186, 2012.

[336] B. Wienke. *Science of Diving: Concepts and Applications*. CRC Press, 2015.

[337] R Arieli and A Marmur. Decompression sickness bubbles: are gas micronuclei formed on a flat hydrophobic surface? *Respiratory physiology & neurobiology*, 177(1):19–23, 2011.

[338] D. E. Yount. A microscopic investigation of bubble formation nuclei. *The Journal of the Acoustical Society of America*, 76(5):1511, 1984.

[339] Saul Goldman. The stability of bubbles formed from supersaturated solutions, and homogeneous nucleation of gas bubbles from solution, both revisited. *The Journal of Physical Chemistry B*, 112(51):16701–16709, 2008.

[340] E.G. Perkins and American Oil Chemists' Society. *Analysis of lipids and lipoproteins*. American Oil Chemists' Society, 1975.

[341] Malgorzata Czarny, Giusy Fiucci, Yaakov Lavie, Yoshiko Banno, Yoshinori Nozawa, and Mordechai Liscovitch. Phospholipase d2: functional interaction with caveolin in low-density membrane microdomains. *FEBS letters*, 467(2-3):326–332, 2000.

[342] Noah S Tan. *Engineering a Tissue Mimic for Predictive Nanoparticle Assessment*. PhD thesis, UCL (University College London), 2015.

[343] Erich A Müller and Keith E Gubbins. Molecular simulation study of hydrophilic and hydrophobic behavior of activated carbon surfaces. *Carbon*, 36(10):1433–1438, 1998.

[344] Benjamin Rotenberg, Amish J Patel, and David Chandler. Molecular explanation for why talc surfaces can be both hydrophilic and hydrophobic. *Journal of the American Chemical Society*, 133(50):20521–20527, 2011.

[345] Alexandrine During, Guillaume Penel, and Pierre Hardouin. Understanding the local actions of lipids in bone physiology. *Progress in lipid research*, 59:126–146, 2015.

[346] Christian Couppe, Philip Hansen, Mads Kongsgaard, Vuokko Kovanen, Charlotte Suetta, Per Aagaard, Michael Kjaer, and S Peter Magnusson. Mechanical properties and collagen cross-linking of the patellar tendon in old and young men. *Journal of applied physiology*, 107(3):880–886, 2009.

[347] Min-Xin Fu, Kevin J Wells-Knecht, James A Blackledge, Thorpe J Lyons, Suzanne R Thorpe, and John W Baynes. Glycation, glycoxidation, and cross-linking of collagen by glucose: kinetics, mechanisms, and inhibition of late stages of the maillard reaction. *Diabetes*, 43(5):676–683, 1994.

[348] MJ Christine Kent, Nicholas D Light, and Allen J Bailey. Evidence for glucose-mediated covalent cross-linking of collagen after glycosylation in vitro. *Biochemical Journal*, 225(3):745–752, 1985.

[349] Simon P Robins, Massami Shimokomaki, and Allen J Bailey. The chemistry of the collagen cross-links. age-related changes in the reducible components of intact bovine collagen fibres. *Biochemical Journal*, 131(4):771–780, 1973.

[350] H Hofmann, PP Fietzek, and K Kühn. The role of polar and hydrophobic interactions for the molecular packing of type i collagen: a three-dimensional evaluation of the amino acid sequence. *Journal of molecular biology*, 125(2):137–165, 1978.

[351] Lisa M Larkin, Sarah Calve, Tatiana Y Kostrominova, and Ellen M Arruda. Structure and functional evaluation of tendon-skeletal muscle constructs engineered in vitro. *Tissue engineering*, 12(11):3149–3158, 2006.

[352] EN Harvey and AH Whiteley. The effect of mechanical disturbance on bubble formation in single cells and tissue after saturation with high gas pressures. *Journal of Cellular . . .* , pages 325–337, 1946.

[353] Hans-Ulrich Gremlich and Bing Yan. *Infrared and Raman spectroscopy of biological materials*. CRC Press, 2000.

[354] Jemma G Kerns, Kevin Buckley, John Churchwell, Anthony W Parker, Pavel Matousek, and Allen E Goodship. Is the collagen primed for mineralization in specific regions of the turkey tendon? an investigation of the protein–mineral interface using raman spectroscopy. *Analytical chemistry*, 88(3):1559–1563, 2016.

[355] Nakul C Maiti, Mihaela M Apetri, Michael G Zagorski, Paul R Carey, and Vernon E Anderson. Raman spectroscopic characterization of secondary structure in natively unfolded proteins: α-synuclein. *Journal of the American Chemical Society*, 126(8):2399–2408, 2004.

[356] Qihong Zhang, KL Andrew Chan, Guojin Zhang, Timothy Gillece, Laurence Senak, David J Moore, Richard Mendelsohn, and Carol R Flach. Raman microspectroscopic and dynamic vapor sorption characterization of hydration in collagen and dermal tissue. *Biopolymers*, 95(9):607–615, 2011.

[357] TT Nguyen, C Gobinet, J Feru, S Brassart Pasco, M Manfait, and O Piot. Characterization of type i and iv collagens by raman microspectroscopy: Identification of spectral markers of the dermo-epidermal junction. *Journal of Spectroscopy*, 27(5-6):421–427, 2012.

[358] Joke De Gelder, Kris De Gussem, Peter Vandenabeele, and Luc Moens. Reference database of raman spectra of biological molecules. *Journal of Raman Spectroscopy*, 38(9):1133–1147, 2007.

[359] K Czamara, K Majzner, MZ Pacia, K Kochan, A Kaczor, and M Baranska. Raman spectroscopy of lipids: a review. *Journal of Raman Spectroscopy*, 46(1):4–20, 2015.

[360] EA Hemmingsen, BB Hemmingsen, JO Owe, and HT Andersen. Lack of bubble formation in hypobarically decompressed cells. *Aviation, space, and environmental medicine*, 58(8):742–746, 1987.

[361] Abdou Rachid Thiam, Robert V Farese Jr, and Tobias C Walther. The biophysics and cell biology of lipid droplets. *Nature reviews Molecular cell biology*, 14(12):775–786, 2013.

[362] Sally Martin and Robert G Parton. Lipid droplets: a unified view of a dynamic organelle. *Nature reviews Molecular cell biology*, 7(5):373–378, 2006.

[363] Guillaume Lajoinie, Ine De Cock, Constantin C Coussios, Ine Lentacker, Séverine Le Gac, Eleanor Stride, and Michel Versluis. In vitro methods to study bubble-cell interactions: Fundamentals and therapeutic applications. *Biomicrofluidics*, 10(1):011501, 2016.

[364] Eva Bianconi, Allison Piovesan, Federica Facchin, Alina Beraudi, Raffaella Casadei, Flavia Frabetti, Lorenza Vitale, Maria Chiara Pelleri, Simone Tassani, Francesco Piva, et al. An estimation of the number of cells in the human body. *Annals of human biology*, 40(6):463–471, 2013.

[365] Wayne A Gerth and David J Doolette. VVal-18 and VVal-18M Thalmann Algorithm Air Decompression Tables and Procedures. Technical report, Navy Experimental Diving Unit (NEDU), 2007.

[366] Anthony J McGoron, Pankajam Nair, and Roy W Schubert. Michaelis-menten kinetics model of oxygen consumption by rat brain slices following hypoxia. *Annals of biomedical engineering*, 25(3):565–572, 1997.

[367] RJ Shipley, Adam J Davidson, K Chan, Julian B Chaudhuri, SL Waters, and Marianne J Ellis. A strategy to determine operating parameters in tissue engineering hollow fiber bioreactors. *Biotechnology and bioengineering*, 108(6):1450–1461, 2011.

[368] Donald G. Buerk and Gerald M. Saidel. Local kinetics of oxygen metabolism in brain and liver tissues. *Microvascular Research*, 16(3):391 – 405, 1978.

[369] Brett A Wagner, Sujatha Venkataraman, and Garry R Buettner. The rate of oxygen utilization by cells. *Free Radical Biology and Medicine*, 51(3):700–712, 2011.

[370] Ian Streeter and Umber Cheema. Oxygen consumption rate of cells in 3d culture: the use of experiment and simulation to measure kinetic parameters and optimise culture conditions. *Analyst*, 136(19):4013–4019, 2011.

[371] Albert A Bühlmann. *Decompression—Decompression Sickness*. Springer Science & Business Media, 2013.

[372] David J Doolette and Wayne A Gerth. Vval-79 maximum permissible tissue tension table for thalmann algorithm support of air diving. Technical report, Navy experimental diving unit, 2012.

[373] Virginie Papadopoulou, Meng-Xing Tang, Costantino Balestra, Robert J Eckersley, and Thodoris D Karapantsios. Circulatory bubble dynamics: from physical to biological aspects. *Advances in colloid and interface science*, 206:239–249, 2014.

[374] A Arefmanesh and S G Advani. Diffusion-induced growth of a gas bubble in a viscoelastic fluid. *Rheologica Acta*, 30:274–283, 1991.

[375] Johns. E. Bubble nucleation in tissue constructs. Master's thesis, UCL CoMPLEX, 2016.